UNIVERSITY OF THESSALY

SCHOOL OF ENGINEERING

DEPARTMENT OF MECHANICAL ENGINEERING

Ph.D. Thesis

Rarefied gas pipe network analysis via kinetic theory

by

Serafeim G. Misdanitis

M.Sc. Mechanical Engineer U.Th.

Department of Mechanical Engineering

University of Thessaly

A Thesis Report Submitted for the Partial Fulfillment of the Requirements for the Degree of

Doctor of Philosophy

September 2021

The approval of the present Ph.D. Thesis by the Department of Mechanical Engineering of the University of Thessaly does not imply acceptance of the author's opinions. (Law 5343/32, article 202, paragraph 2).

i

Certified by the members of the Dissertation Committee

1st member Professor Valougeorgis Dimitris
(Supervisor)   Department of Mechanical Engineering
               University of Thessaly

2nd member Professor Bontozoglou Vasilis
               Department of Mechanical Engineering
               University of Thessaly

3rd member Professor Mathioulakis Dimitris
               Department of Mechanical Engineering
               National Technical University of Athens

4th member Professor Andritsos Nikolaos
               Department of Mechanical Engineering
               University of Thessaly

5th member Professor Karakasidis Theodoros
               Department of Civil Engineering
               University of Thessaly

6th member Professor Liberopoulos George
               Department of Mechanical Engineering
               University of Thessaly

7th member Professor Pelekasis Nikos
               Department of Mechanical Engineering
               University of Thessaly

To my loving parents . . .

Acknowledgments

First of all, I would like to express my respect and gratitude to my supervisor Professor Dimitris Valougeorgis. Without his constant support and mentorship, this dissertation would not have been completed. His patience and significant assistance, provided throughout the course of our cooperation, are the two key factors that contributed to the completion of this thesis.

I am also grateful to the rest members of the thesis committee: Prof. Vasilis Bontozoglou, Prof. Dimitrios Mathioulakis, Prof. Nikolaos Andritsos, Prof. Theodoros Karakasidis, Prof. George Liberopoulos and Prof. Nikos Pelekasis for dedicating their time to review my thesis and provide useful and insightful comments.

Besides the thesis committee, I would like to thank all my friends and colleagues at the Laboratory of Transport Phenomena and Process Equipment. First, I would like to express my gratitude to Dr. Steryios Naris, Dr. Stelios Varoutis, Dr. Sarantis Pantazis, Dr. Christos Tantos and Dr. John Lihnaropoulos for sharing their knowledge with me. Special thanks to Dr. Giorgos Tatsios, Dr. Alexandros Tsimpoukis and Thanasis Basdanis for all the stimulating discussions and great times we had during our collaboration. I would also like to offer my special gratitude to Dr. Nikos Vasileiadis whose help and support was of great importance for the completion of the final stages of the present thesis, as well as to Mr. Christos Botsikas for all the moral boost, the support and of course his programing skills for the implementation of the graphical interface.

I would also like to thank Despoina Markidou for her endless patience and encouragement throughout these years. Finally, above all, I am grateful to my parents, Georgios and Eleni Misdaniti, as well as to my brother Yiannis, for their love and continuous support. This dissertation would not have been completed without their help.

Serafeim G. Misdanitis

Rarefied gas pipe network analysis via kinetic theory

Serafeim G. Misdanitis

Department of Mechanical Engineering

University of Thessaly

September 2021

Steady-state isothermal rarefied gas flows in long circular channels have been extensively investigated via linear kinetic theory since 1960s, implementing various semi-analytical and numerical schemes. It is noted that linear kinetic modeling is applicable, when the local pressure gradient along the tube is small. This condition is satisfied in the case of long tubes (e.g. the ratio of the length over the radius to be approximately larger than 100), resulting to a low speed isothermal flow even if the overall difference between the inlet and outlet pressure is large. Overall it has been demonstrated that for rarefied gas flows in long channels, linear kinetic modeling, as described by suitable kinetic model equations, may take advantage of all flow characteristics and properties and yield very accurate results in the whole range of the Knudsen number with minimal computational effort.

In many applications however, the rarefied gaseous distribution system consists not only of a single channel but of many channels accordingly combined to form a network. Such distribution systems are commonly found in several technological fields including vacuum pumping, metrology, industrial aerosol, porous media, and micro-fluidics. It is pointed out that computational algorithms dedicated to the design of gas pipe networks (e.g., compressed air, natural gas, etc.) in the viscous regime are well developed while corresponding tools for the design of gaseous pipe networks operating under any (e.g. low, medium and high) vacuum conditions are very limited.

In order to achieve this, kinetic results obtained for the rarefied flow through each tube of the network are successfully integrated into a typical network algorithm solving the whole distribution system. In particular, for channels with $L/D_h > 50$, where L is the length and D_h the hydraulic diameter, the channel is considered as long and the available kinetic conductance results based on the theory of the infinite long channels are applied. For channels of moderate length $5 < L/D_h < 50$, the end correction theory is introduced. This theory has been recently successfully implemented to

define the fictitious increment length which must be added to the channel length in order to provide accurate results for the conductance by taking into account the channel end effects. Thus, the kinetic data base has been enriched with the values of the increment length in terms of the gas rarefaction. Finally, for short channels, i.e. $L/D_h < 5$, the above theory is not valid and depending on the local pressure gradient, extensive simulations based on either linear or non-linear kinetic theory have been performed to provide a complete set of results for the channel conductance in terms of gas rarefaction, pressure difference and channel length. These simulations are computationally very expensive.

The complete data base consists of a very dense grid to allow accurate representation of the operational conditions of an arbitrary gas pipe network. Interpolation between the available data points is performed by cubic splines for the flow rates in the case of long channels, by high order curve fitting for the increment lengths for the case of channels of moderate length and trilinear interpolation for the flow rate in terms of the pressure, length and rarefaction in the case of short channels. Next, the enriched data base has been successfully integrated into the network algorithm which is build to cover distribution systems consisting of channels of any length.

The developed Algorithm for Rarefied gas flow in Arbitrary Distribution Networks (ARIADNE) includes first the drawing of the network in a graphical environment and then the formulation and solution of the governing equations describing the flow conditions of the distribution system. In the drawing process of the network, the user, through the developed graphical interface, is capable of providing the input data including the coordinates of the nodes in a 3D space, the length and the diameter of the pipe elements, the pressure heads of the fixed-grade nodes and information for the type of the gas and its properties. Even more, the demands (if any) at the nodes may also be provided. Once the geometry of the network is fixed, an iterative process is initiated between the pressure drop equations and the system of mass and energy conservation equations in order to successfully handle gas pipe networks operating from the free molecular, through the transition up to the slip and hydrodynamic regimes.

The feasibility and the effectiveness of the developed algorithm is tested by simulating various distribution systems in the hydrodynamic regime and comparing the corresponding results with the ones derived by the typical hydrodynamic solver report-

x

ing excellent agreement in terms of the mass flow rate (and the conductance) through the pipes as well as the pressure heads at the nodes of the network. Further more, some preliminary comparisons with ITERVAC, (which is a computational tool for the estimation of the mass flow through ducts at isothermal conditions in a wide flow regime, however, it is based mainly on empirical expressions), for networks consisting of long channels resulted to very good agreement between the two approaches.

It is hoped that the present work will constitute a significant part of a more general algorithm which will be used as a significant engineering tool in the design and optimization of gaseous distribution networks operating under any rarefied conditions.

Ανάλυση αραιοποιημένης ροής αερίων σε δίκτυα σωληνώσεων μέσω κινητικής θεωρίας

Σεραφείμ Γ. Μισδανίτης

Τμήμα Μηχανολόγων Μηχανικών

Πανεπιστήμιο Θεσσαλίας

Σεπτέμβριος 2021

Το θέμα της παρούσας διδακτορικής διατριβής εστιάζει στην ανάπτυξη ενός αλγορίθμου προσομοίωσης δικτύων αερίων υπό αραιοποιημένες συνθήκες μέσω κινητικής θεωρίας. Η περιοχή αυτή είναι γνωστή σαν αραιοποιημένη αεροδυναμική (rarefied gas dynamics) με πολλές τεχνολογικές εφαρμογές εκ των οποίων τα μικρο-ηλεκτρομηχανολογικά συστήματα και η τεχνολογία κενού να είναι αυτές που εξελίσσονται με πολύ γρήγορους ρυθμούς. Σημειώνεται ότι ενώ στο συνεχές όριο, υπολογιστικά πακέτα (αλγόριθμοι) σχεδιασμού δικτύων σωληνώσεων (όπως δίκτυα συμπιεσμένου αέρα ή φυσικού αερίου, κτλ.) είναι ευρέως διαδεδομένα, αντίστοιχα υπολογιστικά εργαλεία για το σχεδιασμό δικτύων σε συνθήκες χαμηλής πίεσης (υψηλού, μέτριου ή χαμηλού κενού) είναι αρκετά περιορισμένα. Αξιοποιώντας την πολύχρονη εμπειρία του Εργαστηρίου Φυσικών & Χημικών Διεργασιών σε αριθμητικές μεθόδους μεσοκλίμακας, στο πλαίσιο της διατριβής αναπτύσσεται και εφαρμόζεται σύνθετο λογισμικό προσομοίωσης κυκλοφορίας αραιοποιημένων αερίων σε δίκτυα σωληνώσεων σε όλο το εύρος του αριθμού Knudsen.

Για την υλοποίηση αυτού του εγχειρήματος δημιουργείται εκτενής βάση δεδομένων για πλήρως ανεπτυγμένες και αναπτυσσόμενες ροές μέσα από αγωγούς μεγάλου, μεσαίου και μικρού μήκους, συμπεριλαμβανομένων των φαινομένων εισόδου/εξόδου στα άκρα των αγωγών. Αυτό επιτυγχάνεται επιλύοντας κινητικές εξισώσεις με αναβαθμισμένους και παράλληλους αλγορίθμους διακριτών μοριακών ταχυτήτων, ενώ η χρήση του λογισμικού υποβοηθείται από ένα γραφικό περιβάλλον το οποίο αναπτύχθηκε για το σκοπό αυτό.

Η τελική μορφή του αλγορίθμου αποτελείται από α) την εισαγωγή των γεωμετρικών χαρακτηριστικών και λειτουργικών χαρακτηριστικών του δικτύου προς επίλυση, β) τον ορισμό των βρόχων και των ψευδο-βρόχων, γ) τη διαμόρφωση και επίλυση των εξισώσεων διατήρησης μάζας και ενέργειας, δ) τη βάση δεδομένων που έχει προκύψει από αποτελέσματα κινητικών εξισώσεων και χρησιμοποιείται

για την επίλυση των εξισώσεων διατήρησης και ε) τα αποτελέσματα του αλγο-
ρίθμου τα οποία αναφέρονται σε τιμές πίεσης στους κόμβους του δικτύου καθώς
και σε τιμές μαζικής και ογκομετρικής παροχής μέσα από τις σωληνώσεις του
δικτύου.

Πιο συγκεκριμένα, το σύστημα των εξισώσεων το οποίο περιγράφει το δίκτυο
αποτελείται από τις εξισώσεις πτώσης πίεσης σε κάθε έναν από τους αγωγούς του
δικτύου σε συνδυασμό με τις εξισώσεις διατήρησης μάζας σε κάθε έναν από τους
κόμβους του δικτύου. Στην περίπτωση που το δίκτυο είναι πλήρως ορισμένο, οι
εξισώσεις πτώσης πίεσης ανάγονται σε ισοζύγια ενέργειας ανάμεσα στους κλει-
στούς βρόχους του δικτύου και τους ψευδο-βρόχους που ενώνουν κόμβους γνωστών
ιδιοτήτων (π.χ. γνωστές τιμές πίεσης). Το σύστημα των εξισώσεων λύνεται επα-
ναληπτικά έχοντας ως άγνωστο τις τιμές των παροχών υποθέτοντας αρχικά τις
τιμές των πιέσεων στους κόμβους του δικτύου, όπου αυτές δεν είναι από την αρχή
γνωστές. Σε κάθε βήμα, μετά την επίλυση του συστήματος των εξισώσεων, οι
τιμές των πιέσεων ανανεώνονται σύμφωνα με τις τιμές της αδιάστατης παροχής
κάνοντας χρήση των σχέσεων πτώσης πίεσης για κάθε έναν από τους αγωγούς
του δικτύου. Τα βήματα αυτά αποτελούν τον πυρήνα μιας επαναληπτικής δια-
δικασίας η οποία τερματίζεται με την ικανοποίηση του κριτηρίου σύγκλισης το
οποίο εφαρμόζεται στις τιμές των πιέσεων στους κόμβους.

Το υπολογιστικό πακέτο φέρει το όνομα ARIADNE (Algorithm for Rarefied gas
flow in Arbitrary Distribution Networks). Η αποτελεσματικότητα και η ακρίβεια
του αλγορίθμου ελέγχθηκε με την προσομοίωση διαφόρων δικτύων σωληνώσε-
ων στο υδροδυναμικό όριο, συγκρίνοντας τα αποτελέσματα με αντίστοιχα που
προκύπτουν από τυπικό αλγόριθμο που βασίζεται στις υδροδυναμικές εξισώσεις
επιστρέφοντας πολύ καλή συμφωνία τόσο στις παροχές των αγωγών, όσο και
στις πιέσεις των κόμβων του δικτύου. Επιπλέον, στην ελεύθερη μοριακή περιοχή
και στην μεταβατική πραγματοποιήθηκαν συγκρίσεις με το λογισμικό ITERVAC,
το οποίο είναι ένας ημι-εμπειρικός αλγόριθμος, επιστρέφοντας πολύ καλή συμφω-
νία. Τέλος, το λογισμικό εφαρμόστηκε στην επίλυση δικτύων που προσεγγίζουν
το σύστημα άντλησης αερίων του αντιδραστήρα σύντηξης ITER.

Με βάση τα παραπάνω η παρούσα διδακτορική διατριβή αναμένεται να απο-
τελέσει τον πυρήνα ενός γενικότερου αλγορίθμου για τη μελέτη ροών αερίων σε
δίκτυα σωληνώσεων σε όλο το εύρος αραιοποίησης.

Contents

CONTENTS

List of Algorithms

List of Tables

List of Figures

Nomenclature

Roman Symbols

B Big base of trapezoidal channel [m]

b Small base of trapezoidal channel [m]

C Channel conductance [lt/s]

$\mathbf{c}$ Dimensionless molecular velocity vector

F Complex function

f Molecular distribution function

f^M Maxwellian distribution function

f_{ne} Number of fixed-grade nodes of the network

G Dimensionless flow rate for long piping elements

H_{ch} Distance between plates / Height of rectangular channel [m]

h Perturbation of the distribution function

I_0 Modified Bessel function of the 1st kind and 0th order

k_B Boltzmann constant [J/K]

Kn   Knudsen number

L_{dev} Development length

L_{left} Left container size

L Channel length [m]

L_0 Reference length [m]

L_{right} Right container size

l_{ne} Number of closed loops of the network

NOMENCLATURE

$\dot{M}$	Dimensional flow rate [kg/s]
$\dot{M}_{FM}$	Free molecular solution for zero length channel
Ma	Mach number
m	Molar mass [kg]
n_{ne}	Number of junction nodes of the network
$n\,(\mathbf{x}, t)$	Dimensional number density [m^{-3}]
n_0	Reference number density [m^{-3}]
p_{ne}	Number of piping elements of the network
P_{in}	Upstream pressure [Pa]
Po	Poiseuille number
P_{out}	Downstream pressure [Pa]
$\hat{P}\,(\mathbf{x}, t)$	Dimensional pressure [Pa]
Pr	Prandtl number
P_0	Reference pressure [Pa]
$P_{ij}\,(\mathbf{x}, t)$	Dimensional stress tensor [N/m^2]
$P_{ij}\,(x, t)$	Dimensionless stress tensor
$Q\,(f, f')$	Collision operator of the Boltzmann equation
$\hat{\mathbf{q}}\,(\mathbf{x}, t)$	Dimensional heat flux vector [W/m^2]
$\mathbf{q}\,(x, t)$	Dimensionless heat flux vector (or perturbation)
R_g	Ideal gas law constant (specific for each gas)
Re	Reynolds number
$R\,(\boldsymbol{\xi}' \to \boldsymbol{\xi})$	Gas-wall interaction scattering kernel

R_u	Universal gas constant [J/(kg·K)]
$T(\mathbf{x}, t)$	Dimensional temperature [K]
T_0	Reference temperature [K]
$\hat{\mathbf{u}}(\mathbf{x}, t)$	Dimensional macroscopic velocity vector [m/s]
$\mathbf{u}(x, t)$	Dimensionless macroscopic velocity vector (or perturbation)
W	Dimensionless flow rate for short piping elements
W_{ch}	Width of rectangular channel [m]
$\hat{\mathbf{x}}$	Dimensional position vector
$\mathbf{x}$	Dimensionless position vector
X_P	Dimensionless pressure gradient

Greek Symbols

A'	Surface of piping element [m^2]
Γ'	Perimeter of piping element [m]
α	Accommodation coefficient
γ	A simply closed curve on a complex plane
ΔL	Effective length increment [m]
ΔP	Pressure difference [Pa]
ΔT	Temperature difference [K]
δ	Rarefaction parameter
δ_D	Dirac function
δ_{ij}	Kronecker delta

NOMENCLATURE

ι	Unit imaginary number $\sqrt{-1}$
λ	Molecular mean free path [m]
μ	Dynamic viscosity [Pa·s]
ν	Collision frequency [s^{-1}]
$\boldsymbol{\xi}$	Dimensional molecular velocity vector [m/s]
π	$\simeq 3.14159265359\ldots$
$\rho(x, t)$	Dimensionless number density (or perturbation)
σ_p	Viscous slip coefficient
$\tau(x, t)$	Dimensionless temperature (or perturbation)
υ_0	Most probable molecular velocity [m/s]
ω	Inverse Power Law parameter

Superscripts

j	Superscript index

Subscripts

0	Index denoting reference conditions
1	Index denoting upstream conditions
2	Index denoting downstream conditions
EE	Index referring to results based on the end-effect theory
FD	Index referring to results based on the theory for fully developed flows
FM	Index referring to results for the free molecular regime

LIN   Index referring to results based on linear theory

NL   Index referring to results based on non-linear theory

Other Symbols

$\mathcal{H}$ The H-theorem

$\oint_\gamma$ Integration around a curve γ

Acronyms

ARIADNE   Algorithm for Rarefied gas flow in Arbitrary Distribution Networks

CSS   Cascading Style Sheets

CUDA   Compute Unified Device Architecture

DFS   Depth-first search algorithm

DSMC   Direct Simulation Monte Carlo

DVM   Discrete Velocity (or Discrete Ordinates) Method

GPL   GNU General Public License

GPU   Graphics Processing Unit

GUI   Graphical User Interface

MEMS   Micro-Electro-Mechanical Systems

MLI   Multi-layer Insulation

UHV   Ultra High Vacuum

VBS   Visual Basic Script

1

Introduction and literature review

1.1 General concepts

The importance of gas flows, in a wide variety of technological applications, is encountered in daily basis. In most cases, the physics explaining their behavior is adequately modeled by employing the equations of mass, momentum and energy equilibrium, combined with the Newton-Fourier-Fick constitutive equations. However, this Navier-Stokes type formulation, which is subject to the underlying assumption that the gas must be considered as a continuum medium, fails when the mean free path is comparable to a characteristic length of the problem. Such conditions may be present in gas flows in sufficiently low pressure or in channels of very small dimensions. In these cases alternative formulations are needed.

In transport phenomena where the continuum approach fails and the typical macroscopic equations are not applicable, the gas is considered to be far from local thermodynamic equilibrium in a "rarefied" state and it is required not only to take into account the molecular nature of the gas, but the intermolecular collisions taking place as well. In order to properly describe such flows, concepts derived from statistical mechanics and kinetic theory of gases need to be involved. Our purpose is to provide a description of the macroscopic behavior, starting from the microscopic equations which govern the motion of molecules from which the gas is constituted [76]. The governing equation in this regime is the Boltzmann equation, which is an evolution equation of the unknown particle distribution function consisting of seven independent variables, namely the time, the position vector and the molecular velocity

vector. The Boltzmann equation is nonlinear with a very complex collision term. It can be solved analytically only for very specific situations, while it is commonly solved numerically after its complex collisions term is substituted by a reliable collision model.

Despite the complexity of the Boltzmann equation, it is important to extend our studies to such cases, since many emerging technologies would benefit. Vacuum gas flows, for example, are encountered in many applications, ranging from simple pressure sensors [59] to the maze-like complexity met in vacuum systems of fusion reactors [26]. Also, the creation of micro- and nanometer-sized devices is very important since they offer increased reliability, low cost and high efficiency [50, 109] in comparison to their normal-sized counterparts. In addition, high altitude aerodynamics need to be investigated very carefully for the correct operation and maneuverability of spacecrafts [39] and satellites [83]. Thus, accurate and computationally efficient simulations involving the solution of the Boltzmann equations or alternatively of reliable kinetic model equations are of high importance in the design, manufacturing and optimization of many devices involving transport phenomena far from local equilibrium.

1.2 Historical overview and basic principles of kinetic theory

The beginning of the statistical approach to the physical description of gases is attributed to Maxwell [90] and Boltzmann [15]. Maxwell was the first one to point out that not all molecules move with the same velocity, but in a random manner. Then, he proceeded to calculate the distribution of molecular velocities and his findings were extended by Boltzmann. The distribution function, describing a gas in local equilibrium, well-known as the "Maxwellian" (or, more correctly, Maxwell-Boltzmann) distribution, is a Gaussian according to the local conditions and it is given by

$$f^M(\mathbf{x}, \boldsymbol{\xi}, t) = n(\mathbf{x}, t) \left[\frac{m}{2\pi k_B T(\mathbf{x}, t)} \right]^{3/2} \exp\left\{ -\frac{m[\boldsymbol{\xi} - \mathbf{u}(\mathbf{x}, t)]^2}{2k_B T(\mathbf{x}, t)} \right\} \qquad (1.2.1)$$

Here, f^M is the Maxwellian distribution and it is given at physical point $\mathbf{x}$, time t and for the molecular velocity vector $\boldsymbol{\xi}$ in terms of the local macroscopic properties of number density $n(\mathbf{x}, t)$, macroscopic (bulk) velocity $\mathbf{u}(\mathbf{x}, t)$ and temper-

ature $T(\mathbf{x}, t)$. The parameter m denotes the molar mass and $k_B = 1.38065 \times 10^{-23}(\text{kg} \cdot \text{m}^2)/(\text{K} \cdot \text{sec}^2)$ is a constant named after Boltzmann.

By further investigating these phenomena, Boltzmann managed to derive an integro-differential equation describing the evolution of molecular velocity distribution in time and space. This derivation is based on two main assumptions *i)* only binary collisions take place (which is true for low densities) and *ii)* the hypothesis of "molecular chaos" (stosszahlansatz, assumption about the collision number), according to which a two-particle distribution function may be substituted by a product of two one-particle distribution functions. As a result, the term molecular chaos refers to the statistical independence of molecules [10]. The Boltzmann equation is

$$\frac{\partial f}{\partial t} + \boldsymbol{\xi} \cdot \frac{\partial f}{\partial \mathbf{x}} + \mathbf{F} \cdot \frac{\partial f}{\partial \boldsymbol{\xi}} = Q\left(f, f'\right) \tag{1.2.2}$$

where $\mathbf{F}$ is an external force vector and the collision term is given by

$$Q\left(f, f'\right) = \int \int \int \left(f' \, f'_* - f \, f_*\right) g b db d\epsilon d\boldsymbol{\xi}_* \tag{1.2.3}$$

and $g = |\boldsymbol{\xi} - \boldsymbol{\xi}_*|$ represents the relative velocity, b is the impact parameter and ϵ determines the azimuthal angle, as defined in [31]. The collision term contains the gain part which refers to the contribution of particles obtaining a velocity in $\boldsymbol{\xi} + d\boldsymbol{\xi}$ after a collision and the loss part which refers to particles with pre-collisional velocities in $\boldsymbol{\xi} + d\boldsymbol{\xi}$ but scattering to other velocity vectors after the collision. Boltzmann also proved that the Maxwellian distribution is a solution of this equation when the gas is in local equilibrium. The existence and uniqueness of the solution for the Boltzmann equation were confirmed for Hard Sphere molecules in 1910 by Hilbert [48]. Grad [40] also proved that solving the Boltzmann equation is equivalent of solving the Navier-Stokes equations, in different, however, time and space scale. Even more, by applying the appropriate projections, the Boltzmann equation also leads to the conservation principles.

In the case of hydrodynamic equations, the values of the transport coefficients, namely the viscosity, heat conductivity and diffusion coefficient, are required to obtain a closed system. The estimation of these values is linked to the determination of the intermolecular potential. In the case where it is specified, the complete solution of

the problem can be obtained without the need for the determination of the transport coefficients.

In the same works, Boltzmann further investigated these phenomena and formulated the H-Theorem, which practically expresses the irreversibility of physical processes. The quantity

$$\mathcal{H} = \int\limits_{-\infty}^{\infty} f \log f d\boldsymbol{\xi} \qquad (1.2.4)$$

if integrated in the physical space, must always decrease (or remain constant in the special case of a Maxwellian distribution function). This is directly connected to the second law of thermodynamics and the entropy increase according to which molecules tend to approach the equilibrium state, where molecular velocities follow the local Maxwell distribution, since this is the state of maximum entropy.

By solving the Boltzmann equation for the unknown distribution function, any quantity of practical interest may be determined by appropriate moments of the distribution function as follows:

- Number density

$$n(\mathbf{x}, t) = \int\limits_{-\infty}^{\infty} f d\boldsymbol{\xi} \qquad (1.2.5)$$

- Velocity vector

$$\hat{\mathbf{u}}(\mathbf{x}, t) = \frac{1}{n(\mathbf{x}, t)} \int\limits_{-\infty}^{\infty} \boldsymbol{\xi} f d\boldsymbol{\xi} \qquad (1.2.6)$$

- Pressure

$$P(\mathbf{x}, t) = \frac{m}{3} \int\limits_{-\infty}^{\infty} (\boldsymbol{\xi} - \mathbf{u})^2 f d\boldsymbol{\xi} \qquad (1.2.7)$$

- Stress tensor

$$\hat{P}_{ij}(\mathbf{x}, t) = m \int\limits_{-\infty}^{\infty} (\xi_i - u_i)(\xi_j - u_j) f d\boldsymbol{\xi} \qquad (1.2.8)$$

- Temperature

$$T\left(\mathbf{x}, t\right) = \frac{m}{3k_B n\left(\mathbf{x}, t\right)} \int\limits_{-\infty}^{\infty} \left(\boldsymbol{\xi} - \mathbf{u}\right)^2 f d\boldsymbol{\xi} \qquad (1.2.9)$$

- Heat flux vector

$$\hat{\mathbf{q}}\left(\mathbf{x}, t\right) = \frac{m}{2} \int\limits_{-\infty}^{\infty} \left(\boldsymbol{\xi} - \mathbf{u}\right)^2 \left(\boldsymbol{\xi} - \mathbf{u}\right) f d\boldsymbol{\xi} \qquad (1.2.10)$$

By taking into account the above described equations, the ideal law of gases

$$P\left(\mathbf{x}, t\right) = n\left(\mathbf{x}, t\right) k_B T\left(\mathbf{x}, t\right) \qquad (1.2.11)$$

is readily deduced and it is valid even in non-equilibrium systems.

During the early 1900s, the subject of gas flows under low pressure conditions has driven the interest of many scientists. Knudsen, in 1909, managed to define a dimensionless number [65], nowadays named after himself, describing the rarefaction condition of a gas, according to

$$\text{Kn} = \frac{\lambda}{L} \qquad (1.2.12)$$

Here, L is a characteristic dimension of the geometry under consideration or the length scale of a macroscopic gradient, such as the density, found by $L = \rho / \left(\partial\rho / \partial x\right)$. Also, λ is the mean free path of gas molecules, defined as the mean distance traveled by a molecules between two successive collisions. In the case where molecules are interacting with each other as hard spheres, the mean free path is given by

$$\lambda = \frac{1}{\sqrt{2}\pi d^2 n} \qquad (1.2.13)$$

where d is the molecular diameter and n is the number density. In terms of macroscopic quantities, it can also be expressed as

$$\lambda = \frac{\sqrt{\pi}}{2} \frac{\mu v_0}{P} \qquad (1.2.14)$$

where P is the pressure, μ the dynamic viscosity of the gas in temperature T and v_0

is the most probable molecular speed defined as

$$v_0 = \sqrt{\frac{2k_B T}{m}}.$$ (1.2.15)

Alternatively, instead of the Knudsen number, the gas rarefaction parameter δ is used. It is inverse proportional to the Knudsen number and is given by

$$\delta = \frac{\sqrt{\pi}}{2} \frac{L}{\lambda} = \frac{\sqrt{\pi}}{2} \frac{1}{\mathsf{Kn}}$$ (1.2.16)

In terms of measurable quantities the gas rarefaction parameter is given by

$$\delta = \frac{LP}{\mu v_0}$$ (1.2.17)

The Knudsen number is related to the Mach and Reynolds numbers according to

$$\mathsf{Kn} = \sqrt{\frac{\gamma\pi}{2} \frac{\mathsf{Ma}}{\mathsf{Re}}}.$$ (1.2.18)

The Knudsen number, Kn (or the gas rarefaction parameter, δ) is used to define and classify the gas rarefaction levels in four regimes, namely the hydrodynamic, slip, transitional and free molecular regime. The most widely acceptable boundaries of these regimes, the borders of which are not that strictly defined, are:

- $\mathsf{Kn} < 10^{-3}$ (or $\delta > 1000$): **Hydrodynamic regime**

  The gas may be considered as a continuum medium and the Navier-Stokes equations may be applied.

- $10^{-3} < \mathsf{Kn} < 10^{-1}$ (or $1000 > \delta > 10$): **Slip regime**

  Non-equilibrium phenomena appear in the boundary regions of the domain. In particular, velocity slip and temperature jump are observed on the walls.

- $10^{-1} < \mathsf{Kn} < 100$ (or $10 > \delta > 10^{-2}$): **Transition regime**

  Intermolecular collisions are reduced and the distribution function is not of Maxwellian type. Kinetic theory of gases is employed to simulate the flow properties.

- Kn > 100 (or $\delta < 10^{-2}$): **Free molecular regime**

    The motion of the molecules is described as ballistic and there are no intermolecular collisions.

While we move from the continuum regime towards more rarefied conditions, several phenomena that may not be "captured" from the classical hydrodynamic equations can appear. Such phenomena may vary from temperature and velocity jumps or even secondary flows due to temperature gradients. In an attempt to overcome this, appropriate computational tools have to be implemented.

For the limiting case of Kn=0, the Euler equations may be applied. For the cases where we move down to rarefaction, the Navier-Stokes equations are valid. Their applicability may be further extended by incorporating velocity slip and temperature jump boundary conditions [109, 125]. However, only a limited range of rarefaction (Kn ≤ 0.1) can be simulated.

There have been some attempts of extending the applicability of this approach with higher-order boundary conditions [27, 62] or by changing the constitutive relations [72]. The most successful treatment is attributed to Sone with a development of a hydrodynamic system of equations for rarefied gas flows, generated by an asymptotic expansion of kinetic equations [127]. Also, higher order equation systems have been considered.

Chapman [21] and Enskog [30] independently described the distribution function f of molecules in terms of a deviation series from the equilibrium Maxwell distribution, according to

$$f = f^{(0)} + \text{Kn}f^{(1)} + \text{Kn}^2 f^{(2)} + \text{Kn}^3 f^{(3)} + ... \qquad (1.2.19)$$

By replacing this expression in the Boltzmann equation, we obtain a system of integro-differential equations. The zeroth, first, second order and third order terms lead to the Euler, Navier-Stokes, Burnett and super-Burnett equations respectively [126]. However, the solution of the Burnett equations is still considerably limited since they face severe difficulties with the derivation of suitable boundary conditions and more important numerical stability [157]. Overall, the Chapman-Enskog analysis, is of great importance for the kinetic theory since it allowed the derivation of closed form expressions and the estimation of the transport coefficients from first principles [31].

7

1.3 Kinetic models

In order to deal with the significant computational effort required for the solution of the Boltzmann equation several kinetic collision models, that replace the Boltzmann five-fold integral collision operator with simplified expressions, have been proposed. In general, a collision model should satisfy *i)* the collision invariants, namely the mass, momentum and energy invariants, while it should also satisfy *ii)* the H-Theorem and *iii)* provide the correct values for the transport coefficients.

The BGK model, proposed in [12] and independently in [155], was the first model to appear and has been widely applied, mostly due to its simplicity and effectiveness. It is given by

$$Q_{BGK} = \nu \left(f^M - f \right) \tag{1.3.1}$$

where ν is the collision frequency, assumed to be independent of the molecular velocity, and f^M is the local Maxwellian, calculated with the local number density, temperature and velocity.

The BGK model satisfies the collision invariants and the H-Theorem. Even more, the provided results are satisfying and in good agreement with the corresponding one derived by the Boltzmann equation in the whole range of the rarefaction [125]. However, its major drawback is that it cannot provide the correct values for the gas viscosity and thermal conductivity simultaneously (it provides a Prandlt number $Pr = 1$ instead of the correct one, which is $Pr = 2/3$). Therefore, it is well-known that it cannot accurately tackle flow configurations where mass and heat transfer phenomena are coupled. In the BGK model, the collision frequency must be multiplied by 3/2 for the solution of heat transfer problems and therefore it is not appropriate for the simulation of coupled flow and heat transfer phenomena.

Two more models were produced in the same manner but also keeping higher moments of the collision term, namely the Shakhov model [113]

$$Q_S = \nu \left\{ f^M \left[1 + \frac{2}{5} \frac{m}{n \left(k_B T \right)^2} \left(1 - Pr \right) \mathbf{q} \cdot \left(\boldsymbol{\xi} - \mathbf{u} \right) \left(\frac{m(\boldsymbol{\xi} - \mathbf{u})^2}{2 k_B T} - \frac{5}{2} \right) \right] - f \right\} \tag{1.3.2}$$

and the Ellipsoidal model [52]

$$Q_{ES} = \nu \Pr \left\{ f^M \left[\frac{n}{\pi^{3/2}} \sqrt{|A|} \exp\left(-\sum_{i,j=1}^{3} (\xi_i - u_i) A_{ij} (\xi_j - u_j) \right) \right] - f \right\} \quad (1.3.3)$$

where

$$A_{ij} = \left[\frac{2k_B T \delta_{ij}}{m \Pr} - \frac{2(1 - \Pr) P_{ij}}{nm \Pr} \right]^{-1} \quad (1.3.4)$$

Pr is the Prandtl number, k_B is the Boltzmann constant, m is the molar mass and δ_{ij} the Kronecker delta. It can be seen that by substituting $\Pr = 1$ in Eqs. 1.3.2 and 1.3.3 the BGK expression is retrieved.

The S model satisfies the collision invariants and provides the correct value for the transport coefficients. However, it has been only proven to satisfy the H-Theorem in its linearized form. Although, the H-Theorem has not been proven for the S model it is generally regarded as a reliable model and has been widely used in the literature providing accurate results in the whole range of the Knudsen number for various flow configurations.

The ES model satisfies the collision invariants and the H-Theorem and also provides the correct values for the transport coefficients [6]. However, it involves a higher computational cost compared to the BGK and S model equations.

Other models have been proposed in [71, 78, 156]. In the case of mixtures, kinetic models have been derived by Morse [84], Hamel [45], McCormack [75] and Kosuge [66]. Their application is more complicated [19, 88] and additional mixture-dependent information may be required [22, 49].

1.4 Boundary conditions

The implemented kinetic model equations, as well as the Boltzmann equation itself, in order to return accurate results, have to be accompanied by the proper boundary conditions (BCs) in order to sufficiently interpret the physics of the flow in the interface between fluid and solid. In determining these boundaries, our main concern is the correlation between the distribution function of particles emitted from the wall f^+ and that of particles that come to wall f^-. In general, this behaviour can be expressed

9

1. INTRODUCTION AND LITERATURE REVIEW

mathematically as [17]

$$f^+ = -\int \frac{\boldsymbol{\xi}' \cdot \mathbf{n}}{\boldsymbol{\xi} \cdot \mathbf{n}} R\left(\boldsymbol{\xi}', \boldsymbol{\xi}\right) f^-(\boldsymbol{\xi}') d^3 \boldsymbol{\xi}' \qquad (1.4.1)$$

where the scattering kernel $R\left(\boldsymbol{\xi}' \to \boldsymbol{\xi}\right)$ represents the probability that a gas molecule with incident velocity $\boldsymbol{\xi}'$ is scattered from boundary with outgoing velocity $\boldsymbol{\xi}$. The hypothesis described for the first time was referring in the distribution of the incoming particles in the flow. According to that, the particles follow the Maxwell distribution as defined by the properties of the wall [20]. This hypothesis was first described by Maxwell and referred to as diffuse scattering boundary condition. However, in high rarefied flows, the results are not always consistent with the corresponding experimental. To deal with this phenomenon, it was considered necessary to amend the diffusion boundary conditions. Under the amended theory, a percentage α of particles, reflects on the wall and continues with the same and symmetrical speed in a plane perpendicular to the wall. In this case the kernel has the form

$$R_s\left(\boldsymbol{\xi}' \to \boldsymbol{\xi}\right) = \delta_D\left(\boldsymbol{\xi}' - \boldsymbol{\xi} + 2\left(\boldsymbol{\xi} \cdot \mathbf{n}\right)\mathbf{n}\right) \qquad (1.4.2)$$

where δ_D denotes the Dirac function and $\mathbf{n}$ denotes the unit vector normal to the boundary facing towards the flow domain. The coefficient α is called accommodation coefficient and is the percentage of particles that are absorbed by the wall and emitted according to the properties of the wall while $1 - \alpha$ is the percentage of particles reflected from the wall without interacting with it. This factor is a characteristic feature of the gas-wall interaction and is obtained from experimental data. Then the kernel takes the form

$$R\left(\boldsymbol{\xi}' \to \boldsymbol{\xi}\right) = \left(1 - \alpha\right)\delta_D\left(\boldsymbol{\xi}' - \boldsymbol{\xi} + 2\mathbf{n}\left[\boldsymbol{\xi} \cdot \mathbf{n}\right]\right) + \alpha \frac{m^2 \boldsymbol{\xi}' \cdot \mathbf{n}}{2\pi\left(k_B T_w\right)^2} e^{-\frac{m\boldsymbol{\xi}^2}{2k_B T_w}} \qquad (1.4.3)$$

This amended hypothesis was first described by Maxwell [74] and is known as specular diffuse.

The Maxwell boundary conditions are used in the vast majority of the cases. It is quite easy to use and the results are consistent with the corresponding experimental. Nevertheless, the way the fluid-wall interaction is treated, from physical aspect, can

10

not be described accurately, and there are flows that result in significant errors. In such cases other kinds of boundary conditions are used, which in some cases their application is complex, which offer greater accuracy [98, 117, 118].

1.5 Numerical methods

As it has been already mentioned, the computational cost required for the solution of the Boltzmann equation due to the seven dimensions of the distribution function and the complicated collision integral is still considered prohibitive. Only in the recent years, some works have appeared in the corresponding literature [67, 93, 121]. However, most of them refer to the linearized form of the Boltzmann equation or they are limited to hard sphere interaction.

Another simulation method characterized of its increased computational cost is the method of the Molecular Dynamics. According to this method, the computational domain is simulated in molecular level and all molecules inside obey the laws of motion. This method has no approximations, however, due to the enormous amount of molecules in real conditions, the method is only applicable for problems of very small dimensions, of the order of a few nanometers, and for very small time intervals.

Moving forward to more computationally efficient numerical methods, kinetic model equations are more frequently proposed as methods for simulating rarefied flows. The method is based on solid theoretical background and has been studied and tested thoroughly in the last decades. The Discrete Velocity (or Discrete Ordinates) Method (DVM) [54] is one of the most widely used methods and it is extensively applied in the present work for various conditions using both the linearized and non-linear kinetic formulations. The method is completely deterministic and the main concept characterizing it is that only a discrete set of molecular velocities is examined, chosen in such a manner that a high accuracy of the integration of the distribution function during the calculation of the bulk quantities is achieved. As a result, the kinetic equations are discretized in both the physical and molecular velocity space and solved in an iterative manner for the predefined, specifically chosen, set of molecular velocities. Several works making use of this method may be found in the literature [87, 104, 146]. Not only in the cases where the distribution function can be linearized in terms of a small parameter [86, 141], but also when the kinetic models

are in their non-linear form [79, 100].

Apart from the well established and described deterministic methods, a different method well known for its wide applicability in rarefied gas flows is the Direct Simulation Monte Carlo (DSMC) method. The method, formulated by Bird [13, 35], is based on the direct simulation of the interaction between computational particles, each one representing a large number of real molecules. The method allows the study of the free motion of the simulated particles separately to the study the intermolecular collisions, all taking place in a small time increment. In the case where the number of computational particles is large enough, it has been proven [153] that the method is equivalent of solving the Boltzmann equation itself. Despite the fact that the DSMC method is well established, simple and its results are characterized by accuracy in flows far from the equilibrium state, however, in low speed flows, the method suffers from strong statistical noise. In the recent years, several techniques to face this issue have been proposed [9, 108] but they are not easily applied.

The DVM and DSMC methods are just two of the numerical methods which can be found in the literature. Several other numerical methods such as Analytical Discrete Ordinates [112, 139], Moment [128], Integromoment [149], Variational [18], Information Preservation [126, 130], Lattice Boltzmann [1, 91] and Extended hydrodynamics [127] are also effective. However, issues such accuracy and complexity affect their range and ease of applicability.

Along with the more advanced numerical methods being proposed, the technological growth of the last decades gave access to more advanced high performance computing systems (HPCs) [44]. These systems are characterized by extremely high computational power that are able to solve hugely complex and demanding problems. As a result, numerical methods like the ones described here can be implemented even faster.

Even more, paralellization protocols are further updated and in combination to the applicability of extended parallelization programming techniques in Graphics Processing Units (GPUs) by the CUDA architecture (Compute Unified Device Architecture) [32, 64], it is expected that computational techniques will receive an even more increased attention in the near future.

1.6 Technological fields with gas flows far from local equilibrium

This very same technological growth and today's technology is the basis on which people who envisioned, from the very beginning, the current technological evolution in several fields are proven to be right.

The vision along with the need to reduce the size, weight and energy savings coupled with increased needs for credibility and proper functioning of conventional-sized machines led towards the microcosm. The invention of the microscope brought this need even closer to reality. Smaller and smaller in size devices continued to be manufactured reaching to a peak with the construction of integrated circuits (l0nm).

Micro-and nano-devices with dimensions less than 100mm are now a reality. This evolution of technology with applications in micro fluid-dynamics [33], in vacuum devices [26, 138], in micro-(MEMS) and nano-electro-mechanical systems (NEMS) [50, 109] and in devices used at high altitudes and in space technology (> 50 Km) [39, 56] raised the need for better and more detailed understanding of the phenomena that are developed in such conditions, since in many cases it is quite limited.

Several applications also exist in the emerging field of microfluidics [85]. In the case of MEMS with moving parts, such as microresonators [11] and comb drive sensors [70], the damping forces induced by the ambient rarefied gas can significantly alter the performance and the sensitivity characteristics. The flow field around micro heat flux sensors [92] plays an important role in the accuracy of the device. Flows through porous media are also considered as rarefied flows with many applications in filters and membranes [136]. Read-head sliders in hard disk drives can be designed optimally only if the air flow in the microgap is simulated properly [62].

The detailed modeling of vacuum pumps [14, 37, 122] and gas separators [131] is also very important to obtain the maximum efficiency. Multilayer insulation (MLI) and blankets, extensively used in numerous applications, consist of several layers of thin sheets with vacuum conditions between them to ensure that heat is transferred only through radiation. However, ideal vacuum conditions are not achievable and therefore, the performance of the insulation in the case of degraded vacuum [129] should be investigated. Vacuum deposition systems are used for the fabrication of thin-film

materials in the manufacture of integrated circuits, MEMS and nanocomposites [151]. Furthermore, the technological branch of cryogenics [58], requires extended usage of vacuum facilities.

Application with increased technological interest though are not encountered only in nano- and micro- dimensions. Large scale applications include the EURO fusion programme and more specifically the thermonuclear fusion reactor ITER, that is currently under construction in Cadarache, France. This is a promising inter-national programme for covering future energy needs. Due to the high pumping requirements and the prevention of certain vacuum conditions [26] (insulation vacuum, low pressure to maintain plasma, fuel pumping, etc.), flow conditions usually correspond to the transitional or free molecular ranges. The AIA prototype [53] is a robotic long reach carrier, able to move inside a fusion reactor and perform various tasks without deconditioning the torus vessel. One of its most promising features is leak sniffing in which it is important to know the characteristics of the rarefied gas mixture sample flow in the umbilicus connecting the sensor tip with the detector. It is important to note that the present work has been performed within the EURO fusion program.

As far as high altitude aerodynamics is concerned, hypersonic flows around space vehicles [29, 39] and satellites [83, 119] are frequently encountered in rarefied atmospheres particularly during the reentry in the earth's atmosphere. In particular, the reentry angle for large Mach number is one of the most important parameters. The DSMC method is frequently employed in such cases and large organizations, including NASA [69], develop their own code versions of this numerical algorithm [55]. The numerical study of such phenomena is a very important factor for the development of new technologies [23, 63]. The construction of microscale propulsion devices such as mono- and bi-propellant thrusters and resistojets, has also increased the needs for the accurate simulation and measurement of rarefied gas flows [5].

Other applications include the field of aerosols [57], chemical vapor deposition [24] and vacuum metrology [61, 89].

1.7 Network solvers

In many of the applications however, the rarefied gaseous distribution system implemented in order to achieve the required operational conditions, consists not only of a

single channel but of many channels accordingly combined to form a network. In the hydrodynamic regime, computational algorithms dedicated to the hydraulic design and optimization of gas pipe networks (e.g. compressed air, natural gas, etc.) are well established and widely available [41, 94, 106]. A typical example is the Pipe2020 computational package that has been under development since 1973 from the University of Kentucky [36, 105]. It analyzes one-dimensional, isothermal flow for ideal and non-ideal variable density gases and can accommodate large networks, looped systems and multiple load and supply points. In addition, several scenarios can be set up in a single model such as load or supply changes and open or closed valves. Pipe2020 offers an integrated GUI from which the user can provide all the required input data such as the piping elements length and diameter, pipe fittings (e.g. bends, T's, reducers, etc.), node load or supply as well as compressors and fans. For the simulation of the gas network the linear pressure loss at each tube is taken from the Darcy-Weisbach equation as

$$\Delta P = f_D \frac{L}{D} \frac{\rho V^2}{2} \tag{1.7.1}$$

where f_D is the Darcy friction factor, L and D are the length and diameter of the pipe, while ρ and V are the mean density and velocity of the gas inside the pipe. The Darcy friction factor is calculated from well-known empirical expressions and depends on the characteristics of the flow inside the tube. A more detailed approach on both the estimation of the Darcy friction factor and the derivation of the Darcy-Weisbach equation are presented in Section 3.4 and Appendix A, respectively.

Following the Pipe2020 software, an in-house Matlab code simulating gas pipe networks in the hydrodynamic regime has been also developed at the Laboratory of Transport Phenomena of the University of Thessaly. This software has been implemented in the past in several diploma and master theses [107, 143]. In its current version, the Matlab algorithm is further updated and employed in the present work for validation purposes.

Recently, the so-called ITERVAC, a numerical tool for gas network simulations has been developed at the Karlsruhe Institute of Technology (KIT) for gas network calculations in the whole range of the Knudsen number [25]. The input data are provided through a GUI that allows the user to build 2D networks. Then, ITERVAC uses semi-empirical expressions to determine the mass flow rates inside a pipe as

a function of the corresponding pressure drop between the hydrodynamic and free molecular limits. The expression for the flow rate is given as

$$\dot{M} = F\frac{\pi}{8}\frac{D_h^3}{v_0}\frac{\partial P}{\partial x} \tag{1.7.2}$$

where D_h is the hydraulic diameter of the tube, v_0 is the most probable velocity and F is given as a function of four fitting parameters given by

$$F = \frac{C_1}{\mathrm{Kn}} + C_2 + \frac{C_3\mathrm{Kn}}{C_4 + \mathrm{Kn}} \tag{1.7.3}$$

Taking the limit of Eq. 1.7.3 in the viscous regime ($\mathrm{Kn} \to 0$) yields

$$\lim_{\mathrm{Kn}\to 0} F = \frac{C_1}{\mathrm{Kn}} = F_{visc} \Rightarrow C_1 = \frac{4\sqrt{\pi}}{f_D \mathrm{Re}} \tag{1.7.4}$$

where f_D is the Darcy friction factor and Re is the Reynolds number. A more general approach is to take

$$C_1 = \frac{C_{lam}}{\sqrt{\pi}D_h^2}\frac{16}{\mathrm{Re}}\frac{A}{f_D} \tag{1.7.5}$$

Then, taking the limit of Eq. 1.7.3 in the free molecular regime ($\mathrm{Kn} \to \infty$) yields

$$\lim_{\mathrm{Kn}\to\infty} F = C_2 + C_3 = F_{mol} \tag{1.7.6}$$

Also, assuming an isothermal Maxwellian distribution inside a circular channel yields

$$C_3 + C_4 = \frac{2W}{\sqrt{\pi}}\frac{L}{D} \tag{1.7.7}$$

where W is the dimensionless free molecular flow rate through the circular tube. Finally, the fitting parameter C_4 is taken as a fixed parameter that describes the beaming effects. Values for the four coefficients are presented for some common tube cross sections in Table 1.1.

For short channels ($L/D_h < 80$), C_2 and C_3 are weighted by a correction factor while C_1 is corrected for end effects. The empirical expressions of ITERVAC have been validated computationally and experimentally. The largest deviation in the viscous and free molecular regimes is 3% increasing up to 40% in the transition regime.

Table 1.1: Fitting parameters of Eq. 1.7.3 for channels of various cross sections.

Geometry	C_{lam}	C_2	C_3	C_4
Circular	1.000	1.116	0.329	1.400
Rectangular (1x1)	1.124	1.486	0.574	1.400
Rectangular (2x1)	1.029	1.666	0.732	1.400
Triangular	1.200	1.340	0.963	1.400

1.8 Dissertation structure and contents

The aim of this dissertation is to numerically investigate gas pipe networks in the whole range of the Knudsen number. This is achieved by integrating kinetic results of gas flow through single channels into a code modeling pipe networks and providing detailed results concerning the flow rates and pressures of the network. The contents of the chapters of the thesis are as follows:

- Chapter 1 presents an introduction in kinetic theory and a short literature review on the Boltzmann equation, the main kinetic model equations and the associated computational schemes, as well as a description of the technological fields and conditions where the implementation of kinetic-type approaches is needed. It also includes the novelties and the scientific contributions of the present work.

- Chapter 2 provides a description of all pressure driven flow configurations involved in the present work. This includes three main setups, namely the flow through a) long, b) moderate and c) short channels of various cross sections. These flows are treated based on the linear theory for long and short channels, when the latter is applicable, as well as end effect theories for channels of moderate length and the more general nonlinear approach for short channels. The corresponding kinetic equations along with the associated formulations are provided and they are numerically solved to deduce adequate dense kinetic results to be integrated into the network code. The range of validity of each approach is also examined.

- Chapter 3 contains a detailed description of the developed Algorithm for Rar-

efied gas flow in Arbitrary Distribution Networks (ARIADNE). This includes the basic concepts and definitions of a pipe gas network, the graphical interface in order to introduce the network geometry, the kinetic data base providing the flow rates for each pipe element, the mass and pressure balance equations to model the whole network and above all the computational algorithm integrating all this information and providing the solution.

- Chapters 4 and 5 are devoted to the validation of the proposed algorithm and on its implementation in solving certain gas pipe networks of certain complexity. Chapter 4 is devoted to networks consisting of long channels or channels of moderate length with circular, orthogonal and trapezoidal cross channels. Results are based on the infinite capillary and the end effect theories. The code validation and benchmarking is achieved in the viscous regime by comparisons with typical hydrodynamic solvers and in a wide range of the Knudsen number by comparisons with the ITERVAC code. Then, various pipe networks are simulated to demonstrate the effectiveness of the code.

- Chapter 5 is devoted to the more general and challenging case of networks consisting of channels of arbitrary length. Following the code validation several networks of arbitrary complexity are simulated. This effort includes the neutral gas flow based on the geometrical characteristics of the ITER divertor pumping system.

- Chapter 6 includes the main concluding remarks of the Ph.D. thesis. It also points out several directions and fields where this work could be extended in the near future.

1.9 Novelty and scientific contributions

The simulation of gas pipe networks in the hydrodynamic regime based on the Navier-Stokes equations has been extensively investigated by developing several in-house and commercial codes. This is well expected and understood due to the importance of gas pipe networks in various technological applications. The corresponding work in the case of gas pipe networks operating at pressures lower than the atmospheric one

is very limited, although this type of networks may be found in microfluidics and vacuum applications. This is mainly contributed to the complexity of the problem which requires the merging of expertise in kinetic modeling and pipe networking.

The present Ph.D. thesis fills exactly this gap and actually is the first systematic and successful scientific effort in integrating the modeling gas flows through channels of various lengths and cross sections under any vacuum conditions in a gas pipe network solver. Furthermore, ARIADNE, through the developed graphical interface, is considered to be a complete computational tool capable of simulating any pipe gas network of arbitrary complexity operating at any pressure from the atmospheric down to ultra-high vacuum. The software is validated and then is applied to solve various gas pipe networks including the neutral gas pipe network of the ITER divertor pumping system which is considered as one of the most complex ones worldwide.

2

Pressure driven rarefied gas flows through single piping elements

A review of the four main approaches modeling rarefied gas flows through channels, implemented in the present work, is provided. The approaches include the infinite capillary and end effect theories for long and medium capillaries, as well as the linear and the nonlinear approach for short capillaries. Furthermore, these methodologies are organized and presented in a manner which is useful for their implementation in the present work. In addition, the kinetic data base of the deduced dimensionless flow rates in terms of the specific flow configurations has been enriched with results in order to efficiently support the integrated network code.

2.1 Flows through long capillaries of various cross sections: The infinite capillary theory

The main flow configuration consists of an upstream and a downstream vessel connected by a channel of length L and cross section having surface A and perimeter Γ. The hydraulic diameter of the channel is defined by:

$$D_h = \frac{4A'}{\Gamma'} \tag{2.1.1}$$

The conditions in the upstream and downstream vessels are characterized by the pressure and temperature of the gas denoted by (P_1, T_1) and (P_2, T_2) respectively.

Depending upon the application the reference pressure may be the average pressure or the pressure of the upstream vessel, while since in this work only pressure driven flows are considered the upstream and downstream temperatures are considered as equal, i.e. $T_0 = T_1 = T_2$, with T_0 denoting the reference temperature.

The main flow parameter characterizing the rarefaction of the flow conditions is the local Knudsen number or the local gas rarefaction parameter, denoted by Kn and δ respectively, which are defined as

$$\text{Kn} = \frac{\sqrt{\pi}}{2} \frac{\mu v_0}{D_h P} \tag{2.1.2}$$

and

$$\delta = \frac{D_h P}{\mu v_0} \tag{2.1.3}$$

where P_0 is the local pressure defined as the average of the upstream and downstream pressure conditions i.e. $P_0 = (P_1 + P_2)/2$, D_h the local hydraulic diameter, μ the viscosity of the gas and v_0 the most probable molecular velocity. It is seen that the gas rarefaction is proportional to the inverse Knudsen number. Here, all results are presented in terms of the gas rarefaction δ.

2.1.1 Flow configuration

The flow configuration presented in this section applies to long channels of arbitrary cross section. Consider the isothermal flow of a monatomic gas at a reference temperature T_0 through a long channel of length L and hydraulic diameter D_h, connecting two reservoirs maintained at pressures P_1 and P_2 respectively, with $P_1 > P_2$. The area and the perimeter of the cross section are denoted by A' and Γ' respectively, while the hydraulic diameter is given by $D_h = 4A'/\Gamma'$. The reference pressure is defined as $P_0 = (P_1 + P_2)/2$. The flow is in the z' direction, while x' and y' are the lateral coordinates. By taking $D_h << L$ the flow is considered as fully developed and end effects at the inlet and the outlet of the channel are ignored. In addition pressure (and density) varies only in the flow direction z' and it remains constant at each cross section (x', y') of the channel, i.e. $P = P(z') \in [P_1, P_2]$, with $z' \in [0, L]$.

The flow is driven by the imposed pressure difference $\Delta P = P_1 - P_2$, while the

dimensionless local pressure gradient is given by

$$X_P = \frac{D_h}{P_0} \frac{dP}{dz'} \tag{2.1.4}$$

In this fully developed flow configuration the only nonzero component of the macroscopic (bulk) velocity is the z' direction denoted by $u'(x', y')$.

The basic parameter of the flow is the rarefaction parameter defined by

$$\delta = \frac{D_h P}{\mu_0 \upsilon_0} \sim \frac{1}{\mathsf{Kn}} \tag{2.1.5}$$

where μ_0 is the gas viscosity at temperature T_0 and $\upsilon_0 = \sqrt{2RT_0}$ is the most probable molecular velocity ($R = k/m$ is the gas constant where k is the Boltzmann constant and m the molecular mass). The rarefaction parameter δ, is inversely proportional to the Knudsen number ($\delta = 0$ and $\delta \to \infty$ correspond to the free molecular and hydrodynamic limits respectively). The reference rarefaction parameter characterizing the flow is given by

$$\delta_0 = \frac{D_h P_0}{\mu_0 \upsilon_0} \sim \frac{1}{\mathsf{Kn}_0} \tag{2.1.6}$$

The hydraulic diameter D_h and the molecular velocity υ_0 are taken as the characteristic length and velocity respectively. Then, it is convenient to introduce the dimensionless spatial variables $x = x'/D_h$, $y = y'/D_h$ and $z = z'/D_h$, the dimensionless cross section $A = A'/D_h^2$ and perimeter $\Gamma = \Gamma'/D_h$, as well as the dimensionless velocity $u = \tilde{u}/(\upsilon_0 X_P)$. Finally, the dimensionless flow rate is defined with regard of dimensionless quantities according to

$$G = \frac{2}{A} \int_A u(x, y) dA \tag{2.1.7}$$

At this point it is important to note that under the assumption of $D_h \ll L$ the dimensionless pressure gradient is always much less than one, i.e. $X_P \ll 1$, even for large pressure differences ΔP. Therefore, the quantity X_P is used as a very small parameter to linearize the flow equations even at large pressure drops. The analysis introduced to solve fully developed flows in long channels is also known as the infinite capillary theory.

2.1.2   Formulation of the infinite capillary theory

Since the problem is solved based on kinetic theory the main unknown is the distribution function which obeys a kinetic equation. It has been shown that fully developed, isothermal, pressure driven flows, as the ones described in the previous section, can be simulated efficiently by the linearized BGK model equation given by [116]

$$c_x \frac{\partial \Phi}{\partial x} + c_y \frac{\partial \Phi}{\partial y} + \delta_0 \Phi = \delta_0 u - \frac{1}{2} \qquad (2.1.8)$$

subject to Maxwell diffuse-specular reflection boundary condition $\Phi^+ = (1 - \alpha) \Phi^-$. Here, $\Phi = \Phi(x, y, c_x, c_y)$ is the reduced linearized distribution function, c_x and c_y the two components of the molecular velocity vector lateral to the flow direction, δ_0 the reference rarefaction parameter and

$$u(x, y) = \frac{u'}{\upsilon_0 X_P} = \frac{1}{\pi} \int\limits_{-\infty}^{\infty} \int\limits_{-\infty}^{\infty} \Phi \exp\left[-c_x^2 - c_y^2\right] dc_x dc_y \qquad (2.1.9)$$

is the dimensionless macroscopic velocity. Along the perimeter Γ, the boundary conditions are $\Phi^+ = (1 - \alpha) \Phi^-$, $\mathbf{c} \cdot \mathbf{n} > 0$, where Φ^+ and Φ^- are reduced distributions representing particles departing and arriving at the wall respectively, $\mathbf{c} = (c_x, c_y)$ and $\mathbf{n}$ is a unit vector normal to the surface oriented towards the flow side, while the parameter $\alpha \in [0, 1]$ is the so called tangential momentum accommodation coefficient and denotes the portion of the particles reflecting diffusively from the wall.

A brief description of the computational approach for solving this problem is presented here in a unified manner covering all various cross sections under consideration. Eq. 2.1.8 is written in the compact form

$$D[\Phi] + \delta_0 \Phi = \delta_0 u - \frac{1}{2} \qquad (2.1.10)$$

where

$$D = c_x \frac{\partial}{\partial x} + c_y \frac{\partial}{\partial y} \qquad (2.1.11)$$

is the linear streaming operator acting on Φ. Then, the two component dimensionless

molecular velocity vector is defined by its magnitude ζ and its polar angle θ as

$$\zeta = \sqrt{c_x^2 + c_y^2} \quad \text{and} \quad \theta = \tan^{-1}\left(c_y/c_x\right) \tag{2.1.12}$$

respectively, where $0 \leq \zeta \leq \infty$ and $0 \leq \theta \leq 2\pi$ ($c_x = \zeta \cos\theta$, $c_y = \zeta \sin\theta$). For each cross section the operator D may be expressed in a different, more convenient, form for numerical simulation. Even more, dimensional and dimensionless values for the estimation of the hydraulic diameter, surface and perimeter for capillaries of various cross sections may be found in Table 2.1.

In particular, in the case of flows through circular cross sections, due to the axisymmetric conditions, the flow becomes one-dimensional in space, i.e. $\Phi = \Phi\left(r, \zeta, \theta\right)$, where r denotes the radial direction and we write [124]

$$D = \zeta \left(\cos\theta \frac{\partial}{\partial r} - \frac{\sin\theta}{r} \frac{\partial}{\partial\theta}\right) \tag{2.1.13}$$

In the case of flows through orthogonal cross sections, $\Phi = \Phi\left(x, y, \zeta, \theta\right)$ is a function of four independent variables and the streaming operator is written in the form [116]

$$D = \zeta \left(\cos\theta \frac{\partial}{\partial x} + \sin\theta \frac{\partial}{\partial y}\right) \tag{2.1.14}$$

In the case of triangular and trapezoidal cross sections, again $\Phi = \Phi\left(x, y, \zeta, \theta\right)$. However, in order to have a boundary fitted grid it is necessary to write, using the method of characteristics, the streaming operator as [87]

$$D = \zeta \frac{\partial}{\partial s} \tag{2.1.15}$$

where $s = s\left(x, y, \theta\right)$ denotes the direction of the characteristic line, passing from the point (x, y) and defined by the polar angle θ of the molecular velocity vector. This approach has been shown recently to be very efficient for triangular and trapezoidal cross sections [87]. It is concluded that for all cross sections, Eq. 2.1.10 is the governing equation, with the operator D however, accordingly defined.

Finally, in terms of the polar coordinates the macroscopic velocity is defined as:

$$u\left(x,y\right)=\frac{1}{\pi}\int\limits_{0}^{2\pi}\int\limits_{0}^{\infty}\Phi\exp\left[-\zeta^{2}\right]\zeta d\zeta d\theta \tag{2.1.16}$$

The kinetic equation 2.1.10 is discretized properly in the molecular velocity and physical spaces and then its discretized version is solved numerically in an iterative manner. The discretization in the molecular velocity space for all cross sections is performed by choosing a suitable set of discrete velocities (ζ_m, θ_n), defined by $0 \leq \zeta_m < \infty$ and $0 \leq \theta_n \leq 2\pi$, with $m = 1, 2, ..., M$ and $n = 1, 2, ..., N$. Introducing this discretization into Eq. 2.1.10, yields, in the case of rectangular cross sections, a system of partial differential equations while, in the other three cases, systems of ordinary differential equations are deduced. The macroscopic quantities are computed by numerical integration. More specifically, the Gauss-Legengre quadrature is used in the ζ variable and the trapezoidal rule in the θ variable. The discretization in the physical space (i.e. the dimensionless area A of the cross section), depends on the type of cross section. The flow through a circular channel is one-dimensional in space and in this case the spatial discretization is trivial. In the case of an orthogonal channel the elements of the computational grid are orthogonal having an aspect ratio equal to the aspect ratio of the channel. The kinetic equation is discretized at the geometrical center of each orthogonal element (i, j), with $i = 1, 2, ..., I$ and $j = 1, 2, ..., J$, resulting to a second order difference scheme. The computational grids for the triangular and trapezoidal channels consist of triangular elements. The implemented numerical scheme is first order accurate and therefore a relative large number of nodes in the physical space is required. Details on this specific numerical scheme are given in [62].

Overall the problem is solved numerically in an iterative manner between the kinetic equation for Φ and the integral expression for u. The iterations start by assuming some initial values for u. Then, in each iteration the system of algebraic equations deduced from the discretization of the kinetic equation is solved by a marching scheme. For each discrete velocity (ζ_m, θ_n) the distribution function is computed explicitly marching through the physical lattice. The marching process starts always from the boundary and its direction depends upon the polar angle θ_n. Following this proce-

dure, no matrix inversion is required. Then, based on the estimated distributions the macroscopic velocity is computed by numerical integration. The new values of u are plugged back into the kinetic equation and the iterative procedure is ended when the imposed termination criterion on the convergence of u is satisfied. Following the above procedure, supplemented by a reasonable dense grid and an adequate large set of discrete velocities, we are able to obtain grid independent results with modest computational effort.

2.1.3 Mass flow rate and axial pressure distribution

The mass flow rate $\dot{M}$ is obtained, based on the computed dimensionless flow rates G, in a straightforward manner [125]. In general, the mass flow rate is given by integrating over any cross section of the channel according to

$$
\begin{aligned}
\dot{M} &= \int_{A'} \rho\left(z'\right) u'\left(x', y'\right) dA' = \rho\left(z\right) v_0 X_p D_h^2 \int_A u\left(x, y\right) dA = \\
&= \frac{2P}{v_0} X_p D_h^2 \int_A u\left(x, y\right) dA = \frac{2}{v_0} \frac{dP}{dz'} D_h^3 \int_A u\left(x, y\right) dA = \\
&= \frac{A D_h^3}{v_0} \frac{dP}{dz'} G
\end{aligned}
\tag{2.1.17}
$$

Define arbitrarily a new quantity which we will call G^* so that

$$
\dot{M} = \frac{A D_h^3}{v_0} \frac{\Delta P}{L} G^*
\tag{2.1.18}
$$

Since due to mass conservation the two expressions of the mass flow rate must be equal to each other as:

$$
G \frac{dP}{dz'} = G^* \frac{\left(P_2 - P_1\right)}{L} \Rightarrow G \frac{dP}{P_2 - P_1} = G^* \frac{dz'}{L}
\tag{2.1.19}
$$

From the definition of δ and since all quantities other than P remain constant it is deduced that

$$
\frac{dP}{P_2 - P_1} = \frac{d\delta}{\delta_2 - \delta_1}
\tag{2.1.20}
$$

Then,

$$G \frac{d\delta}{\delta_2 - \delta_1} = G^* \frac{dz'}{L} \quad \Rightarrow \quad \frac{1}{\delta_2 - \delta_1} \int_{\delta_1}^{\delta_2} G d\delta = \frac{G^*}{L} \int_0^L dz' \Rightarrow$$

$$\Rightarrow \quad G^* = \frac{1}{\delta_2 - \delta_1} \int_{\delta_1}^{\delta_2} G d\delta \qquad (2.1.21)$$

Now given the dimensional quantities, i.e. the cross section A', hydraulic diameter D_h and length L of the channel, the upstream and downstream pressure P_1 and P_2 respectively, the isothermal flow temperature T_0, the molecular mass m and viscosity μ_0 of the gas, the mass flow rate $\dot{M}$ may be computed. In particular, the kinetic code for a large set of values for δ covering the range $[\delta_1, \delta_2]$ is run to obtain the corresponding values of G and then G^* is found from Eq. 2.1.21. Next, from Eq. 2.1.18 the mass flow rate is estimated.

The pressure distribution may be also computed by rewriting Eq. 2.1.18 in the form

$$\frac{dP}{dz'} = \frac{\dot{M}\upsilon_0}{AD_h^3 G(\delta)} \qquad (2.1.22)$$

and solving this ordinary differential equation, based on a typical integration scheme, for $P = P(z')$, along $z' \in [0, L]$, with initial condition $P(0) = P_1$. This may be easily achieved by dividing the channel length z' into N intervals of length $\Delta z'$ and applying a first order Euler scheme to yield the finite difference expression

$$P_{i+1} = P_i + \Delta z' \frac{\dot{M}\upsilon_0}{AD_h^3 G(\delta_i)}, \quad i = 0, 1, ..., N \qquad (2.1.23)$$

with $P_0 = P(0)$, which produces the pressure distribution along the channel. Then, provided that the discretization is dense enough and that the mass flow rate $\dot{M}$ has been estimated correctly, the downstream pressure P_2 at $z' = L$ is recovered. It is obvious that this analysis can be also used in cases where the downstream pressure is unknown provided that the mass flow rate is given.

The above described methodology has been implemented in the pipe network algorithm to compute the mass flow rates through long channels of various cross

sections. As it is clearly seen the methodology is based on the computation of the dimensionless flow rate G versus the gas rarefaction parameter δ. This information is provided in Tables 2.2 to 2.5 where tabulated values of the dimensionless flow rate in terms of the gas rarefaction parameter for long channels of various cross sections are provided.

2.1.4 Complementary quantities

Other characteristic and commonly used numbers of the flow are the reference Reynolds and Mach numbers defined as $\mathrm{Re} = \rho_0 \bar{u}' D_h / \mu_0$ and $\mathrm{Ma} = \bar{u}'/c_0$ respectively, where, $\rho_0 = P_0/(RT_0)$ is the reference mass density, $c_0 = \sqrt{\gamma R T_0}$ is the adiabatic sound velocity at temperature T_0 (γ is the specific heat and is equal to 5/3 for a monatomic gas) and

$$\bar{u}' = \frac{1}{A'} \int\limits_{A'} u'(x', y') dA' \qquad (2.1.24)$$

is the mean macroscopic velocity. Then, the reference Reynolds and Mach numbers are associated to the reference rarefaction parameter, Eq. 2.1.6, according to

$$\delta_0 = \frac{1}{\sqrt{2\gamma}} \frac{\mathrm{Re}}{\mathrm{Ma}} \qquad (2.1.25)$$

Another quantity of practical interest is the conductance C. Conductance is the "PV flow" or "pump PV flow", i.e. the throughput through any desired pipe element and it expressed as [60]:

$$C = \frac{\dot{M}}{m} \frac{R^* T_0}{\Delta P} \qquad (2.1.26)$$

with m denoting the molar mass of the gas and R^* the universal gas constant. The conductance depends on geometry via the pressure difference term and it is always positive. In ultrahigh and high vacuum is almost independent of pressure, while in medium and rough vacuum depends on pressure.

In the same context, if we consider a fluid of volume V passing through the intake port of a pump at time t, then $S = dV/dt$ is the pumping speed, i.e., the volumetric flow rate (m^3/s) through the intake port of the pump. If the pumping speed is constant then $S = \Delta V/\Delta t$.

The "PV flow" or "pump PV flow" (or pump throughput) is often more interesting

in vacuum technology than the mass or weight of a quantity of gas and it embraces an energy dimension and is given by

$$Q_{PV} = \frac{P \times V}{t}, \tag{2.1.27}$$

where P is the pressure in the intake side of the pump and S the pumping speed. The units of the throughput are in Pam^3/s, which is equivalent to Watt. If P and V are constant at the intake side of the pump, the throughput of the pump can be expressed as $Q_{PV} = P \times S$.

Apart from the conductance and throughput defined above, another parameter characterizing viscous flows is the friction factor. In the case of internal fully developed laminar flows, instead of the friction factor it is more appropriate to estimate the Poiseuille number of the flow, which is defined as [140]

$$\text{Po} = \frac{8\bar{\tau}_w' D_h}{\mu_0 \bar{u}'} \tag{2.1.28}$$

Here, $\bar{\tau}_w'$ is the mean wall shear stress, which is estimated by integrating the wall shear stress τ_w' over the perimeter Γ', $\bar{u}'$ is the mean macroscopic velocity given by Eq. 2.1.24. It may be useful to note that the Poiseuille number is given as $\text{Po} = f_D \times \text{Re}$, where f_D is the Darcy friction factor and Re is the Reynolds number of the flow based on the hydraulic diameter. The two expressions for the Po number, from a mathematical point of view, are identical. The dependence of Poiseuille number on the gas rarefaction for channels of various cross sections has been investigated in [16, 145, 147].

Since the flow is fully developed and there is no net momentum flux in the z' direction, the net pressure and the wall shear stress are equated to yield

$$\bar{\tau}_w' = \frac{A'}{\Gamma'} \frac{dP}{dz'} \tag{2.1.29}$$

By nondimensionalizing the above expression and using the relation $A/\Gamma = 1/4$, it is easily deduced that

$$\bar{\tau}_w = \frac{\bar{\tau}_w'}{2P_0 X_P} = \frac{A}{2\Gamma} = \frac{1}{8} \tag{2.1.30}$$

This result is always valid independent of the channel cross section, the rarefaction

parameter δ_0 and the accommodation coefficient α and therefore it may be used as a benchmark to test the accuracy of the kinetic calculations.

Then, by introducing Eq. 2.1.29 into Eq. 2.1.28 and implementing Eq. 2.1.6 it is readily deduced that

$$\mathrm{Po} = \frac{8\bar{\tau}_w 2P_0 X_P D_h}{\mu_0 \bar{u} \upsilon_0 X_P} = \frac{16\bar{\tau}_w \delta_0}{\bar{u}} \tag{2.1.31}$$

where

$$\bar{u} = \frac{\bar{u}'}{\upsilon_0 X_P} = \frac{1}{A} \int\limits_A u(x, y) dA \tag{2.1.32}$$

is the dimensionless mean velocity and it is related to the kinetic coefficient G given by Eq. 2.1.7 according to $G = 2\bar{u}$. Finally, substituting Eq. 2.1.30 into Eq. 2.1.31 yields

$$\mathrm{Po} = \frac{2\delta_0}{\bar{u}} = \frac{4\delta_0}{G} \tag{2.1.33}$$

This expression is of major importance and it is valid for any cross section and gas rarefaction level.

In Table 2.6 tabulated results for the Poiseuille number in terms of the rarefaction parameter δ for channels of various cross sections, with a constant value of tangential momentum accommodation coefficient $\alpha = 1$, are provided. In all cases the Po number is monotonically increased with δ_0, reaching at large values of δ_0 the corresponding well known analytical results at the hydrodynamic limit $(\delta_0 \to \infty)$ [145].

2.2 Flow through circular capillaries of moderate length: The end effect theory

In many practical situations the assumptions of the fully developed flow are not applicable. In the case of channels of moderate length and relatively small pressure drops the so-called end effect theory may be implemented to extend the validity of the infinite capillary theory to channels of finite length. More specifically, the capillary length L is corrected by an additional length ΔL related to the end effect. Once the end correction L is known, the flow rate through the finite capillary can be calculated by multiplying the flow rate for an infinitely long capillary by $L/(L + \Delta L)$. It is

important to note that ΔL depends only on the gas rarefaction parameter and it is independent of the capillary length.

2.2.1 Flow configuration and formulation

The end correction approach is well known in viscous flows [154], while in rarefied gas flows is introduced in [125]. The same idea was also used [3, 4, 114, 135], where however, the concept was based on computing the pressure gradient in the middle section of the capillary.

Let us consider the rarefied flow of a gas through a tube with length L and radius R connecting two large reservoirs. The channel is divided into three segments as seen in Figure 2.1, denoted by the terms "inlet part", "middle part" and "outlet part". These are distinguished by the transformation of the flow field, which is two-dimensional in the inlet and outlet parts and one-dimensional in the middle part, which is characterized by the fully developed flow conditions. The introduced methodology is exactly the same for the inlet and outlet regions and therefore we may consider either of them as shown in Figure 2.2. A cylindrical coordinate system (x, r) with its origin at the center of the junction between the container and tube is introduced. The region $x > 0$ represents the container, while the region $x \leq 0$ corresponds to the tube. The gas flows from (or into) the long tube in the x direction into (or from) the infinitely large container. The interface between the middle and outlet parts is taken adequately far to ensure that at the cross section (A) the flow is fully developed. Also, the size of the container is sufficiently large to ensure that at (D) and (E) the gas pressure and temperature recovers the reference values P_0 and T_0.

The expected pressure distribution along the symmetry axis in the case of gas flow from the tube towards the container (outer region) is the one shown in Figure 2.3. The reference pressure P_R is also shown. The pressure difference $\Delta P = P - P_R$ in the tube far from the outlet is approaching a constant value, which represents the pressure jump due to the end effect and can be taken into account by adding the increment ΔL to the tube length. From Figure 2.3 it is readily seen that

$$\Delta L = -\Delta P / (dP/dx) \tag{2.2.1}$$

The flow setup is described by the linearized BGK model equation. More specifi-

cally, the velocity distribution function $f(x.r, \mathbf{c})$ is linearized as

$$f(x.r, \mathbf{c}) = f_R\left[1 + \xi h(x, r, \mathbf{c})\right] \tag{2.2.2}$$

where $\xi = (1/P_0)/(dP/dx)$ and the reference Maxwellian is

$$f_R(x, \mathbf{c}) = \frac{n_R(x)}{\pi^{3/2}\upsilon_0^3} \exp\left(-c^2\right) \tag{2.2.3}$$

with

$$n_R(x) = P_R(x)/(k_B T_0) \tag{2.2.4}$$

while $P_R(x) = P_0$ for $x \geq 0$ and $P_R(x) = P_0(1 + x\xi)$ for $x < 0$. Then, the linearized BGK model equation is given by

$$c_p \cos\theta \frac{\partial h}{\partial r} - \frac{c_p \sin\theta}{r}\frac{\partial h}{\partial \theta} + c_x \frac{\partial h}{\partial x} + \delta h = \delta\left[\rho + 2\mathbf{c}\cdot\mathbf{u} + \tau\left(c^2 - \frac{3}{2}\right)\right] + g(x, c_x) \tag{2.2.5}$$

where the source term is

$$g(x, c_x) = \begin{cases} 0 & , \quad x > 0 \\ -c_x & , \quad x \leqslant 0 \end{cases} \tag{2.2.6}$$

while the perturbed quantities of density, pressure, temperature and velocity are given by the following moments:

$$\mathbf{x} = \frac{\hat{\mathbf{x}}}{R}, \quad \mathbf{c} = \frac{\xi}{\upsilon_0}, \quad \upsilon_0 = \sqrt{2\frac{k_B}{m}T_0},$$

$$\rho(\mathbf{x}) = \frac{n(\mathbf{x}) - n_R}{n_R X_P}, \quad \tau(\mathbf{x}) = \frac{T(\mathbf{x}) - T_0}{T_0 X_P}, \tag{2.2.7}$$

$$p(\mathbf{x}) = \frac{\hat{P}(\mathbf{x}) - P_R}{P_R X_P}, \quad \mathbf{u}(\mathbf{x}) = \frac{\hat{\mathbf{u}}(\mathbf{x})}{\upsilon_0 X_P}$$

with $\upsilon_0 = \sqrt{2k_B T_0/m}$ being the most probable molecular velocity, k_B is the Boltzmann constant and $\rho, \tau, \mathbf{u}, p$ are the perturbations of density, temperature, velocity and pressure.

Even though this formulation is valid for the outlet part of the channel, it can also

be used to model the inlet part by noting that the dimensionless pressure gradient X_P has the opposite sign and thus the flow direction is reversed. The final objective of this study is to calculate the pressure perturbation at the fully developed cross-section of the end geometry, which will finally serve for the correct connection at the interfaces between the middle and the end parts.

As far as the boundary conditions are concerned, at the free surfaces (D),(E) incoming molecules conform to the Maxwellian distribution at the local reference values and therefore the perturbation of the distribution function is zero ($h^+ = 0$). The impermeability condition ($u_n = 0$) is imposed at the walls (D),(E), i.e. $h^+ = \rho_w$, where ρ_w is a constant which must be adjusted to keep the normal velocity equal to zero. At the axis of symmetry ($x = 0$) molecules are reflected specularly. At the incoming surface of the channel (A), the distribution function takes the form

$$c_p \cos\theta \frac{\partial h_{in}}{\partial r} - \frac{c_p \sin\theta}{r} \frac{\partial h_{in}}{\partial \theta} + \delta h_{in} = \delta \left[\rho_{in} + 2c_x u_{x,in} \right] + g\left(x, c_x \right) \qquad (2.2.8)$$

As a final step, the unprojected distribution at the incoming surface (A) can be retrieved by the expression

$$h_{in}\left(r, c_p, \theta \right) = 2c_x Z\left(r, c_p, \theta \right) + \rho_{in}\left(r \right) \qquad (2.2.9)$$

and used as incoming boundary conditions. To summarize, the boundary distributions, denoted by the "plus" superscript, are equal to

$$h^+_{wall} = \rho_w, \quad h^+_{container} = 0, \quad h^+_{channel} = h_{in}, \quad h^+_{center} = h_{specular} \qquad (2.2.10)$$

2.2.2 Effective length increment and corrected flow rate

The pressure perturbation at cross-section (A) is the main quantity of interest here. Its value can be used to determine the entrance/exit pressure and, along with a well known integration procedure for the fully developed part of the flow [115], the complete pressure profile along a channel can be obtained. From Figure 2.3 it can be seen that

$$\delta P = P - P_R = p\left(-L_{dev}, x_2 \right) P_R X_P \qquad (2.2.11)$$

and

$$\tan^{-1}\phi = -X_P P_R \qquad (2.2.12)$$

leading to

$$\Delta L_{out} = -p\left(-L_{dev}, x_2\right) \qquad (2.2.13)$$

Similarly, when the geometry represents an inlet part ($X_P > 0$) we get

$$\Delta L_{in} = p\left(-L_{dev}, x_2\right) \qquad (2.2.14)$$

Thus, we may obtain a very good agreement for the middle part of the complete channel (which usually is the largest part), if we apply the integration procedure at a "modified" geometry, where L has been increased by a fictional ΔL_{in} at the inlet and ΔL_{out} at the outlet. Alternatively, we may get the complete pressure profile by properly combining fully developed and end results during the dimensionalization.

The integration procedure is performed according to

$$\dot{M} = -G_{FD}\left(\delta\right)\frac{\pi R^3}{\upsilon_0}\frac{dP}{dx_1} = -G\frac{\pi R^3}{\upsilon_0}\frac{\Delta P}{L} \qquad (2.2.15)$$

where the x_1 coordinate takes values in $[0, L]$ and G_{FD} is the fully developed solution for a channel of infinite length. The quantity G is a constant, adjusted to obtain this equality. From Eq. 2.2.15 we get

$$G_{FD}\left(\delta\right)\frac{dP}{dx_1} = G\frac{\Delta P}{L} \qquad (2.2.16)$$

and using the definition of the rarefaction parameter

$$G_{FD}\left(\delta\right)\frac{d\delta}{dx_1} = G\frac{\delta_{in} - \delta_{out}}{L} \qquad (2.2.17)$$

If we separate the variables and integrate, we get

$$\frac{1}{\delta_{in} - \delta_{out}}\int_{\delta_{in}}^{\delta_{out}} G_{FD}\left(\delta\right) d\delta = \frac{G}{L}\int_{0}^{L} dx_1 \qquad (2.2.18)$$

and therefore the expression for G is obtained

$$G = \frac{1}{\delta_{in} - \delta_{out}} \int\limits_{\delta_{in}}^{\delta_{out}} G_{FD}(\delta) \, d\delta \qquad (2.2.19)$$

Finally, if we repeat the same procedure shown in the previous paragraph, but this time taking the end effect into account (by changing the integration limits in the right hand side of Eq. 2.2.18 to $-\Delta L_{in}$ and $L + \Delta L_{in}$) we deduce that

$$G = \frac{L}{L + \Delta L_{in} + \Delta L_{out}} \frac{1}{\delta_{in} - \delta_{out}} \int\limits_{\delta_{in}}^{\delta_{out}} G_{FD}(\delta) \, d\delta \qquad (2.2.20)$$

or in a more simplified way [125]

$$G(L, \delta) = \frac{L}{L + \Delta L_{in} + \Delta L_{out}} G_{FD}\left(\frac{\delta_{in} + \delta_{out}}{2}\right) \qquad (2.2.21)$$

The geometrical parameters for the end effect problem are given in Table 2.7, based on which, the fictional length increments ΔL, provide the extra "effective" length and are shown in Table 2.8 for various rarefaction levels. The fictional length increments, which are equal to the pressure perturbation found in the end geometry as shown before, their values becomes smaller for larger δ, showing that the end effect is more important for highly rarefied flows. The decrease in ΔL is also steeper for small δ.

Indicative results for the density perturbation and streamlines are plotted in Figure 2.4 in two dimensional contours for the area close to $x = 0$ and three values of the rarefaction parameter δ. Inside the tube $(x < 0)$, the density field progressively becomes one-dimensional, i.e. r is constant in each cross section and the streamlines are parallel far from $x = 0$ inside the tube [103].

Moreover, The numerical results obtained in [101, 133] for the complete domain of the flow due to a small pressure drop confirm the linear pressure distribution. It is more interesting to compare the pressure distribution when its drop is large, e.g. $P_{out}/P_{in} = 0.5$. In this case, the pressure distributions were calculated for a cylindrical channel with the length $L = 5$ and for the rarefaction parameter $\delta = 1$ and 10. The

results are plotted in Figure 2.5 and compared with those obtained by considering the complete flow domain. It can be seen that the pressure distribution is practically linear and in a good agreement with the exact results for $\delta = 1$. The pressure profile is slightly different from the straight line for $\delta = 10$. In this case, the difference between the two methodologies is larger, but the approximate approach still provides reasonable results [103].

Finally, a part of the density perturbation field is also plotted in Figure 2.6 for some representative values of δ, namely $\delta = 0.2, 1, 10$. In this two-dimensional plot, it can be seen that the density perturbation progressively becomes constant along each cross section as we move far from the channel end. Furthermore, for highly rarefied conditions the expansion structure spans to a larger area inside the container in fact in the longitudinal direction. The dimensionless horizontal velocity u_x also displays a nearly developed velocity profile at the left end of the channel, which coincides with the solution of the fully developed problem at the inlet cross-section. The maximum value of the macroscopic velocity also seems to behave according to the Knudsen minimum, taking its smallest value around $\delta = 1$.

The main characteristics of the numerical scheme applied, are similar to the ones found in previously formulated discrete velocity schemes, such as the one described in section 2.1.2. The continuum spectrum of the molecular velocity magnitudes c_p and c_x are discretized to M values, their values being chosen according to the roots of the Mth order Legendre polynomial mapped in $[0, c_{p,max}]$ and $[0, c_{x,max}]$ respectively, while the molecular velocity angles N_θ are uniformly distributed in $[0, \pi]$ due to the axisymmetrical properties of the flow. The distribution functions, bulk quantity fields and governing equations are further discretized by a finite volume scheme in the physical space to $N_x \times N_r$ points.

The discrete velocity method algorithm is then applied. The iterations start by assuming some initial values for bulk quantity perturbations ρ, **u** and τu. In the case of the end-geometry, incoming distributions in cross-section (A) is estimated from Eq. 2.2.9. According to the marching scheme applied, for each discrete velocity, the distribution function is computed explicitly through the physical lattice. Then, based on the estimated distributions, new estimations for the bulk quantities are calculated. The iterative procedure is ended when the imposed termination criterion on the convergence of the macroscopic quantities is satisfied.

2.3 Flow through circular capillaries of finite length: The linear approach

Despite the fact that reliable results for linear fully developed flows through long capillaries may be obtained with moderate computational effort, however, when the flow becomes nonlinear, i.e. in the case of fast flows through channels of finite length, including flows through slits and orifices, the computational effort is significantly increased. In the former case, the flow is simulated only in one cross section of the channel and then the mass flow rate is estimated, while in the case of capillaries of finite length, the incoming distribution functions at the entrance and the exit of the channel are not Maxwellians and therefore adequately large computational domains must be included before and after the channel to properly impose the boundary conditions.

2.3.1 Flow configuration and formulation

However, for the case of the flow through a capillary of finite length due to small pressure differences between the upstream and the downstream vessel, i.e. $\Delta P / P_0 \ll 1$, a linear approach may be applied. Due to the small pressure difference, we may linearize the distribution function according to

$$f\left(\hat{\mathbf{x}}, \boldsymbol{\xi}\right) = f_0\left[1 + h\left(\hat{\mathbf{x}}, \boldsymbol{\xi}\right) \Delta P / P_0\right] \tag{2.3.1}$$

where $h\left(\hat{\mathbf{x}}, \mathbf{c}\right)$ is the perturbation of the distribution function $f\left(\hat{\mathbf{x}}, \mathbf{c}\right)$ from the equilibrium state at the reference conditions, with $\Delta P = \hat{P}_{out} - \hat{P}_{in}$

$$f_0 = n_0 / \left(2\pi k_B T_0\right)^{3/2} \exp\left[-\left(\boldsymbol{\xi} - \hat{\mathbf{u}}\right)^2 / \left(2RT_0\right)\right] \tag{2.3.2}$$

All quantities are then expressed in dimensionless form as follows:

$$\mathbf{x} = \frac{\hat{\mathbf{x}}}{L_0}, \quad \mathbf{c} = \frac{\boldsymbol{\xi}}{\upsilon_0}, \quad \upsilon_0 = \sqrt{2\frac{k_B}{m}T_0},$$

$$\rho\left(\mathbf{x}\right) = \frac{n\left(\mathbf{x}\right) - n_0}{n_0}\frac{P_0}{\Delta P}, \quad \tau\left(\mathbf{x}\right) = \frac{T\left(\mathbf{x}\right) - T_0}{T_0}\frac{P_0}{\Delta P}, \tag{2.3.3}$$

$$p(\mathbf{x}) = \frac{\hat{P}(\mathbf{x}) - P_0}{P_0} \frac{P_0}{\Delta P}, \quad \mathbf{u}(\mathbf{x}) = \frac{\hat{\mathbf{u}}(\mathbf{x})}{\upsilon_0} \frac{P_0}{\Delta P}$$

with υ_0 being the most probable molecular velocity, k_B is the Boltzmann constant and $\rho, \tau, \mathbf{u}, p$ are the perturbations of density, temperature, velocity and pressure and $n_0 = P_0/(k_B T_0)$. The degree of rarefaction is described by the rarefaction parameter δ, defined here as

$$\delta = \frac{P_0 L_0}{\mu_0 \upsilon_0} \tag{2.3.4}$$

where μ_0 is the gas viscocity at reference temperature T_0.

The BGK model (1.3.1) substitutes the collision term due to its simplicity and the nearly isothermal properties of this flow. The kinetic equation becomes

$$\mathbf{c} \cdot \frac{\partial h}{\partial \mathbf{x}} = \delta \left[\rho + \tau \left(c^2 - \frac{3}{2} \right) + 2\mathbf{c} \cdot \mathbf{u} - h \right] \tag{2.3.5}$$

Similarly, the macroscopic quantity perturbations are expressed in terms of the perturbation h as

$$\rho = \frac{1}{\pi^{3/2}} \int_{-\infty}^{\infty} \int_{-\infty}^{\infty} \int_{-\infty}^{\infty} h \exp\left(-c^2\right) dc_1 dc_2 dc_3$$

$$\mathbf{u} = \frac{1}{\pi^{3/2}} \int_{-\infty}^{\infty} \int_{-\infty}^{\infty} \int_{-\infty}^{\infty} h\mathbf{c} \exp\left(-c^2\right) dc_1 dc_2 dc_3 \tag{2.3.6}$$

$$\tau = \frac{1}{\pi^{3/2}} \int_{-\infty}^{\infty} \int_{-\infty}^{\infty} \int_{-\infty}^{\infty} h \left(\frac{2}{3}c^2 - 1 \right) \exp\left(-c^2\right) dc_1 dc_2 dc_3$$

The pressure perturbation is calculated by the ideal gas law, we get $p(\mathbf{x}) = \rho(\mathbf{x}) + \tau(\mathbf{x})$.

The molecular velocity vector is transformed to cylindrical coordinates and byy properly acting on the governing equation, we finally obtain

$$c_p \cos\theta \frac{\partial h}{\partial r} - \frac{c_p \sin\theta}{r} \frac{\partial h}{\partial \theta} + c_x \frac{\partial h}{\partial x} + \delta h = \delta \left[\rho + \tau \left(c^2 - \frac{3}{2} \right) + 2\mathbf{c} \cdot \mathbf{u} \right] \tag{2.3.7}$$

The macroscopic perturbations are expressed by

$$\rho = \frac{1}{\pi^{3/2}} \int\limits_{-\infty}^{\infty} \int\limits_{0}^{2\pi} \int\limits_{0}^{\infty} h c_p \exp\left(-c^2\right) dc_p d\theta dc_x \tag{2.3.8}$$

$$u_r = \frac{1}{\pi^{3/2}} \int\limits_{-\infty}^{\infty} \int\limits_{0}^{2\pi} \int\limits_{0}^{\infty} h\left(c_p \cos\theta\right) c_p \exp\left(-c^2\right) dc_p d\theta dc_x \tag{2.3.9}$$

$$u_x = \frac{1}{\pi^{3/2}} \int\limits_{-\infty}^{\infty} \int\limits_{0}^{2\pi} \int\limits_{0}^{\infty} h c_x c_p \exp\left(-c^2\right) dc_p d\theta dc_x \tag{2.3.10}$$

$$\tau = \frac{1}{\pi^{3/2}} \int\limits_{-\infty}^{\infty} \int\limits_{0}^{2\pi} \int\limits_{0}^{\infty} h\left(\frac{2}{3}c^2 - 1\right) c_p \exp\left(-c^2\right) dc_p d\theta dc_x \tag{2.3.11}$$

2.3.2 Boundary conditions

The formulation is completed by providing the boundary conditions for h. Molecules entering from the free surfaces (A),(B),(F),(G) (as shown in Figure 2.7) conform to a Maxwellian distribution according to the conditions of the corresponding vessel. Thus, for the left vessel, we have $n = n_{in}$, $T = T_0$ and $\hat{\mathbf{u}} = 0$ and therefore the perturbation from the equilibrium distribution is

$$h^+ = \rho_{in} = \frac{n_{in} - n_0}{n_0 \left(\Delta P / P_0\right)} = \frac{\left(P_0 + \Delta P\right) - P_0}{P_0 \left(\Delta P / P_0\right)} = 1 \tag{2.3.12}$$

Similarly, it is found that in downstream free surfaces (F),(G), where $n = n_{out}$, $T = T_0$ and $\hat{\mathbf{u}} = 0$, the perturbation of the incoming distribution is $h^+ = V^+ = X^+ = 0$.

For the walls (C),(D),(E), the diffuse boundary conditions are imposed according to the impermeability condition (the velocity component normal to the wall must be equal to zero). Diffuse-specular boundary conditions are taken into account by adjusting the accommodation coefficient α according to

$$h^+ = \alpha \rho_w + \left(1 - \alpha\right) h^-$$

and the ρ_w constants are given by no penetration condition. Finally, at the axis of

symmetry ($x_2 = 0$) the molecules are reflected specularly.

2.3.3 Mass flow rate

The most important quantity for the practical applications is the mass flow rate through the channel, defined by

$$\dot{M} = \int \left[mn\left(\hat{\mathbf{x}}\right) \right] \hat{u}_x\left(\hat{\mathbf{x}}\right) d\hat{A} \tag{2.3.13}$$

with $\hat{A}$ being the channel cross-section. In both cases, the flow rate is non-dimensionalized by the analytical free molecular solution ($\delta_{in} = \delta_{out} = 0$) for flow through a channel of zero length. This solution can be easily extracted by the method of characteristics and yields $\dot{M}_{FM} = R^2\sqrt{\pi}\Delta P/\upsilon_0$. Results are presented for the dimensionless flow rate

$$W = \frac{\dot{M}}{\dot{M}_{FM}} = 4\sqrt{\pi}G \tag{2.3.14}$$

where

$$G|_x = \int\limits_0^1 u_x\left(x, r\right) r dr \tag{2.3.15}$$

is the reduced flow rate obtained by the simulations. Tabulated results for the flow rate W_{LIN} through a tube for various values of the rarefaction parameter δ and dimensionless length L/R, based on the linear BGK kinetic model with diffuse boundary conditions are shown in Table 2.9

With respect to the behavior of the macroscopic quantities, for all cases considered here, the field is symmetric around $x = L/\left(2L_0\right)$ for any channel length and in the whole range of the Knudsen number, as expected. Indicative results for the influence of δ is shown in Figures 2.8 and 2.9 for a cylindrical tube of $L/L_0 = 2$ and $\delta = 0.1, 1$ and 10. No significant changes occur for pressure for this length, besides a slightly larger deviation of pressure in the containers from the equilibrium values as δ is increased. The axial velocity values are also increased along with δ. The behavior is similar for the case of a cylindrical tube of $L/L_0 = 5$ and the same δ values, shown in Figures 2.10 and 2.11. The velocity profile in this case seems to develop to a nearly constant profile inside the channel for $\delta = 10$, which implies that the end

effect treatment, as shown in previous section, may be applied under these conditions to provide results with decent accuracy while avoiding the complete solution of the problem. For smaller δ or shorter channels, the fully developed flow characteristics are not so strong [96].

2.4 Flow through circular capillaries of finite length: The non-linear theory

Despite the fact that reliable results for linear fully developed flows through long capillaries may be obtained with moderate computational effort, however, when the flow becomes nonlinear, i.e. in the case of fast flows through channels of finite length, including flows through slits and orifices, the computational effort is significantly increased. In the former case, the flow is simulated only in one cross section of the channel and then the mass flow rate is estimated, while in the case of capillaries of finite length, the incoming distribution functions at the entrance and the exit of the channel are not Maxwellians and therefore adequately large computational domains must be included before and after the channel to properly impose the boundary conditions.

2.4.1 Flow configuration and formulation

Consider the axisymmetric nonisothermal flow of a monatomic gas through a circular microchannel of length L and radius R, connecting two reservoirs maintained at pressures P_1 and P_2 respectively, with $P_1 > P_2$. The walls of the reservoirs and of the channel as well as of the gas in the container far from the tube are maintained at reference temperature T_0. In the case of capillaries of finite length, the assumption of the fully developed flow, independent of the magnitude of the pressure difference, is not valid and the macroscopic distributions vary both in the radial $\hat{r}$ and axial $\hat{z}$ directions. Furthermore, the end effects must be considered and computational domains in the inlet and outlet of the channel must be added to ensure the proper implementation of Maxwellian boundary conditions. The flow configuration with the associated numerical grid in the physical space, are shown in Figure 2.12.

This flow configuration may be modeled based on the nonlinear BGK model given

by [80]

$$\xi_p \cos\theta \frac{\partial f}{\partial \hat{r}} - \frac{\xi_p \sin\theta}{\hat{r}} \frac{\partial f}{\partial \theta} + \xi_z \frac{\partial f}{\partial \hat{z}} = \nu\left(f^M - f\right) \tag{2.4.1}$$

where $f = f\left(\hat{r}, \hat{z}, \xi_p, \theta, \xi_z\right)$ is the unknown distribution function, $\xi = \left(\xi_p, \theta, \xi_z\right)$ the molecular velocity vector, ν the collision frequency and

$$f^M = n\left(\frac{m}{2\pi kT}\right)^{3/2} \exp\left[-\frac{m(\xi - \hat{\mathbf{u}})^2}{2kT}\right] \tag{2.4.2}$$

is the local Maxwellian, while the quantities n, $\hat{\mathbf{u}} = \hat{u}\left(\hat{u}_r, \hat{u}_z\right)$ and T denote the number density, velocity and temperature respectively. The following dimensionless quantities are introduced:

$$r = \frac{\hat{r}}{R}, \quad z = \frac{\hat{z}}{R}, \quad \mathbf{c} = \frac{\xi}{\upsilon_0}, \quad g = \frac{f\upsilon_0^3}{n_0},$$
$$\rho = \frac{n}{n_0}, \quad \mathbf{u} = \frac{\hat{\mathbf{u}}}{\upsilon_0}, \quad \tau = \frac{T}{T_0}, \quad p = \frac{P}{P_0} \tag{2.4.3}$$

Then, following a straightforward manipulation, Eq. 2.4.1 is reduced to its dimensionless form given by

$$c_p \cos\theta \frac{\partial g}{\partial r} - \frac{c_p \sin\theta}{r} \frac{\partial g}{\partial \theta} + c_x \frac{\partial g}{\partial x} = \delta_0 \rho \sqrt{\tau}\left(g^M - g\right) \tag{2.4.4}$$

where $g = g\left(r, z, c_p, \theta, c_z\right)$, the Maxwellian

$$g^M = \frac{\rho}{\left(\pi\tau\right)^{3/2}} \exp\left[-\frac{(\mathbf{c} - \mathbf{u})^2}{\tau}\right] \tag{2.4.5}$$

and the reference rarefaction parameter

$$\delta_0 = \frac{P_0 R}{\mu_0 \upsilon_0} \tag{2.4.6}$$

In the derivation of Eq. 2.4.4 the hard sphere molecular model has been applied assuming that $\mu \sim \sqrt{T}$. The bulk quantities are also nondimensionalized leading to

the following expressions

$$\rho = 2 \int\limits_{0}^{\infty} \int\limits_{0}^{\pi} \int\limits_{-\infty}^{\infty} g c_p dc_z d\theta dc_p \tag{2.4.7}$$

$$u_r = \frac{2}{\rho} \int\limits_{0}^{\infty} \int\limits_{0}^{\pi} \int\limits_{-\infty}^{\infty} c_p \cos\theta g c_p dc_z d\theta dc_p \tag{2.4.8}$$

$$u_z = \frac{2}{\rho} \int\limits_{0}^{\infty} \int\limits_{0}^{\pi} \int\limits_{-\infty}^{\infty} c_z g c_p dc_z d\theta dc_p \tag{2.4.9}$$

$$\tau = \frac{4}{3\rho} \int\limits_{0}^{\infty} \int\limits_{0}^{\pi} \int\limits_{-\infty}^{\infty} \left[(c_p \cos\theta - u_r)^2 + (c_p \sin\theta)^2 + (c_z - u_z)^2 \right] g c_p dc_z d\theta dc_p \tag{2.4.10}$$

$$p = \rho\tau \tag{2.4.11}$$

The incoming boundary distributions at the open and wall surfaces have a Maxwellian form according to

$$g^+ = \frac{C}{(\pi\tau)^{3/2}} \exp\left[-\frac{(\mathbf{c} - \mathbf{u})^2}{\tau} \right] \tag{2.4.12}$$

where $C = 1$ at boundaries (A) and (B), $C = P_2/P_1$ at boundaries (F) and (G) and $C = \rho_w$ at boundaries (C), (D) and (E), while $\tau = 1$. The parameter ρ_w is defined by the wall no penetration condition. Finally, specular reflection is imposed along the center line (H) due to the axial symmetry.

2.4.2   Mass flow rate

In addition to the macroscopic distributions, a quantity of major importance is the mass flow rate defined as

$$\dot{M} = 2\pi \int\limits_{0}^{R} mn\left(\hat{r}, \hat{z}\right) \hat{u}_z \left(\hat{r}, \hat{z}\right) \hat{r} d\hat{r} \tag{2.4.13}$$

Following common practice, the mass flow rate is nondimensionalized by the analytical free molecular solution for flow through an orifice given by $\dot{M}_{FM} = \sqrt{\pi}R^2 P_1/\upsilon_0$ to yield the dimensionless flow rate

$$W = \frac{\dot{M}}{\dot{M}_{FM}} = 4\sqrt{\pi} \int\limits_0^1 \rho\left(r,z\right) u_z\left(r,z\right) rdr \qquad (2.4.14)$$

Recently, Eq. 2.4.4 with the associated expressions for the macroscopic quantities and the proper boundary conditions has been numerically solved in a deterministic manner applying the discrete velocity method in the velocity space and a second order control volume scheme in the physical space. Since this is a five-dimensional problem the involved computational effort is significant. In the next section results are provided for the flow rate and the bulk distributions in terms of the three parameters characterizing the flow: the reference rarefaction parameter δ_0, the microtube aspect ratio L/R and the pressure ratio P_2/P_1.

As far the as behavior of the macroscopic quantities is concerned, indicative results for the density and axial velocity fields, as well as the streamlines and their dependence on the tube length is given in Figures 2.13 - 2.14, for $L/R = 0, 5, 10$, $P_{out} = 0.5$ and $\delta_0 = 10$. These cases are chosen here since the differences become more apparent, due to the high rarefaction parameter: as the tube becomes longer, the vortex becomes smaller, the velocity magnitude drops and the density isolines become nearly vertical inside the tube. The same characteristics are seen for increasing pressure ratio from 0.1 up to 0.9 in Figures 2.15 - 2.16 for $L/R = 1$ and $\delta_0 = 2$ [96].

For the needs of the present work the DSMC results for flow through tubes up to $L/R = 10$ into vacuum and various pressure ratios, reported in [148] and [150] respectively, have been introduced. The results in [134], based on the Shakhov model, have been implemented for flow through longer tubes with $10 \leq L/R \leq 50$ into vacuum. Furthermore, additional results based on the BGK and Shakhov models have been obtained here, within the aforementioned range of parameters, in order to have an adequately dense database of the nonlinear flowrates. In all cases modeling is based on hard sphere molecules with purely diffuse gas-surface interaction. As noted in [8, 34, 111], all approaches provide corresponding results in very good agreement and therefore using either the DSMC method or the BGK or the Shakhov models

to build the flowrate database does not affect the concluding remarks concerning the applicability range of the linear schemes. The implemented DSMC solver is described in detail in [148, 150]. The solution of the BGK and Shakhov models is obtained discretizing the physical space by a second order scheme and the molecular velocity space by the discrete velocity method. This deterministic approach has been described and successfully applied in several flow and heat transfer configurations [7, 77, 99, 101, 132]. The introduced numerical error (uncertainty) in the computed flow rates is always taken less than 1%. These nonlinear flowrates are used as the reference ones, in order to investigate the applicability of the linear approaches.

In general, the computational effort is increased as δ_1 is increased and the gas flow becomes less rarefied as well as the tube aspect ratio L/R is increased. In the implemented DSMC algorithm the computational effort is also increased as the pressure ratio P_2/P_1 approaches one, while on the contrary, the convergence speed of the deterministic discrete velocity codes remains the same at any pressure ratio. In addition, the DSMC code runs in serial mode, while the deterministic codes are highly parallelized. The involved computational effort depends on the set of flow parameters and on the code optimization and for the prescribed accuracy it may vary from few hours up to several days of CPU time.

The flow rate W through a tube for various values of the rarefaction parameter δ_0, the pressure ratio P_2/P_1 and dimensionless length L/R, based on the nonlinear BGK kinetic model with diffuse boundary conditions, is provided in Tables 2.10 and 2.11.

2.5 Range of validity of infinite, end effect and non-linear theories

Recently, the range of validity of the various linear theories has been investigated by comparing the flow rates with the corresponding ones obtained by the nonlinear approach [142]. Here, a brief review is presented mainly for completeness purposes.

As it has been noted above, the three parameters characterizing pressure driven flow through capillaries include the reference rarefaction parameter δ_0, the tube aspect ratio L/R and the pressure ratio P_2/P_1. It has been computationally confirmed in

[142] that the implementation of a linear approach introduces an error of less than 10%, provided that

$$\delta_0 \left(\frac{L}{R}\right) \left(1 - \frac{P_2}{P_1}\right) \leq 1 \qquad (2.5.1)$$

plus some complimentary restrictions. More specifically, the implementation of the infinite capillary theory without the end effect correction will result to a deviation within $\pm 10\%$ provided that inequality 2.5.1 is fulfilled and $L/R \geq 50$. A great improvement is achieved when the end correction is introduced. The implementation of the infinite capillary theory with the end effect correction will result to a deviation within $\pm 10\%$ provided that inequality 2.5.1 is fulfilled and $L/R \geq 20$. In addition, the deviation norm remains $\leq 10\%$ even for $L/R = 10$ provided that inequality 2.5.1 is fulfilled, while $P_2/P_1 \geq 0.1$ and $\delta_1 \geq 10^{-2}$. This is exactly the great advantage of the end effect correction, since the range of applicability of the infinite capillary theory is significantly enhanced, while the involved computational effort remains negligible.

In an attempt to quantify this behavior, the mass flow rate through a channel of cylindrical cross section, for a variety of flow conditions, is evaluated by implementing three different methodologies, as they have been described in previous sections, namely *i)* fully developed flow methodology denoted by $\dot{M}_{FD}$, *ii)* results obtained by using the end effect treatment $\dot{M}_{EE}$ and *iii)* $\dot{M}_{LIN}$ for the case where the complete geometry is considered in the simulation. It is expected that the ratio of mass flow rates, using complete simulation and typical integration with/without end effects, should approach unity as the tube length increases. These ratio values are given in Table 2.12 for a variety of flow conditions. It is seen that the maximum discrepancy for the end effect treatment (2%) occurs for highly rarefied conditions ($\delta = 0.2$). This is due to the fact that the tube is quite short in comparison to the development length required to achieve a constant pressure perturbation. However, as δ obtains values over unity, we observe that the discrepancies drop significantly for the end effect treatment (less than 2 % at all cases examined here), in comparison to the fully developed flow simulation (up to 7-19 %). The lowest discrepancies are found for the extra cases of $L/R = 20$, executed in the complete geometry to enhance our trust on this methodology. It is seen that discrepancies in this case drop for both methods and we reach the conclusion that errors below 1% may be obtained by the end effect simulation if $\delta \geq 1$ and $L/R \geq 20$ are considered [96]

2. SINGLE PIPING ELEMENTS

It is noted that in the present work, the computed flow rates are obtained based on the infinite capillary theory with the end effect correction provided that the above specified restrictions are fulfilled. Otherwise, the flow rates are obtained based on the nonlinear approach. In this latter case the computational effort is significant.

Table 2.1: Definitions of D_h, A', A, Γ', Γ for various channels.

Cross section	D_h	A'	$A = A'/D_h^2$	Γ'	Γ
Circular	D	$\frac{\pi D^2}{4}$	$\frac{\pi}{4}$	πD	π
Orthogonal	$2\frac{W \times H}{W + H}$	$W \times H$	$\frac{1}{4}\frac{H}{W}\left(1 + \frac{W}{H}\right)^2$	$2\left(W + H\right)$	$\frac{H}{W}\left(1 + \frac{W}{H}\right)^2$
Triangular	$\frac{\alpha}{\sqrt{3}}$	$\frac{\sqrt{3}}{4}\alpha^2$	$\frac{3\sqrt{3}}{4}$	3α	$3\sqrt{3}$
Trapezoidal	$\frac{2(B+b)h}{B+b+\frac{2h}{\sin\theta}}$	$\frac{B+b}{2}h$	$\frac{1}{8}\frac{\left(1+\frac{b}{B}+\frac{h}{B}\frac{2}{\sin\theta}\right)^2}{\left(1+\frac{b}{B}\right)\frac{h}{B}}$	$B + b + \frac{2h}{\sin\theta}$	$\frac{1}{2}\frac{\left(1+\frac{b}{B}+\frac{h}{B}\frac{2}{\sin\theta}\right)^2}{\left(1+\frac{b}{B}\right)\frac{h}{B}}$

Table 2.2: Dimensionless flow rate G in terms of the rarefaction parameter δ, for channels of circular cross section and specular-diffuse boundary conditions (α=1, 0.85 and 0.7).

		G	
δ	$\alpha = 1$	$\alpha = 0.85$	$\alpha = 0.7$
10^{-3}	0.751	1.01	1.39
10^{-2}	0.744	0.999	1.36
0.1	0.715	0.941	1.25
0.3	0.695	0.896	1.18
0.5	0.689	0.879	1.14
1	0.693	0.870	1.12
1.5	0.709	0.879	1.12
2	0.729	0.896	1.13
3	0.777	0.941	1.17
4	0.829	0.992	1.22
5	0.884	1.05	1.28
6	0.940	1.10	1.33
7	0.997	1.16	1.39
8	1.06	1.22	1.45
9	1.11	1.28	1.51
10	1.17	1.34	1.57
11	1.23	1.40	1.63
13	1.35	1.52	1.75
15	1.48	1.64	1.87
20	1.78	1.95	2.18
30	2.40	2.56	2.80
40	3.02	3.19	3.42
50	3.64	3.81	4.04
100	6.76	6.93	7.16
200	13.0	13.2	13.4
500	31.7	31.9	32.1
1000	62.6	63.0	62.8

Table 2.3: Dimensionless flow rate G in terms of the rarefaction parameter δ, for channels of orthogonal cross section and specular-diffuse boundary conditions (α=1, 0.85 and 0.7).

	G								
	$H/W = 1$			$H/W = 0.5$			$H/W = 0.1$		
	α			α			α		
δ	1	0.85	0.7	1	0.85	0.7	1	0.85	0.7
10^{-3}	0.837	1.06	1.39	0.862	1.10	1.44	1.09	1.40	1.86
10^{-2}	0.828	1.05	1.36	0.852	1.08	1.41	1.06	1.36	1.79
0.1	0.793	0.987	1.27	0.813	1.01	1.30	0.961	1.20	1.54
0.3	0.769	0.944	1.19	0.783	0.963	1.22	0.877	1.08	1.37
0.5	0.762	0.929	1.17	0.773	0.944	1.19	0.838	1.03	1.29
1	0.768	0.926	1.15	0.773	0.935	1.17	0.797	0.970	1.21
1.5	0.786	0.942	1.16	0.787	0.945	1.17	0.785	0.952	1.19
2	0.810	0.964	1.19	0.807	0.964	1.19	0.786	0.950	1.18
4	0.924	1.08	1.30	0.908	1.07	1.29	0.833	0.993	1.22
6	1.05	1.21	1.44	1.02	1.18	1.41	0.905	1.07	1.29
8	1.18	1.35	1.51	1.14	1.31	1.54	0.985	1.15	1.38
10	1.32	1.48	1.65	1.26	1.43	1.67	1.07	1.23	1.46
15	1.66	1.83	1.93	1.57	1.74	1.99	1.29	1.45	1.69
20	2.00	2.18	2.28	1.89	2.06	2.31	1.52	1.68	1.92
30	2.70	2.88	2.98	2.52	2.70	2.95	1.98	2.15	2.38
40	3.40	3.58	3.69	3.16	3.34	3.59	2.44	2.61	2.85
50	4.10	4.28	4.39	3.80	3.98	4.24	2.91	3.08	3.32
100	7.61	7.79	7.70	7.01	7.19	7.45	5.26	5.44	5.68
200	14.6	14.8	11.6	13.4	13.6	13.9	9.98	10.2	10.4
500	35.7	35.9	36.2	32.7	32.9	33.2	24.2	24.3	24.6
1000	70.9	71.0	71.3	64.9	65.1	65.3	47.8	47.9	48.2

Table 2.4: Dimensionless flow rate G in terms of the rarefaction parameter δ, for channels of triangular cross section and diffuse boundary conditions (α=1).

	G	
δ	Equilateral $\phi = 60°$	Isosceles $\phi = 54.74°$
10^{-3}	0.927	0.932
10^{-2}	0.916	0.921
0.1	0.872	0.876
0.3	0.841	0.844
0.5	0.831	0.834
1	0.833	0.836
1.5	0.851	0.854
2	0.875	0.878
3	0.931	0.934
4	0.994	0.997
5	1.06	1.06
6	1.13	1.13
7	1.20	1.20
8	1.26	1.27
9	1.34	1.34
10	1.41	1.41
20	2.14	2.14
30	2.88	2.88
40	3.62	3.62
50	4.36	4.37
100	8.05	8.07

Table 2.5: Dimensionless flow rate G in terms of the rarefaction parameter δ, for channels of trapezoidal cross section and diffuse boundary conditions (α=1).

	G	
δ	Isosceles $\phi = 63.43°$	Isosceles $b/B = 0.78$ $\phi = 54.74°$
10^{-3}	0.877	1.02
10^{-2}	0.867	0.999
0.1	0.827	0.925
0.3	0.799	0.864
0.5	0.790	0.836
1	0.793	0.810
1.5	0.809	0.807
2	0.832	0.814
3	0.885	0.841
4	0.944	0.877
5	1.01	0.919
6	1.07	0.962
7	1.13	1.01
8	1.20	1.06
9	1.26	1.10
10	1.33	1.15
20	2.02	1.66
30	2.71	2.18
40	3.40	2.71
50	4.10	3.23
100	7.55	5.85

Table 2.6: The Poiseuille number in terms of the rarefaction parameter δ_0 for channels of various cross sections, with $\alpha=1$.

δ_0	Po								
	Circular	Orthogonal ($\gamma = H/W$)				Triangular		Trapezoidal	
		$\gamma = 1$	$\gamma = 0.5$	$\gamma = 0.1$	$\gamma = 0.01$	Equilateral $\phi = 60°$	Isosceles $\phi = 54.74°$	Isosceles $b/B = 0.5$ $\phi = 63.43°$	Isosceles $b/B = 0.78$ $\phi = 54.74°$
10^{-3}	0.00533	0.00478	0.00464	0.00367	0.00248	0.00431	0.00429	0.00456	0.00393
10^{-2}	0.0538	0.0483	0.0469	0.0376	0.0272	0.0437	0.0434	0.0461	0.0400
0.1	0.560	0.504	0.492	0.416	0.356	0.458	0.456	0.483	0.432
0.5	2.90	2.62	2.59	2.39	2.30	2.41	2.40	2.53	2.40
1	5.77	5.21	5.17	5.02	4.99	4.80	4.78	5.05	4.94
2	11.0	9.88	9.91	10.2	10.4	9.14	9.11	9.62	9.83
3	15.4	13.9	14.0	14.9	15.4	12.9	12.8	13.6	14.3
4	19.3	17.3	17.6	19.2	20.0	16.1	16.0	16.9	18.2
5	22.6	20.3	20.7	23.1	24.1	18.9	18.8	19.8	21.8
6	25.5	22.8	23.5	26.5	27.9	21.3	21.2	22.4	25.0
7	28.1	25.1	25.9	29.7	31.3	23.4	23.3	24.7	27.8
8	30.3	27.0	28.0	32.5	34.4	25.3	25.2	26.7	30.3
9	32.3	28.8	29.9	35.1	37.3	27.0	26.8	28.5	32.6
10	34.0	30.4	31.7	37.4	39.9	28.4	28.3	30.0	34.7
20	44.9	39.9	42.4	52.8	57.2	37.4	37.4	39.7	48.3
30	50.0	44.5	47.6	60.7	66.4	41.7	41.6	44.3	55.0
40	53.0	47.1	50.6	65.5	71.9	44.2	44.2	47.0	59.1
50	54.9	48.8	52.6	68.7	75.7	45.9	45.8	48.8	61.9
100	59.1	52.6	57.1	76.0	84.3	49.7	49.6	52.9	68.4
·	·	·	·	·	·	·	·	·	·
∞	64.0	56.9	62.2	84.7	94.7	53.3	-	-	74.6

Table 2.7: Geometric parameters for the end geometry

δ	0.2	0.4	1	2	4	8	10
L_{dev}/L_0	60	50	40	30	30	20	20
L_{right}/L_0	10	10	12	12	15	15	15

Table 2.8: Length increment ΔL_{tube} for various values of the rarefaction parameter δ.

δ	0.005	0.05	0.1	0.2	0.4	0.6	0.8	1	2
ΔL_{tube}	2.22	1.72	1.52	1.33	1.16	1.07	1.01	0.964	0.841

δ	4	6	8	10	...	∞
ΔL_{tube}	0.735	0.704	0.688	0.682	...	0.680

Table 2.9: Flow rate W_{LIN} through a tube for various values of the rarefaction parameter δ and dimensionless length L/R, based on the linear BGK kinetic model with diffuse boundary conditions.

| L/R | W_{LIN} | | | | | |
| | δ | | | | | |
	0	0.1	1	2	5	10
0	0.999	1.04	1.37	1.72	2.77	4.35
1	0.672	0.696	0.892	1.10	1.70	2.63
5	0.311	0.316	0.373	0.440	0.642	0.988
10	0.191	0.192	0.217	0.251	0.362	0.554
20	0.110	0.108	0.118	0.136	0.195	0.296

Table 2.10: Dimensionless flow rate W through short capillaries of cylindrical cross section vs. rarefaction parameter, pressure ratio and length (1/2).

		W						
L/R	P_2/P_1	Rarefaction parameter of high pressure chamber (δ_1)						
		0	0.1	0.5	1	2	5	10
0	0.0	1.000	1.014	1.069	1.129	1.221	1.374	1.463
	0.1	0.900	0.910	1.000	1.032	1.180	1.350	1.435
	0.3	0.700	0.719	0.788	0.862	0.987	1.221	1.366
	0.5	0.500	0.509	0.582	0.613	0.778	1.040	1.188
	0.7	0.3	0.305	0.354	0.38	0.493	0.717	0.914
	0.9	0.1	0.102	0.121	0.14	0.176	0.28	0.432
0.1	0.0	0.953	0.965	1.018	1.074	1.165	1.312	1.404
	0.1	0.856	0.869	0.924	0.984	1.08	1.27	1.380
	0.3	0.669	0.687	0.752	0.823	0.942	1.171	1.321
	0.5	0.475	0.486	0.528	0.583	0.688	0.948	1.150
	0.7	0.286	0.292	0.321	0.361	0.436	0.654	0.885
	0.9	0.095	0.099	0.114	0.131	0.164	0.246	0.333
0.5	0.0	0.801	0.812	0.855	0.902	0.981	1.117	1.220
	0.1	0.721	0.731	0.775	0.826	0.911	1.080	1.200
	0.3	0.562	0.577	0.630	0.688	0.786	0.994	1.223
	0.5	0.399	0.409	0.444	0.488	0.573	0.796	1.010
	0.7	0.241	0.246	0.270	0.300	0.363	0.541	0.762
	0.9	0.080	0.083	0.095	0.109	0.135	0.212	0.299
1	0.0	0.672	0.680	0.715	0.754	0.819	0.948	1.062
	0.1	0.605	0.613	0.648	0.689	0.761	0.913	1.050
	0.3	0.471	0.483	0.525	0.571	0.652	0.834	1.000
	0.5	0.336	0.343	0.370	0.405	0.474	0.658	0.866
	0.7	0.201	0.205	0.224	0.249	0.298	0.440	0.640
	0.9	0.067	0.070	0.080	0.091	0.112	0.170	0.264
2	0.0	0.514	0.52	0.544	0.572	0.62	0.732	0.855
	0.1	0.463	0.468	0.493	0.521	0.573	0.699	0.842
	0.3	0.36	0.368	0.396	0.428	0.486	0.63	0.795
	0.5	0.256	0.26	0.28	0.304	0.351	0.486	0.669
	0.7	0.153	0.156	0.17	0.19	0.22	0.319	0.471
	0.9	0.051	0.053	0.059	0.066	0.08	0.119	0.176
5	0.0	0.311	0.312	0.322	0.334	0.361	0.436	0.543
	0.1	0.279	0.281	0.291	0.304	0.33	0.412	0.529
	0.3	0.217	0.22	0.232	0.247	0.275	0.36	0.485
	0.5	0.155	0.156	0.163	0.175	0.197	0.271	0.388
	0.7	0.093	0.093	0.1	0.106	0.123	0.174	0.263
	0.9	0.031	0.031	0.035	0.038	0.044	0.064	0.098

Table 2.11: Dimensionless flow rate W through short capillaries of cylindrical cross section vs. rarefaction parameter, pressure ratio and length (2/2).

| | | W | | | | | | |
| | | Rarefaction parameter of high pressure chamber (δ_1) | | | | | | |
L/R	P_2/P_1	20	50	100	200	500	1000	2000
0	0.0	1.512	1.534	1.533	1.529	1.526	1.523	1.522
	0.1	1.500	1.510	1.520	1.52	1.52	1.52	1.52
	0.3	1.437	1.440	1.450	1.45	1.46	1.46	1.46
	0.5	1.300	1.310	1.340	1.35	1.36	1.36	1.36
	0.7	1.05	1.09	1.13	1.13	1.15	1.14	1.14
	0.9	0.584	0.606	0.628	0.628	0.64	0.634	0.634
0.1	0.0	1.462	1.498	1.508	1.512	1.515	1.515	1.517
	0.1	1.45	1.49	1.51	1.51	1.51	1.51	1.51
	0.3	1.406	1.420	1.440	1.45	1.45	1.45	1.45
	0.5	1.270	1.350	1.370	1.39	1.39	1.39	1.39
	0.7	1.030	1.120	1.150	1.16	1.17	1.16	1.16
	0.9	0.387	0.421	0.433	0.436	0.44	0.436	0.436
0.5	0.0	1.302	1.383	1.435	1.462	1.484	1.494	1.493
	0.1	1.290	1.380	1.430	1.46	1.48	1.49	1.49
	0.3	1.267	1.330	1.390	1.43	1.45	1.46	1.46
	0.5	1.150	1.280	1.350	1.39	1.41	1.42	1.42
	0.7	0.937	1.080	1.150	1.19	1.20	1.20	1.20
	0.9	0.367	0.423	0.451	0.466	0.47	0.47	0.47
1	0.0	1.168	1.287	1.358	1.412	1.449	1.456	1.458
	0.1	1.160	1.280	1.350	1.41	1.45	1.46	1.46
	0.3	1.136	1.24	1.32	1.38	1.42	1.43	1.43
	0.5	1.04	1.20	1.29	1.35	1.39	1.40	1.40
	0.7	0.831	1.00	1.10	1.16	1.19	1.19	1.19
	0.9	0.415	0.499	0.549	0.579	0.594	0.594	0.594
2	0.0	0.974	1.156	1.259	1.339	1.397	1.406	1.404
	0.1	0.985	1.15	1.26	1.34	1.39	1.4	1.40
	0.3	0.96	1.11	1.23	1.31	1.36	1.37	1.37
	0.5	0.864	1.07	1.19	1.28	1.32	1.34	1.34
	0.7	0.672	0.884	1.00	1.09	1.13	1.13	1.13
	0.9	0.251	0.33	0.373	0.407	0.422	0.422	0.422
5	0.0	0.695	0.917	1.068	1.184	1.271	1.282	1.284
	0.1	0.695	0.917	1.068	1.184	1.271	1.282	1.284
	0.3	0.663	0.87	1.03	1.15	1.23	1.24	1.23
	0.5	0.571	0.828	0.993	1.11	1.18	1.2	1.19
	0.7	0.411	0.658	0.814	0.922	0.975	0.98	0.986
	0.9	0.164	0.263	0.325	0.368	0.389	0.391	0.393

Table 2.12: Flow rate ratio between the different methodologies implemented for linear flow

	L/R	$\dot{M}_{FD}/\dot{M}_{LIN}$	$\dot{M}_{EE}/\dot{M}_{LIN}$	$\dot{M}_{FD}/\dot{M}_{EE}$
$\delta = 0.2$	10	1.28	1.02	1.26
$\delta = 1$	10	1.19	1.00	1.19
$\delta = 2$	10	1.17	1.00	1.17
$\delta = 10$	10	1.14	1.01	1.13
$\delta = 1$	20	1.10	1.00	1.09
$\delta = 10$	20	1.07	1.00	1.07
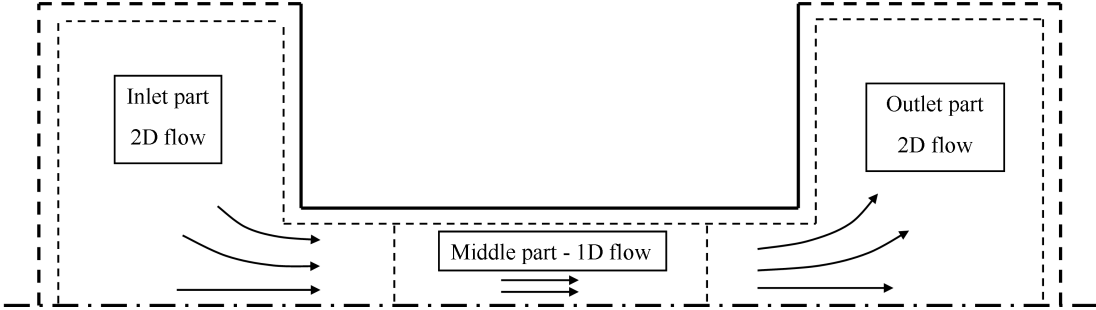
Figure 2.1: Division of the channel geometry into three parts
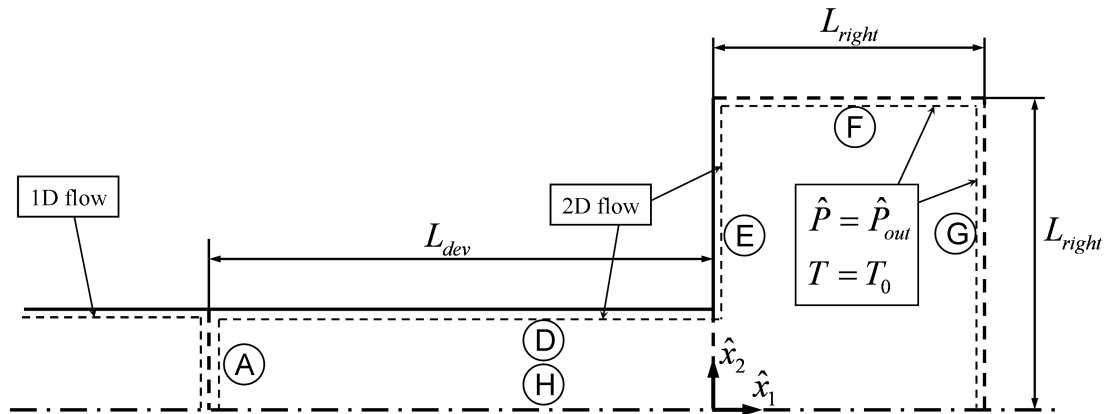
Figure 2.2: Division of the flow into the inlet, middle and outlet parts

$$\delta P = \hat{P} - P_R = \text{constant}$$

Real pressure $\hat{P}$

$\hat{P}$

Reference pressure P_R

$$\hat{P} = P_{out}$$

$$\phi = -\tan^{-1}\left(\frac{d\hat{P}_R}{d\hat{x}}\right)$$

$\hat{x}$

Channel

Outlet region

$$\hat{x} = \Delta L_{out}$$
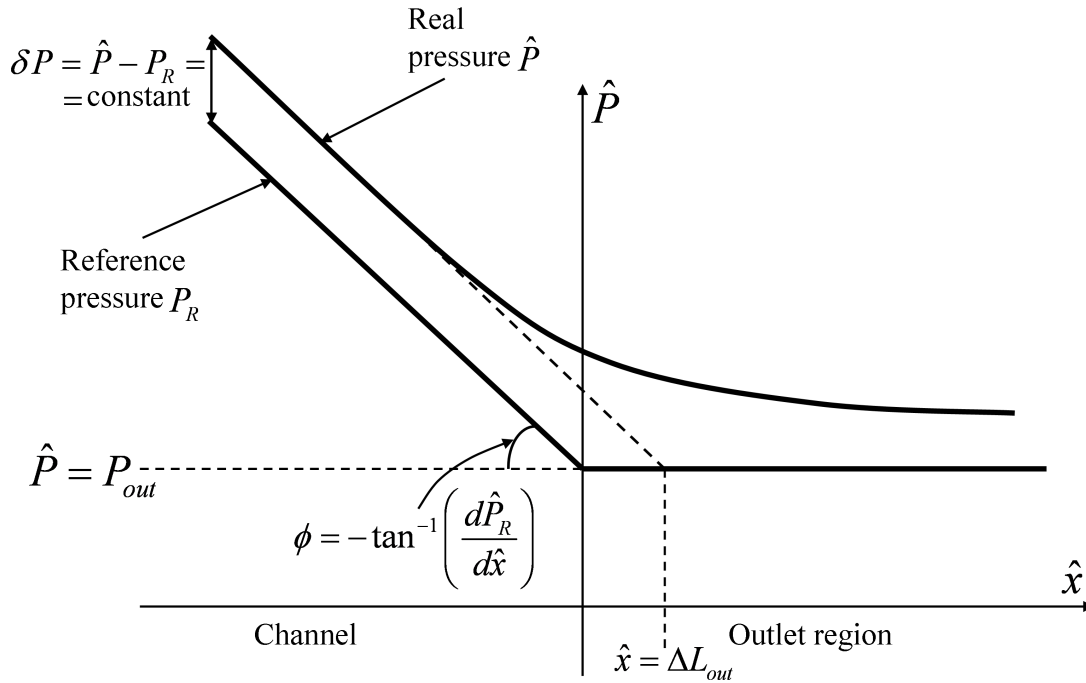
Figure 2.3: Indicative pressure distribution along the central axis at the outlet part to justify constant density perturbation
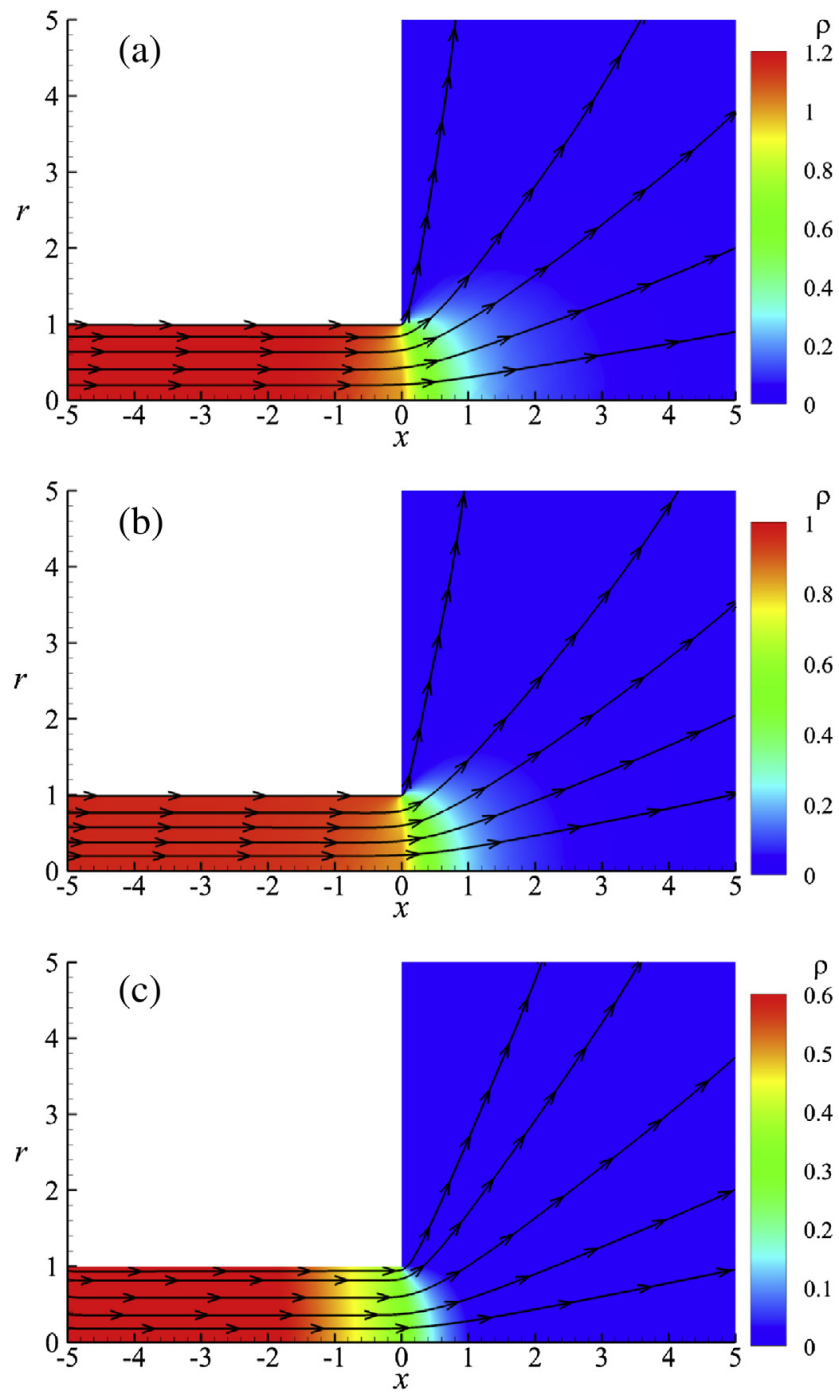
Figure 2.4: Density distributions and streamlines: (a) $\delta_0 = 0.2$, (b) $\delta_0 = 1$ and (c) $\delta_0 = 10$
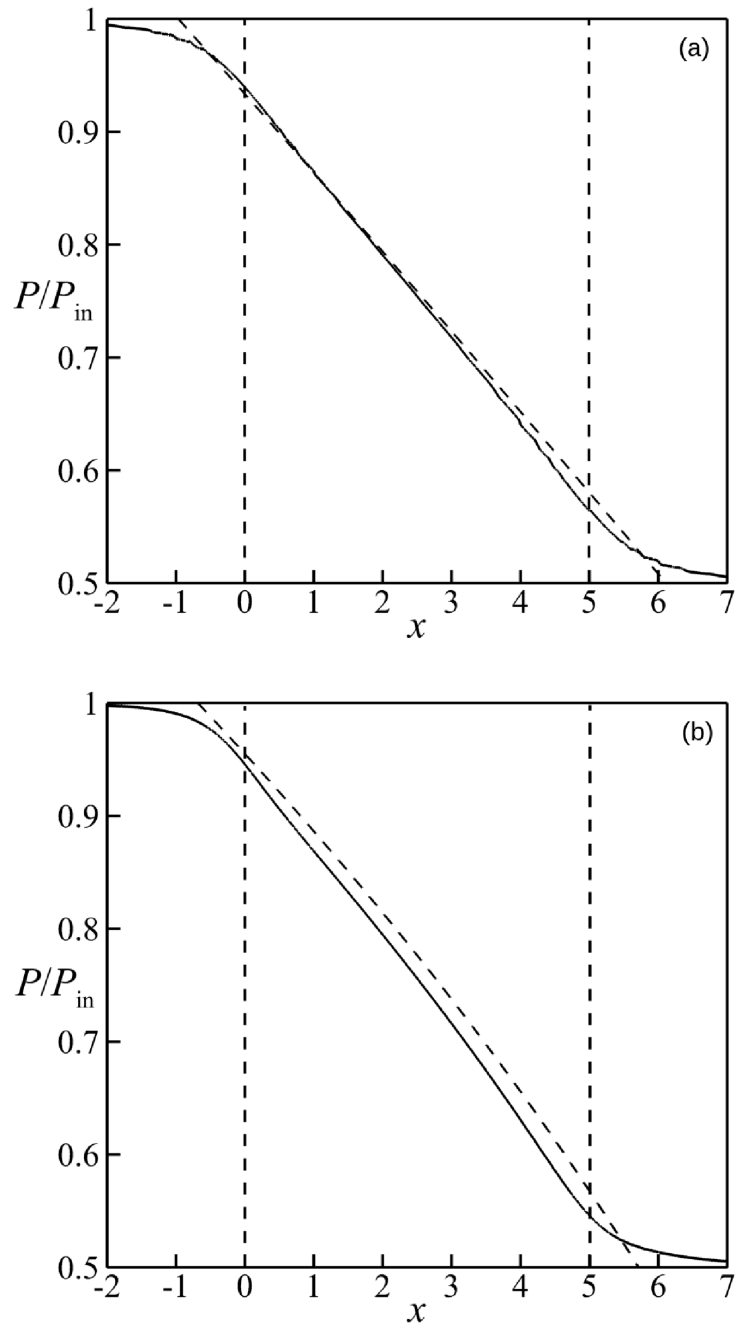
Figure 2.5: Pressure distribution along the symmetry axis at $L = 5$ and $P_{in}/P_{out} = 0.5$ with (a) $\delta_0 = 1$ and (b) $\delta_0 = 10$; solid line: solution for the complete flow domain, dashed line: present solution.
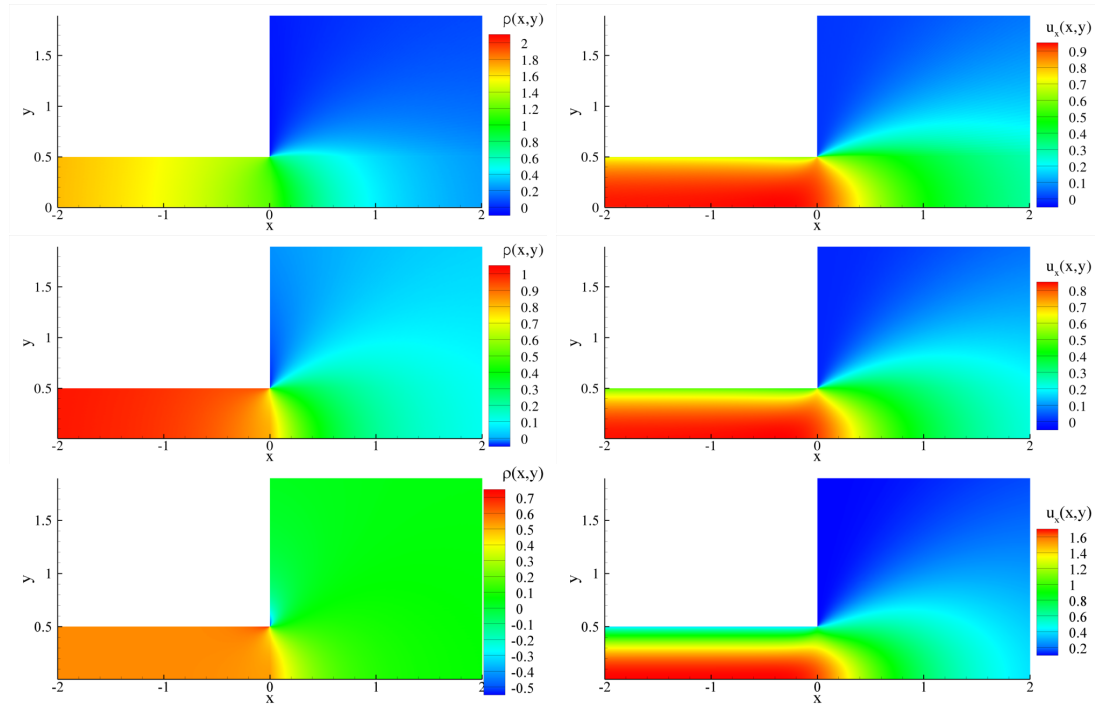
Figure 2.6: Density (left) and horizontal velocity (right) perturbation distributions for $\delta = 0.2$(up), $\delta = 1$(middle) and $\delta = 10$(below)
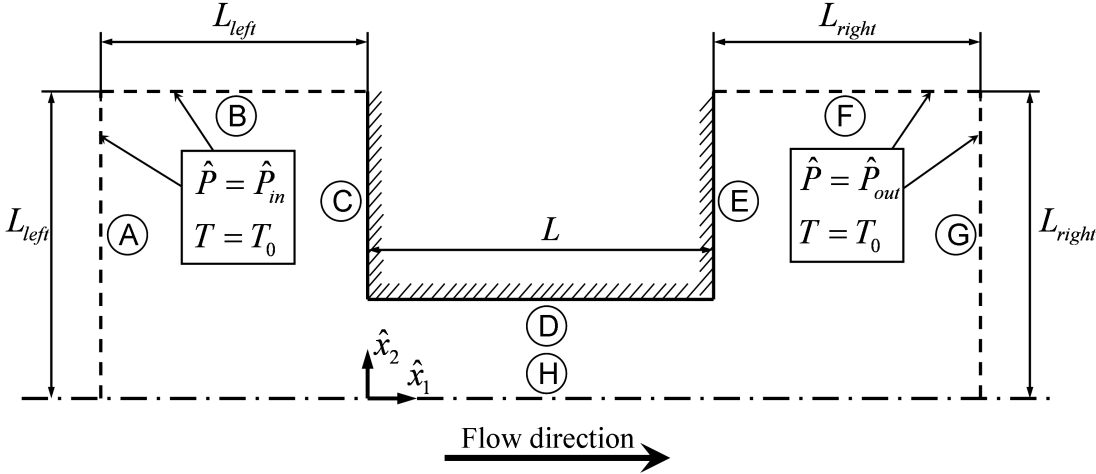
Figure 2.7: Flow configuration and coordinate system
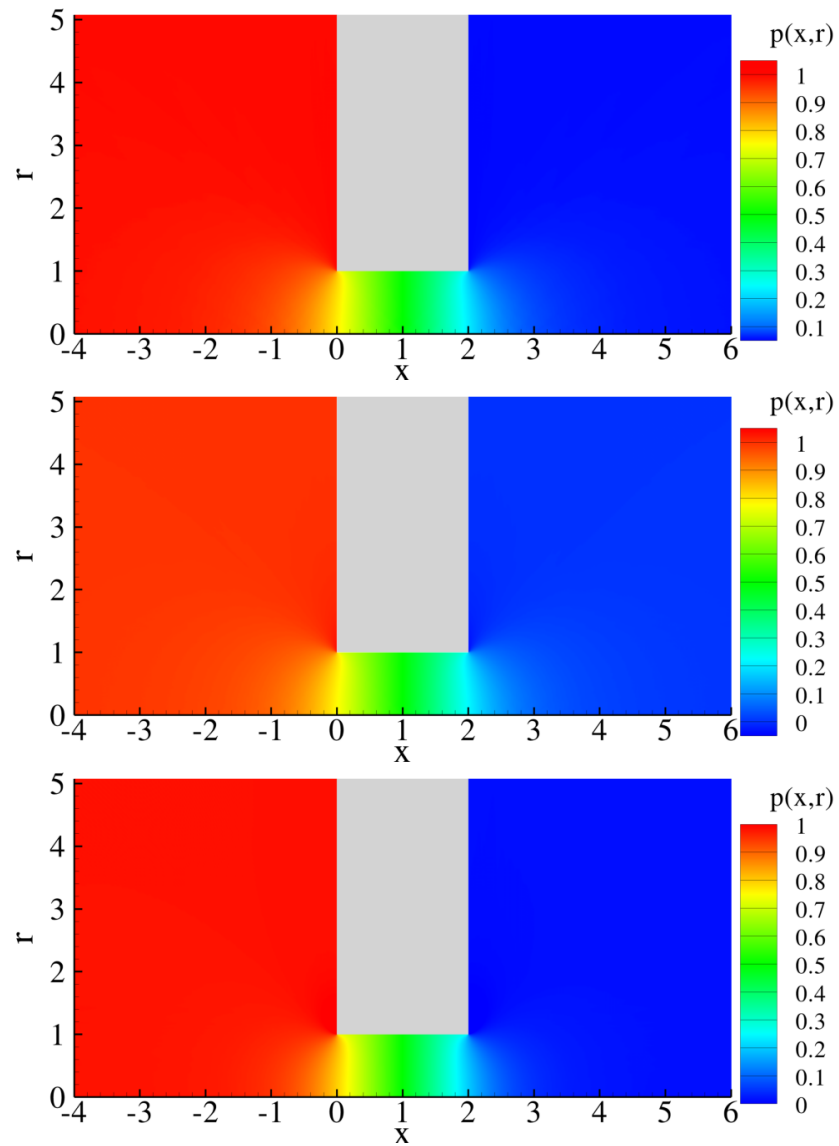
Figure 2.8: Pressure perturbation for the tube geometry with $L/L_0 = 2$ and $\delta = 0.1$ (up), $\delta = 1$ (middle), $\delta = 10$ (down)
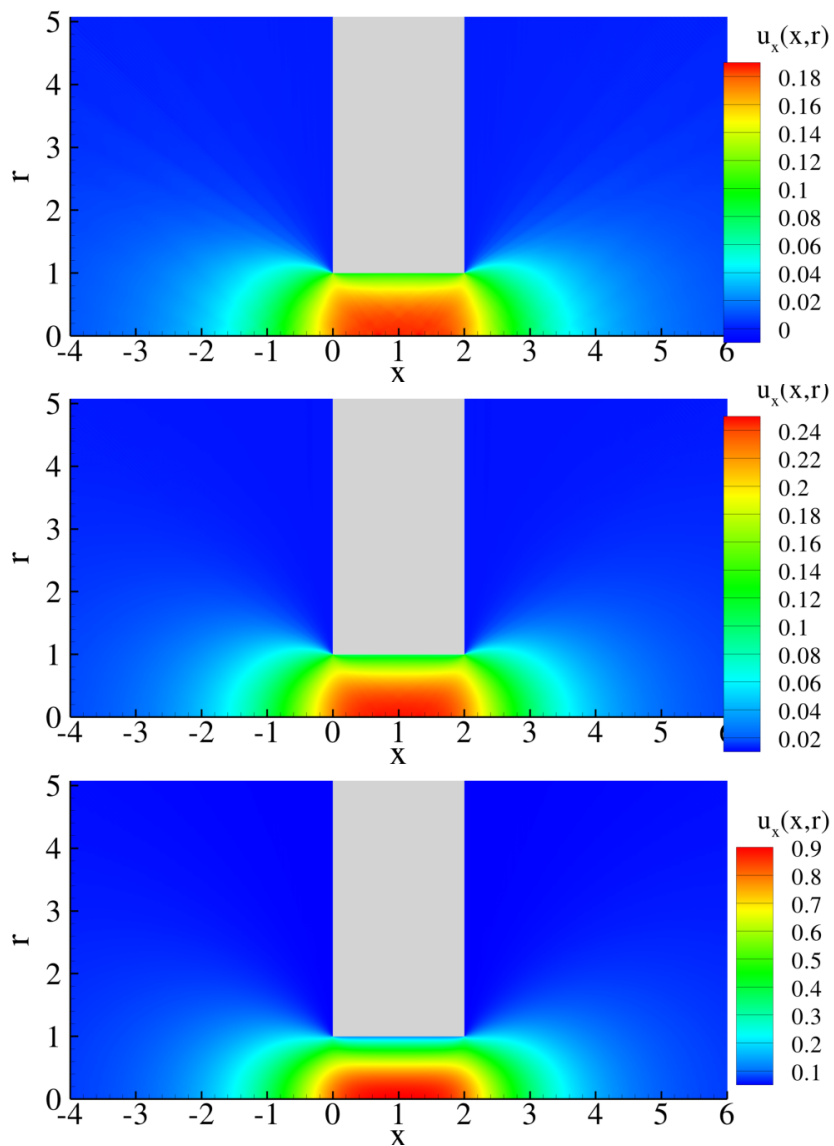
Figure 2.9: Axial velocity for the tube geometry with $L/L_0 = 2$ and $\delta = 0.1$ (up), $\delta = 1$ (middle), $\delta = 10$ (down)
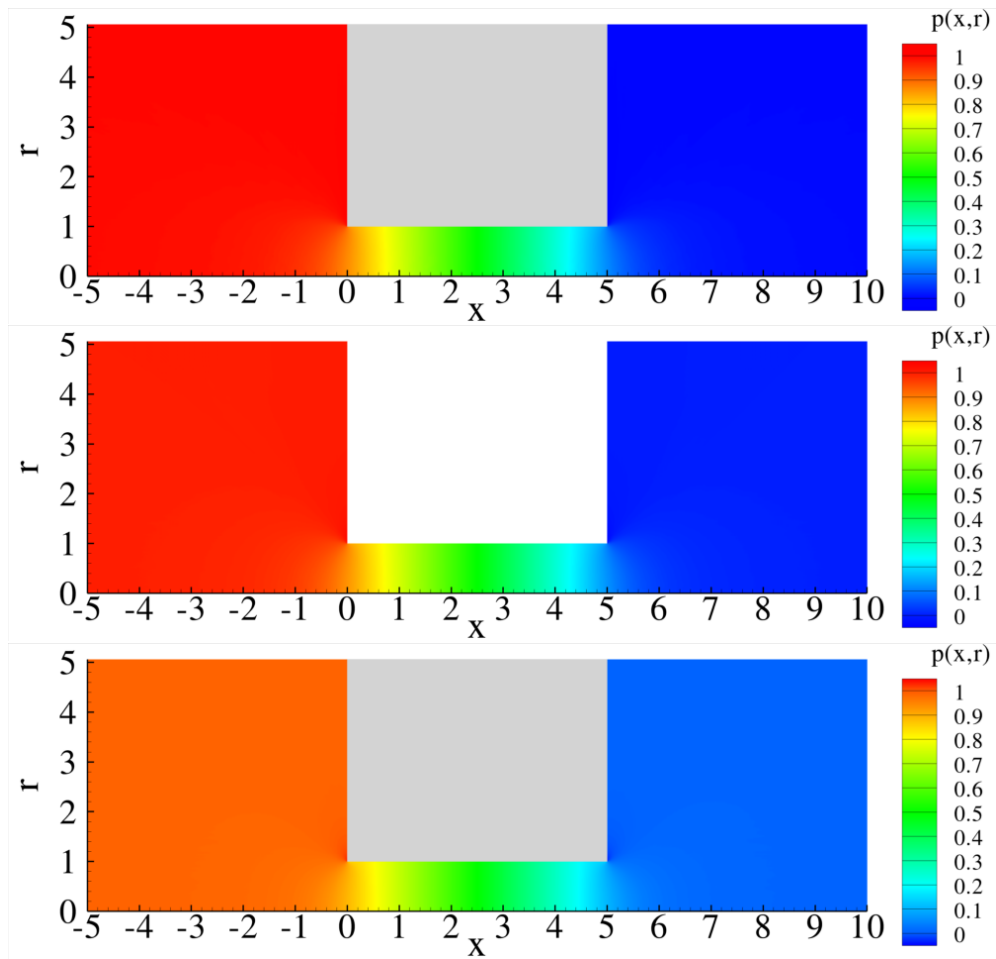
Figure 2.10: Pressure perturbation for the tube geometry with $L/L_0 = 5$ and $\delta = 0.1$ (up), $\delta = 1$ (middle), $\delta = 10$ (down)
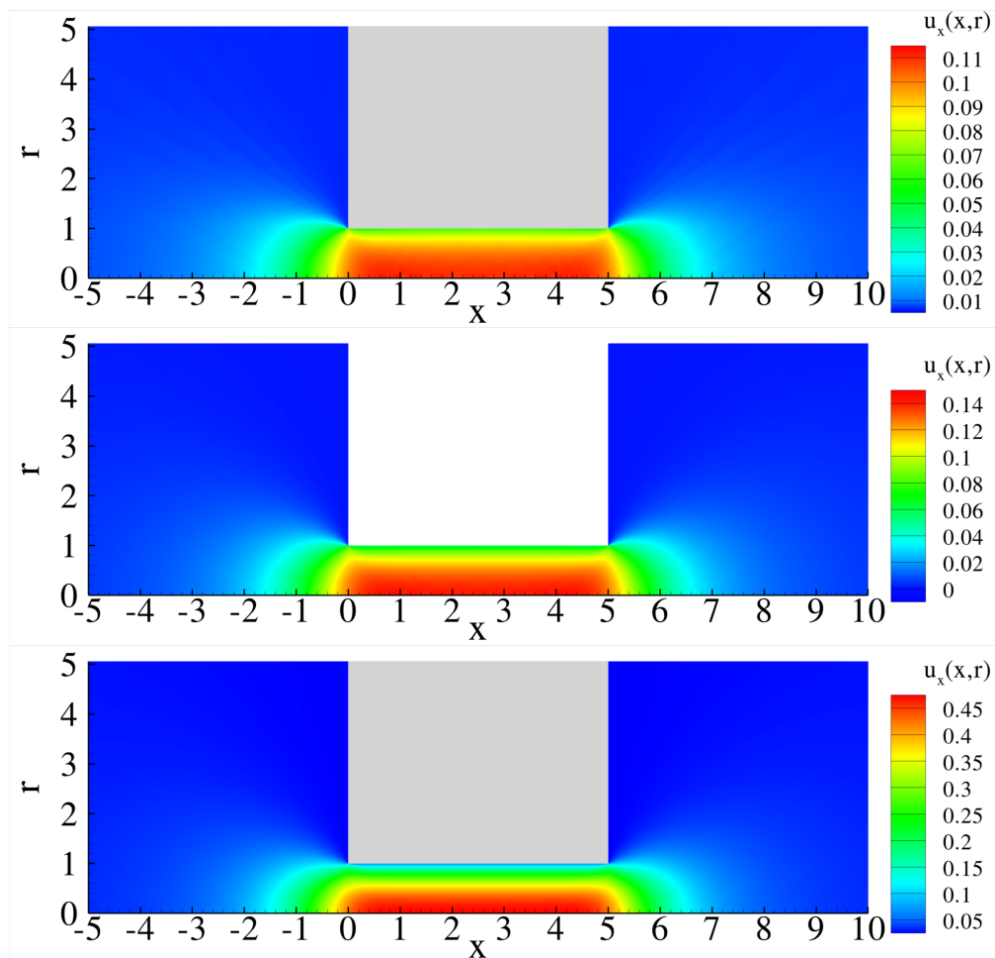
Figure 2.11: Axial velocity for the tube geometry with $L/L_0 = 5$ and $\delta = 0.1$ (up), $\delta = 1$ (middle), $\delta = 10$ (down)
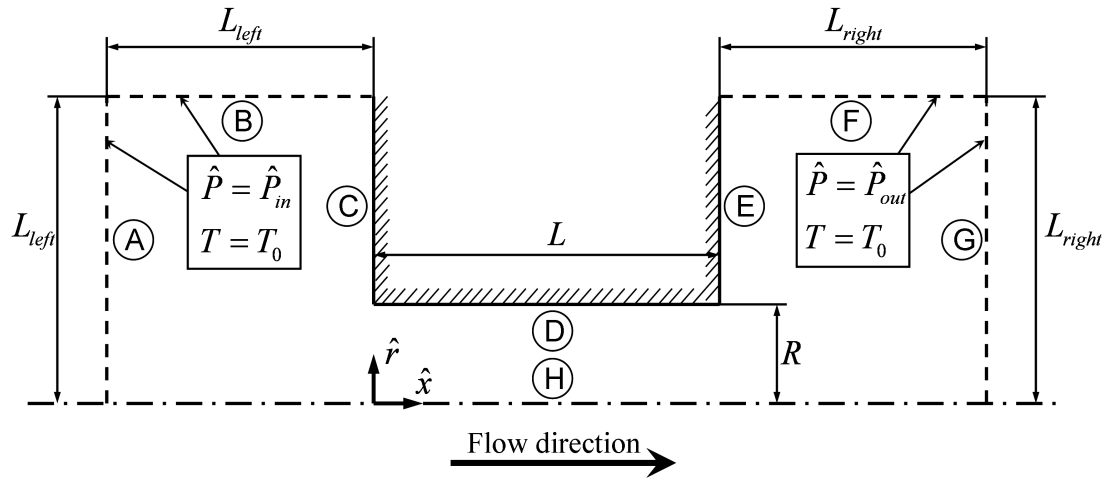
Figure 2.12: Flow configuration and coordinate system
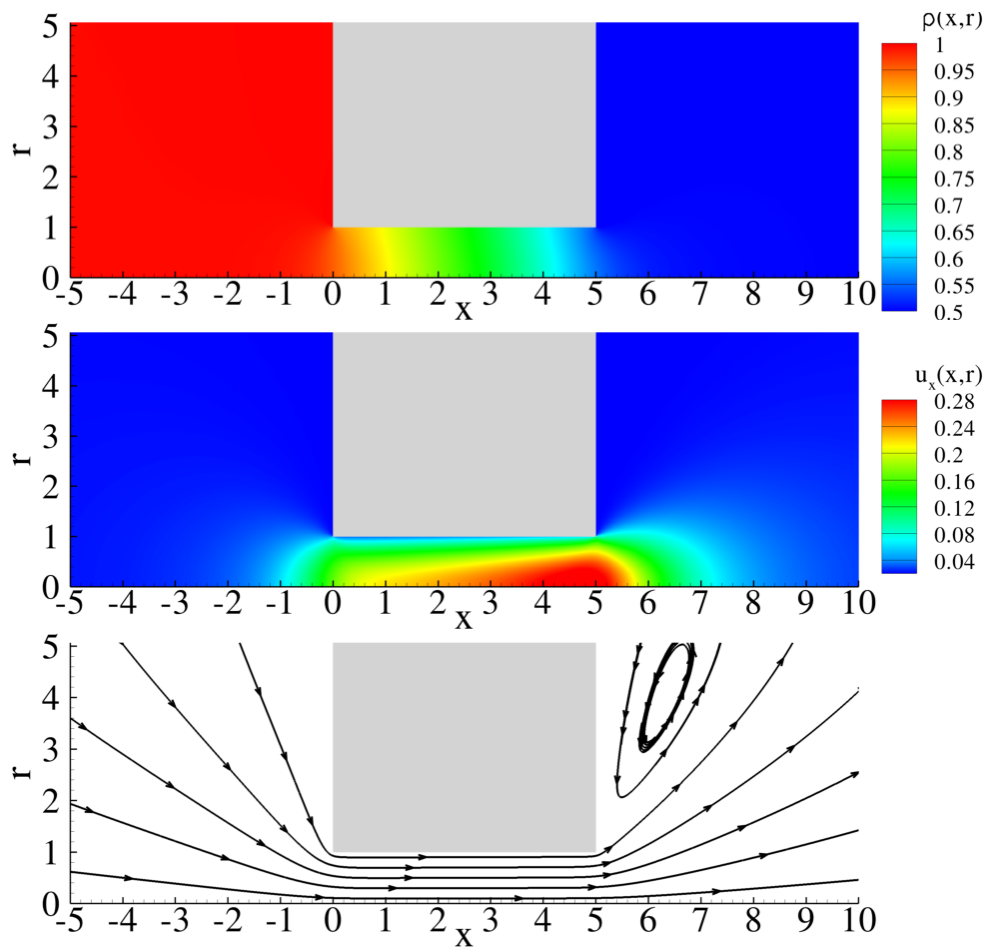
Figure 2.13: Density (up) and axial velocity (middle) contours, as well as streamlines (down) for the short tube geometry and $L/R = 5$, $P_{out} = 0.5$, $\delta_0 = 10$
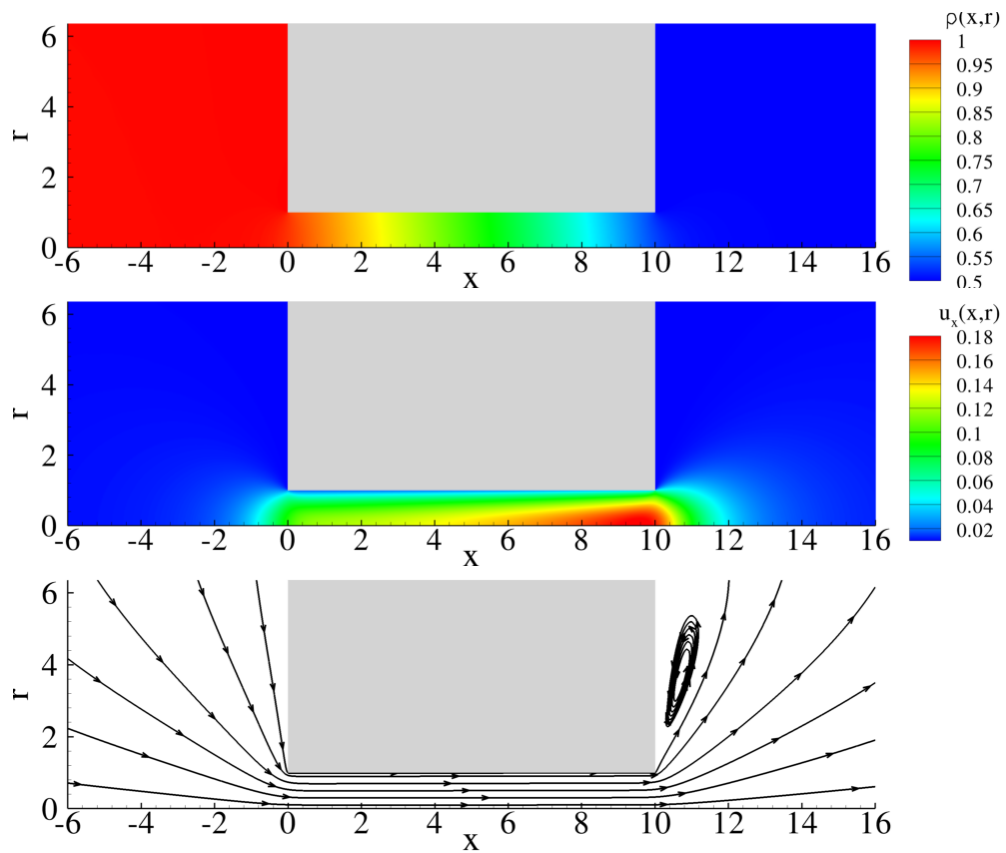
Figure 2.14: Density (up) and axial velocity (middle) contours, as well as streamlines (down) for the short tube geometry and $L/R = 10$, $P_{out} = 0.5$, $\delta_0 = 10$
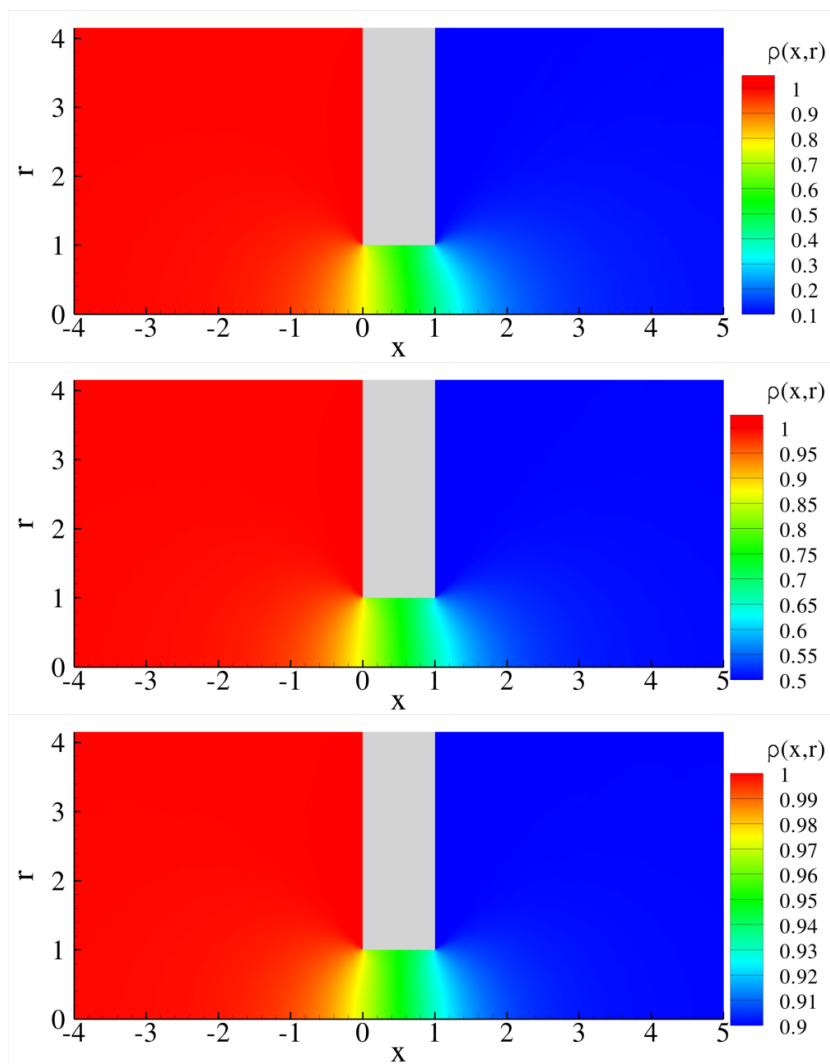
Figure 2.15: Density contour for the short tube geometry and $L/R = 1$, $\delta_0 = 2$ with $P_{out} = 0.1$ (up), $P_{out} = 0.5$ (middle) and $P_{out} = 0.9$ (down)
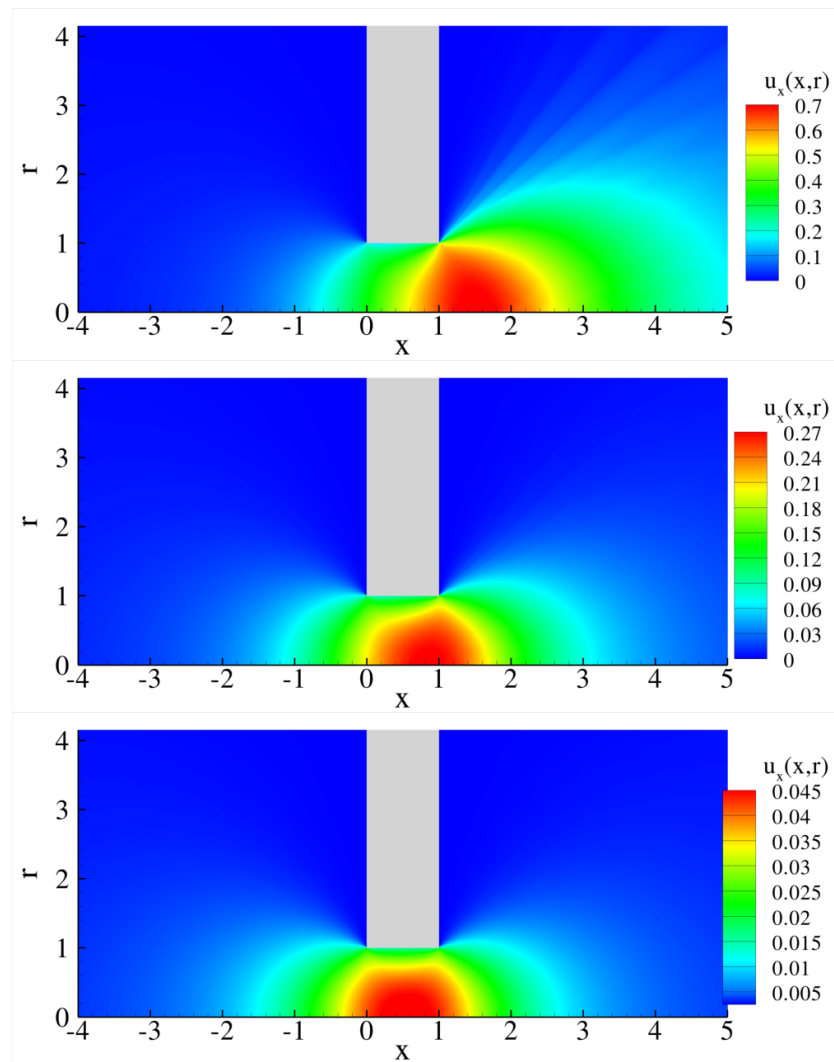
Figure 2.16: Axial velocity contour for the short tube geometry and $L/R = 1$, $\delta_0 = 2$ with $P_{out} = 0.1$ (up), $P_{out} = 0.5$ (middle) and $P_{out} = 0.9$ (down)

3

The main algorithm for simulating gas distribution systems in the whole range of the Knudsen number

In the previous chapter, steady-state isothermal rarefied gas flows in channels of various lengths and cross sections have been investigated by applying the discrete velocity and DSMC methods. In the present chapter, the investigation of complex gaseous distribution systems which consist not only of a single channel but of many channels accordingly combined to form a network is presented.

Such distribution systems are commonly found in several technological fields including vacuum pumping, metrology, industrial aerosol, porous media, and microfluidics. It is pointed out that computational algorithms dedicated to the design of gas pipe networks (e.g., compressed air, natural gas, etc.) in the viscous regime are well developed, while corresponding tools for the design of gaseous pipe networks operating under any (e.g. low, medium and high) vacuum conditions are very limited. In the free molecular limit a vacuum system consisting of many elements has been simulated by converting it first into a vacuum circuit network and then to an analogous electric circuit. This concept is valid when the whole system is under very high vacuum conditions and intermolecular collisions are negligible. Simulations of complex gas distribution systems in the transition regime have been performed only by the ITERVAC code, briefly presented in section 1.7 of the thesis.

3. PIPE NETWORK ALGORITHM

3.1 Basic definitions

Before considering a generalized set of network equations, it is worthwhile to examine a specific example of a piping network to observe the degree of complexity involved. A typical pipe network may be considered as a directed linear graph consisting of a finite number of pipe sections interconnected in a specified configuration. Each pipe is characterized of its length L, diameter D and some roughness. Usually the geometry of the network is specified and the objective is to compute the flow quantities, i.e., the mass flow rate (or the conductance) through each tube and the pressure head at each node. Figure 3.1 shows a relatively simple network consisting of seven pipes and two pressure reservoirs denoted by numbers 1 and 6, whose pressure values are known. These two nodes are termed as fixed-grade nodes. Outflow demands are present at nodes 3 and 4. Nodes 3 and 4 along with nodes 2 and 5 are called interior nodes or junction nodes. Flow directions, even though not initially known, are assumed to be in the directions as shown by the arrows. Let the drop in each piping element i be designated as $F[M_i]$ indicating a function of the mass flow rate of the corresponding piping element. Then, the system of equations is given as follows:

1. Energy balance for each pipe (seven equations):

$$P_1 - P_2 = F[M_1] \qquad\qquad P_5 - P_3 = F[M_5]$$

$$P_3 - P_2 = F[M_2] \qquad\qquad P_4 - P_5 = F[M_6]$$

$$\qquad\qquad\qquad\qquad\qquad\qquad\qquad\qquad\qquad\qquad (3.1.1)$$

$$P_2 - P_4 = F[M_3] \qquad\qquad P_5 - P_6 = F[M_7]$$

$$P_4 - P_3 = F[M_4]$$

2. Continuity balance for each interior node (four equations):

$$
\begin{aligned}
M_1 + M_2 - M_3 &= 0 \\
-M_2 + M_4 + M_5 &= Q_3 \\
M_3 - M_4 - M_6 &= Q_4 \\
-M_5 + M_6 - M_7 &= 0
\end{aligned}
\qquad (3.1.2)
$$

78

The unknowns are $M_1, \ldots, M_7, P_2, P_3, P_4$ and P_5. Thus, there are 11 unknowns and 11 equations to solve simultaneously. Since the energy equations are non-linear, it is necessary to resort to some type of successive iteration solution. The 11 equations can be reduced in number by combining the energy equations along special paths. Let the drop in each piping element i be designated as W_i and therefore $W_i = F[M_i]$. For the system under consideration, two closed paths, or interior loops (closed path formed by adjacent pipes), as shown in Figure 3.2. Flow is considered positive in a clockwise sense around each loop. Energy balances, written around loops *I* and *II*, are

$$-W_4 - W_3 - W_2 = 0$$
$$-W_5 - W_6 + W_4 = 0 \qquad (3.1.3)$$

To account for the flow in pipes 1 and 7, a path can be defined along nodes 1, 2, 3, 5 and 6, as shown in Figure 3.2. Then, the energy balance from 1 to 6 is

$$-W_7 + W_5 + W_2 - W_1 = P_1 - P_6 \qquad (3.1.4)$$

Note that the path energy equation connects two fixed-grade nodes. Such a path is sometimes termed a pseudo-loop, since an imaginary pipe with infinite resistance, or no flow, can be considered to connect the two reservoirs. The imaginary pipe is denoted by *III* in 3.2. Substituting the friction equations into the energy relations above results in the following reduced set of equations:

$$
\begin{aligned}
-F[M_4] - F[M_3] - F[M_2] &= 0 \\
-F[M_5] - F[M_6] + F[M_4] &= 0 \\
-F[M_7] + F[M_5] + F[M_2] - F[M_1] - P_1 + P_6 &= 0 \\
M_1 + M_2 - M_3 &= 0 \\
-M_2 + M_4 + M_5 &= Q_3 \\
M_3 - M_4 - M_6 &= Q_4 \\
-M_5 + M_6 - M_7 &= 0 \qquad (3.1.5)
\end{aligned}
$$

There are now seven unknowns $(M_1, \ldots, M_7)$ and seven equations to solve. The

energy relations are non-linear since the loss terms are presented as polynomials with respect to the discharges. For a well-defined network with p pipes, n junction nodes, l loops and f fixed-grade nodes the following relation holds:

$$p = n + l + f - 1 \tag{3.1.6}$$

The former equation derives from Euler's formula for planar graphs [68]. In graph theory, a graph $G = (v, e)$ is defined as a set v of vertices and a set e of edges – referring to nodes and pipes, respectively, for the network formulation. In the general case, each edge joins one vertex to another, or starts and ends at the same vertex. However, in case of network graph representation, self-loops are never present.

According to graph theory, a planar graph is a graph that can be embedded in the plane, i.e., it can be drawn on the plane in such a way that its edges intersect only at their endpoints. In other words, it can be drawn in such a way that no edges cross each other [137]. Such a drawing is called a plane graph or planar embedding of the graph. A plane graph can be defined as a planar graph with a mapping from every node to a point on a plane, and from every edge to a plane curve on that plane, such that the extreme points of each curve are the points mapped from its end nodes, and all curves are disjoint except on their extreme points.

Euler's formula states that if a finite, connected, planar graph is drawn in the plane without any edge intersections, and v is the number of vertices, e is the number of edges and f is the number of faces (regions bounded by edges, including the outer, infinitely large region), then

$$v - e + f = 2. \tag{3.1.7}$$

In the case of a network, the former equation, taking into account that $v = n + f$, $e = p$ and the fact that one of the faces is the infinitely large region, transforms into $(n + f) - p + (l + 1) = 2$ which is identical to the one described above.

3.2 Pipe network equations

Independent of the flow regime, the system of equations describing such a network consists of the pressure drop equations along each pipe element and the mass conservation equations at each node of the network. The pressure drop equations may be

reduced to a set of the energy balance equations for the closed loops of the network, which along with the mass conservation equations form a closed set to be solved for the unknown mass flow rates. Then, the pressure heads at the nodes are estimated through the pressure drop equations.

As mentioned above the initial system of equations describing the network consists of the pressure drop equations along each piping element and the mass conservation equations at each node of the network. The mass conservation equations may be expressed as

$$\left[\sum_j (\pm)\dot{M}_j - Q\right]_i = 0 \qquad (3.2.1)$$

where the index $1 \leq i \leq n$ denotes each of the n junction nodes of the network, while the summation index j refers to the pipes connected to the node i, while $Q = Q_i$ is the external demand (if any) at node i. The plus and minus signs are used for flow into and out of the node respectively. Moreover, the energy balance equations are applied in each of the closed loops l of the network described by

$$\left[\sum_j (\pm)(\Delta P_j)\right]_k = 0. \qquad (3.2.2)$$

Here, the summation index j pertains to the pipes that make up a loop, while the index $1 \leq k \leq l$, denotes each of the l loops. The plus sign is used if the flow in the element is positive in the clockwise sense; otherwise the minus sign is employed. When there are fixed-grade nodes in the network then, the system of equations for the mass flow rates is amplified by the energy balance equation around each pseudo-loop connecting two fixed-grade nodes according to

$$\left[\sum_j (\pm)(\Delta P_j) + \Delta H\right]_k = 0. \qquad (3.2.3)$$

Here, the summation index j pertains to the pipes that make up a pseudo-loop, the index $1 \leq m \leq f - 1$, denotes each of the $f - 1$ pseudo-loops (f is the number of fixed grade nodes) and ΔH is the difference in magnitude of the fixed-grade nodes in the path ordered in a clockwise fashion across the imaginary pipe in the pseudo-loop.

The plus and minus signs follow the same arguments given for Eqs. 3.2.1 and 3.2.2. Based on the above the final system of equations will consist of $n+l+f-1$ equations to be solved for the p unknown mass flow rates $\dot{M}_j$. This clearly explains why for a well defined pipe network relation 3.1.6 must be satisfied.

3.3 Algorithm implementation

The final version of the network algorithm is a more complete and versatile version of the algorithm presented in [81, 82]. The in-house developed **A**lgorithm for **R**arefied gas flow **I**n **A**rbitrary **D**istribution **NE**tworks (ARIADNE) (Figure 3.3). Just like, according to the Greek mythology, Ariadne provided Theseus with a sword and a ball of thread so that he could retrace his way out of the labyrinth of the Minotaur, in the present case, ARIADNE, by employing the necessary CPU threads, provides the numerical solution for the maze-like network of piping elements. In its latest version, the developed algorithm consists of the following main blocks:

a. The input of geometrical and operational data

b. The definition of the unique set of loops and pseudo-loops

c. The formulation and solution of the mass and energy conservation equations

d. The kinetic data base supporting explicitly the solution of the conservation equations

e. The output data (mainly node pressures and pipe mass flow rates/conductances)

In an effort to make the drawing of the network to be solved easier for the user and therefore, all the input data required for the algorithm to be executed easier to be prepared and managed, a graphical user interface (GUI) has been developed. Once the network is drawn, Ariadne is employed in order to formulate and solve, based on solid kinetic principles, the governing equations describing the flow conditions of the distribution system. It is noted that the developed algorithm is capable of solving pipe networks of any complexity.

3.3.1   Graphical interface

The application of the interface is based on the idea of utilizing the tools available of a web page, thus, a web page created and saved locally on the computer is executed to run the GUI. The main parts of the application consist of:

- An html page, which serves the purpose of the main algorithm.

- The corresponding style sheet file (CSS) and visual basic script (VBS), which organize the outline and appearance of the GUI.

- 26 libraries written is javascript to match the requirements of the developed GUI. These libraries are a combination of already available ones, free distributed under the GNU General Public License (GPL) and some newly created to match the needs of the application.

The network is drawn in a way to reproduce as closely as possible the real geometry of the system under consideration. For the needs of the example network shown in Figure 3.1, the aforementioned GUI is utilized. The representation of the example network in the GUI is shown in Figure 3.4. The user is able to draw the desired network by adding nodes (Figure 3.5) and pipe sections (Figure 3.6) and the corresponding data, i.e., the coordinates of the nodes in a 3D space, the length and the diameter of the pipe elements, the pressure heads of the fixed-grade nodes and information for the type of the gas and its properties (viscosity, most probable molecular velocity, etc.). The demands or possible leaks, if any, at the nodes may also be provided. During the pipe drawing procedure, the user is asked to define from which node the pipe starts (From Node ID) and to which node the pipe ends (To Node ID), indicating at the same time an initial guess for the flow direction in each piping element comprising the network.

As a result, a connectivity matrix for each node and tube of the network is formed providing all necessary information. For the needs of the example network studied here, the corresponding connectivity matrix is shown in Table 3.2. This information may be saved in such a way so that it can be imported again from the GUI itself and be further manipulated or changed, or even it may be exported as a text file fulfilling the needs of an input data file to be introduced in the main algorithm described in the following sections.

3.3.2 Formulation of kinetic equations

In the case when the Knudsen number characterizing the flow through the network is very small and the flow is in the continuum (or viscous) or slip regimes, then the pressure drop equations along each channel are given by closed form algebraic expressions and their integration in the whole algorithm is straightforward. In contrary, when the flow is in the transition regime such expressions are not available. This is a serious pitfall which may be circumvented if the pressure drop will be provided by solving these channel flows under any vacuum conditions. The flow of rarefied gases through tubes of various lengths in the whole range of the Knudsen number is a fundamental problem in rarefied gas dynamics and has been (and still is) the subject of many theoretical, computational and experimental investigations. An extended description of flows through single piping elements of infinite, moderate or finite length has been presented in Chapter 2.

The proposed methodology of simulating gas distribution systems operating under rarefied conditions includes the computed mass flow rates through single pipe elements of various lengths via DSMC and discrete velocity kinetic codes, which are stored in a data base for the needs of the network algorithm.

In general, the pressure driven flow of a rarefied gas through a tube of length L and radius R with the tube inlet and outlet pressures maintained at P_1 and P_2 respectively ($P_1 > P_2$) is prescribed by three dimensionless parameters namely

- the geometrical ratio L/R

- the pressure ratio P_2/P_1

- the reference Knudsen number (Kn) or alternatively the reference rarefaction parameter (δ)

The case of a tube much longer than its radius ($R/L << 1$) with a small pressure difference between the tube inlet and outlet is the most widely considered. It is tackled by the infinite capillary theory where the flow is considered as fully developed, the pressure varies only in the flow direction and end effects are neglected. Once the reduced flow rate $G(\delta)$, which is a function only of δ at each cross section, is known,

the mass flow rate is obtained by [125]

$$\dot{M}_{FD} = G^* \frac{\pi R^3}{\upsilon_0} \frac{P_1 - P_2}{L} \tag{3.3.1}$$

where

$$G^* = \frac{1}{\delta_1 - \delta_2} \int_{\delta_1}^{\delta_2} G(\delta) d\delta \tag{3.3.2}$$

is computed by integrating $G(\delta)$ between the inlet and outlet rarefaction parameters δ_1 and δ_2 respectively accordingly defined by the corresponding pressures P_1 and P_2. In the network algorithm the reduced flow rate $G(\delta)$ is computed by implementing the recently introduced interpolation formula [123]

$$G(\delta) = \frac{1.505 + 0.0524\delta^{0.75} \ln \delta}{1 + 0.738\delta^{0.78}} + \left(\frac{\delta}{4} + 1.018\right) \frac{\delta}{1.073 + \delta} \tag{3.3.3}$$

This infinite length expression interpolates the numerical data based on the solution of the linear BGK kinetic model equation via the discrete velocity method within the uncertainty of 0.2% in a wide range of the Knudsen number.

To extend the range of applicability of the infinite capillary theory, which is computationally very efficient for very long channels, to channels of moderate length the end effect correction concept is incorporated in the network algorithm. Following the end effect theory the overall reduced flow rate G^*, given by Eq. 3.3.2, is revised according to [102, 103]

$$G^* = \frac{1}{(1 + \Delta L_1/L + \Delta L_2/L)} \frac{1}{\delta_1 - \delta_2} \int_{\delta_1}^{\delta_2} G(\delta) d\delta \tag{3.3.4}$$

where $\Delta L_1/L$ and $\Delta L_2/L$ are the additional lengths at the inlet and outlet of the channel correcting the real length of the channel by taking into account the end effects. The corrective lengths introduced in the code are provided in [103]. As pointed out in [102], the consideration of the end effect correction, compared to the case of no end effect consideration, will always improve the accuracy of the simulations and therefore, it is always applied in the network algorithm when $\Delta L/L > 0.01$. The

values of G^*, according to Eq. 3.3.4 are introduced into Eq. 3.3.1 to deduce by taking into consideration the end effects the corrected values of the mass flow rate $\dot{M}_{EE}$.

The great advantage of the infinite capillary and end effect theories is that the dimensionless solutions solely depend on the gas rarefaction parameter (they do not depend on L/R and P_2/P_1). However, they are both based on linear kinetic analysis and are valid when the Mach number of the flow is sufficiently small [124]. To satisfy this requirement and after some extensive numerical experimentation the mass flow rate is obtained according to the above analysis provided that $L/R \geq 10$ and the inlet rarefaction parameter $\delta_1 \leq 100$.

In the case of $L/R < 10$ if the pressure ratio $P_2/P_1 \geq 0.9$, i.e., the pressure difference is small, the flow is linear even in short tubes and the solution is obtained by solving the linearized BGK equation in the whole flow field (not just in a cross section as before) [101]. The mass flow rate is obtained by

$$\dot{M}_{LIN} = W_{LIN}\sqrt{\pi}R^2\left(P_1 - P_2\right)/\upsilon_0 \tag{3.3.5}$$

where the dimensionless flow rate W_{LIN} is computed in terms of L/R and the reference rarefaction parameter δ (W_{LIN} does not depend on P_2/P_1). Indicative results of W_{LIN} are given in [101].

Otherwise, in the case of $L/R < 10$ with $P_2/P_1 < 0.9$ the flow is considered as nonlinear and it is tackled based on the DSMC method [148, 150] and on nonlinear kinetic model equations solved by the discrete velocity method [80, 96, 97, 133, 134]. The mass flow rate is obtained by

$$\dot{M}_{NL} = W_{NL}\sqrt{\pi}R^2P_1/\upsilon_0 \tag{3.3.6}$$

where W_{NL} is the dimensionless nonlinear flow rate and depends on all three parameters (L/R, δ and P_2/P_1). Then the pressure difference between the inlet and the outlet of the tube is given by

$$P_1 - P_2 = P_1\left(1 - \frac{P_2}{P_1}\right) = \frac{\dot{M}_{NL}\upsilon_0}{W_{NL}\sqrt{\pi}R^2}\left(1 - \frac{P_2}{P_1}\right) \tag{3.3.7}$$

This case is the most computationally demanding one and extensive computations

have been performed to prepare an adequate large data base in a wide range of the involved parameters. Indicative results are reported in Tables 2.10 and 2.11.

In the case of channels with arbitrary cross section the flow is simulated by converting the noncircular cross section to an equivalent circular one based on two different approaches. In the first approach the radius of the equivalent circular channel is defined according to the hydraulic radius concept [16, 145], while in the second one it is defined by equating the areas of the noncircular and circular cross sections ($A = A_{eq}$) [144]. Computational experimentation will be performed (Chapter 4, Section 4.3) to deduce that in rectangular cross section channels with various aspect ratios, including very slender ones, the overall results provided by the latter approach are more accurate. Since orthogonal channels are very common in the ITER divertor pumping system, this second approach will be implemented in the simulation of this system presented in Chapter 5, Section 5.4.

All this information related to the computed mass flow rates through single tubes, i.e., Eqs. 3.3.1, 3.3.5 and 3.3.7, is provided through the kinetic data base as an input to the network algorithm described in the next section.

3.3.3 Programming in Fortran environment

Once the network is drawn in the graphical interface, as it has been described in sub-section 3.3.1, the resulting input file is introduced into Ariadne.

Based on the connectivity matrix, formulated through the GUI, an adjacency matrix for each node of the network is formed. For the sample network shown in Figure 3.1, the corresponding adjacency matrix is shown in Table 3.1. Then, the set of loops and pseudo-loops is determined by implementing the well-known depth-first-search (DFS) algorithm [28]. The method for finding a loop or pseudo-loop in the network can be visualized as a depth-first-search (DFS) traversal of a tree data structure, as shown in Figure 3.7. In the DFS the search starts at the root and explores as far as possible into deeper levels along each branch before backtracking, i.e. before going back to the last explored node from which it was possible to visit a new branch of the tree.

An explanation of how the search algorithm works is given next. The algorithm generates a list of nodes that represents a path in the search tree by systematically

$$A_{i,j} = \begin{pmatrix} 0 & 1 & 0 & 0 & 0 & 0 \\ 1 & 0 & 1 & 1 & 0 & 0 \\ 0 & 1 & 0 & 1 & 1 & 0 \\ 0 & 1 & 1 & 0 & 1 & 0 \\ 0 & 0 & 1 & 1 & 0 & 1 \\ 0 & 0 & 0 & 0 & 1 & 0 \end{pmatrix}$$

Table 3.1: Adjacency matrix for the sample network of Figure 3.1.

selecting one node at a time from successive levels, until it is not possible to lengthen it further. When a node is being considered, the forward search part of the algorithm first checks to see if this node is a legal node, and if it is the algorithm next checks to see if the size of the new path formed is as large or larger than the current largest path, in which case it is saved. At a given level n of the tree, at most one node can be selected. Note the initial value of n is 0 which represents the root of the tree. Following the selection of a node at level n, the algorithm seeks to expand the clique by adding the next available legal node at level $n + 1$. After considering all the nodes in a group at level $n + 1$, a null node is registered for level $n + 1$ and an attempt is made to select a node from level $n + 2$ without including a node from level $n + 1$. A null node is a right-most child for each node and always stores the value 0. When all possible nodes have been considered that allows movement in a forward direction away from the root of the tree, then the algorithm backtracks and tries to expand along a different branch of the tree. When backtracking occurs, the nodes are removed from the list one at a time until a node is reached from which the remaining path can be re-expanded or until all possibilities are exhausted. The length of the longest list (excluding any null node entries) as well as its composition is maintained. This information is updated, as needed. This process is described in Algorithms 3.4.1 and 3.4.2.

Once the scanning of the tree data structure is completed, the search algorithm returns all possible loops and pseudo-loops detected through the traversal process. In the case of the sample network under consideration, all possible paths are shown in color code in Figure 3.7. The nodes which indicate the beginning end the ending of the paths of the closed loops are noted in green, yellow and purple colors respectively,

while for the case of pseudo-loops, the corresponding nodes are noted with red circles.

For a network of p pipes, n nodes and f fixed pressure nodes the DFS technique is traversing the network extracting the $(f-1)$ pseudo-loops and $l = p-n-(f-1)$ loops which are linearly independent. This approach has been found to be computationally powerful and efficient even in networks consisting of thousands of pipes as in the ITER primary vacuum distribution system simulated in the next section. The identified paths of the loops and pseudo-loops of the network are stored in separate matrices in order to be available for the formulation of the conservation equations.

Once the linearly independent loops and pseudo-loops of the network are identified, the main core of Ariadne is based on an iterative process between the pressure drop equations and the system of mass and energy conservation equations as these are described in section 3.2. To sum up the required information, the algebraic system of balance equations to be solved consists of a) the mass conservation equations at each node

$$\sum_j \left(\pm \dot{M}_{i,j} \right) \pm \dot{M}_i = 0, \quad i = 1, \dots, n \tag{3.3.8}$$

b) the energy conservation equations along each closed loop, and

$$\sum_j \left(\pm \Delta P_{k,j} \right) = 0, \quad k = 1, \dots, l \tag{3.3.9}$$

c) the energy conservation equations along each pseudo-loop

$$\sum_j \left(\pm \Delta P_{m,j} \right) + \Delta P_m = 0, \quad m = 1, \dots, (f-1) \tag{3.3.10}$$

In Eq. 3.3.8 the summation index j refers to all pipes connected to node i, $\pm \dot{M}_{i,j}$ denotes the mass flow rate into or out of node i respectively through pipe j and $\dot{M}_i$ denotes an external mass flow rate gain or loss (if any) at node i. In Eqs. 3.3.9 and 3.3.10, the summation index j pertains to the pipes that make up loop k and pseudo-loop m. Also, $\pm \Delta P_{k,j}$ and $\pm \Delta P_{m,j}$ refer to the difference between the inlet and outlet pressure of pipe j (the plus sign is used if the flow in the pipe is positive in the clockwise sense or otherwise the minus sign is employed), while ΔP_m is the difference in magnitude of the fixed pressure nodes.

3. PIPE NETWORK ALGORITHM

The pressure difference $\Delta P = P_1 - P_2$ of each pipe element in Eqs. 3.3.9 and 3.3.10 is substituted accordingly from Eqs. 3.3.1 or 3.3.5 or 3.3.7, depending upon the specific geometrical and operational data L/R and P_2/P_1. The dimensionless flow rates G^*, W_{LIN} and W_{NL} are obtained from the kinetic data base.

For the cases where the flow is linear, interpolation formulas are introduced for the deduction of the required values. However, for the case of W_{NL}, which is a function of three independent variables, namely δ, P_2/P_1 and L/R, a trilinear interpolation algorithm has been implemented. In general, the result of trilinear interpolation is independent of the order of the interpolation steps along the three axes: any other order, for instance along x, then along y, and finally along z, produces the same value. First, the eight corners of a cube that surround our point of interest are located. These corners have the values W_{000}, W_{100}, W_{010}, W_{110}, W_{001}, W_{101}, W_{011}, W_{111}. Next, linear interpolation is performed between W_{000} and W_{100} to find W_{00}, W_{001} and W_{101} to find W_{01}, W_{011} and W_{111} to find W_{11}, W_{010} and W_{110} to find W_{10}. In the next step, interpolation is performed between W_{00} and W_{10} to find W_0, W_{01} and W_{11} to find W_1. Finally, in order to calculate the value W, linear interpolation between W_0 and W_1 is applied. In practice, a trilinear interpolation is identical to two bilinear interpolations combined with a linear interpolation. The above operations can be visualized in Figure 3.8 and the corresponding process is described in Algorithm 3.4.4.

The resulting set of equations, along with Eq. 3.3.8, yield a linear system of algebraic equations which is solved for the unknowns $\dot{M}_i$. Once the mass flow rates are computed the node pressures are easily deduced from the corresponding equations. An iteration process between the pressures at the nodes and the mass flow rates through the pipes is applied, which is terminated when the convergence criterion imposed on the pressures is fulfilled. In each iteration the linear algebraic system is solved via Gauss elimination with partial pivoting, as this is described in Algorithm 3.4.5.

The output data include the pressures P_i, $i = 1, \dots, n$ and the mass flow rates $\dot{M}_i$, $i = 1, \dots, p$ at all nodes and pipes respectively of the network, where these quantities were unknowns. In addition, for each pipe element $i = 1, \dots, n$, the conductance

$$C_i = \frac{\dot{M}_i}{(\Delta P)_i} R_g T \tag{3.3.11}$$

and the pump throughput or the so-called PV-flow

$$Q_i = \frac{d(PV)_i}{dt} = \dot{M}_i R_g T = \dot{N}_i R^* T \qquad (3.3.12)$$

may be computed. In Eqs. 3.3.11 and 3.3.12, $R^* = 8.314 Jmol^{-1}K^{-1}$ is the global gas constant, R_g is the gas constant and $\dot{N}_i$ is the molar flow rate. These quantities are of practical interest and characterize the performance of the system.

In summary, Ariadne, in its latest version can handle networks of any geometrical complexity operating under any vacuum conditions since the kinetic data base has been accordingly enlarged to include channels of any length in a wide range of the Knudsen number. It is noted that the iterative process will converge under any initial conditions provided that all data characterizing the loops and pseudo-loops of the network are properly given, i.e. the network is well defined and Eq. 3.1.6 is satisfied. All steps followed are shown in the corresponding flowchart in Figure 3.9.

3.4 Numerical formulation in the viscous regime

To benchmark the present formulation and results this network subject to exactly the same conditions has been also solved using a typical hydrodynamic solver for gas pipe networks [107, 143] and a comparison between the results is performed. A gaseous pipe network in the viscous regime is still described by the same network equations and the only difference is that the pressure drop along each pipe element is obtained by a corresponding expression based on hydrodynamic principles. For the purposes of the thesis, the Darcy-Weisbach equation is implemented:

$$P_L = (P_1 - P_2)_j = \frac{M_j^2}{2(\rho_m)_j A_j^2} \left(2\ln \frac{P_1}{P_2} + (f_D)_j \frac{L_j}{D_j} \right) \qquad (3.4.1)$$

Here, the index $1 \leq j \leq p$ denotes again each of the p pipes of the network, $(\rho_m)_j$ is the average value of the mass density and $(f_D)_j$ is the Darcy friction factor. A detailed derivation of Eq. 3.4.1 is provided in Appendix A while a more detailed description about the computation of the proper values of the friction factor is given in the following section. It is noted that in the present case, the pressure drop along two points depends on the pressure at the points into consideration. As a result, the

pressure drop cannot be evaluated directly as a function of the length, the diameter, the mass flow rate and the friction factor, but in the case where the pressures upstream and downstream the pipe are unknown, an iterative procedure is necessary, increasing significantly the computational cost.

3.4.1   Estimation of the friction factor

The friction factor for subsonic compressible flows, which is the case of interest in the present work, agrees with the relations for the evaluation of the friction factor for incompressible flows. On the other hand, for the case of supersonic flows, the friction factor is almost the half of the one computed for the case of the uncompressed flows.

The most convenient and relatively precise approximation method is by means of the diagram Moody, which plots the dependence of the friction factor on the Reynolds number of the flow and the roughness of the pipe. Besides Moody diagram, there are several analytical expressions that may be used for specific regimes of the Reynolds number. One of the most accurate is the Colebrook expression

$$\frac{1}{\sqrt{f_D}} = -2 \log\left(\frac{\frac{\varepsilon}{d}}{3.7} + \frac{2.51}{\text{Re}\sqrt{f_D}}\right) \tag{3.4.2}$$

where ϵ is the roughness of the pipe and d is its diameter. The Colebrook expression is accurate for $Re > 4000$, while the major disadvantage is that it requires a Newton iterative procedure. For this reason, the expression used in the hydrodynamic solver is the Swamee-Jain which returns essentially the same results with the Colebrook expression without an iterative process needed. The Swamee-Jain expression is given by

$$f_D = \frac{1.325}{\left[\ln\left(0.27\frac{\varepsilon}{d} + 5.74\frac{1}{\text{Re}^{0.9}}\right)\right]^2} \tag{3.4.3}$$

which returns accurate results for $5000 < \text{Re} < 10^8$ and $10^{-8} < \epsilon/d < 0.01$.

Similar expressions used for the estimation of the friction factor as a function of Reynolds number are

- $f_D = \frac{64}{\text{Re}}$, for $\text{Re} \leq 2000$

- $f_D = \frac{0.3164}{\text{Re}^{1/4}}$, for $4000 < \text{Re} < 10^5$ (deriving from Blasius equation)

- $\frac{1}{\sqrt{f_D}} = 2\log\left(\text{Re}\sqrt{f_D}\right) - 0.8$, for $\text{Re} > 10^5$ (deriving from Prandtl equation)

- $\frac{1}{\sqrt{f_D}} = 2\log\left(\frac{d}{\epsilon}\right) + 1.14$, for $\frac{d/\epsilon}{\text{Re}\sqrt{f_D}} > 0.005$

However, in many occasions, instead of the friction factor, the Poiseuille number

$$\text{Po} = f_D \times \text{Re} \tag{3.4.4}$$

defined as the product of the friction factor times the Reynolds number of the flow, is utilized. Over the years, the Poiseuille number has been determined for an extensive number of flow configurations. As it has been mentioned before, for the cases where the flow is in the transition regime or at the free molecular regime, medium and highly rarefied flows, the hydrodynamic equations are not valid and a kinetic approach based on the Boltzmann equation or reliable kinetic models is required. As described in Section 2.1.4, the Poiseuille number has been evaluated in the whole range of the rarefaction for the case of the flow through a circular tube. By introducing the required mathematical manipulation, Eq. 3.4.4 results to [140]

$$f_D = 64 \left/ \text{Re}\left(1 + \frac{16\sigma_p \text{Kn}}{\sqrt{\pi}}\right)\right. \tag{3.4.5}$$

where σ_p is the viscous slip coefficient, equal to 1.016, and it is computed by solving the corresponding half-space viscous slip fow setup (or Kramers problem) based on the linearized BGK model equation [120]. At the hydrodynamic limit, Eq. 3.4.5 is reduced to the well-known result $Po = 64$. In principle, it is valid in the slip (or viscous) regime, but due to its simplicity it may be used, at some extent, in the transition regime to provide rough estimates. It is reported that the accuracy of Eq. 3.4.5 is about 1.3% for $1/Kn = 20$, 3.5%, for $1/Kn = 10$ and 8%, for $1/Kn = 5$.

As a result, this expression is implemented in the hydrodynamic solver to expand the validity of the corresponding results in the viscous or even transition regimes.

3.4.2 Formulation of equations for the hydrodynamic solver

Similar to the case of the solver based on kinetic principles, similar formulation is used for the case of the hydrodynamic solver. For the simulation of a gas network distribution system where the flow is compressible, two non-linear systems are formed.

The first one comprises of the pressure drop equations for each of the pipes consisting the network equal to the number of the piping elements forming the network as described by Eq. 3.4.1, while the friction factor values are evaluated by making use of Eq. 3.4.5. The second part of the system to be solved results from the application of the continuity equation given by Eq. 3.2.1 at each of the nodes of the network resulting to a set of equations equal to the number of the nodes of the network. Having defined the system of equations for the pressure drop at each of the pipe elements we can solve it since the number of equations ($i+j$) matches the number of unknowns (j pressure values at each of the nodes and i values for the mass flow rates at each of the piping elements). As it has already been described for the case of the kinetic solver, the use of energy balance equations along the closed loops (Eq. 3.2.2) and the pseudo-loops of the network (Eq. 3.2.3) is implemented as the least computationally demanding also for the hydrodynamic solver. In this way, an optimized system of equations describing the network is formed and the number of non-linear equations to be solved, regarding the mass flow rates, is decreased from i equations to $l + f - 1$. By following a procedure similar to the one described for the case of the kinetic solver, the system is solved by assuming pressure and density values and verifying the pressure drop at each piping element through Eqs. 3.4.1 and 3.4.5 in an iterative manner, reducing at the same time the computational cost.

3.4.3 Programming in Matlab environment

An in-house hydrodynamic solver, built in Matlab environment, simulating gas pipe networks in the hydrodynamic regime has been also developed at the Laboratory of Transport Phenomena of the University of Thessaly. This software has been implemented in the past in several diploma and master theses [107, 143]. In its current version, after introducing the slip solution results through the correct estimation of the friction factor, the Matlab algorithm is further updated and employed in the present work for validation purposes. The steps followed for the solution of the system of equations may be described as:

1. Introduce the operational characteristics of the network such as lengths and diameters of the piping elements as well as number of nodes, pipes, fixed-grade nodes and the corresponding pressure values, demands at the nodes of the

network (if any), number of loops and pseudo-loops and finally the properties of the gas (viscosity, specific heat ratio γ, temperature T, molar mass and specific gas constant R^*.

2. Based on the pressure values at the fixed-grade nodes, assume the initial pressure values at each node of the network and the resulting density values and initial pressure drop values.

3. Solve the continuity equations along with the equations for the loops and the pseudo-loops by making use of a Newton iterative procedure. After the system of equations is solved, the new values of the mass flow rates are calculated. The procedure is repeated until the convergence criterion of the applied methodology is satisfied. Once this is achieved, the correct values for the mass flow rates, based on the initial assumption of the pressure and the density values, are computed.

4. Compute the new pressure values and densities that satisfy the new values for the flow rates computed after the system of equations is solved. Once again, the system is non-linear since the pressure drop equations depend on the pressure values. Also in this case, a Newton iterative procedure is implemented.

5. If the convergence criterion for the pressure drops between the iterations is not satisfied, the algorithm returns at the 2nd step where the values for the pressure and the density computed at the previous iteration are used as initial assumption.

All five steps followed are shown in the corresponding flowchart in Figure 3.10.

As it has already been mentioned, for the solution of the resulting non-linear system of equations, the Gauss-Newton algorithm, embedded in Matlab by making use of the command "fsolve" is applied.

In order to develop the required algorithm under the Matlab environment for the analysis of the compressible gas flow inside the network, 12 subroutines have been constructed in order to construct the network, solve the system of equations and present the corresponding results. More specifically:

- Pipeinput.m: Dimensions of piping elements, geometry and topology of the network (number of nodes, pipes, fixed-grade nodes), physical properties of the gas running through the network and initial assumptions for the values of the pressure heads.

- Pipe.m: The basic algorithm where the needed subroutines are called and the overall iterative procedure for the satisfaction of the convergence criterion.

- Pipefriction.m: Evaluation of the friction factor at each of the piping elements based on the computed Reynolds and Knudsen numbers where the slip solution is implemented.

- Pipedensity.m: Evaluation of the average density value at each of the piping element.

- Loss.m: Evaluation of part of the pressure drop for each piping element.

- Pipeloss.m: Evaluation of the total pressure drop for each piping element based on the Darcy-Weisbach equation.

- Pipeloop.m: Assign the plus or minus signs at the closed loop and pseudo-loop equations.

- Pipeflow.m: Interconnection between the Pipeflowqn.m subroutine and Pipe.m main algorithm.

- Pipeflowqn.m: The non-linear system of equations formed by the continuity equations and the ones for the closed and pseudo-loops.

- Pipepr.m: The evaluation of the pressure heads at each of the nodes of the network based on the total pressure drop.

- Pipeoutput.m: Printing the corresponding results in a file.

- Pipeplot.m: Schematic representation of the simulated network.

The link between the items described is shown in the corresponding flowchart in Figure 3.11.

Algorithm 3.4.1: PSEUDO-LOOP: Algorithm for locating pseudo-loops in network

---

Input   : The graph $G = (v, e)$ of the network and two of fixed-grade nodes u and z

Output: A closed path between the two given vertices u and z

---

1 *flag(v, VISITED)*
2 *S.push(v)*
3 **if** $v = z$ **then**
4 | **return** *S.elements()*
5 **end**
6 **for all** $e \in$ *G.incidentEdges(v)* **do**   // checking edges
7 | **if** *flag(e) = UNEXPLORED* **then**
8 | | $w \leftarrow$ *opposite(v, e)*
9 | | **if** *flag(w) = UNEXPLORED* **then**   // building the path
10 | | | *flag(e, DISCOVERY)*
11 | | | *S.push(e)*
12 | | | *pathDFS(G, w, z)*
13 | | | *S.pop(e)*
14 | | **else**
15 | | | *flag(e, BACK)*   // back tracking
16 | | **end**
17 | **end**
18 | **end**
19 **end**
20 **return** *S.pop(v)*

Algorithm 3.4.2: LOOP: Algorithm for locating loops in network

   Input   : The graph $G = (v, e)$ of the network
   Output: stack S of the path between the start vertex and the current vertex

1 *flag(v, VISITED)*
2 *S.push(v)*
3 **for all** $e \in$ *G.incidentEdges(v)* **do**   // checking edges
4   **if** *flag(e) = UNEXPLORED* **then**
5   *w ← opposite(v, e)*
6   *S.push(e)*
7   **if** *flag(w) = UNEXPLORED* **then**   // building the path
8   *flag(e, DISCOVERY)*
9   *pathDFS(G, w, z)*
10   *S.pop(e)*
11   **else**
12   *T ← newemptystack*   // forming new stack
13   **repeat**
14   *o ← S.pop()*
15   *T.push(o)*
16   **until** *o = w*
17   **return** *T.elements()*
18   **end**
19   **end**
20   **end**
21 **end**
22 **return** *S.pop(v)*

Algorithm 3.4.3: FIND DUPLICATE: Algorithm for discarding duplicate loops

---

    Input: A sequence of integers $\langle a_1, a_2, \ldots, a_n \rangle$
    Output: The index of first location with the same value as in a previous
                 location in the sequence

1   *location* $\leftarrow 0$
2   $i \leftarrow 2$
3   **while** $i \leq n$ **and** *location* $= 0$ **do**
4     $j \leftarrow 1$
5   **while** $j < i$ **and** *location* $= 0$ **do**
6   **if** $a_i = a_j$ **then**
7   *location* $\leftarrow i$
8   **else**
9         $j \leftarrow j + 1$
10   **end**
11   **end**
12    $i \leftarrow i + 1$
13 **end**
14 **return** *location*

Algorithm 3.4.4: TRILINEAR: Trilinear Interpolation Algorithm

---

Input : Values of L/R, δ and P_2/P_1
Output: Value of the dimensionless flow rate W_{NL}

1 **if** $(P_2/P_{1_{min}} \leq x \leq P_2/P_{1_{max}})$ **and** $(L/R_{min} \leq y \leq L/R_{max})$ **and** $(\delta_{min} \leq z \leq \delta_{max})$ **then**

2 $\quad$ $z1$ *location* $\leftarrow zmax - (z1)$ `// Compute x,y,z for the local tube`

3 $\quad$ $z0$ *location* $\leftarrow zmin - (z0)$

4 $\quad$ $y1$ *location* $\leftarrow ymax - (y1)$

5 $\quad$ $y0$ *location* $\leftarrow ymin - (y0)$

6 $\quad$ $x1$ *location* $\leftarrow xmax - (x1)$

7 $\quad$ $x0$ *location* $\leftarrow xmin - (x0)$

8 $\quad$ **begin** $\quad\quad\quad\quad$ `// Compute f at 8 corners of the local cube`

9 $\quad\quad$ $f(x0, y0, z0)$

10 $\quad\quad$ $f(x0, y0, z1)$

11 $\quad\quad$ $f(x0, y1, z0)$

12 $\quad\quad$ $f(x0, y1, z1)$

13 $\quad\quad$ $f(x1, y0, z0)$

14 $\quad\quad$ $f(x1, y0, z1)$

15 $\quad\quad$ $f(x1, y1, z0)$

16 $\quad\quad$ $f(x1, y1, z1)$

17 $\quad$ **end**

18 $\quad$ **begin** $\quad\quad\quad\quad\quad\quad\quad\quad\quad$ `// Compute dx, dy and dz`

19 $\quad\quad$ $dx \leftarrow (x - x0)/(x1 - x0)$

20 $\quad\quad$ $dy \leftarrow (y - y0)/(y1 - y0)$

21 $\quad\quad$ $dz \leftarrow (z - z0)/(z1 - z0)$

22 $\quad$ **end**

23 $\quad$ **begin** $\quad\quad\quad\quad\quad\quad\quad\quad$ `// Compute weighting factors`

24 $\quad\quad$ $c0 \leftarrow fx0y0z0$

25 $\quad\quad$ $c1 \leftarrow fx1y0z0 - fx0y0z0$

26 $\quad\quad$ $c2 \leftarrow fx0y1z0 - fx0y0z0$

27 $\quad\quad$ $c3 \leftarrow fx0y0z1 - fx0y0z0$

28 $\quad\quad$ $c4 \leftarrow fx1y1z0 - fx0y1z0 - fx1y0z0 + fx0y0z0$

29 $\quad\quad$ $c5 \leftarrow fx0y1z1 - fx0y0z1 - fx0y1z0 + fx0y0z0$

30 $\quad\quad$ $c6 \leftarrow fx1y0z1 - fx0y0z1 - fx1y0z0 + fx0y0z0$

31 $\quad\quad$ $c7 \leftarrow fx1y1z1 - fx0y1z1 - fx1y0z1 - fx1y1z0 +$
$\quad\quad\quad +fx1y0z0 + fx0y0z1 + fx0y1z0 - fx0y0z0$

32 $\quad$ **end**

33 $\quad$ $g \leftarrow c0 + c1 * dx + c2 * dy + c3 * dz + c4 * dx * dy +$
$\quad\quad +c5 * dy * dz + c6 * dx * dz + c7 * dx * dy * dz$ `// Interpolating`

34 **end**

35 **return** W_{NL}

Algorithm 3.4.5: GAUSS: Gauss Elimination Algorithm − Partial Pivoting

---

   Input   : System coefficients defined by network characteristics
   Output: Values of the Mass flow rates

---

1 **for** $i \leftarrow 1$ **to** n **do**   // Gaussian Elimination
2 | $s_i = 0$ // computes array of row maximal elements
3 | **for** $j \leftarrow 1$ **to** n **do**
4 | | $s_i = \max(s_i, |a_{ij}|)$
5 | **end**
6 | $p_i = i$ // initialize row pointers to row numbers
7 **end**
8 **for** $k \leftarrow 1$ **to** $n-1$ **do**
9 | $r_{\max} = 0$ // largest scaled column entry
10 | **for** $i \leftarrow k$ **to** n **do**
11 | | $r = |a_{p_i k}/s_{p_i}|$
12 | | **if** $r > r_{max}$ **then**
13 | | | $r_{\max} = r$
14 | | | $j = i$ // row index of largest scaled entry
15 | | **end**
16 | **end**
17 | $\text{temp} = p_k$ // exchange row pointers
18 | $p_k = p_j$
19 | $p_j = \text{temp}$
20 | **for** $i \leftarrow k+1$ **to** n **do**   // perform elimination on submatrix
21 | | $a_{p_i k} = a_{p_i k}/a_{p_k k}$
22 | | **for** $j = k+1$ **to** n **do**
23 | | | $a_{p_i j} = a_{p_i j} - a_{p_i k}\, a_{p_k j}$
24 | | **end**
25 | **end**
26 **end**
27 **for** $k \leftarrow 1$ **to** $n-1$ **do**   // Forward Elimination
28 | **for** $i \leftarrow k+1$ **to** n **do**
29 | | $b_{p_i} = b_{p_i} - a_{p_i k}\, b_{p_k}$
30 | **end**
31 **end**
32 **for** $i \leftarrow n$ **downto** 1 **do**   // Backward Solve
33 | $s = b_{p_i}$
34 | **for** $j \leftarrow i+1$ **to** n **do**
35 | | $s = s - a_{p_i j}\, x_j$
36 | **end**
37 | $x_i = s/a_{p_i i}$
38 **end**

Table 3.2: Connectivity matrix for the sample network of Figure 3.1 as a result from the drawing in the graphical interface.

Piping Element ID (#)	From Node ID (#)	To Node ID (#)
1	1	2
2	3	2
3	2	4
4	4	3
5	5	3
6	4	5
7	5	6
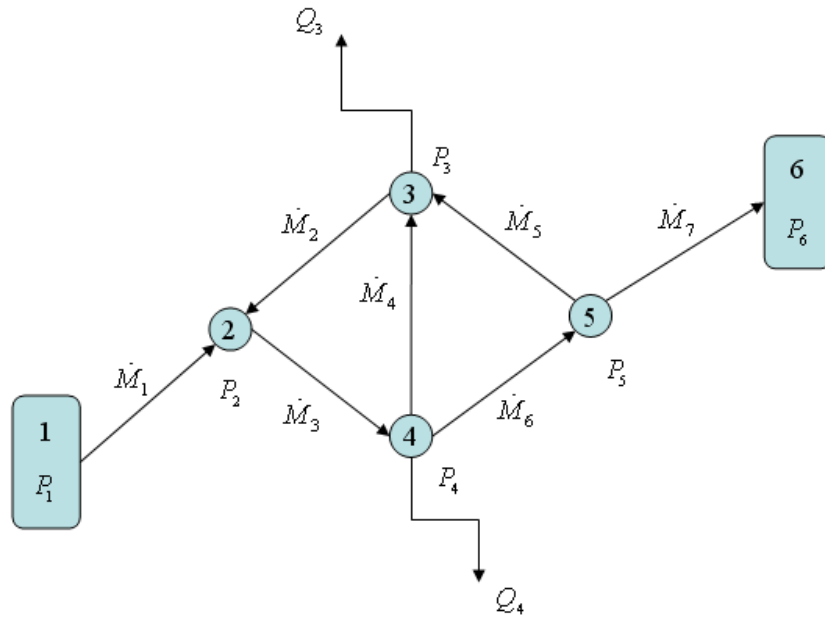
Figure 3.1: Example network.
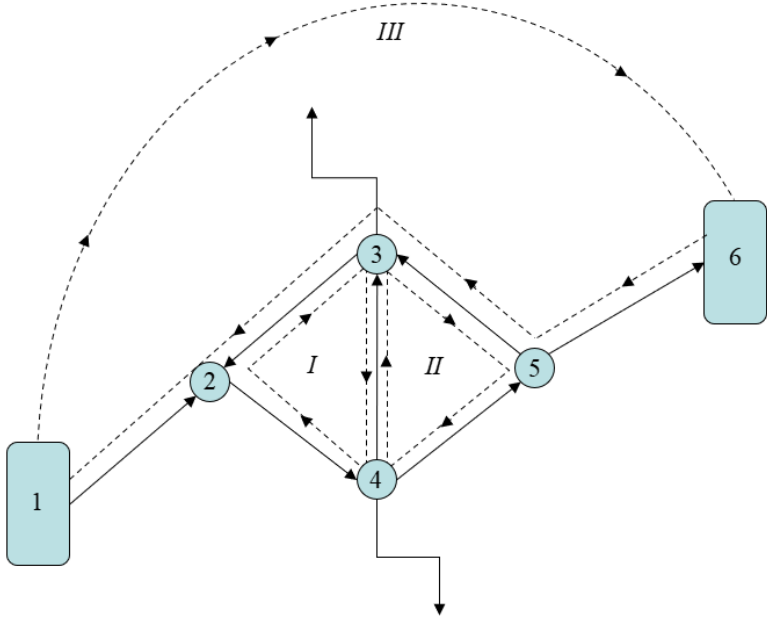
Figure 3.2: Example network loops.

Figure 3.3: Logo of the in-house developed algorithm ARIADNE.
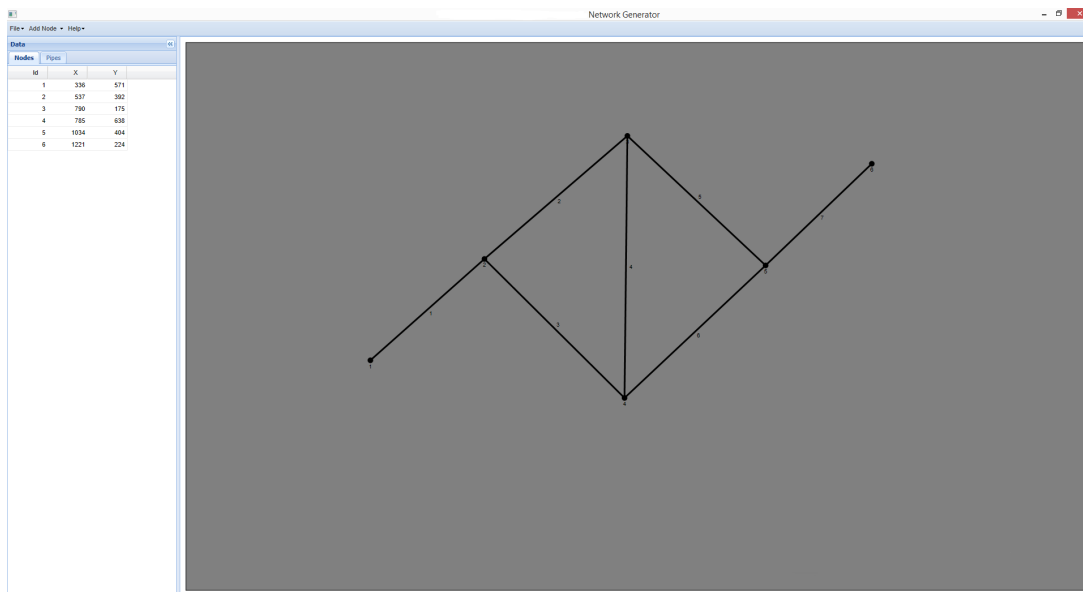
Figure 3.4: Representation of the sample network in the developed graphical interface.
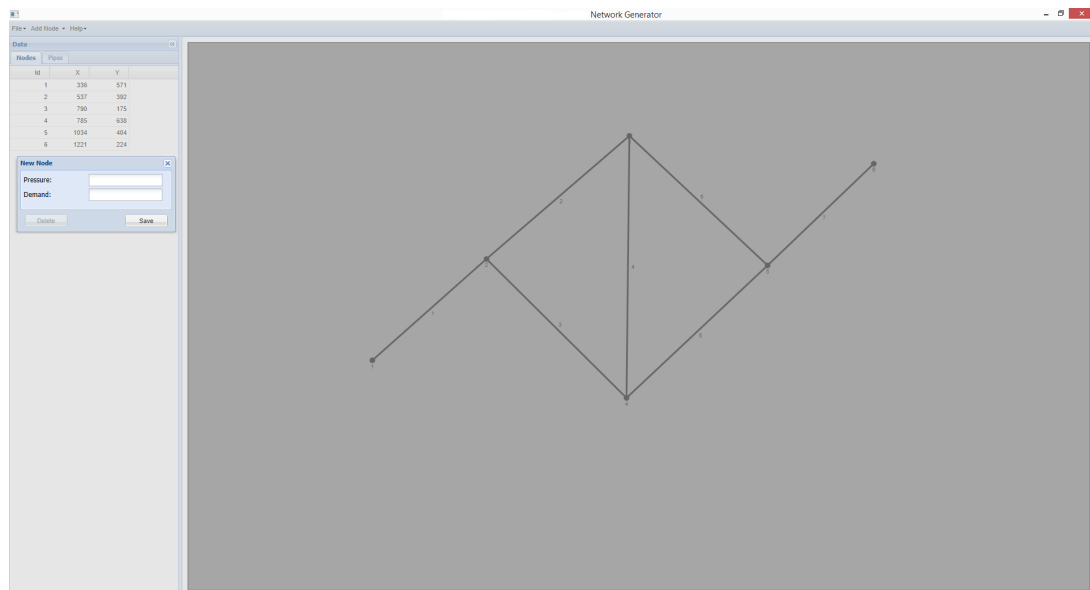
Figure 3.5: Adding new nodes in a network and defining local pressure value or possible leak/demand values in the developed graphical interface.
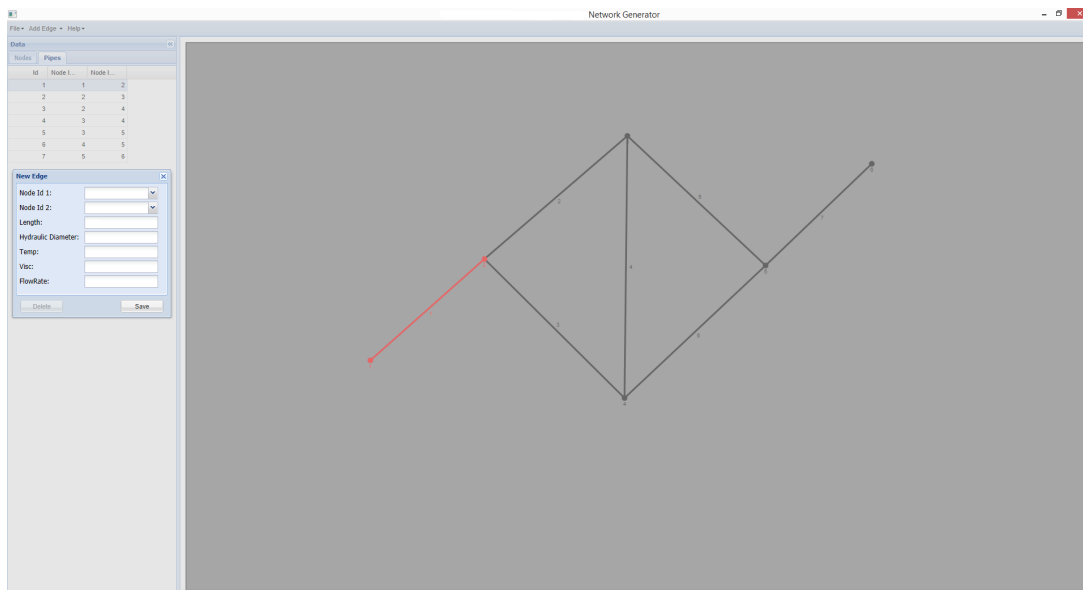
Figure 3.6: Adding new pipes/edges in a network and defining local characteristics of the piping element in the developed graphical interface.
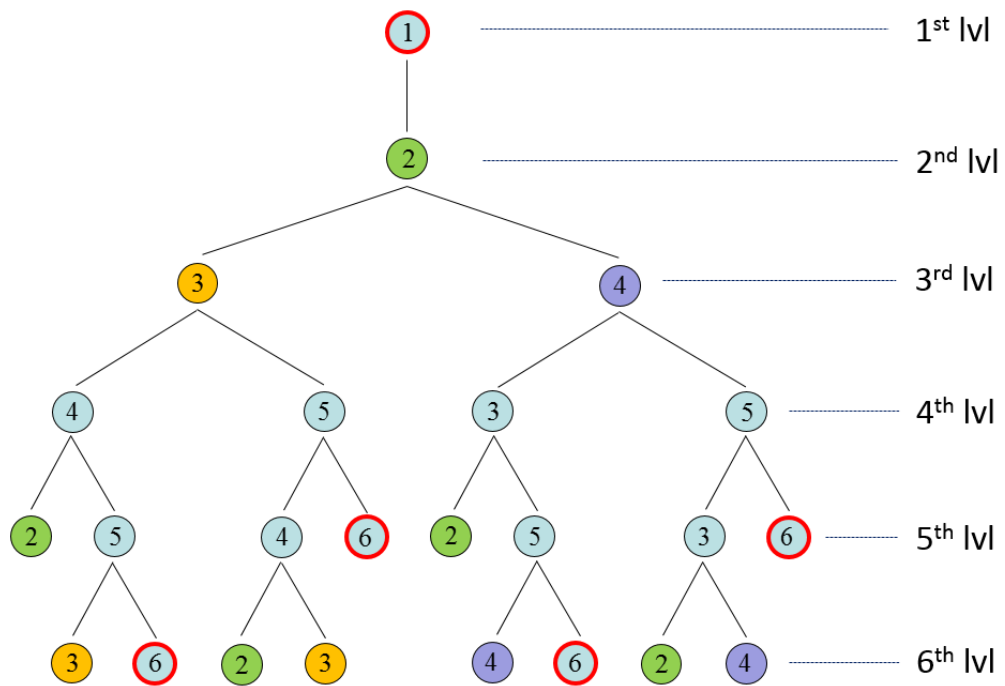
Figure 3.7: Schematic representation of the graph used for the implementation of the DFS algorithm.
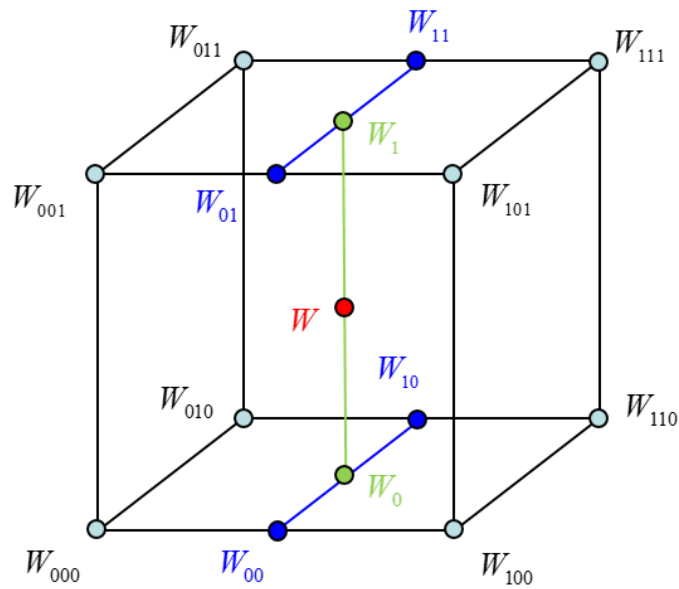
Figure 3.8: Schematic representation of trilinear interpolation algorithm.
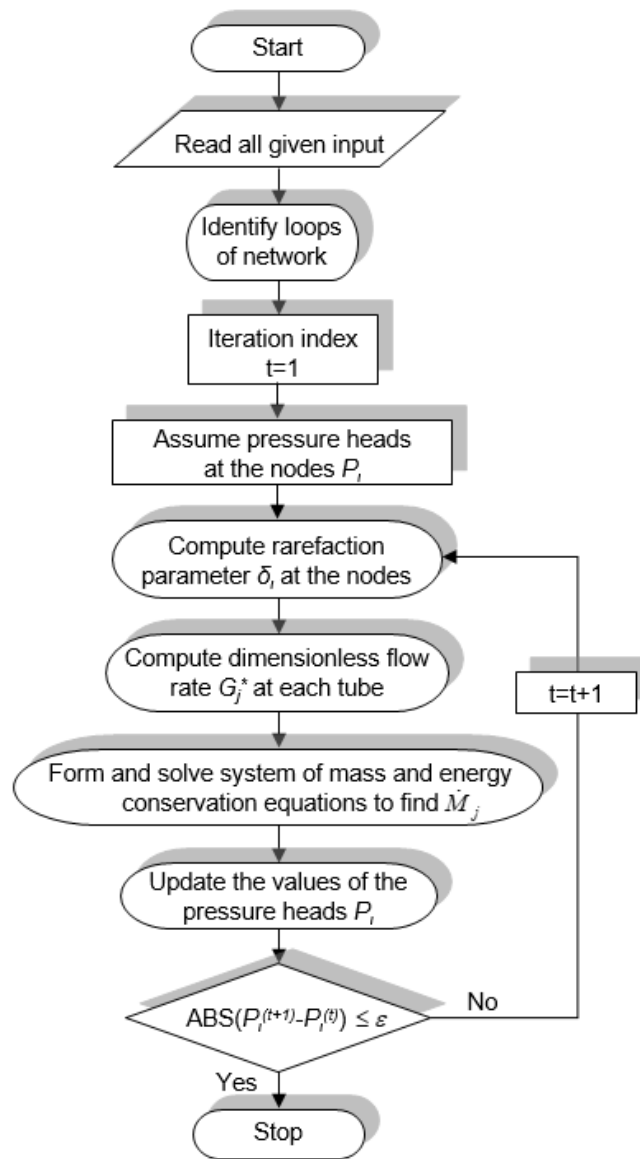
Figure 3.9: Flowchart for ARIADNE.
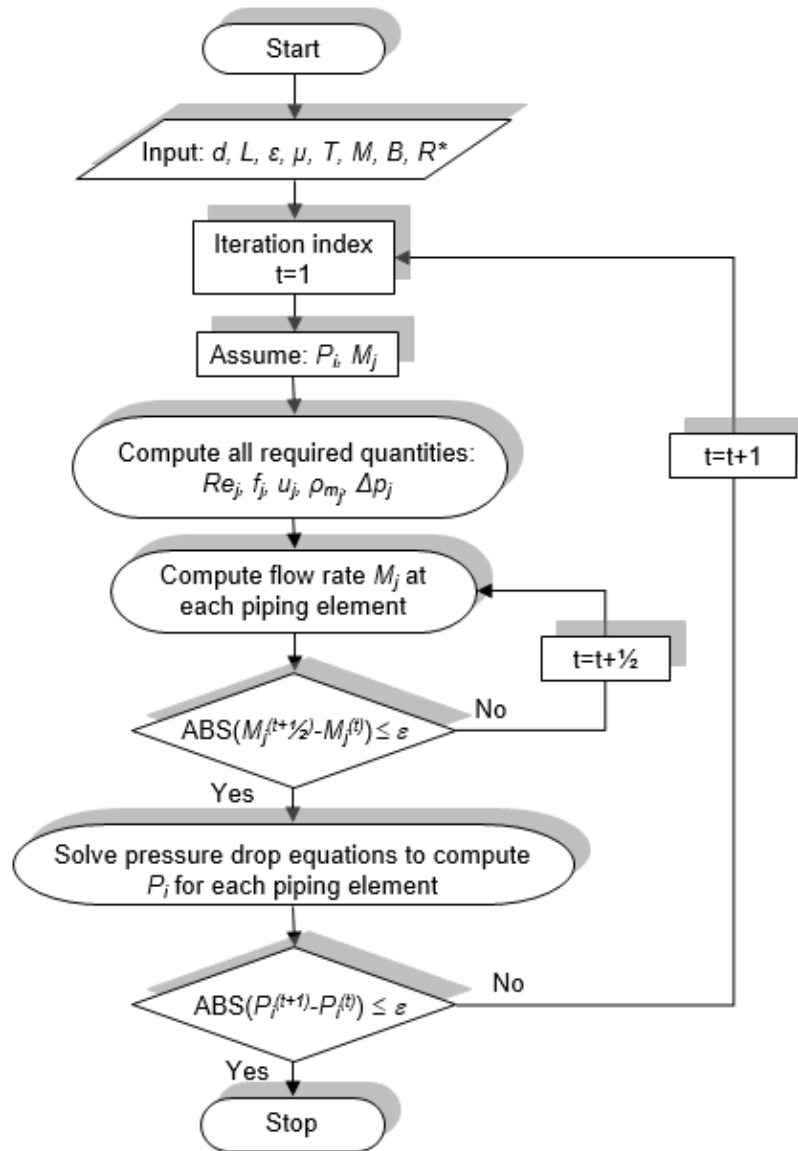
Figure 3.10: Flowchart for the algorithm developed in Matlab.
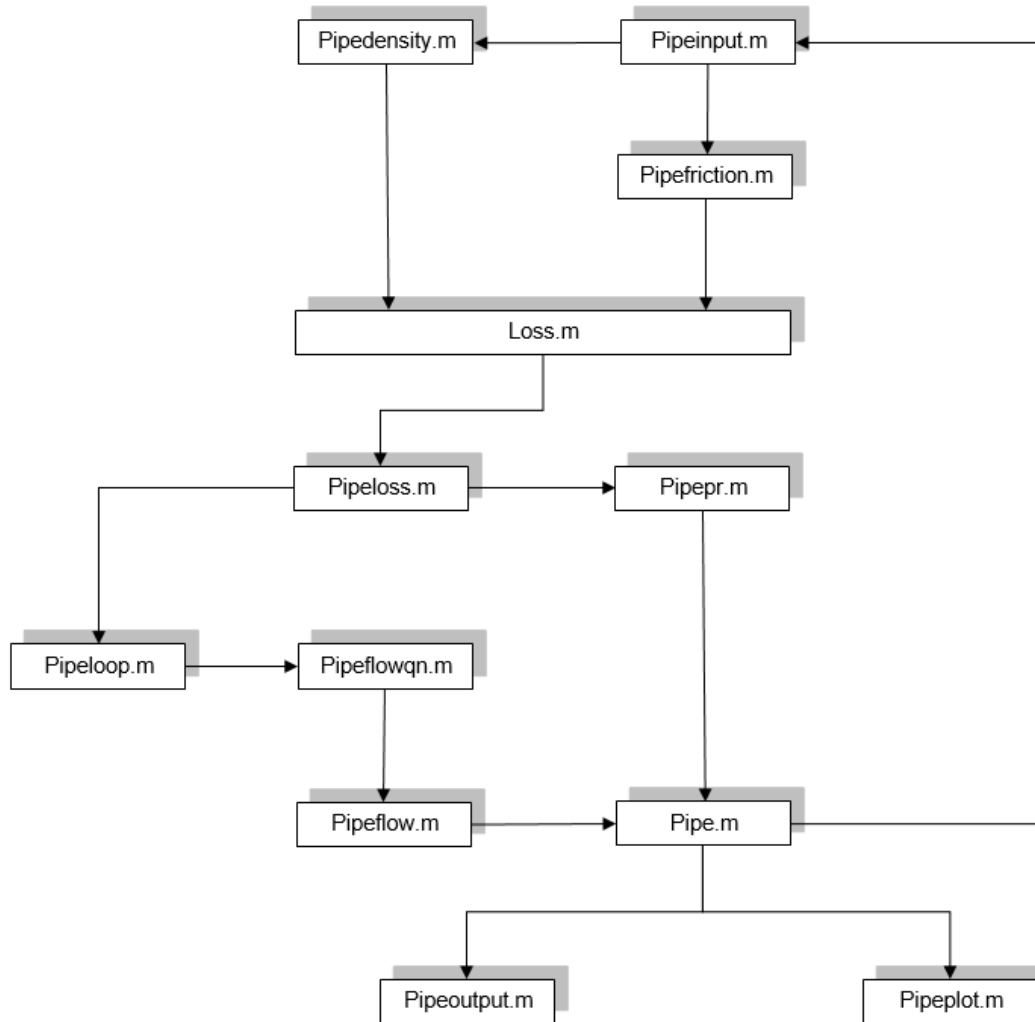
Figure 3.11: Flowchart of the subroutine dependencies for the algorithm developed in Matlab.

4

Gas distribution systems consisting of piping elements of long and moderate length

4.1 Flow characteristics in distribution systems consisting of piping elements with L/D≥5

Linear, fully developed flows of rarefied gases through piping elements of various cross sections have been studied extensively by several deterministic methods, as seen in previous chapters. This state is characterized by zero velocity in the transversal directions and constant density at each cross-section, based on the underlying assumption that the channel is sufficiently long. However, in many practical situations, there are significant deviations from this behavior near the channel ends, where the assumption of constant density at each cross-section is not valid and the flow becomes two- or three-dimensional. This effect is particularly apparent in short channels, even for linear flows, and the fully developed profile may not be observed at all. Furthermore, even when the channel is long, the channel end effect may be significant in applications where high accuracy is required.

4.2 Benchmarking in networks consisting of circular pipes

The methodology described in subsection 3.3.2 is applied in three hypothetical networks of small, moderate and increased complexity, respectively, while the piping elements are of circular cross sections. For the networks of small and increased complexity, the flow is described by the principles in the hydrodynamic regime in an attempt to allow a comparison with the corresponding results obtained by the hydrodynamic pipe network solver based on the Darcy-Weisbach equation including the correction of the slip solution for the proper evaluation of the friction factor. For the third network examined, the results cover a wide range of rarefaction. In this latter case, the comparison is performed with the corresponding results obtained by ITERVAC algorithm.

4.2.1 Network of small complexity in the hydrodynamic regime − A chess-board network

The sample network shown in Figure 4.1, named as "Network 4.2.1/4.5.1", is simulated. The network consists of $p = 42$ tubes, $n = 25$ junction nodes $\{2, 3, ..., 25, 26\}$, $f = 2$ fixed-grade nodes $\{1, 27\}$ and $l = 16$ loops. Nodes 1 and 27 refer to two reservoirs, where the pressure is held constant. All tubes are taken to have the same length and diameter, which are equal to $L = 10$ m and $D = 0.1$ m respectively. The reference temperature is set to $T_0 = 290.68$K. The conveying gas is nitrogen, with molar mass $m = 28.0314$ gr/mol, gas constant $R_{N_2} = 296.92$ J/(kg·K), most probable molecular velocity $v_0 = 415.47$ m/s and viscosity $\mu = 17.3562$ μPa·s. Then, the system of governing equations includes 25 mass conservation equations at the junction nodes, 16 balance equations for the closed loops and 1 energy balance equation for the open pseudo-loop formed along the nodes $\{1, 2, 3, 4, 5, 6, 11, 16, 21, 26, 27\}$. The total number of equations of the system is 42 and its solution returns the 42 unknown mass flow rates $\{\dot{M}_1, \dot{M}_2, ..., \dot{M}_{42}\}$ and the corresponding conductances $\{C_1. C_2, ..., C_{42}\}$. Then, from the pressure drop equations the pressure heads $\{P_2, ..., P_{26}\}$ are found. Finally, the pressure distribution along each pipe element of the network may also be estimated.

In order to simulate the flow characteristics at the hydrodynamic regime, the pressure at nodes 1 and 27 is set equal to $P_1 = 70$ Pa and $P_{27} = 60$ Pa. The corresponding Knudsen numbers are 9.13×10^{-4} and 1.07×10^{-3}, which clearly indicates that the flow in the network is in the slip (or hydrodynamic) regime. For generality purposes, demands (or leakages) have been added at nodes 6 and 22, which are equal to $Q_6 = 1.40 \times 10^{-5}$ kg/s and $Q_{22} = 2.10 \times 10^{-5}$ kg/s, respectively.

To benchmark the present formulation and results Network 4.2.1, subject to exactly the same conditions, has been also solved using a typical hydrodynamic solver for gas pipe networks and a comparison between the results is performed. For the purposes of the present work the Darcy-Weisbach equation combined with the slip solution for the estimation of the friction factor.

In Table 4.1, the computed Knudsen number and pressure at each node of the network are tabulated by applying both solvers, while in Table 4.2, the mass flow rate and the conductance along each tube of the network are presented. The negative values at some of the mass flow rates indicate that the final direction of the flow in this tube is opposite to the one initially assumed. The total mass flow in tube 1 is $\dot{M}_1 = 4.33 \times 10^{-5}$ kg/s, while in tube 42 is $\dot{M}_{42} = 8.32 \times 10^{-6}$ kg/s and, as expected, the following relation is satisfied $\{\dot{M}_1 = \dot{M}_{42} + Q_6 + Q_{22}\}$.

The agreement between the results based on the hydrodynamic analysis and the ones based in kinetic theory, shown in Tables 4.1 and 4.2, is excellent. In particular, the corresponding results of pressure at each node and mass flow rate in each tube, agree up to at least two significant figures.

4.2.2 Network of increased complexity in the hydrodynamic regime – An ITER-like network

An ITER like network is applied to further validate the present algorithm. Here, the algorithm makes use of the end effect correction principles, extending its validity, in addition to long channels, to channels of moderate length 5<L/D<50. For demonstration purposes, a similar geometry to the one of ITER's lower port region (Figure 4.2) is simulated. The schematic representation of the resulting network, named as "Network 4.2.2/4.5.2", is shown in the right hand side of Figure 4.3.

The network consists of $p = 190$ tubes, $n = 124$ junction nodes, $f = 58$ fixed-

grade nodes and $I = 9$ loops. From the 58 fixed grade nodes, where the pressure is held constant, 54 nodes $\{1, 5, 8, 11, ..., 158, 161\}$ refer to the divertor's entrance while nodes $\{167, 172, 177, 182\}$ refer to the four direct pumps located at the ends of the vacuum ducts connected to the lower part of the torus. For comparison purposes, all tubes are taken to have the same length and diameter, which are equal to $L = 2$m and $D = 0.2$ m respectively. The reference temperature is set to $T_0 = 410$ K corresponding to the temperature of the ITER's burn phase scenario. The conveying gas is helium, with molar mass $m = 4.0026$ gr/mol, gas constant $R_{He} = 2076.9$ J/(kg·K), most probable molecular velocity $\upsilon_0 = 415.47$ m/s and viscosity $\mu = 24.68$ μPa·s.

Then, the system of governing equations includes 124 mass conservation equations at the junction nodes, 9 energy balance equations for the closed loops and 57 energy balance equation for the open pseudo-loops. The total number of equations of the system is 190 and its solution returns the 190 unknown mass flow rates $\{\dot{M}_1, \dot{M}_2, ..., \dot{M}_{190}\}$. Then, from the pressure drop equations the pressure heads $\{P_1, ..., P_{182}\}$ are found.

The pressure at the entrance of the divertor for the 54 nodes equals 10Pa while the pressure at the pumps is equal to 1Pa. The corresponding Knudsen numbers are 1.43×10^{-2} and 1.43×10^{-1} which clearly indicates that the flow in the network is in the viscous (or hydrodynamic) regime.

The provided results refer to a part of the simulated network, more specifically for the one shown enlarged in the left hand side of Figure 4.3 and in more detail in Figure 4.4. The flow path as well as the pressure at each node and the mass flow rate along each tube are shown in Figures 4.5, 4.6(up) and 4.6(down), respectively. The negative values at some of the mass flow rates indicate that the final direction of the flow is opposite to the one initially assumed.

Following the same benchmark procedure, the current network configuration under the prescribed flow conditions is simulated by implementing the hydrodynamic equation combined with the slip correction for the friction factor. The agreement between the results based on the hydrodynamic analysis and the ones based in kinetic theory, shown in Figure 4.6, is very good. In particular, the corresponding results of pressure at each node have a maximum relative difference of 3.84% and the corresponding difference for the mass flow rate has a maximum value of 2.73%.

4.2.3 Network of average complexity in the whole range of the rarefaction – A honeycomb network

A comparison is performed between the kinetic solver and the empirical algorithm ITERVAC. The comparison refers to a hypothetical network, named as "Network 4.2.3", consisting of $p = 22$ elements, $n = 14$ junction nodes, $f = 4$ fixed-grade nodes and $l = 5$ loops. In Figure 4.7, the schematic representation of the simulated network is shown. For this comparison, all elements have the same length and diameter, which are equal to $L = 5$ mm and $D_h = 35\mu$m respectively, resulting to a big ratio of L/D_h and therefore the kinetic analysis is based on the infinite channel theory. The conveying gas is argon (Ar) held in ambient temperature. Two indicative simulations are performed. In the first case, the two left reservoirs are held in $P_1 = 220$Pa and $P_2 = 210$Pa, while the two right reservoirs have a fixed pressure of $P_{17} = 1.20$ Pa and $P_{18} = 1.10$ Pa, respectively, resulting to high values of Knudsen number.

In the second scenario for the flow conditions characterizing the network, all four pressure values at the entrance and the exit of the network have lower values compared to the ones of the previous scenario. For the containers playing the role of the entrance nodes of the network the pressure values are set to $P_1 = 14$ kPa and $P_2 = 13$ kPa, respectively, while for the exit nodes the pressure values are set to $P_{17} = 120$ Pa and $P_{18} = 110$ Pa, leading to a wide range of gas rarefaction and a comparison of the two approaches in all flow regimes is performed.

In both simulated scenarios, the system of governing equations includes fourteen mass conservation equations at nodes $\{3, 4, ..., 16\}$, five energy balance equations along the closed loops of three energy balance equations along the opes pseudo-loops. The total number of equations of the system is 22 and its solution returns the 22 unknown mass flow rates $\{\dot{M}_1, ..., \dot{M}_{22}\}$. Then, from the pressure drop equations, the pressure heads $\{P_3, ..., P_{16}\}$ are found.

The results are shown in Table 4.3 for the pressure heads [Pa] and Table 4.4 for the mass flow rates [kg/s] for the first scenario simulated, while for the second scenario, the corresponding results are provided in Table 4.5 for the pressure values and Table 4.6 for the mass flow rates, respectively. In both scenarios simulated, the agreement in the pressure values is excellent, while the deviation in the mass flow rates does not exceed 4.3%.

4.3 Distribution networks consisting of ducts with orthogonal and trapezoidal cross section

In the present section, the attention is drawn in the comparison between networks consisting of non-circular piping elements and the corresponding configurations based on cylindrical elements by employing either the same hydraulic diameter or the same cross section area.

To demonstrate the feasibility and the effectiveness of the proposed methodology the sample network shown in Figure 4.8 (left) is simulated. "Network 4.3/4.4" consists of $p = 14$ tubes, $n = 9$ junction nodes, $f = 2$ fixed-grade nodes and $l = 4$ loops. Nodes 1 and 11 refer to two reservoirs, where the pressure is held constant. The micro distribution system is characterized by the availability of introducing demands at nodes 4 and 8, however, for comparison reasons these two values are set to 0. The reference temperature is set to $T_0 = 293.7$ K. The conveying gas is argon (Ar), with molar mass $m = 0.039948$ kg/mol, gas constant $R = 208$ J/(kg·K), most probable molecular velocity $v_0 = 347.74$ m/s and viscosity $\mu = 22.7985$ µPa·s.

The system of governing equations includes nine mass conservation equations at nodes $\{2, 3, ..., 10\}$, four energy balance equations along the closed loops I, II, III, IV and one energy balance equation along the open pseudo-loop formed along the nodes $\{1, 2, 3, 4, 5, 6, 11\}$. The total number of equations of the system is 14 and its solution returns the 14 unknown mass flow rates $\{\dot{M}_1, ..., \dot{M}_{14}\}$. Then, from the pressure drop equations, the pressure heads $\{P_2, ..., P_{10}\}$ are found.

Two networks of different geometries are simulated. The first one refers to a network which consists of rectangular micro-channels with $H = 2.00$ µm and $W = 20.00$ µm, leading to an aspect ratio of $H/W = 0.1$ and, according to the equations shown in Table 2.1, a hydraulic diameter $D_h = 3.63$ µm. The second network simulated, where the micro-distribution system consists of equilateral trapezoidal elements, with size of big base $B = 6.87$ µm, small base $b = 1.80$ µm, height $h = 3.60$ µm and acute angle $\phi = 54.74°$, leading to a hydraulic diameter $D_h = 3.56$ µm. In all cases considered, the length of the piping elements is kept constant and equal to $L = 5.00$ mm, while the pressures at both the upstream and downstream reservoirs are fixed to $P_1 = 0.125$ MPa and $P_{11} = 140$ Pa, respectively. Both networks simulated are

compared, while keeping the same configuration, to two additional networks consisting of cylindrical tubes of either the equivalent hydraulic diameter D_h, or the same cross section area A'. It is noted that for the case of the networks of rectangular and trapezoidal cross section, all the kinetic coefficients required for the simulation are based on the actual data bases for the corresponding geometrical characteristics of the ducts in the network.

The results are shown in Figure 4.9 and in Tables 4.7 - 4.10 for the rarefaction parameter, the pressure heads [Pa] and the mass flow rates [kg/s] for both networks under consideration. The corresponding results using the hydraulic diameter concept are also included. The rarefaction parameter covers the range $0.0642 \leq 1/\text{Kn} \leq 57.33$ for the rectangular case and $0.0630 \leq 1/\text{Kn} \leq 56.28$ for the trapezoidal one. The flow in the network covers the slip, transition and free molecular regimes. The negative values at some of the mass flow rates indicate that the final direction of the flow is opposite to the one initially assumed. The red arrows shown in Figure 4.8 (right) indicate the corrected flow direction obtained after convergence of the code.

Next, we comment on the comparison of the simulated networks with the corresponding ones consisting of cylindrical channels with the equivalent hydraulic diameter. In the case where all channels have the same hydraulic diameter, the friction factor is the same and therefore the pressure drop is similar. As a result, the rarefaction parameter is close for every node of the network in both geometries simulated. The relative error between the rectangular channels and the cylindrical ones is less than 4.11% for the pressure heads. Similar results can be seen for the comparison between the trapezoidal and the cylindrical channels, where the relative error is less than 0.09% for the pressure heads. However, in both comparisons, despite the good agreement between the pressure heads, the comparison with regard to the mass flow rate through each of the piping elements of the networks shows that there are significant differences. For the case of the rectangular channels there is a discrepancy around 220% for the flow rates and for the case of the trapezoidal channels around 85%.

Moreover, for comparison purposes, the same simulation is performed but, instead of employing the hydraulic diameter concept, the diameter of the cylindrical channels introduced is computed on the basis of maintaining the cross section area A' constant. As a result, for the case of the rectangular channels the diameter used for the

simulation is equal to $D = 7.14$ μm, while for the case of the equilateral trapezoidal elements, the computer diameter is equal to $D = 4.46$ μm. In the present scenario the relative error computed between the rectangular channels and the cylindrical ones reaches a maximum value of 9.22% for the pressure heads. The increase in the pressure head deviation between the former and the latter comparison is well expected, since the friction factor is not kept the same in this configuration. Similar results can be seen for the comparison between the trapezoidal and the cylindrical channels, where the relative error is less than 2.29% for the pressure heads, following the same trend with the rectangular channels. In contrary, in both comparisons, despite the increased deviation in the pressure head values, the comparison with regard to the mass flow rate through each of the piping elements of the networks shows that there are smaller differences. For the case of the rectangular channels there is a discrepancy around 75.74% for the flow rates and for the case of the trapezoidal channels around 20.96%.

4.4 Extension to networks consisting of tubes with various lengths and diameters

The network simulated in this section has the same topological characteristics as the one described in Figure 4.8 (left). However, the specific geometrical characteristics of each piping element of the network are different to each other. The main goal here is to demonstrate the solver's generalized applicability in networks consisting of elements of various lengths and diameters.

As in the network simulated in the previous section, "Network 4.3/4.4" consists of $p = 14$ tubes, $n = 9$ junction nodes, $f = 2$ fixed-grade nodes and $l = 4$ loops. Nodes 1 and 11 refer to two reservoirs, where the pressure is held constant. Once again, the reference temperature is set to $T_0 = 293.7$ K. The conveying gas is argon (Ar), with molar mass $m = 0.039948$ kg/mol, gas constant $R = 208$ J/(kg·K), most probable molecular velocity $v_0 = 349.54$ m/s and viscosity $\mu = 22.7985$ μPa·s.

Since the topological characteristics of the network under consideration remain the same with the network simulated in the previous section, the system of governing equations remains unchanged, i.e. nine mass conservation equations at nodes

$\{2, 3, ..., 10\}$, four energy balance equations along the closed loops I, II, III, IV and one energy balance equation along the open pseudo-loop formed along the nodes $\{1, 2, 3, 4, 5, 6, 11\}$. The total number of equations of the system is 14 and its solution returns the 14 unknown mass flow rates $\{\dot{M}_1, ..., \dot{M}_{14}\}$. Then, from the pressure drop equations, the pressure heads $\{P_2, ..., P_{10}\}$ are found.

However, the geometrical characteristics of each piping element forming the network are not constant. The individual geometrical properties of each of the piping elements are shown in Table 4.11.

Two simulations are performed. Considering the initial simulation, the pressure at the upstream reservoir is equal to $P_1 = 50$ kPa, while the pressure at the downstream reservoir is fixed to $P_{11} = 23$ kPa. The pressure values are selected in order for the rarefaction parameter to cover the range $15.46 \leq 1/\text{Kn} \leq 62.74$, i.e. within the limits of the hydrodynamic and slip regimes. As a result, a comparison is performed by implementing the hydrodynamic equation combined with the slip correction for the friction factor. The agreement between the results based on the hydrodynamic analysis and the ones based in kinetic theory, shown in Table 4.12, for the rarefaction parameter and the pressure heads [Pa], and Table 4.13, for the mass flow rates [kg/s], is very good. In particular, the corresponding results of pressure at each node have an agreement of at least three significant figures and the corresponding difference for the mass flow rate in each tube has a maximum value of 2.73%.

Based on the good agreement observed in the comparison performed for the case of the first simulation, the second simulation performed covers a wider range of rarefaction. In order to achieve this, the pressure at the upstream reservoir is equal to $P_1 = 50$ kPa, while the pressure at the downstream reservoir is fixed to $P_{11} = 0.23$ kPa. In this scenario, the rarefaction parameter covers the range $0.26 \leq 1/\text{Kn} \leq 62.74$, indicating that gas flowing through the network covers the whole range of rarefaction. Indicative results for the aforementioned simulation are shown in Tables 4.14 and 4.15 for the rarefaction parameter, the pressure heads [Pa] and the mass flow rates [kg/s], respectively, for the network under consideration.

It is noted that piping elements 3 and 4 as well as 7 and 8 have identical mass flow rates. This is well expected since at the nodes connecting these elements (nodes 4 and 8 respectively), there is no other connection or a leak/demand present. However, due to their geometrical characteristics, the pressure drop, and as a result the conductance,

in these elements is not identical.

4.5 Complex distribution systems

4.5.1 Network of small complexity in the whole range of the rarefaction - A chess-board network

To demonstrate the feasibility and the effectiveness of the proposed methodology the sample network shown in Figure 4.1 is simulated.

In the present simulation, the pressure at nodes 1 and 27 is set equal 1 Pa and 10^{-3} Pa respectively, while the corresponding Knudsen numbers are 0.0639 and 63.9, which clearly indicates that the flow in the network covers the slip, transition and free molecular regimes. Also, the demands at all nodes have been set equal to zero. The results of the simulation include the computed Knudsen number and pressure at each node of the network in Table 4.16, as well as the mass flow rate and the conductance along each tube of the network in Table 4.17. Again, the negative values at some of the mass flow rates indicate that the final direction of the flow in this tube is opposite to the one initially assumed. The total mass flow rate which is transferred from node 1 through the network to node 27 is equal to 4.58×10^{-8} kg/s and since there are no demands or leakages in the network $\dot{M}_1 = \dot{M}_{42}$. As it is expected, the network solution, due to the specific geometry and data, is symmetric about an axis defined by nodes $\{2, 8, 14, 20$ and $26\}$.

The present network setup has been also simulated by implementing the typical hydrodynamic solver resulting to significant discrepancies compared to the corresponding kinetic results throughout the network (pressure heads off by about 40% and total mass flow rate off by about 100%). It is interesting to note that although most of the nodes are in the slip regime with only one node (Node 27) in the free molecular regime the viscous analysis is not applicable.

124

4.5.2 Network of increased complexity in the whole range of the rarefaction - An ITER-like network

To demonstrate the feasibility and the effectiveness of the proposed methodology the sample network representing the vacuum pumping system of the ITER reactor, shown in Figure 4.2 is simulated. "Network 4.2.2/4.5.2" consists of $p = 190$ tubes, $n = 124$ junction nodes, $f = 58$ fixed-grade nodes and $l = 9$ loops. From the 58 fixed grade nodes, where the pressure is held constant, 54 nodes $\{1, 5, 8, 11, ... , 158, 161\}$ refer to the divertor's entrance while nodes $\{167, 172, 177, 182\}$ refer to the four direct pumps located at the ends of the vacuum ducts connected to the lower part of the torus.

For comparison purposes, all tubes are taken to have the same length and diameter, which are equal to $L = 2$ m and $D = 0.2$ m respectively. The reference temperature is set to $T_0 = 410$ K corresponding to the temperature of the ITER's burn phase scenario. The conveying gas is helium, with molar mass $m = 4.0026$ gr/mol, gas constant $R = 2076.9$J/(kg·K), most probable molecular velocity $\upsilon_0 = 415.47$ m/s and viscosity $\mu = 24.68\mu$Pa·s.

Then, the system of governing equations includes 124 mass conservation equations at the junction nodes, 9 energy balance equations for the closed loops and 57 energy balance equation for the open pseudo-loops. The total number of equations of the system is 190 and its solution returns the 190 unknown mass flow rates. Then, from the pressure drop equations the pressure heads are found.

In this simulation, the pressure referring to the divertor nodes is set equal to 1Pa while the pressure at the pumps is equal to 10^{-5} Pa, respectively, resulting to Knudsen numbers indicating that the flow in the network covers the early slip, transition and free molecular regimes. The results of the simulation include the pressure heads at each node of the network shown in Figure 4.10(up), as well as the mass flow rate through each tube of the network in Figure 4.10(down). Again, the negative values at some of the mass flow rates indicate that the final direction of the flow in this tube is opposite to the one initially assumed.

4.6 Concluding remarks

The algorithm for the design of steady-state, isothermal, gaseous distribution systems consisting of long tubes has been extended in order to take into account tubes of average length. The analysis is based on linear kinetic theory by solving the linearized BGK equation with diffuse boundary conditions in the whole range of the Knudsen number for the estimation of the dimensionless flow rates as well as the quantification of the end effect phenomena which cannot be neglected in piping elements of average length. The drawing of the network is aided by a GUI interface, the output of which is directly linked to the main iterative algorithm for designing gas pipe networks. More important the main algorithm successfully integrates linear kinetic results available from the constructed data bases.

As a result the integrated algorithm may successfully handle gas pipe networks consisting of long and average tubes of any complexity operating under any vacuum conditions through all regimes of rarefaction returning all the information needed for the on-line identification of the flow conditions inside the network. The effectiveness of the methodology has been demonstrated by solving a similar geometry to the one of ITER's lower port region, where two operation scenarios are examined based on the ITER burn phase, resulting to two simulation scenarios, one in the viscous regime and one in the whole range of the Knudsen number.

It is obvious that the algorithm developed will be useful for ITER like applications provided that it will be extended to channels of short length. In this, nonlinear kinetic analysis and DSMC solvers are required increasing the involved computational effort.

Table 4.1: Network 4.2.1 - Comparison between ARIADNE and the Hydrodynamic Solver with respect to the Pressure [Pa] and Knudsen number at each node of the network in the slip regime.

Node number	Kn	ARIADNE Pressure [Pa]	Hydrodynamic Solver Pressure [Pa]
1	9.13×10^{-4}	70.00	70.00
2	9.66×10^{-4}	66.12	66.13
3	9.97×10^{-4}	64.13	64.15
4	1.02×10^{-3}	62.90	62.92
5	1.03×10^{-3}	61.98	62.00
6	1.05×10^{-3}	61.05	61.08
7	9.97×10^{-4}	64.07	64.09
8	1.01×10^{-3}	63.32	63.33
9	1.02×10^{-3}	62.58	62.60
10	1.03×10^{-3}	61.96	61.98
11	1.04×10^{-3}	61.51	61.54
12	1.02×10^{-3}	62.72	62.74
13	1.02×10^{-3}	62.47	62.49
14	1.02×10^{-3}	62.12	62.14
15	1.03×10^{-3}	61.77	61.80
16	1.04×10^{-3}	61.52	61.54
17	1.04×10^{-3}	61.58	61.61
18	1.04×10^{-3}	61.71	61.74
19	1.04×10^{-3}	61.66	61.69
20	1.04×10^{-3}	61.49	61.51
21	1.04×10^{-3}	61.28	61.30
22	1.06×10^{-3}	60.30	60.34
23	1.05×10^{-3}	61.12	61.15
24	1.04×10^{-3}	61.34	61.36
25	1.04×10^{-3}	61.22	61.24
26	1.05×10^{-3}	60.84	60.85
27	1.07×10^{-3}	60.00	60.00

127

Table 4.2: Network 4.2.1 - Comparison between ARIADNE and the Hydrodynamic Solver with respect to the Mass flow rate and conductance at each tube of the network in the slip regime.

Tube # [j]	From node to node	ARIADNE $\dot{M}_j$ [kg/s]	Hydrodynamic $\dot{M}_j$ [kg/s]	C_j [×10² lt/s]	Tube # [j]	From node to node	ARIADNE $\dot{M}_j$ [kg/s]	Hydrodynamic $\dot{M}_j$ [kg/s]	C_j [×10² lt/s]
1	1-2	43.33	43.50	9.06	22	15-14	-3.55	-3.57	8.25
2	2-3	21.31	21.43	8.67	23	16-15	-2.54	-2.55	8.21
3	3-4	12.81	12.88	8.46	24	17-12	-0.12	-0.16	8.28
4	4-5	9.49	9.52	8.32	25	18-13	-7.74	-7.77	8.27
5	5-6	9.35	9.36	8.20	26	19-14	-4.66	-4.69	8.25
6	7-2	-22.19	-22.07	8.67	27	15-20	2.92	2.95	8.21
7	3-8	8.52	8.55	8.49	28	16-21	2.43	2.48	8.18
8	9-4	-3.33	-3.53	8.36	29	17-18	-1.29	-1.27	8.21
9	10-5	-0.15	-0.16	8.26	30	19-18	-0.47	-0.50	8.22
10	6-11	-4.65	-4.63	8.17	31	20-17	-1.81	-1.84	8.20
11	7-8	7.88	7.91	8.48	32	20-21	2.05	2.08	8.18
12	8-9	7.64	7.67	8.38	33	22-17	-12.81	-12.86	8.12
13	10-9	-6.31	-6.33	8.30	34	23-18	-5.98	-5.99	8.18
14	11-10	-4.55	-4.56	8.23	35	24-19	-3.33	-3.35	8.19
15	12-7	-0.14	-0.14	8.44	36	25-20	-2.68	-2.71	8.17
16	8-13	8.76	8.79	8.38	37	21-26	4.48	4.56	8.14
17	9-14	4.66	4.69	8.31	38	23-22	8.15	8.13	8.09
18	10-15	1.91	1.93	8.24	39	24-23	2.17	2.14	8.16
19	11-16	-0.10	-0.07	8.20	40	25-24	-1.16	-1.21	8.16
20	12-13	2.54	2.55	8.34	41	26-25	-3.84	-3.93	8.13
21	13-14	3.55	3.58	8.30	42	26-27	8.32	8.49	8.05

Table 4.3: Network 4.2.3 - Pressure and Knudsen number at each node of the network for high values of Kn number – comparison with ITERVAC.

Node number	Kn	ARIADNE Pressure [Pa]	ITERVAC Pressure [Pa]
1	1.43×10^{-1}	2.20×10^2	2.20×10^2
2	1.54×10^{-1}	2.10×10^2	2.10×10^2
3	1.65×10^0	1.74×10^2	1.74×10^2
4	1.72×10^0	1.70×10^2	1.70×10^2
5	1.80×10^0	1.52×10^2	1.51×10^2
6	1.82×10^0	1.50×10^2	1.50×10^2
7	1.85×10^0	1.49×10^2	1.49×10^2
8	1.98×10^0	1.29×10^2	1.29×10^2
9	2.00×10^0	1.28×10^2	1.28×10^2
10	2.52×10^0	8.57×10^1	8.56×10^1
11	2.54×10^0	8.53×10^1	8.52×10^1
12	3.00×10^0	6.42×10^1	6.41×10^1
13	3.01×10^0	6.40×10^1	6.40×10^1
14	3.02×10^0	6.39×10^1	6.38×10^1
15	3.87×10^0	4.28×10^1	4.28×10^1
16	3.88×10^0	4.27×10^1	4.27×10^1
17	1.67×10^2	1.20×10^0	1.20×10^0
18	1.82×10^2	1.10×10^0	1.10×10^0

Table 4.4: Network 4.2.3 - Mass flow rate and conductance at each tube of the network for high values of Kn number – comparison with ITERVAC.

Tube # [j]	From node to node	ARIADNE $\dot{M}_j$ [kg/s]	ITERVAC $\dot{M}_j$ [kg/s]
1	1-3	6.12×10^{-13}	6.25×10^{-13}
2	2-4	5.35×10^{-13}	5.47×10^{-13}
3	3-5	2.97×10^{-13}	3.04×10^{-13}
4	3-6	3.15×10^{-13}	3.22×10^{-13}
5	4-6	2.59×10^{-13}	2.64×10^{-13}
6	4-7	2.76×10^{-13}	2.82×10^{-13}
7	5-8	2.97×10^{-13}	3.04×10^{-13}
8	6-8	2.76×10^{-13}	2.82×10^{-13}
9	6-9	2.94×10^{-13}	3.00×10^{-13}
10	7-9	2.76×10^{-13}	2.82×10^{-13}
11	8-10	5.77×10^{-13}	5.90×10^{-13}
12	9-11	5.70×10^{-13}	5.82×10^{-13}
13	10-12	2.88×10^{-13}	2.94×10^{-13}
14	10-13	2.90×10^{-13}	2.96×10^{-13}
15	11-13	2.84×10^{-13}	2.90×10^{-13}
16	11-14	2.86×10^{-13}	2.92×10^{-13}
17	12-15	2.88×10^{-13}	2.94×10^{-13}
18	13-15	2.86×10^{-13}	2.92×10^{-13}
19	13-16	2.88×10^{-13}	2.94×10^{-13}
20	14-16	2.86×10^{-13}	2.92×10^{-13}
21	15-17	5.74×10^{-13}	5.86×10^{-13}
22	16-18	5.73×10^{-13}	5.86×10^{-13}

Table 4.5: Network 4.2.3 - Pressure and Knudsen number at each node of the network in the whole range of Kn number – comparison with ITERVAC.

Node number	Kn	ARIADNE Pressure [Pa]	ITERVAC Pressure [Pa]
1	1.43×10^{-2}	1.40×10^4	1.40×10^4
2	1.54×10^{-2}	1.30×10^4	1.30×10^4
3	1.65×10^{-2}	1.21×10^4	1.21×10^4
4	1.72×10^{-2}	1.17×10^4	1.17×10^4
5	1.80×10^{-2}	1.12×10^4	1.12×10^4
6	1.82×10^{-2}	1.10×10^4	1.10×10^4
7	1.85×10^{-2}	1.09×10^4	1.09×10^4
8	1.98×10^{-2}	1.02×10^4	1.01×10^4
9	2.00×10^{-2}	1.00×10^4	1.00×10^4
10	2.52×10^{-2}	7.97×10^3	7.95×10^3
11	2.54×10^{-2}	7.91×10^3	7.88×10^3
12	3.00×10^{-2}	6.69×10^3	6.67×10^3
13	3.01×10^{-2}	6.67×10^3	6.64×10^3
14	3.02×10^{-2}	6.65×10^3	6.62×10^3
15	3.87×10^{-2}	5.19×10^3	5.16×10^3
16	3.88×10^{-2}	5.17×10^3	5.14×10^3
17	1.67×10^0	1.20×10^2	1.20×10^2
18	1.82×10^0	1.10×10^2	1.10×10^2

Table 4.6: Network 4.2.3 - Mass flow rate and conductance at each tube of the network in the whole range of Kn number − comparison with ITERVAC.

Tube # [j]	From node to node	ARIADNE $\dot{M}_j$ [kg/s]	ITERVAC $\dot{M}_j$ [kg/s]
1	1-3	1.49×10^{-10}	1.54×10^{-10}
2	2-4	1.01×10^{-10}	1.05×10^{-10}
3	3-5	6.91×10^{-11}	7.13×10^{-11}
4	3-6	7.98×10^{-11}	8.23×10^{-11}
5	4-6	4.52×10^{-11}	4.69×10^{-11}
6	4-7	5.59×10^{-11}	5.79×10^{-11}
7	5-8	6.91×10^{-11}	7.13×10^{-11}
8	6-8	5.84×10^{-11}	6.03×10^{-11}
9	6-9	6.66×10^{-11}	6.89×10^{-11}
10	7-9	5.59×10^{-11}	5.79×10^{-11}
11	8-10	1.27×10^{-10}	1.32×10^{-10}
12	9-11	1.23×10^{-10}	1.27×10^{-10}
13	10-12	6.32×10^{-11}	6.53×10^{-11}
14	10-13	6.42×10^{-11}	6.64×10^{-11}
15	11-13	6.08×10^{-11}	6.28×10^{-11}
16	11-14	6.18×10^{-11}	6.39×10^{-11}
17	12-15	6.32×10^{-11}	6.53×10^{-11}
18	13-15	6.21×10^{-11}	6.42×10^{-11}
19	13-16	6.29×10^{-11}	6.50×10^{-11}
20	14-16	6.18×10^{-11}	6.39×10^{-11}
21	15-17	1.25×10^{-10}	1.30×10^{-10}
22	16-18	1.25×10^{-10}	1.29×10^{-10}

Table 4.7: Network 4.3 - Pressure and Knudsen number at each node of the network based on rectangular and cylindrical channels with either same D_h or A'.

Node number	1/Kn	Rectangular Pressure [kPa]	Tube (same D_h) Pressure [kPa]	Tube (same A') Pressure [kPa]
1	57.33	125.00	125.00	125.00
2	46.88	102.20	103.11	104.30
3	40.88	89.12	90.53	92.38
4	37.61	82.00	83.66	85.87
5	34.11	74.37	76.30	78.87
6	26.18	57.07	59.52	62.87
7	34.11	74.37	76.30	78.87
8	37.61	82.00	83.66	85.87
9	40.88	89.12	90.53	92.38
10	37.61	82.00	83.66	85.87
11	0.06	0.14	0.14	0.14

Table 4.8: Network 4.3 - Mass flow rate comparison for each pipe of the network based on rectangular and cylindrical channels with either same D_h or A'.

Tube # [j]	From node to node	Rectangular $\dot{M}_j$ [kg/s]	Tube (same D_h) $\dot{M}_j$ [kg/s]	Tube (same A') $\dot{M}_j$ [kg/s]
1	1-2	5.74×10^{-12}	1.79×10^{-12}	2.37×10^{-11}
2	2-3	2.87×10^{-12}	8.94×10^{-13}	1.18×10^{-11}
3	3-4	1.44×10^{-12}	4.47×10^{-13}	5.92×10^{-12}
4	4-5	1.44×10^{-12}	4.47×10^{-13}	5.92×10^{-12}
5	5-6	2.87×10^{-12}	8.94×10^{-13}	1.18×10^{-11}
6	6-7	-2.87×10^{-12}	-8.94×10^{-13}	-1.18×10^{-11}
7	7-8	-1.44×10^{-12}	-4.47×10^{-13}	-5.92×10^{-12}
8	8-9	-1.44×10^{-12}	-4.47×10^{-13}	-5.92×10^{-12}
9	9-2	-2.87×10^{-12}	-8.94×10^{-13}	-1.18×10^{-11}
10	9-10	1.44×10^{-12}	4.47×10^{-13}	5.92×10^{-12}
11	10-5	1.44×10^{-12}	4.47×10^{-13}	5.92×10^{-12}
12	10-7	1.44×10^{-12}	4.47×10^{-13}	5.92×10^{-12}
13	3-10	1.44×10^{-12}	4.47×10^{-13}	5.92×10^{-12}
14	6-11	5.74×10^{-12}	1.79×10^{-12}	2.37×10^{-11}

Table 4.9: Network 4.3 - Pressure and Knudsen number at each node of the network based on trapezoidal and cylindrical channels with either same D_h or A'.

Node number	1/Kn	Trapezoidal Pressure [kPa]	Tube (same D_h) Pressure [kPa]	Tube (same A') Pressure [kPa]
1	56.28	125.00	125.00	125.00
2	46.39	103.03	103.06	103.55
3	40.71	90.41	90.46	91.21
4	37.61	83.53	83.58	84.47
5	34.29	76.15	76.20	77.23
6	26.72	59.34	59.40	60.73
7	34.29	76.15	76.20	77.24
8	37.61	83.53	83.58	84.47
9	40.71	90.41	90.46	91.21
10	37.61	83.53	83.58	84.46
11	0.06	0.14	0.14	0.14

Table 4.10: Network 4.3 - Mass flow rate comparison for each pipe of the network based on trapezoidal and cylindrical channels with either same D_h or A'.

Tube # [j]	From node to node	Trapezoidal $\dot{M}_j$ [kg/s]	Tube (same D_h) $\dot{M}_j$ [kg/s]	Tube (same A') $\dot{M}_j$ [kg/s]
1	1-2	3.07×10^{-12}	1.66×10^{-12}	3.89×10^{-12}
2	2-3	1.54×10^{-12}	8.31×10^{-13}	1.95×10^{-12}
3	3-4	7.69×10^{-13}	4.16×10^{-13}	9.73×10^{-13}
4	4-5	7.69×10^{-13}	4.16×10^{-13}	9.73×10^{-13}
5	5-6	1.54×10^{-12}	8.31×10^{-13}	1.95×10^{-12}
6	6-7	-1.54×10^{-12}	-8.31×10^{-13}	-1.95×10^{-12}
7	7-8	-7.69×10^{-13}	-4.16×10^{-13}	-9.73×10^{-13}
8	8-9	-7.69×10^{-13}	-4.16×10^{-13}	-9.73×10^{-13}
9	9-2	-1.54×10^{-12}	-8.31×10^{-13}	-1.95×10^{-12}
10	9-10	7.69×10^{-13}	4.16×10^{-13}	9.73×10^{-13}
11	10-5	7.69×10^{-13}	4.16×10^{-13}	9.73×10^{-13}
12	10-7	7.69×10^{-13}	4.16×10^{-13}	9.73×10^{-13}
13	3-10	7.69×10^{-13}	4.16×10^{-13}	9.73×10^{-13}
14	6-11	3.07×10^{-12}	1.66×10^{-12}	3.89×10^{-12}

Table 4.11: Network 4.4 - Geometrical characteristics of each piping element.

Tube # [j]	1	2	3	4	5	6	7
L [μm]	1000	500	700	400	800	300	550
D_h [μm]	20	10	15	10	20	8	7
Tube # [j]	8	9	10	11	12	13	14
L [μm]	1000	300	200	500	900	400	900
D_h [μm]	30	5	5	5	10	8	18

Table 4.12: Network 4.4 - Comparison between ARIADNE and the Hydrodynamic Solver with respect to the Pressure [Pa] and Knudsen number at each node of the network in the slip regime.

Node number	1/Kn	ARIADNE Pressure [kPa]	Hydrodynamic Solver Pressure [kPa]
1	62.74	50.00	50.00
2	35.63	48.67	48.67
3	26.85	38.90	38.90
4	28.41	36.23	36.22
5	20.35	27.80	27.79
6	25.38	26.39	26.38
7	16.53	31.62	31.60
8	43.07	37.10	37.10
9	31.07	37.14	37.13
10	15.46	35.20	35.20
11	25.98	23.00	23.00

Table 4.13: Network 4.4 - Comparison between ARIADNE and the Hydrodynamic Solver with respect to the Mass flow rate and conductance at each tube of the network in the slip regime.

Tube # [j]	From node to node	ARIADNE M_j [kg/s]	Hydrodynamic Solver $\dot{M}_j$ [kg/s]	C_j [lt/s]
1	1-2	1.95×10^{-10}	1.97×10^{-10}	8.94×10^{-6}
2	2-3	1.71×10^{-10}	1.73×10^{-10}	1.07×10^{-6}
3	3-4	1.41×10^{-10}	1.43×10^{-10}	3.22×10^{-6}
4	4-5	1.41×10^{-10}	1.43×10^{-10}	1.02×10^{-6}
5	5-6	1.48×10^{-10}	1.50×10^{-10}	6.44×10^{-6}
6	6-7	-4.62×10^{-11}	-4.66×10^{-11}	5.40×10^{-7}
7	7-8	-1.84×10^{-11}	-1.85×10^{-11}	2.05×10^{-7}
8	8-9	-1.84×10^{-11}	-1.85×10^{-11}	3.36×10^{-5}
9	9-2	-2.36×10^{-11}	-2.37×10^{-11}	1.25×10^{-7}
10	9-10	5.21×10^{-12}	5.23×10^{-12}	1.64×10^{-7}
11	10-5	7.30×10^{-12}	7.27×10^{-12}	6.03×10^{-8}
12	10-7	2.79×10^{-11}	2.81×10^{-11}	4.76×10^{-7}
13	3-10	2.99×10^{-11}	3.02×10^{-11}	4.94×10^{-7}
14	6-11	1.95×10^{-10}	1.97×10^{-10}	3.52×10^{-6}

Table 4.14: Network 4.4 - Pressure and Knudsen number at each node of the network in the whole range of the Kn number.

Node number	1/Kn	Pressure [kPa]
1	62.74	50.00
2	35.29	48.21
3	23.82	34.51
4	23.89	30.46
5	11.70	15.98
6	12.27	12.76
7	11.93	22.82
8	36.78	31.69
9	26.55	31.74
10	12.64	28.79
11	0.26	0.23

Table 4.15: Network 4.4 - Mass flow rate and conductance at each tube of the network in the whole range of the Kn number.

Tube # [j]	From node to node	$\dot{M}_j$ [kg/s]	C_j [lt/s]
1	1-2	2.60×10^{-10}	8.90×10^{-6}
2	2-3	2.28×10^{-10}	1.02×10^{-6}
3	3-4	1.88×10^{-10}	2.83×10^{-6}
4	4-5	1.88×10^{-10}	7.92×10^{-7}
5	5-6	1.98×10^{-10}	3.75×10^{-6}
6	6-7	-6.26×10^{-11}	3.80×10^{-7}
7	7-8	-2.49×10^{-11}	1.72×10^{-7}
8	8-9	-2.49×10^{-11}	2.90×10^{-5}
9	9-2	-3.19×10^{-11}	1.19×10^{-7}
10	9-10	7.01×10^{-12}	1.45×10^{-7}
11	10-5	1.01×10^{-11}	4.84×10^{-8}
12	10-7	3.77×10^{-11}	3.86×10^{-7}
13	3-10	4.08×10^{-11}	4.35×10^{-7}
14	6-11	2.60×10^{-10}	1.27×10^{-6}

Table 4.16: Network 4.5.1 - Pressure and Knudsen number at each node of the network in the viscous regime.

Node number	Kn	Pressure [Pa]
1	6.39×10^{-2}	1.00
2	7.81×10^{-2}	8.18×10^{-1}
3	8.90×10^{-2}	7.18×10^{-1}
4	9.74×10^{-2}	6.56×10^{-1}
5	1.04×10^{-1}	6.16×10^{-1}
6	1.07×10^{-1}	5.96×10^{-1}
7	8.90×10^{-2}	7.18×10^{-1}
8	9.46×10^{-2}	6.75×10^{-1}
9	1.01×10^{-1}	6.31×10^{-1}
10	1.07×10^{-1}	5.96×10^{-1}
11	1.11×10^{-1}	5.75×10^{-1}
12	9.74×10^{-2}	6.56×10^{-1}
13	1.01×10^{-1}	6.31×10^{-1}
14	1.07×10^{-1}	5.96×10^{-1}
15	1.14×10^{-1}	5.59×10^{-1}
16	1.20×10^{-1}	5.33×10^{-1}
17	1.04×10^{-1}	6.16×10^{-1}
18	1.07×10^{-1}	5.96×10^{-1}
19	1.14×10^{-1}	5.59×10^{-1}
20	1.25×10^{-1}	5.11×10^{-1}
21	1.39×10^{-1}	4.60×10^{-1}
22	1.07×10^{-1}	5.96×10^{-1}
23	1.11×10^{-1}	5.75×10^{-1}
24	1.20×10^{-1}	5.33×10^{-1}
25	1.39×10^{-1}	4.60×10^{-1}
26	1.95×10^{-1}	3.27×10^{-1}
27	6.39×10^{1}	1.00×10^{-3}

Table 4.17: Network 4.5.1 - Mass flow rate and conductance at each tube of the network in the viscous regime.

Tube number	From node to node	$\dot{M}_j$ [Pa]	C_j [lt/s]	Tube number	From node to node	$\dot{M}_j$ [Pa]	C_j [lt/s]
1	1-2	4.58×10^{-8}	20.4	22	15-14	-7.28×10^{-9}	16.2
2	2-3	2.29×10^{-8}	18.6	23	16-15	-5.20×10^{-9}	15.8
3	3-4	1.35×10^{-8}	17.6	24	17-12	-8.32×10^{-9}	16.9
4	4-5	8.32×10^{-9}	16.9	25	18-13	-7.28×10^{-9}	16.6
5	5-6	4.16×10^{-9}	16.5	26	19-14	-7.28×10^{-9}	16.2
6	7-2	-2.29×10^{-8}	18.6	27	15-20	9.36×10^{-9}	15.7
7	3-8	9.36×10^{-9}	17.7	28	16-21	1.35×10^{-8}	15.2
8	9-4	-5.20×10^{-9}	17.0	29	17-18	4.16×10^{-9}	16.5
9	10-5	-4.16×10^{-9}	16.5	30	19-18	-7.28×10^{-9}	16.2
10	6-11	4.16×10^{-9}	16.3	31	20-17	-9.36×10^{-9}	15.6
11	7-8	9.36×10^{-9}	17.7	32	20-21	9.36×10^{-9}	15.0
12	8-9	9.36×10^{-9}	17.1	33	22-17	-4.16×10^{-9}	16.5
13	10-9	-7.28×10^{-9}	16.6	34	23-18	-4.16×10^{-9}	16.3
14	11-10	-4.16×10^{-9}	16.3	35	24-19	-5.20×10^{-9}	15.8
15	12-7	-1.35×10^{-8}	17.6	36	25-20	-9.36×10^{-9}	15.0
16	8-13	9.36×10^{-9}	17.1	37	21-26	2.29×10^{-8}	13.9
17	9-14	7.28×10^{-9}	16.6	38	23-22	-4.16×10^{-9}	16.3
18	10-15	7.28×10^{-9}	16.2	39	24-23	-8.32×10^{-9}	15.9
19	11-16	8.32×10^{-9}	15.9	40	25-24	-1.35×10^{-8}	15.2
20	12-13	5.20×10^{-9}	17.0	41	26-25	-2.29×10^{-8}	13.9
21	13-14	7.28×10^{-9}	16.6	42	26-27	4.58×10^{-8}	11.4
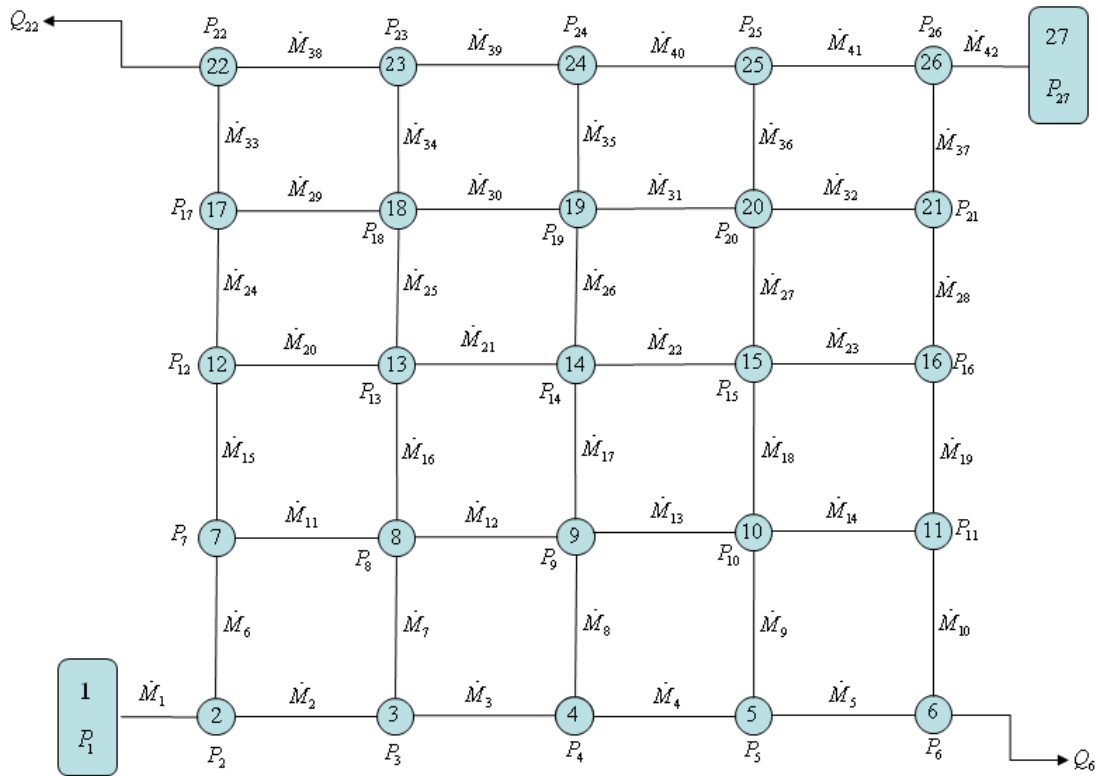
Figure 4.1: Schematic representation of Network 4.2.1/4.5.1.
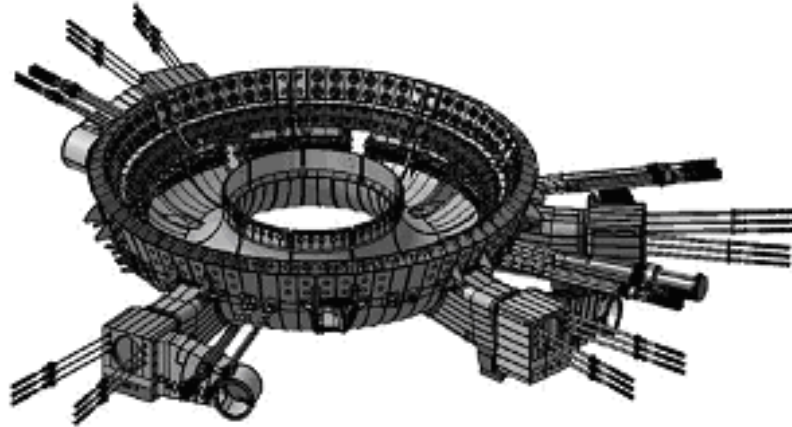
Figure 4.2: ITER lower port region.

Figure 4.3: Network 4.2.2/4.5.2 - Schematic representation of the simulated network with a detailed view of one of four vacuum ducts.
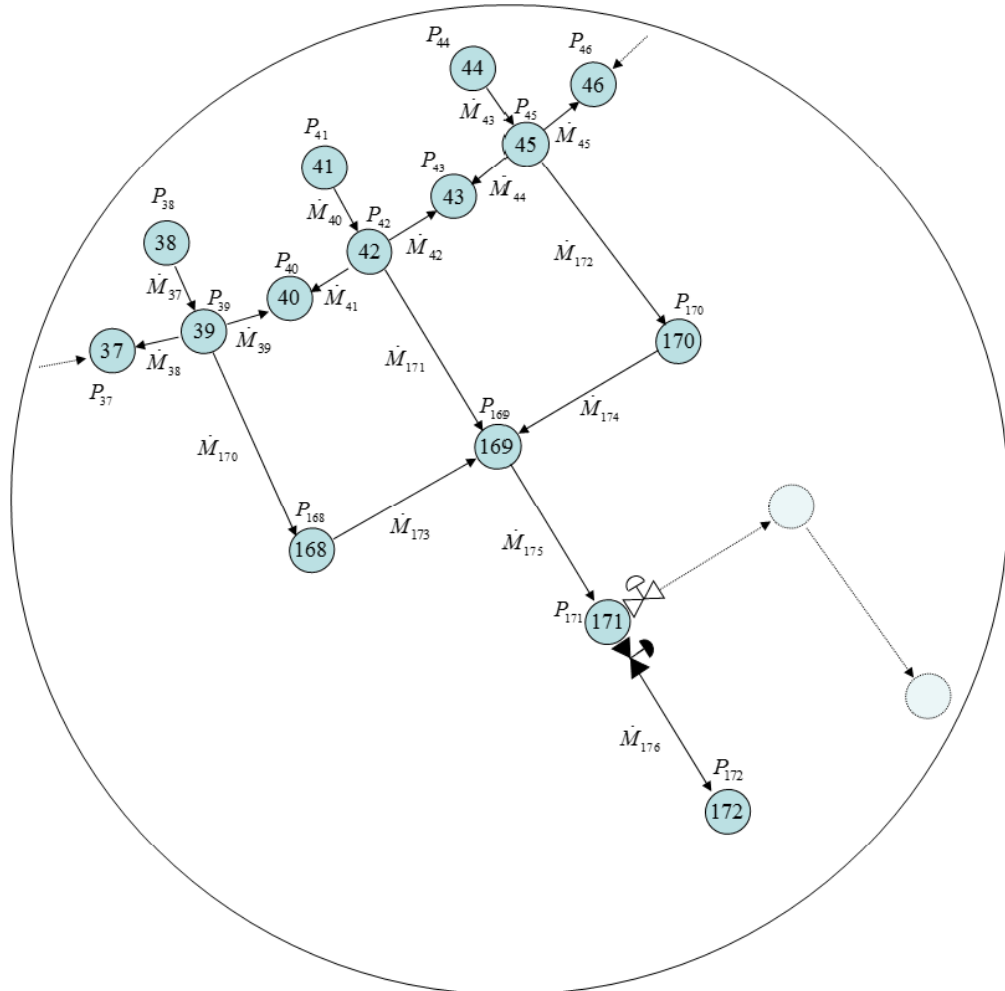
Figure 4.4: Network 4.2.2/4.5.2 - Schematic representation of the simulated network with a detailed view of one of four vacuum ducts.
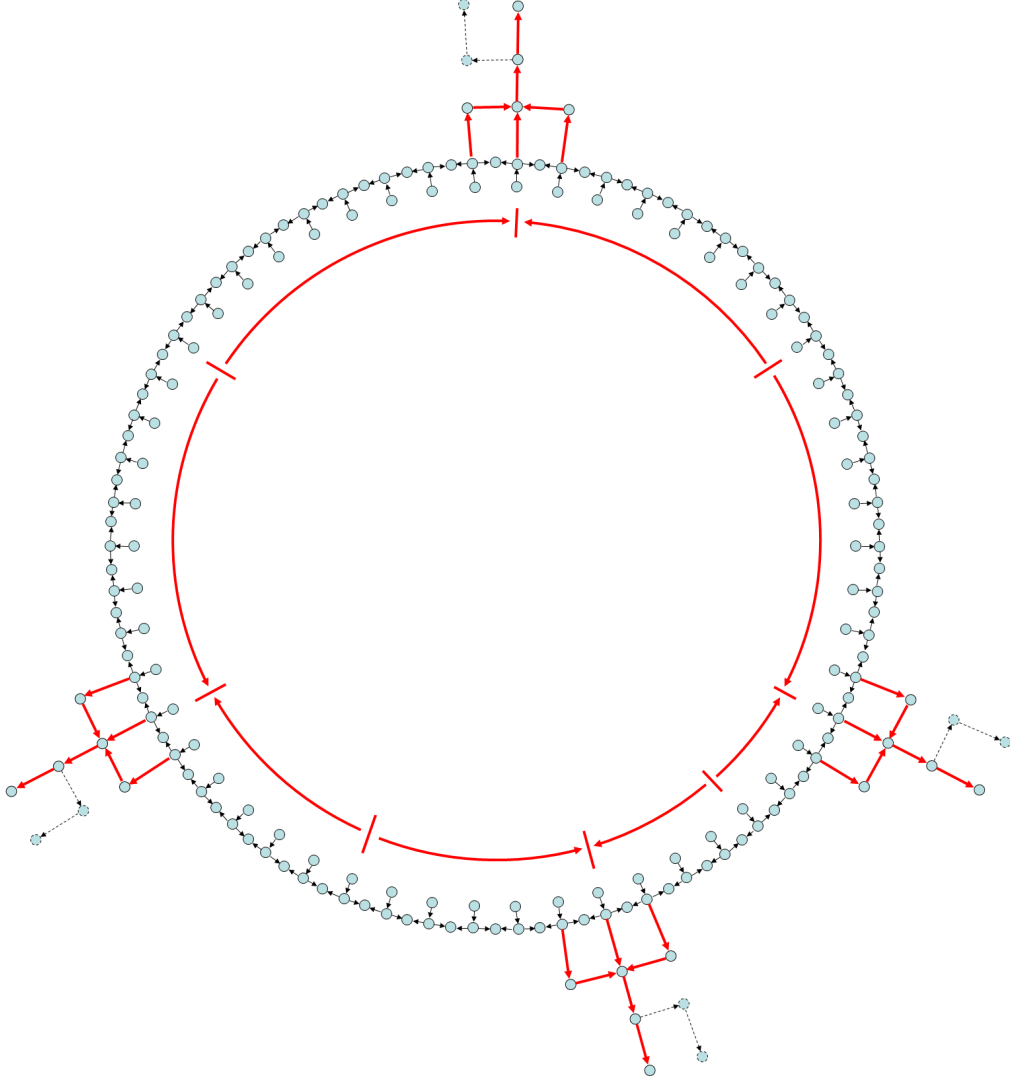
Figure 4.5: Network 4.2.2 - Schematic representation of the simulated network with the actual flow direction in the viscous regime.
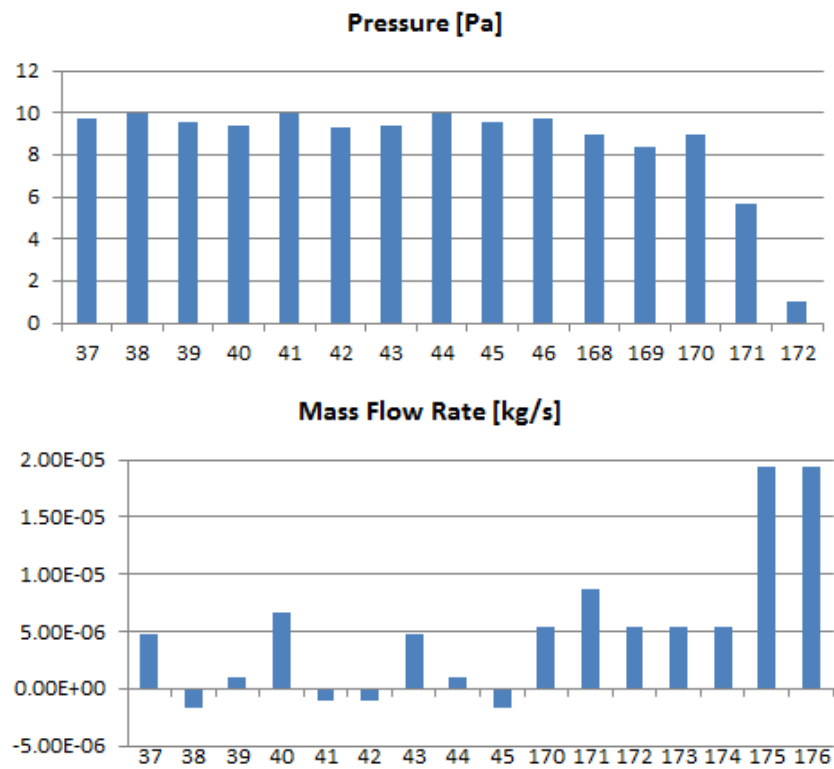
Figure 4.6: Network 4.2.2 - Pressure values at the nodes (up) and mass flow rates at each tube (down) of the network's duct in the viscous regime.
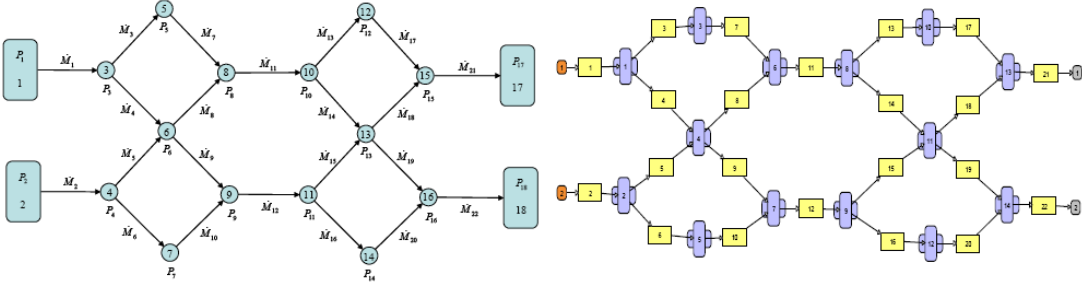
Figure 4.7: Network 4.2.3 - ITERVAC sample network schematic representation
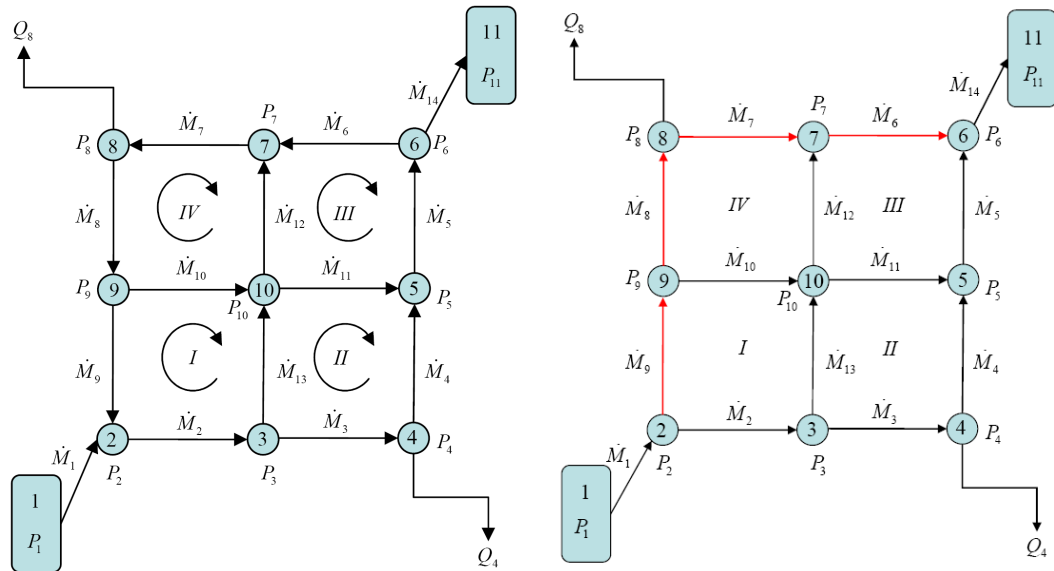
Figure 4.8: Network 4.3/4.4 - Schematic representation of pipe network showing a) the initially assumed flow directions (left) and b) the flow directions derived after the completion of the code (right).
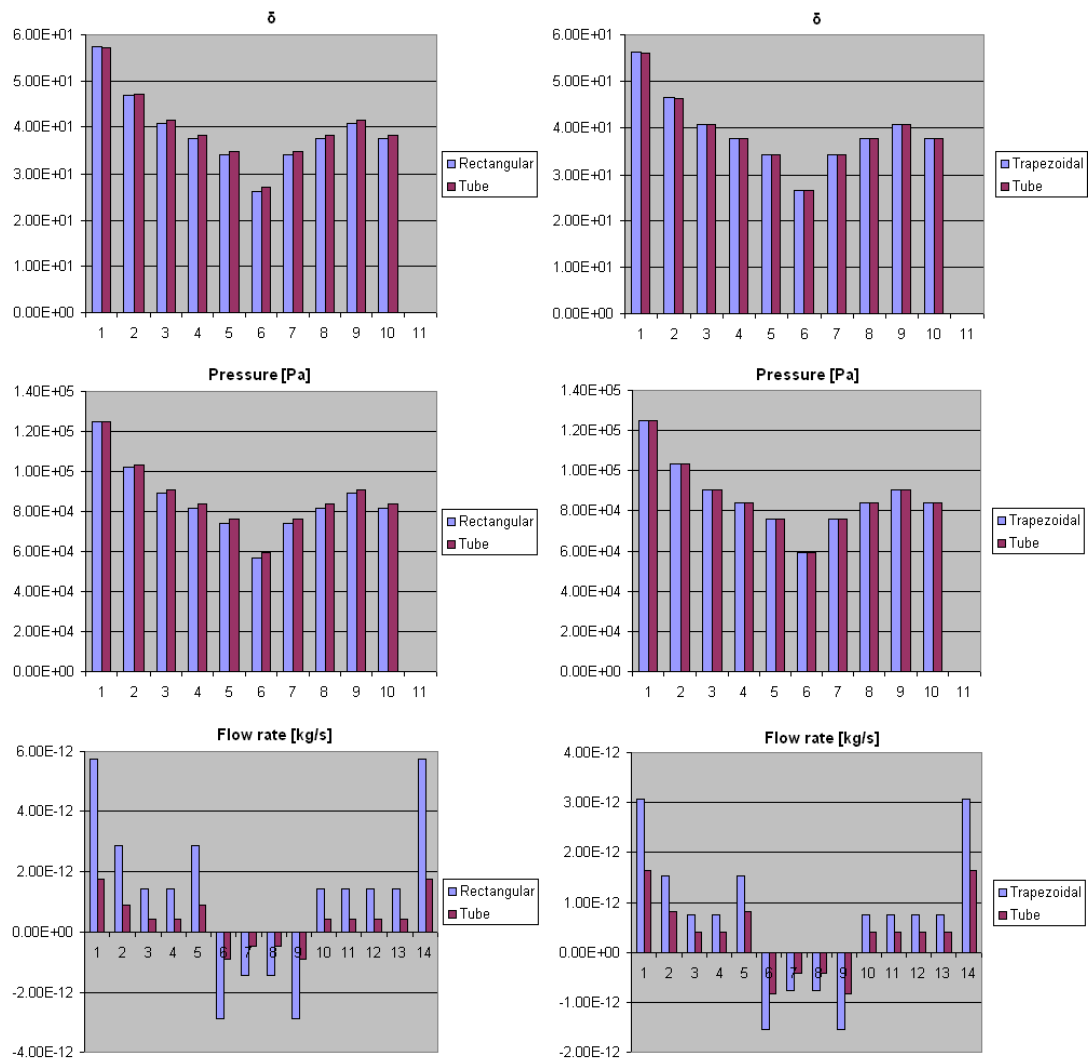
Figure 4.9: Network 4.3 - Rarefaction parameter (top), pressure heads (middle) and flow rates (bottom) for a network consisting of rectangular (left) and trapezoidal (right) channels. The corresponding results with the hydraulic diameter concept are also shown.
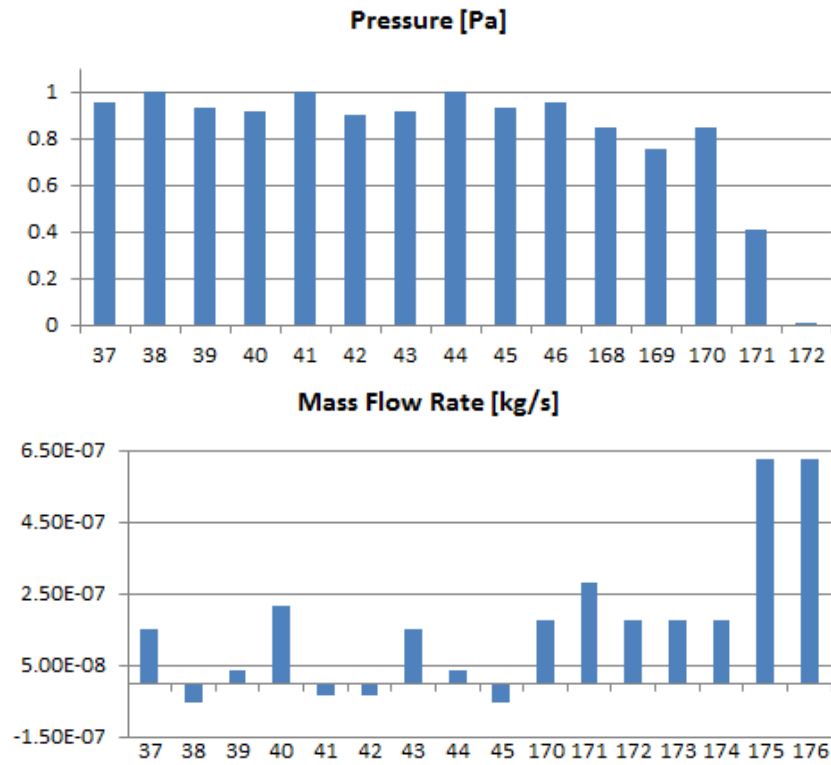
Figure 4.10: Network 4.5.2 - Pressure values at the nodes (left) and mass flow rates at each tube (right) of the network's duct in all regimes.

5

Extension to gas distribution systems consisting of piping elements of any diameter and length

5.1 Flow characteristics in distribution systems consisting of piping elements with L/D<5

Apart from the cases where the channel network consists of long piping elements, the characteristics of which have been described in the previous chapter, the analysis is extended into networks consisting of piping elements of arbitrary length, diameter and cross sections. In this latter case, the vertical component of the velocity vector in not equal to zero and the values of density may vary along the piping element. The presence of short piping elements in a channel network, even when the flow may be described as linear, or even in scenarios where the channel end effects play a major role, affects the overall flow characteristics of the network which are, as a result, described in more than one dimensions. This analysis is presented and benchmarked in the present chapter through various test cases covering the whole range of rarefaction.

5.2 Benchmarking in networks consisting of short circular pipes

Extensive comparisons between the ARIADNE and ITERVAC have been performed covering a wide range of simulating scenarios with respect to the geometrical characteristics, the conveying gas and the complexity. Two different networks have been simulated, named as Network 5.2.1 and 5.2.2, respectively.

5.2.1 Network of minimum complexity in a wide range of rarefaction - A simplified chess-board network

The sample network 5.2.1 consists of 14 elements, 9 junction nodes and 2 nodes where the pressure is fixed. In Figure 5.1, the schematic representation of the simulated network is shown. All elements have the same length and diameter, which are equal to 0.25 m and 0.1 m respectively, resulting to an $L/D_h < 5$ and therefore the kinetic analysis is based on the non-linear theory for short channels. The gas selected for filling the hypothetical network is helium held at 410 K. In the simulation performed, the left reservoir is held in $P_1 = 5$ Pa, while the right reservoir has a fixed pressure of $P_{11} = 10^{-3}$ Pa. The selected pressure values result to Knudsen numbers covering the free molecular and early transition regimes.

The comparison between the algorithms with respect to the pressure at each node of the network is shown in Table 5.1, while for the mass flow rate along each tube is presented in Table 5.2. In general, there is a very good agreement in both the pressure values and the mass flow rates, with the corresponding deviation between the two approaches not exceeding the value of 5.6% for the pressures and 5.4% for the mass flow rates.

5.2.2 Network of small complexity in a wide range of rarefaction - A chess-board network

By increasing the complexity of the network, the sample network 5.2.2 shown in Figure 5.2 is simulated. The network consists of 42 elements, 25 junction nodes and 2 nodes where the pressure is fixed. Since the aim of this comparison is to increase

156

the complexity of the network, i.e. increasing the number of elements and nodes, all elements have the same length and diameter, equal to the ones used in sample network 5.2.1 (L=0.25 m and D_h=0.1 m). For this purpose, all other parameters are identical to the ones of sample network A. Therefore, the conveying gas is helium at 410K and the pressure values at the fixed grade nodes are $P_1 = 5$ Pa and $P_{27} = 10^{-3}$ Pa, respectively.

Once again, very good agreement in both the pressure values and the mass flow rates, is observed. The comparison between the algorithms with respect to the pressure at each node of the network is shown in Table 5.3, while for the mass flow rate along each tube is presented in Table 5.4. Despite the increase of the network complexity, the corresponding deviation between the two approaches is not exceeding the value of 4.8% for the pressure heads and 5% for the mass flow rates. It is noted that these values which are smaller compared to the ones of sample network 5.2.1 which is of smaller complexity.

5.3 Extension to networks consisting of tubes of any diameter and length - A Tree network

The network simulated in this section has the topological characteristics of the network shown in Figure 5.3 which is characterized by piping elements, whose specific geometrical characteristics, are different to each other. In this manner, the solver's applicability is generalized in networks consisting of elements of various lengths and diameters simulating simultaneously channels with big, average and small ratio of L/D.

The simulated network, named as "Network 5.3", consists of $p = 29$ tubes, $n = 20$ internal nodes, $f = 4$ fixed-grade nodes and $l = 6$ loops. Nodes {1, 9, 23 and 24} refer to four fixed grade nodes, where the pressure is held constant. For the present network under investigation, the reference temperature is set to $T_0 = 293.7$K. The conveying gas is air, with molar mass $m = 0.028319$ kg/mol, gas constant $R = 286.9$ J/(kg·K), most probable molecular velocity $v_0 = 410.59$ m/s and viscosity $\mu = 18.370$ μPa·s.

The geometrical characteristics of each piping element are shown in Table 5.5.

The system of governing equations includes nine mass conservation equations at the internal nodes, six energy balance equations along the closed loops and two energy balance equation along the open pseudo-loops. The total number of equations of the system is 29 and its solution returns the 29 unknown mass flow rates $\{\dot{M}_1, ..., \dot{M}_{29}\}$. Then, from the pressure drop equations, the pressure heads $\{P_2, ..., P_{23}\}$ are found.

For the simulation performed, the pressures at the three reservoirs are fixed to $P_1 = 0.4$ Pa, $P_9 = 0.01$ Pa, $P_{23} = 0.1$ Pa and $P_{24} = 0.1$ Pa, respectively. Even more an external demand is present at node 22 equal to $1E - 06$kg/s. The results are shown in Table 5.6 for the rarefaction parameter and the pressure heads [Pa] and in Table 5.7 for the mass flow rates [kg/s].

5.4 Modeling of neutral gas flow in the ITER divertor pumping system

In the present section the latest design of the ITER divertor pumping system is discussed. The drawings referring to the 2012 design have been delivered to UoThly in October 2012. The schematic representation of the cryopump positions is shown in Figure 5.4. As it is seen, ports $\{4, 6, 10, 12, 16, 18\}$ are fitted with cryo-pumps.

By further analyzing the CATIA schematics and the detailed geometrical characteristics of the divertor region, Figures 5.5 and 5.6, an interpretation of the flow path *i)* inside the divertor and *ii)* of the lower port region into a set of channels has been performed. The channels, consisting of various lengths and cross sections, are interconnected in a predefined manner so as to form a network estimating the actual flow path.

The analysis is based on the assumption that each of the 54 cassettes is identical to each other. Based on this assumption, the flow path inside the region of the divertor is simulated by 28 channels, the locations of which are shown in Figure 5.7, as far as the radial gas flow is concerned. Similar analysis has been implemented for the simulation of the gas flow path formed between the divertor and the lower port regions as it is shown by the assembly picture in Figure 5.8, resulting to a channel network consisting of 12 channels, which are interconnected with the network of the divertor path in a predefined configuration. The vacuum ducts are simulated by a

158

network of 6 channels, directly linked to the network formed by the 54 cassettes. In 6 out of the 54 cassettes and more specifically cassettes 11, 17, 29, 35, 47 and 53, corresponding to the lower ports 4, 6, 10, 12, 16 and 18 are connected to the six cryopumps. A schematic representation of all 6 pumping ducts connected to the divertor ring is shown in Figure 5.9.

In order to simulate the toroidal flow of the gas, the interconnection of each of the 54 cassettes to each other had to be defined. For this reason, in the already described networks for the radial flow, some extra nodes had to be added in order for the connections to be simulated. As a result, elements {2, 4, 5, 7, 9, 17, 19, 21, 22, 24, 25 and 26} of Figure 5.7, as well as elements {2, 4, 5, 6, 8, 9} of Figure 5.8 are cut in half in order to host these connections. All of these 12+6=18 channels have various diameters but same length equal to 20 mm to simulate the distance between the cassettes. As far as the connection between the cassettes and the pumps is concerned, this is achieved by directly linking 1 cassette with 1 pump by 8 additional piping elements representing the geometrical characteristics of the pumping ducts.

A representation of the resulting network, approximating the actual gas flow path along the cassette cross-section, is shown in Figure 5.10. The channel flow configurations of the upper and lower parts of the cassette are approximated by 40 and 17 channels of various lengths and diameters, respectively. The upper part, interpreting the radial flow inside the divertor, consists of nodes 1 to 41, shown in light blue color.

The radial flow in the divertor lower part is described by nodes 42 to 60, shown in yellow. These two regions are interconnected with one main piping element resulting to a total of 59 channels and 60 nodes per cassette. The 8+1 nodes {1, 13, 18, 21, 28, 41, 59, 60} and {66}, where the pressure must be specified, shown in dark blue, are provided. Through these 8 nodes the pipe network representing the flow along a cassette is open to the torus.

Even more, the 12 nodes {3, 6, 8, 11, 15, 23, 26, 29, 31, 34, 36, 38} for the divertor path and 6 nodes {43, 46, 48, 50, 53, 55} for the lower region path, shown in red, represent the position where the connections for the simulation of the toroidal flow are located.

Finally, for the case where the cassette is directly linked to one of the 6 cryopump ducts, shown in grey, the pumping duct network consisting of 6 nodes {61, 62, 63, 64, 65, 66} and 8 pipes used to approximate the gas flow is also shown in Figure

[5.10](). The resulting geometric characteristics of the piping elements implemented for the the simulation of the flow though the divertor and lower port regions are shown in Table [5.8]().

In an attempt to study the flow inside the divertor and the lower part region, the case of one cassette directly linked to a cryopump is taken into consideration. Based on this, 3 different operational scenarios, in collaboration with KIT, have been simulated, two of which employing deuterium (D_2, m=4.0282 gr/mol, μ=15.90 μPa·s) as conveying gas held at 420 K and a third one with helium (He, m=4.0026 gr/mol, μ=25.09 μPa·s), held at the same temperature. The different scenarios are employed by introducing predefined pressure values into the fixed grade nodes of the network, i.e. nodes {1, 13, 18, 21, 28, 41, 59, 60 and 66}.

The input parameters for ARIADNE have been obtained from the B2-EIRENE output including particle flux densities, temperatures and pressures of deuterium and helium atoms and deuterium molecules, respectively [110]. One output from B2-Eirene is a pressure profile along the inner target, the under dome region and along the outer target. The conversion of this pressure profile into input pressure values from the locations described in Figure [5.11]() in the aforementioned nodes for the three simulated scenarios are described in Table [5.9](). Based on these data, the local gas rarefaction in the network varies in a wide range of the Knudsen number from the free molecular limit through the transition up to the slip regime.

Indicative results for the flow through one cassette directly connected to one pump during the 3 scenarios studied are shown in Tables [5.10]() and [5.11]() for Scenario A, Tables [5.12]() and [5.13]() for Scenario B and Tables [5.14]() and [5.15]() for Scenario C, respectively.

In Figures [5.12]() - [5.14](), the gas flow path in the cross-section along a cassette is shown for all 3 operational scenarios. This flow pattern is qualitatively the same in all three pressure scenarios investigated. The gas enters the cassette from the fixed pressure nodes at the dome and the inner and the outer slots, defined by the nodes {13, 18, 21, 28 and 41}, respectively. One part of the gas remains in the upper part of the cassette and flows in opposite directions returning finally back into the plasma from the inner and outer divertor arm gaps, nodes 1 and 41, respectively. Another part of the gas reaches the lower part of the cassette and then is separated with (depending on the scenario under consideration) one fraction flowing towards the cryopump and the remaining one returning to the plasma via the outer and inner

160

divertor arm gaps defined by nodes 59 and 60.

The flow back into the vacuum vessel is also observed in Figures 5.12 - 5.14 and is known as back-flow and has been also observed in previous studies [38, 46, 47]. Since the cassette is directly linked to the vacuum pump, the main part of the of the gas throughput entering the divertor is pumped towards the pumping port, while the remaining amount is flowing back into the plasma. The corresponding percentages vary from 87% to 90% for all scenarios simulated.

Concerning the percentage break down of the throughput entering the divertor it is noted that, from about 86%, 70% and 95% is entering from the dome area, nodes 19 and 21 for operational Scenarios A, B and C respectively.

5.5 Concluding remarks

A software tool for modeling and simulation of complex gas distribution systems operating under any vacuum conditions is presented and validated. The code architecture and structure are similar to the ones applied in the design and optimization of typical gas pipe networks in the viscous regime, supplemented however, with a robust kinetic data base to provide the required flow rates in the whole range of the Knudsen number depending on the geometrical and operational data of the network.

The present, more advanced and generalized, algorithm includes the kinetic data base required to take into account flow rates through channels of any length. Validation of the updated software is provided by comparison with the corresponding result provided by ITERVAC for various pressure values and geometrical characteristics for the networks under consideration.

Furthermore, the feasibility and effectiveness of the presented algorithm in simulating large size gas networks of arbitrary complexity is demonstrated by modeling the flow through a cassette of the 2012 ITER torus primary pumping system. Results of the flow patterns and paths along the cassette for various dome pressures are provided.

It is believed that the presented algorithm has a lot of potential in supporting future design work in large vacuum systems of fusion machines and particle accelerators.

Table 5.1: Network 5.2.1 - Pressure and Knudsen number at each node of the network for high values of Kn number – comparison with ITERVAC.

Node number	Kn	ARIADNE Pressure [Pa]	ITERVAC Pressure [Pa]
1	1.83×10^{-2}	5.00	5.00
2	2.32×10^{-2}	3.96	4.05
3	2.72×10^{-2}	3.38	3.51
4	2.98×10^{-2}	3.08	3.23
5	3.33×10^{-2}	2.76	2.93
6	4.53×10^{-2}	2.03	2.28
7	3.33×10^{-2}	2.76	2.93
8	2.98×10^{-2}	3.08	3.23
9	2.72×10^{-2}	3.38	3.51
10	2.98×10^{-2}	3.08	3.23
11	9.19×10^{1}	1.00×10^{-3}	1.00×10^{-3}

Table 5.2: Network 5.2.1 - Mass flow rate and conductance at each tube of the network for high values of Kn number – comparison with ITERVAC.

Tube # [j]	From node to node	ARIADNE $\dot{M}_j$ [kg/s]	ITERVAC $\dot{M}_j$ [kg/s]
1	1-2	2.69×10^{-6}	2.55×10^{-6}
2	2-3	1.34×10^{-6}	1.27×10^{-6}
3	3-4	6.73×10^{-7}	6.36×10^{-7}
4	4-5	6.73×10^{-7}	6.36×10^{-7}
5	5-6	1.34×10^{-6}	1.27×10^{-6}
6	6-7	-1.34×10^{-6}	-1.27×10^{-6}
7	7-8	-6.73×10^{-7}	-6.36×10^{-7}
8	8-9	-6.73×10^{-7}	-6.36×10^{-7}
9	9-2	-1.34×10^{-6}	-1.27×10^{-6}
10	9-10	6.73×10^{-7}	6.36×10^{-7}
11	10-5	6.73×10^{-7}	6.36×10^{-7}
12	10-7	6.73×10^{-7}	6.36×10^{-7}
13	3-10	6.73×10^{-7}	6.36×10^{-7}
14	6-11	2.69×10^{-6}	2.55×10^{-6}

Table 5.3: Network 5.2.2 - Pressure and Knudsen number at each node of the network for high values of Kn number – comparison with ITERVAC.

Node number	Kn	ARIADNE Pressure [Pa]	ITERVAC Pressure [Pa]
1	1.83×10^{-2}	5.00	5.00
2	2.22×10^{-2}	4.13	4.19
3	2.51×10^{-2}	3.65	3.75
4	2.73×10^{-2}	3.36	3.47
5	2.90×10^{-2}	3.17	3.30
6	2.98×10^{-2}	3.08	3.21
7	3.08×10^{-2}	2.98	3.12
8	3.30×10^{-2}	2.78	2.93
9	3.78×10^{-2}	2.43	2.61
10	5.16×10^{-2}	1.78	2.02
11	3.78×10^{-2}	2.43	2.61
12	3.30×10^{-2}	2.78	2.93
13	3.08×10^{-2}	2.98	3.12
14	2.98×10^{-2}	3.08	3.21
15	2.90×10^{-2}	3.17	3.30
16	2.73×10^{-2}	3.36	3.47
17	2.51×10^{-2}	3.65	3.75
18	2.66×10^{-2}	3.45	3.56
19	2.83×10^{-2}	3.24	3.37
20	2.98×10^{-2}	3.08	3.21
21	3.17×10^{-2}	2.90	3.05
22	3.44×10^{-2}	2.67	2.83
23	3.17×10^{-2}	2.90	3.05
24	2.98×10^{-2}	3.08	3.21
25	2.83×10^{-2}	3.24	3.37
26	2.98×10^{-2}	3.08	3.21
27	9.19×10^{1}	1.00×10^{-3}	1.00×10^{-3}

Table 5.4: Network 5.2.2 - Mass flow rate and conductance at each tube of the network in the viscous regime – comparison with ITERVAC.

Tube # [j]	From node to node	ITERVAC $\dot{M}_j$ [kg/s]	Tube number	From node to node	ARIADNE $\dot{M}_j$ [kg/s]	ITERVAC $\dot{M}_j$ [kg/s]
1	1-2	2.29×10^{-6}	22	3-18	4.69×10^{-7}	4.46×10^{-7}
2	2-3	1.14×10^{-6}	23	19-4	-2.61×10^{-7}	-2.47×10^{-7}
3	3-4	6.79×10^{-7}	24	20-5	-2.09×10^{-7}	-1.98×10^{-7}
4	4-5	4.18×10^{-7}	25	18-25	4.69×10^{-7}	4.46×10^{-7}
5	5-6	2.08×10^{-7}	26	19-26	3.65×10^{-7}	3.47×10^{-7}
6	6-7	2.08×10^{-7}	27	20-21	3.66×10^{-7}	3.47×10^{-7}
7	7-8	4.17×10^{-7}	28	16-25	2.61×10^{-7}	2.47×10^{-7}
8	8-9	6.75×10^{-7}	29	25-26	3.65×10^{-7}	3.47×10^{-7}
9	9-10	1.14×10^{-6}	30	21-26	-3.65×10^{-7}	-3.47×10^{-7}
10	10-11	-1.14×10^{-6}	31	8-21	-2.58×10^{-7}	-2.47×10^{-7}
11	11-12	-6.75×10^{-7}	32	24-25	-3.65×10^{-7}	-3.47×10^{-7}
12	12-13	-4.17×10^{-7}	33	23-26	-3.65×10^{-7}	-3.47×10^{-7}
13	13-14	-2.08×10^{-7}	34	21-22	4.73×10^{-7}	4.46×10^{-7}
14	14-15	-2.08×10^{-7}	35	15-24	2.09×10^{-7}	1.98×10^{-7}
15	15-16	-4.18×10^{-7}	36	23-24	-3.66×10^{-7}	-3.47×10^{-7}
16	16-17	-6.79×10^{-7}	37	22-23	-4.73×10^{-7}	-4.46×10^{-7}
17	17-2	-1.14×10^{-6}	38	22-9	4.73×10^{-7}	4.46×10^{-7}
18	17-18	4.69×10^{-7}	39	13-24	-2.08×10^{-7}	-1.98×10^{-7}
19	18-19	4.69×10^{-7}	40	12-23	-2.58×10^{-7}	-2.47×10^{-7}
20	20-19	-3.65×10^{-7}	41	11-22	-4.73×10^{-7}	-4.46×10^{-7}
21	7-20	-2.08×10^{-7}	42	10-27	2.29×10^{-6}	2.18×10^{-6}

The middle column values (ITERVAC $\dot{M}_j$ [kg/s]) for tubes 1–21:

Tube #	ITERVAC $\dot{M}_j$ [kg/s]
1	2.18×10^{-6}
2	1.09×10^{-6}
3	6.44×10^{-7}
4	3.96×10^{-7}
5	1.98×10^{-7}
6	1.98×10^{-7}
7	3.96×10^{-7}
8	6.44×10^{-7}
9	1.09×10^{-6}
10	-1.09×10^{-6}
11	-6.44×10^{-7}
12	-3.96×10^{-7}
13	-1.98×10^{-7}
14	-1.98×10^{-7}
15	-3.96×10^{-7}
16	-6.44×10^{-7}
17	-1.09×10^{-6}
18	4.46×10^{-7}
19	4.46×10^{-7}
20	-3.47×10^{-7}
21	-1.98×10^{-7}

165

Table 5.5: Network 5.3 - Geometrical characteristics of each piping element.

	1	2	3	4	5	6	7	8	9	10
$L[m]$	2.5	2.5	1	0.5	2	2	3	4	6	4
$D_h[m]$	0.5	0.5	0.4	0.5	0.4	0.5	0.8	0.9	0.4	0.9

	11	12	13	14	15	16	17	18	19	20
$L[m]$	3	6	7	6	7	3	8	10	1	1
$D_h[m]$	0.8	0.6	0.6	0.4	0.5	0.8	0.6	0.5	0.4	0.4

	21	22	23	24	25	26	27	28	29
$L[m]$	1	2.5	4	3	3	4	3	2.5	5
$D_h[m]$	0.4	0.5	0.9	0.8	0.8	0.9	0.6	0.5	0.4

166

Table 5.6: Network 5.3 - Pressure and Knudsen number at each node of the network in the viscous regime.

Node number	Kn	Pressure [Pa]
1	3.34×10^{-2}	4.00×10^{-1}
2	3.78×10^{-2}	3.53×10^{-1}
3	4.75×10^{-2}	3.02×10^{-1}
4	5.58×10^{-2}	2.66×10^{-1}
5	5.81×10^{-2}	2.55×10^{-1}
6	6.46×10^{-2}	1.83×10^{-1}
7	4.79×10^{-2}	1.64×10^{-1}
8	5.90×10^{-2}	1.62×10^{-1}
9	1.67×10^{0}	1.00×10^{-2}
10	5.71×10^{-2}	1.67×10^{-1}
11	6.02×10^{-2}	1.64×10^{-1}
12	7.56×10^{-2}	1.59×10^{-1}
13	6.32×10^{-2}	1.76×10^{-1}
14	9.63×10^{-2}	1.46×10^{-1}
15	1.21×10^{-1}	1.38×10^{-1}
16	1.20×10^{-1}	1.29×10^{-1}
17	3.69×10^{-2}	2.13×10^{-1}
18	4.25×10^{-2}	2.14×10^{-1}
19	3.72×10^{-2}	2.11×10^{-1}
20	4.15×10^{-2}	2.10×10^{-1}
21	6.94×10^{-2}	1.93×10^{-1}
22	7.28×10^{-2}	1.84×10^{-1}
23	1.67×10^{-1}	1.00×10^{-1}
24	1.34×10^{-1}	1.00×10^{-1}

Table 5.7: Network 5.3 - Mass flow rate and conductance at each tube of the network in the viscous regime.

Tube # [j]	From node to node	$\dot{M}_j$ [kg/s]	C_j [lt/s]	Tube number	From node to node	$\dot{M}_j$ [kg/s]	C_j [lt/s]
1	1-2	8.21×10^{-6}	1.52×10^{4}	16	6-13	2.97×10^{-6}	4.10×10^{4}
2	2-3	8.21×10^{-6}	1.37×10^{4}	17	13-14	1.99×10^{-6}	5.69×10^{3}
3	3-4	4.98×10^{-6}	1.22×10^{4}	18	3-18	3.23×10^{-6}	3.20×10^{3}
4	4-5	4.98×10^{-6}	3.92×10^{4}	19	14-15	8.22×10^{-7}	8.29×10^{3}
5	5-6	4.98×10^{-6}	5.89×10^{3}	20	14-16	1.66×10^{-6}	8.25×10^{3}
6	6-10	2.01×10^{-6}	1.12×10^{4}	21	15-16	8.22×10^{-7}	8.07×10^{3}
7	10-7	1.30×10^{-6}	3.89×10^{4}	22	16-24	2.48×10^{-6}	7.42×10^{3}
8	7-8	1.30×10^{-6}	4.56×10^{4}	23	17-18	-8.79×10^{-7}	5.53×10^{4}
9	8-9	2.50×10^{-6}	1.42×10^{3}	24	19-17	-8.79×10^{-7}	4.62×10^{4}
10	10-11	1.42×10^{-6}	4.61×10^{4}	25	20-18	-2.35×10^{-6}	4.61×10^{4}
11	11-8	1.20×10^{-6}	3.85×10^{4}	26	19-20	8.79×10^{-7}	5.47×10^{4}
12	11-12	4.87×10^{-7}	7.48×10^{3}	27	20-21	3.23×10^{-6}	1.61×10^{4}
13	13-10	7.19×10^{-7}	6.70×10^{3}	28	22-21	-1.00×10^{-6}	9.59×10^{3}
14	13-11	2.59×10^{-7}	1.88×10^{3}	29	21-23	2.23×10^{-6}	2.08×10^{3}
15	12-14	4.87×10^{-7}	3.31×10^{3}				

168

Table 5.8: Geometric characteristics of the piping elements implemented for the the simulation of the flow though the divertor

Tube # [j]	From node to node	Length [m]	D_h [m]	Tube # [j]	From node to node	Length [m]	D_h [m]
1	1-2	0.1075	0.1830	36	36-35	0.0786	0.2236
2	2-3	0.1875	0.1831	37	37-36	0.0786	0.2236
3	3-4	0.1875	0.1831	38	38-37	0.0579	0.0575
4	4-5	0.1214	0.0579	39	39-38	0.0579	0.0575
5	5-6	0.1276	0.1817	40	40-39	0.2135	0.1907
6	6-7	0.1276	0.1817	41	41-40	0.1015	0.0478
7	7-8	0.2598	0.2693	42	60-42	0.2589	0.1274
8	8-9	0.2598	0.2693	43	42-43	0.1875	0.1831
9	9-10	0.1691	0.0816	44	43-44	0.1875	0.1831
10	10-11	0.2000	0.1962	45	44-45	0.3750	0.1831
11	11-48	0.2000	0.1962	46	45-46	0.1276	0.1817
12	12-11	0.2000	0.1962	47	47-46	0.1276	0.1817
13	14-12	0.0942	0.1461	48	48-47	0.2598	0.2693
14	13-14	0.0482	0.0087	49	49-48	0.2598	0.2693
15	15-14	0.1455	0.1461	50	50-49	0.1875	0.1831
16	16-15	0.1455	0.1461	51	51-50	0.1875	0.1831
17	17-16	0.1455	0.1990	52	52-51	0.4000	0.1962
18	23-17	0.5217	0.2784	53	53-52	0.0471	0.0487
19	18-19	0.2410	0.3645	54	54-53	0.0471	0.0487
20	19-20	0.1646	0.2935	55	55-54	0.1456	0.1461
21	21-22	0.2359	0.3000	56	56-55	0.1456	0.1461
22	22-20	0.1646	0.2935	57	57-56	0.0482	0.0087
23	20-23	0.1519	0.2704	58	58-57	0.3750	0.1831
24	24-23	0.5217	0.2784	59	59-58	0.2410	0.3645
25	25-24	0.1652	0.1098	60	43-61	0.4885	0.8215
26	26-25	0.1137	0.1358	61	46-61	0.9770	0.7361
27	27-26	0.1137	0.1358	62	48-61	1.9540	0.6238
28	28-27	0.1042	0.0210	63	61-62	1.0163	1.1125
29	29-27	0.0589	0.0732	64	62-63	1.4768	1.1125
30	30-29	0.0589	0.0732	65	63-64	0.7050	2.2836
31	31-30	0.1231	0.2026	66	64-65	0.7050	2.6974
32	32-31	0.1231	0.2026	67	65-66	0.4000	1.4700
33	33-32	0.1804	0.0929				
34	34-33	0.1408	0.2587				
35	35-34	0.1408	0.2587				

Table 5.9: Pressure values at predefined positions for each of the 54 cassettes and the four pumps for the 3 proposed operational scenarios.

Gas	Scenario A D_2	Scenario B He	Scenario C D_2
$P_1(Pa)$	8.250×10^{-4}	7.740×10^{-4}	8.120×10^{-4}
$P_2(Pa)$	3.650	3.890×10^{-2}	1.500×10^1
$P_3(Pa)$	1.852	2.848×10^{-2}	7.819
$P_4(Pa)$	1.852	2.848×10^{-2}	7.819
$P_5(Pa)$	1.040×10^1	2.770×10^{-1}	2.360×10^1
$P_6(Pa)$	6.760×10^{-5}	7.010×10^{-6}	8.820×10^{-4}
$P_7(Pa)$	6.760×10^{-5}	7.010×10^{-6}	8.820×10^{-4}
$P_{pump}(Pa)$	1.000×10^{-6}	1.000×10^{-6}	1.000×10^{-6}

Table 5.10: Network 5.4.1 - Pressure and Knudsen number at each node of the network simulating the flow through the divertor and lower port regions - Scenario A.

Node number	Kn	Pressure [Pa]	Node number	Kn	Pressure [Pa]
1	1.449×10^2	8.250×10^{-4}	36	5.742×10^{-2}	1.445
2	7.924×10^0	1.279×10^{-2}	37	9.170×10^{-2}	1.440
3	3.682	2.752×10^{-2}	38	2.783×10^{-1}	1.159
4	3.667	4.198×10^{-2}	39	1.748×10^{-1}	8.554×10^{-1}
5	6.079×10^{-1}	2.547×10^{-1}	40	1.863×10^{-1}	8.353×10^{-1}
6	3.860×10^{-1}	2.645×10^{-1}	41	5.739×10^3	6.760×10^{-5}
7	3.001×10^{-1}	2.742×10^{-1}	42	5.428×10^0	2.202×10^{-2}
8	2.472×10^{-1}	2.788×10^{-1}	43	1.619×10^0	2.894×10^{-2}
9	3.732×10^{-1}	2.834×10^{-1}	44	3.397×10^0	2.983×10^{-2}
10	3.508×10^{-1}	3.807×10^{-1}	45	3.266×10^0	3.114×10^{-2}
11	2.427×10^{-1}	3.896×10^{-1}	46	1.587×10^0	3.191×10^{-2}
12	1.710×10^{-1}	6.341×10^{-1}	47	1.197×10^0	6.876×10^{-2}
13	5.843×10^{-1}	3.650	48	6.305×10^{-1}	8.665×10^{-2}
14	1.919×10^{-1}	9.640×10^{-1}	49	9.470×10^{-1}	8.662×10^{-2}
15	9.699×10^{-2}	1.310	50	1.171×10^0	8.657×10^{-2}
16	6.678×10^{-2}	1.611	51	1.131×10^0	8.651×10^{-2}
17	4.532×10^{-2}	1.715	52	1.753×10^0	8.644×10^{-2}
18	2.748×10^{-2}	1.852	53	4.453×10^0	8.562×10^{-2}
19	3.061×10^{-2}	1.842	54	2.247×10^0	8.479×10^{-2}
20	3.555×10^{-2}	1.826	55	1.500×10^0	8.470×10^{-2}
21	3.339×10^{-2}	1.852	56	2.833×10^0	8.462×10^{-2}
22	3.401×10^{-2}	1.838	57	1.140×10^3	1.697×10^{-4}
23	3.759×10^{-2}	1.790	58	8.418×10^2	8.050×10^{-5}
24	5.329×10^{-2}	1.794	59	7.530×10^2	6.760×10^{-5}
25	8.259×10^{-2}	1.830	60	2.082×10^2	8.250×10^{-4}
26	7.412×10^{-2}	1.844	61	7.730×10^{-1}	2.915×10^{-2}
27	1.303×10^{-1}	1.858	62	8.499×10^{-1}	1.962×10^{-2}
28	8.492×10^{-2}	1.040×10^1	63	1.521×10^0	7.184×10^{-3}
29	1.461×10^{-1}	1.734	64	1.354×10^0	5.504×10^{-3}
30	8.374×10^{-2}	1.607	65	2.056×10^0	4.330×10^{-3}
31	5.731×10^{-2}	1.598	66	1.262×10^4	1.000×10^{-6}
32	7.901×10^{-2}	1.590			
33	7.227×10^{-2}	1.460			
34	4.926×10^{-2}	1.456			
35	5.302×10^{-2}	1.451			

Table 5.11: Network 5.4.1 - Mass flow rate values for each piping element the network simulating the flow through the divertor and lower port regions - Scenario A.

Tube # [j]	From node to node	$\dot{M}_j$ [kg/s]	Tube number	From node to node	$\dot{M}_j$ [kg/s]
1	1-2	-8.682×10^{-8}	36	36-35	-2.399×10^{-7}
2	2-3	-8.682×10^{-8}	37	37-36	-2.399×10^{-7}
3	3-4	-8.682×10^{-8}	38	38-37	-2.399×10^{-7}
4	4-5	-8.682×10^{-8}	39	39-38	-2.399×10^{-7}
5	5-6	-8.682×10^{-8}	40	40-39	-2.399×10^{-7}
6	6-7	-8.682×10^{-8}	41	41-40	-2.399×10^{-7}
7	7-8	-8.682×10^{-8}	42	60-42	-4.111×10^{-8}
8	8-9	-8.682×10^{-8}	43	42-43	-4.111×10^{-8}
9	9-10	-8.682×10^{-8}	44	43-44	-5.323×10^{-9}
10	10-11	-8.682×10^{-8}	45	44-45	-5.323×10^{-9}
11	11-48	2.573×10^{-6}	46	45-46	-5.323×10^{-9}
12	12-11	2.660×10^{-6}	47	47-46	2.620×10^{-7}
13	14-12	2.660×10^{-6}	48	48-47	2.620×10^{-7}
14	13-14	1.253×10^{-8}	49	49-48	-3.533×10^{-10}
15	15-14	2.648×10^{-6}	50	50-49	-3.533×10^{-10}
16	16-15	2.648×10^{-6}	51	51-50	-3.533×10^{-10}
17	17-16	2.648×10^{-6}	52	52-51	-3.533×10^{-10}
18	23-17	2.648×10^{-6}	53	53-52	-3.533×10^{-10}
19	18-19	1.432×10^{-6}	54	54-53	-3.533×10^{-10}
20	19-20	1.432×10^{-6}	55	55-54	-3.533×10^{-10}
21	21-22	1.087×10^{-6}	56	56-55	-3.533×10^{-10}
22	22-20	1.087×10^{-6}	57	57-56	-3.533×10^{-10}
23	20-23	2.519×10^{-6}	58	58-57	-3.533×10^{-10}
24	24-23	1.287×10^{-7}	59	59-58	-3.533×10^{-10}
25	25-24	1.287×10^{-7}	60	43-61	-3.579×10^{-8}
26	26-25	1.287×10^{-7}	61	46-61	2.566×10^{-7}
27	27-26	1.287×10^{-7}	62	48-61	2.311×10^{-6}
28	28-27	3.686×10^{-7}	63	61-62	2.532×10^{-6}
29	29-27	-2.399×10^{-7}	64	62-63	2.532×10^{-6}
30	30-29	-2.399×10^{-7}	65	63-64	2.532×10^{-6}
31	31-30	-2.399×10^{-7}	66	64-65	2.532×10^{-6}
32	32-31	-2.399×10^{-7}	67	65-66	2.532×10^{-6}
33	33-32	-2.399×10^{-7}			
34	34-33	-2.399×10^{-7}			
35	35-34	-2.399×10^{-7}			

Table 5.12: Network 5.4.2 - Pressure and Knudsen number at each node of the network simulating the flow through the divertor and lower port regions - Scenario B.

Node number	Kn	Pressure [Pa]	Node number	Kn	Pressure [Pa]
1	2.445×10^2	7.740×10^{-4}	36	5.991×10^0	2.193×10^{-2}
2	1.869×10^2	8.587×10^{-4}	37	9.630×10^0	2.170×10^{-2}
3	1.663×10^2	9.647×10^{-4}	38	3.074×10^1	1.661×10^{-2}
4	2.276×10^2	1.071×10^{-3}	39	2.057×10^1	1.151×10^{-2}
5	9.326×10^1	2.628×10^{-3}	40	2.235×10^1	1.102×10^{-2}
6	5.943×10^1	2.719×10^{-3}	41	8.759×10^4	7.010×10^{-6}
7	4.633×10^1	2.811×10^{-3}	42	4.785×10^2	3.954×10^{-4}
8	3.816×10^1	2.859×10^{-3}	43	2.763×10^2	2.685×10^{-4}
9	5.760×10^1	2.906×10^{-3}	44	5.830×10^2	2.751×10^{-4}
10	5.738×10^1	3.684×10^{-3}	45	5.657×10^2	2.846×10^{-4}
11	3.963×10^1	3.776×10^{-3}	46	2.760×10^2	2.903×10^{-4}
12	2.511×10^1	6.832×10^{-3}	47	2.072×10^2	6.286×10^{-4}
13	8.678×10^1	3.890×10^{-2}	48	1.075×10^2	8.044×10^{-4}
14	2.573×10^1	1.138×10^{-2}	49	1.615×10^2	8.042×10^{-4}
15	1.198×10^1	1.678×10^{-2}	50	1.996×10^2	8.037×10^{-4}
16	7.680	2.216×10^{-2}	51	1.928×10^2	8.032×10^{-4}
17	4.986	2.468×10^{-2}	52	2.989×10^2	8.025×10^{-4}
18	2.829	2.848×10^{-2}	53	7.589×10^2	7.952×10^{-4}
19	3.169	2.817×10^{-2}	54	3.828×10^2	7.879×10^{-4}
20	3.709	2.771×10^{-2}	55	2.554×10^2	7.871×10^{-4}
21	3.437	2.848×10^{-2}	56	4.827×10^2	7.862×10^{-4}
22	3.525	2.808×10^{-2}	57	3.882×10^4	7.889×10^{-6}
23	3.986	2.672×10^{-2}	58	1.506×10^4	7.121×10^{-6}
24	5.579	2.712×10^{-2}	59	1.149×10^4	7.010×10^{-6}
25	8.134	2.940×10^{-2}	60	3.512×10^2	7.740×10^{-4}
26	7.089	3.052×10^{-2}	61	1.355×10^2	2.632×10^{-4}
27	1.211×10^1	3.163×10^{-2}	62	1.536×10^2	1.719×10^{-4}
28	5.046	2.770×10^{-1}	63	2.771×10^2	6.242×10^{-5}
29	1.393×10^1	2.879×10^{-2}	64	2.498×10^2	4.721×10^{-5}
30	8.206	2.596×10^{-2}	65	3.843×10^2	3.668×10^{-5}
31	5.657	2.563×10^{-2}	66	1.998×10^4	1.000×10^{-6}
32	7.857	2.530×10^{-2}			
33	7.411	2.254×10^{-2}			
34	5.079	2.235×10^{-2}			
35	5.497	2.216×10^{-2}			

Table 5.13: Network 5.4.2 - Mass flow rate values for each piping element the network simulating the flow through the divertor and lower port regions - Scenario B.

Tube # [j]	From node to node	$\dot{M}_j$ [kg/s]	Tube number	From node to node	$\dot{M}_j$ [kg/s]
1	1-2	-6.076×10^{-10}	36	36-35	-2.915×10^{-9}
2	2-3	-6.076×10^{-10}	37	37-36	-2.915×10^{-9}
3	3-4	-6.076×10^{-10}	38	38-37	-2.915×10^{-9}
4	4-5	-6.076×10^{-10}	39	39-38	-2.915×10^{-9}
5	5-6	-6.076×10^{-10}	40	40-39	-2.915×10^{-9}
6	6-7	-6.076×10^{-10}	41	41-40	-2.915×10^{-9}
7	7-8	-6.076×10^{-10}	42	60-42	7.263×10^{-10}
8	8-9	-6.076×10^{-10}	43	42-43	7.263×10^{-10}
9	9-10	-6.076×10^{-10}	44	43-44	-3.761×10^{-11}
10	10-11	-6.076×10^{-10}	45	44-45	-3.761×10^{-11}
11	11-48	1.962×10^{-8}	46	45-46	-3.761×10^{-11}
12	12-11	2.023×10^{-8}	47	47-46	2.241×10^{-9}
13	14-12	2.023×10^{-8}	48	48-47	2.241×10^{-9}
14	13-14	1.178×10^{-10}	49	49-48	-3.029×10^{-12}
15	15-14	2.011×10^{-8}	50	50-49	-3.029×10^{-12}
16	16-15	2.011×10^{-8}	51	51-50	-3.029×10^{-12}
17	17-16	2.011×10^{-8}	52	52-51	-3.029×10^{-12}
18	23-17	2.011×10^{-8}	53	53-52	-3.029×10^{-12}
19	18-19	8.977×10^{-9}	54	54-53	-3.029×10^{-12}
20	19-20	8.977×10^{-9}	55	55-54	-3.029×10^{-12}
21	21-22	7.232×10^{-9}	56	56-55	-3.029×10^{-12}
22	22-20	7.232×10^{-9}	57	57-56	-3.029×10^{-12}
23	20-23	1.621×10^{-8}	58	58-57	-3.029×10^{-12}
24	24-23	3.902×10^{-9}	59	59-58	-3.029×10^{-12}
25	25-24	3.902×10^{-9}	60	43-61	7.640×10^{-10}
26	26-25	3.902×10^{-9}	61	46-61	2.204×10^{-9}
27	27-26	3.902×10^{-9}	62	48-61	1.738×10^{-8}
28	28-27	6.817×10^{-9}	63	61-62	2.034×10^{-8}
29	29-27	-2.915×10^{-9}	64	62-63	2.034×10^{-8}
30	30-29	-2.915×10^{-9}	65	63-64	2.034×10^{-8}
31	31-30	-2.915×10^{-9}	66	64-65	2.034×10^{-8}
32	32-31	-2.915×10^{-9}	67	65-66	2.034×10^{-8}
33	33-32	-2.915×10^{-9}			
34	34-33	-2.915×10^{-9}			
35	35-34	-2.915×10^{-9}			

Table 5.14: Network 5.4.3 - Pressure and Knudsen number at each node of the network simulating the flow through the divertor and lower port regions - Scenario C.

Node number	Kn	Pressure [Pa]	Node number	Kn	Pressure [Pa]
1	1.473×10^2	8.120×10^{-4}	36	1.324×10^{-2}	6.270
2	1.161	8.728×10^{-2}	37	2.111×10^{-2}	6.253
3	5.491×10^{-1}	1.846×10^{-1}	38	6.020×10^{-2}	5.357
4	5.634×10^{-1}	2.733×10^{-1}	39	3.441×10^{-2}	4.345
5	9.713×10^{-2}	1.594	40	3.619×10^{-2}	4.299
6	6.273×10^{-2}	1.628	41	4.398×10^2	8.820×10^{-4}
7	4.956×10^{-2}	1.660	42	8.728×10^{-1}	1.369×10^{-1}
8	4.117×10^{-2}	1.674	43	2.654×10^{-1}	1.766×10^{-1}
9	6.269×10^{-2}	1.687	44	5.610×10^{-1}	1.806×10^{-1}
10	6.240×10^{-2}	2.140	45	5.448×10^{-1}	1.867×10^{-1}
11	4.362×10^{-2}	2.168	46	2.663×10^{-1}	1.901×10^{-1}
12	3.502×10^{-2}	3.096	47	2.065×10^{-1}	3.985×10^{-1}
13	1.422×10^{-1}	$1.500 \times 10^{+1}$	48	1.134×10^{-1}	4.818×10^{-1}
14	4.148×10^{-2}	4.460	49	1.703×10^{-1}	4.818×10^{-1}
15	2.200×10^{-2}	5.774	50	2.104×10^{-1}	4.815×10^{-1}
16	1.562×10^{-2}	6.886	51	2.033×10^{-1}	4.813×10^{-1}
17	1.070×10^{-2}	7.266	52	3.150×10^{-1}	4.810×10^{-1}
18	6.510×10^{-3}	7.819	53	7.995×10^{-1}	4.769×10^{-1}
19	7.259×10^{-3}	7.769	54	4.031×10^{-1}	4.727×10^{-1}
20	8.442×10^{-3}	7.691	55	2.689×10^{-1}	4.723×10^{-1}
21	7.909×10^{-3}	7.819	56	5.080×10^{-1}	4.720×10^{-1}
22	8.063×10^{-3}	7.754	57	1.327×10^2	1.458×10^{-3}
23	8.950×10^{-3}	7.519	58	7.097×10^1	9.548×10^{-4}
24	1.272×10^{-2}	7.514	59	5.771×10^1	8.820×10^{-4}
25	2.024×10^{-2}	7.464	60	2.115×10^2	8.120×10^{-4}
26	1.836×10^{-2}	7.444	61	1.270×10^{-1}	1.774×10^{-1}
27	3.261×10^{-2}	7.423	62	1.294×10^{-1}	1.289×10^{-1}
28	3.742×10^{-2}	$2.360 \times 10^{+1}$	63	2.158×10^{-1}	5.064×10^{-2}
29	3.582×10^{-2}	7.076	64	1.803×10^{-1}	4.132×10^{-2}
30	2.003×10^{-2}	6.717	65	2.556×10^{-1}	3.484×10^{-2}
31	1.368×10^{-2}	6.693	66	1.262×10^4	1.000×10^{-6}
32	1.883×10^{-2}	6.669			
33	1.671×10^{-2}	6.314			
34	1.138×10^{-2}	6.301			
35	1.224×10^{-2}	6.288			

Table 5.15: Network 5.4.3 - Mass flow rate values for each piping element the network simulating the flow through the divertor and lower port regions - Scenario C.

| Tube # [j]	From node to node	$\dot{M}_j$ [kg/s]	Tube number	From node to node	$\dot{M}_j$ [kg/s]
1	1-2	-6.520×10^{-7}	36	36-35	-1.606×10^{-6}
2	2-3	-6.520×10^{-7}	37	37-36	-1.606×10^{-6}
3	3-4	-6.520×10^{-7}	38	38-37	-1.606×10^{-6}
4	4-5	-6.520×10^{-7}	39	39-38	-1.606×10^{-6}
5	5-6	-6.520×10^{-7}	40	40-39	-1.606×10^{-6}
6	6-7	-6.520×10^{-7}	41	41-40	-1.606×10^{-6}
7	7-8	-6.520×10^{-7}	42	60-42	-2.724×10^{-7}
8	8-9	-6.520×10^{-7}	43	42-43	-2.724×10^{-7}
9	9-10	-6.520×10^{-7}	44	43-44	-2.813×10^{-8}
10	10-11	-6.520×10^{-7}	45	44-45	-2.813×10^{-8}
11	11-48	2.319×10^{-5}	46	45-46	-2.813×10^{-8}
12	12-11	2.384×10^{-5}	47	47-46	1.901×10^{-6}
13	14-12	2.384×10^{-5}	48	48-47	1.901×10^{-6}
14	13-14	6.183×10^{-8}	49	49-48	-1.995×10^{-9}
15	15-14	2.378×10^{-5}	50	50-49	-1.995×10^{-9}
16	16-15	2.378×10^{-5}	51	51-50	-1.995×10^{-9}
17	17-16	2.378×10^{-5}	52	52-51	-1.995×10^{-9}
18	23-17	2.378×10^{-5}	53	53-52	-1.995×10^{-9}
19	18-19	1.341×10^{-5}	54	54-53	-1.995×10^{-9}
20	19-20	1.341×10^{-5}	55	55-54	-1.995×10^{-9}
21	21-22	1.084×10^{-5}	56	56-55	-1.995×10^{-9}
22	22-20	1.084×10^{-5}	57	57-56	-1.995×10^{-9}
23	20-23	2.425×10^{-5}	58	58-57	-1.995×10^{-9}
24	24-23	-4.701×10^{-7}	59	59-58	-1.995×10^{-9}
25	25-24	-4.701×10^{-7}	60	43-61	-2.443×10^{-7}
26	26-25	-4.701×10^{-7}	61	46-61	1.873×10^{-6}
27	27-26	-4.701×10^{-7}	62	48-61	2.128×10^{-5}
28	28-27	1.136×10^{-6}	63	61-62	2.291×10^{-5}
29	29-27	-1.606×10^{-6}	64	62-63	2.291×10^{-5}
30	30-29	-1.606×10^{-6}	65	63-64	2.291×10^{-5}
31	31-30	-1.606×10^{-6}	66	64-65	2.291×10^{-5}
32	32-31	-1.606×10^{-6}	67	65-66	2.291×10^{-5}
33	33-32	-1.606×10^{-6}			
34	34-33	-1.606×10^{-6}			
35	35-34	-1.606×10^{-6}			
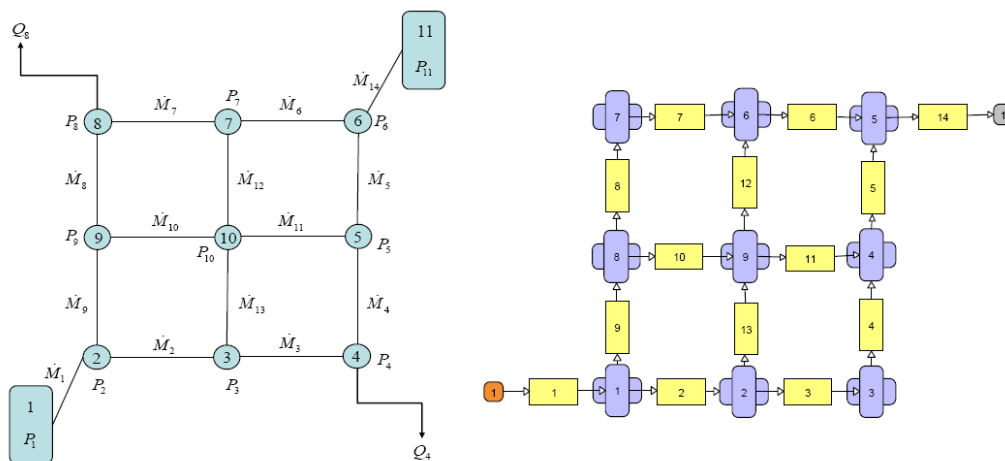
Figure 5.1: Schematic representation of the sample network 5.2.1 for the kinetic solver (left) and ITERVAC (right).
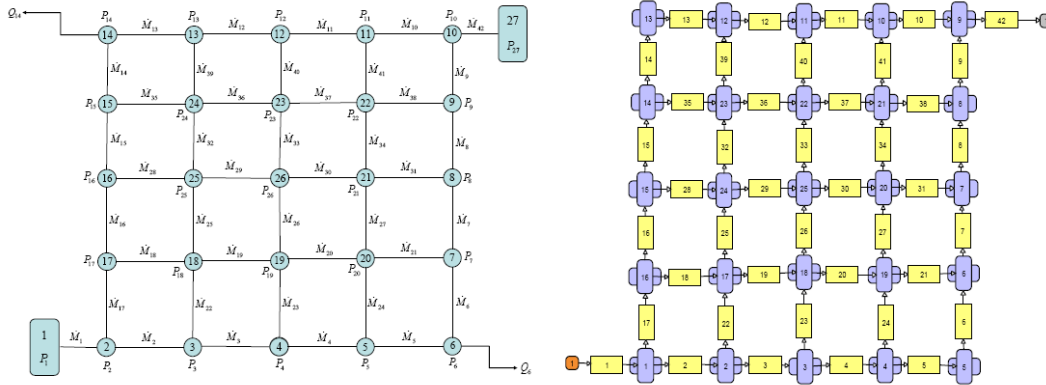
Figure 5.2: Schematic representation of the sample network 5.2.2 for the kinetic solver (left) and ITERVAC (right).

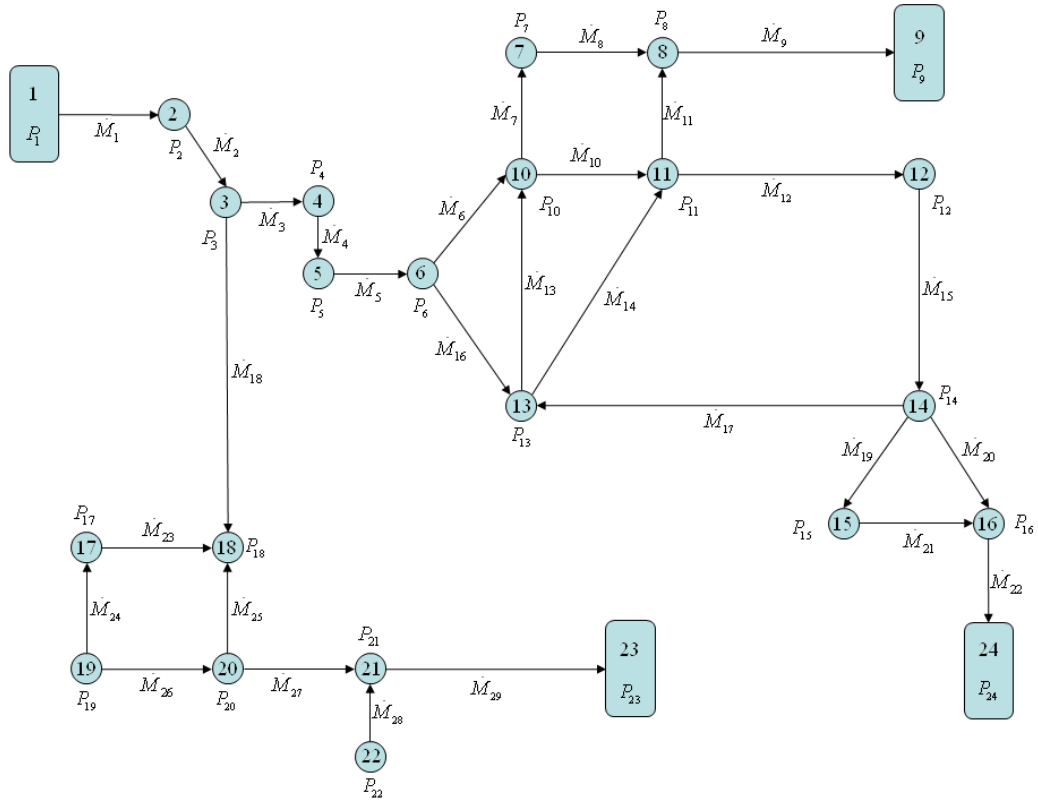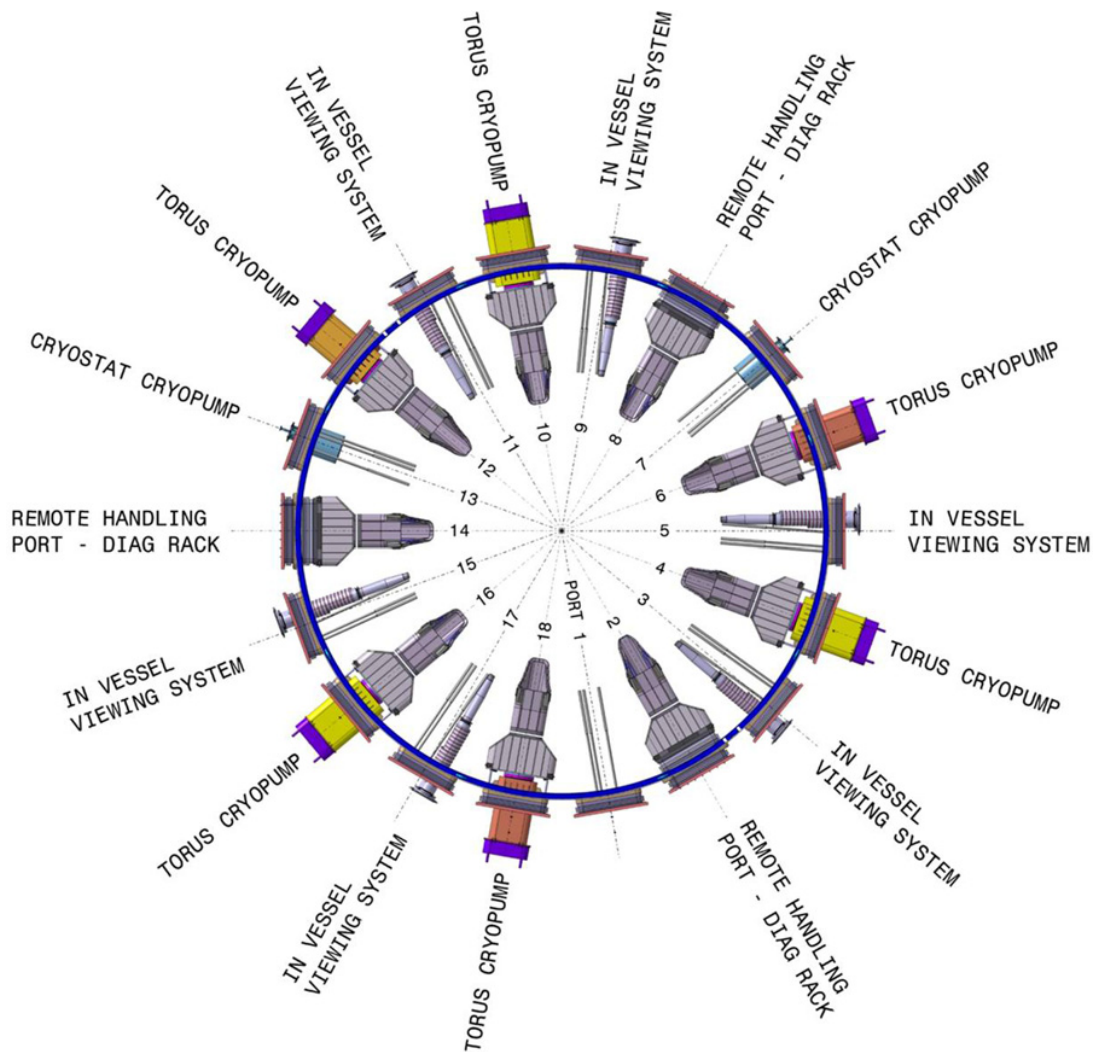Figure 5.3: Schematic representation of the tree network, Network 5.3.

Figure 5.4: Schematic representation of the cryopump position for ITER's latest design.
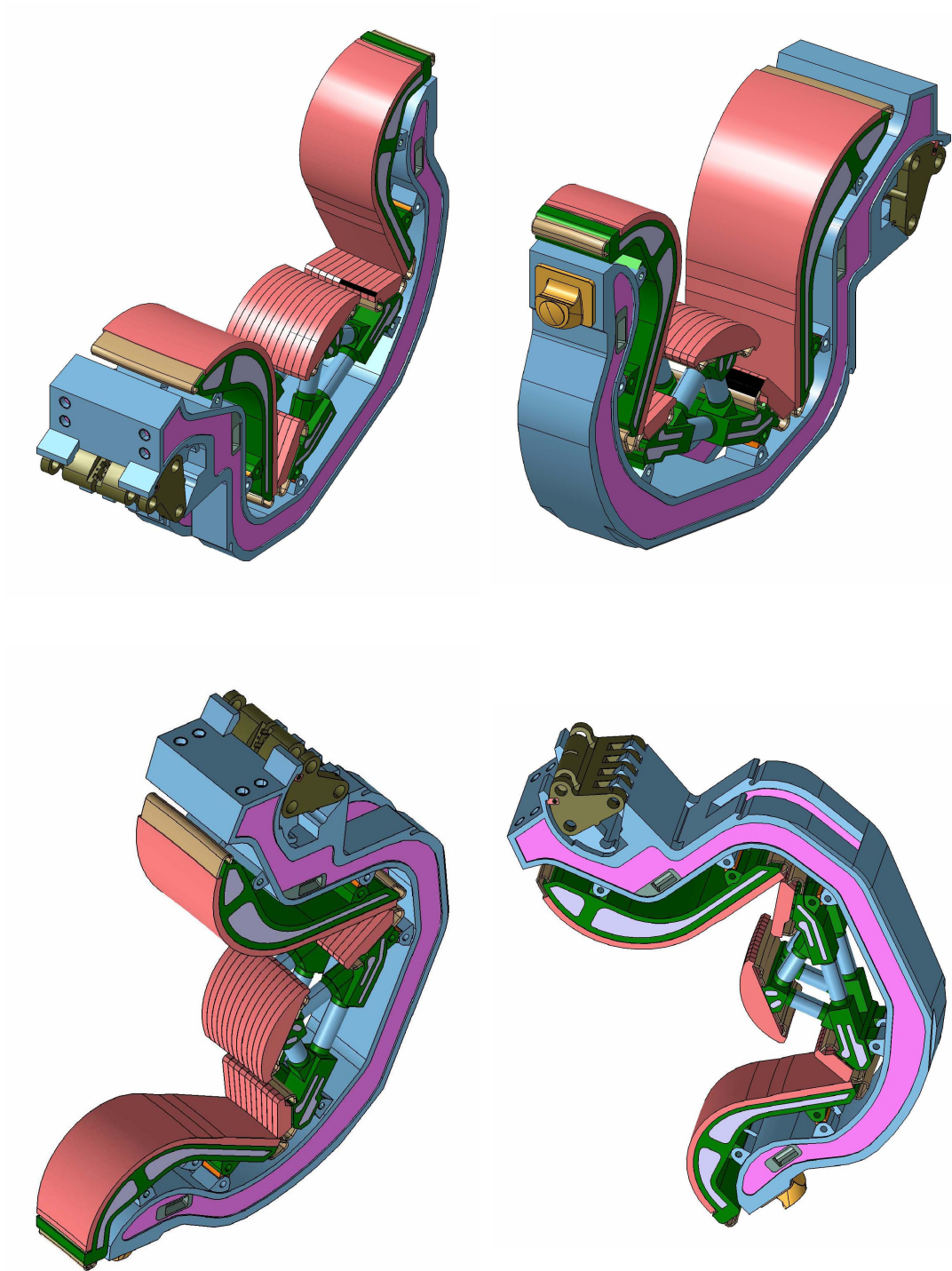
Figure 5.5: Catia schematics of the divertor configuration(2012).
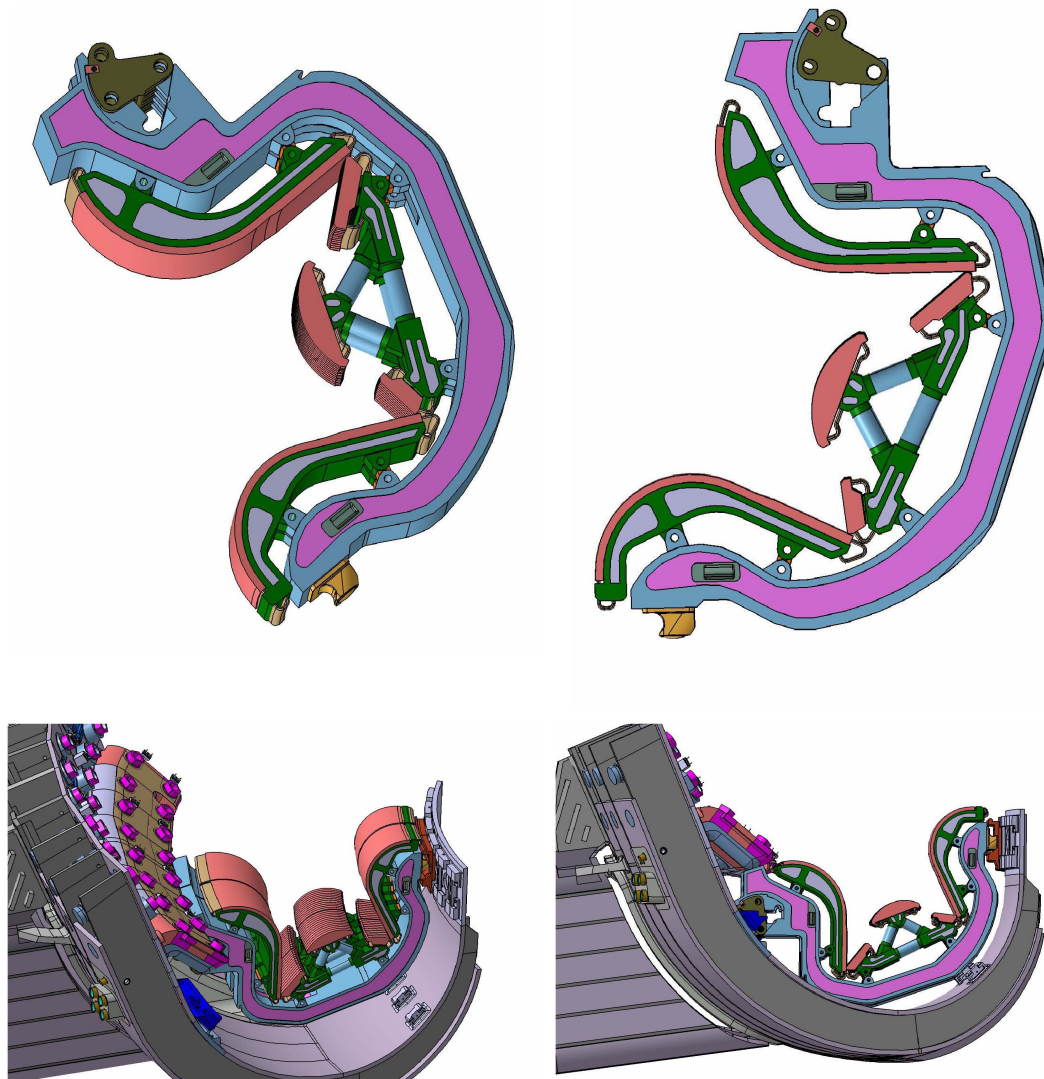
Figure 5.6: Catia schematics of the divertor and lower port region configurations(2012).
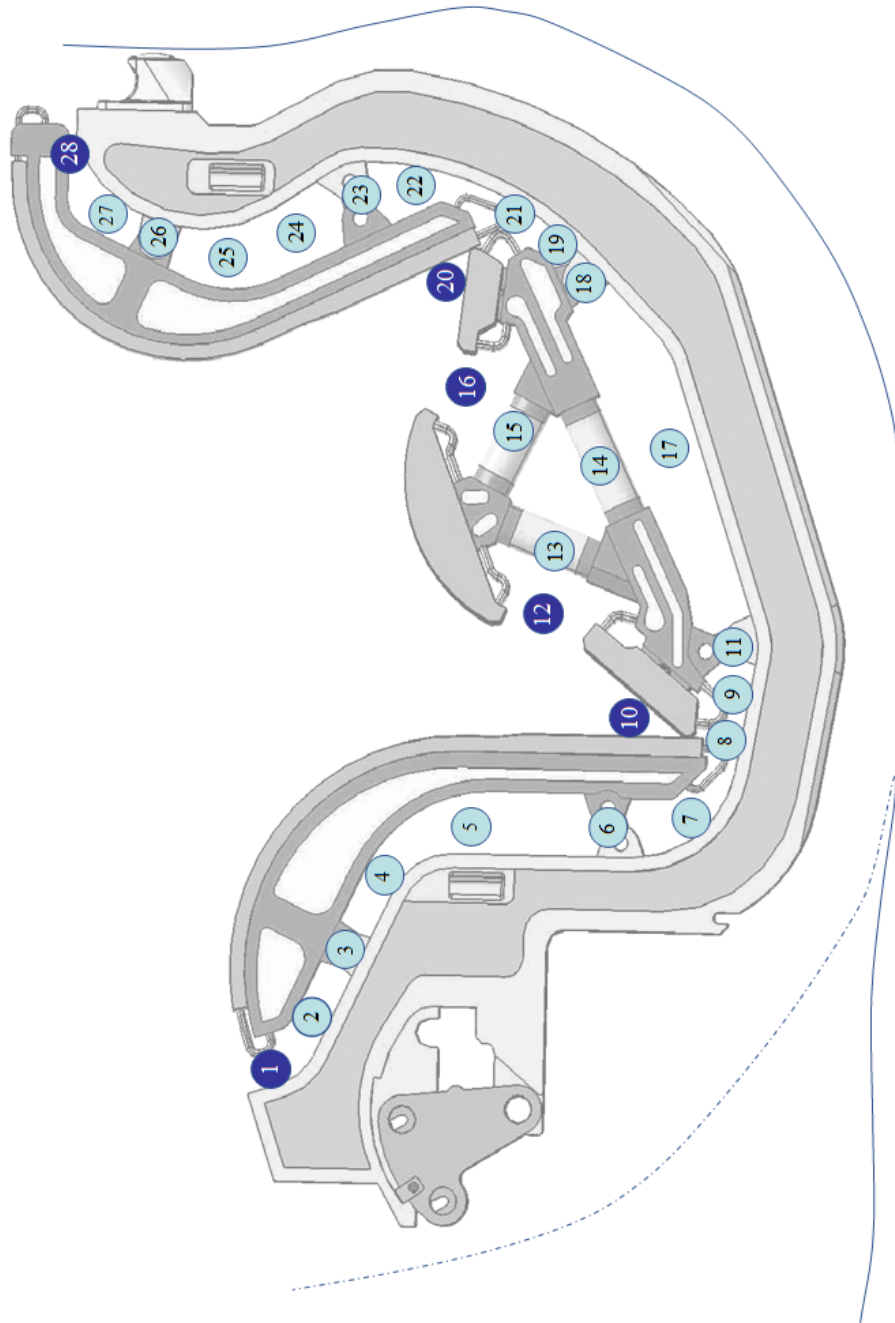
Figure 5.7: Schematic representation of the network channel configuration for the simulation of the radial gas flow inside the divertor region.
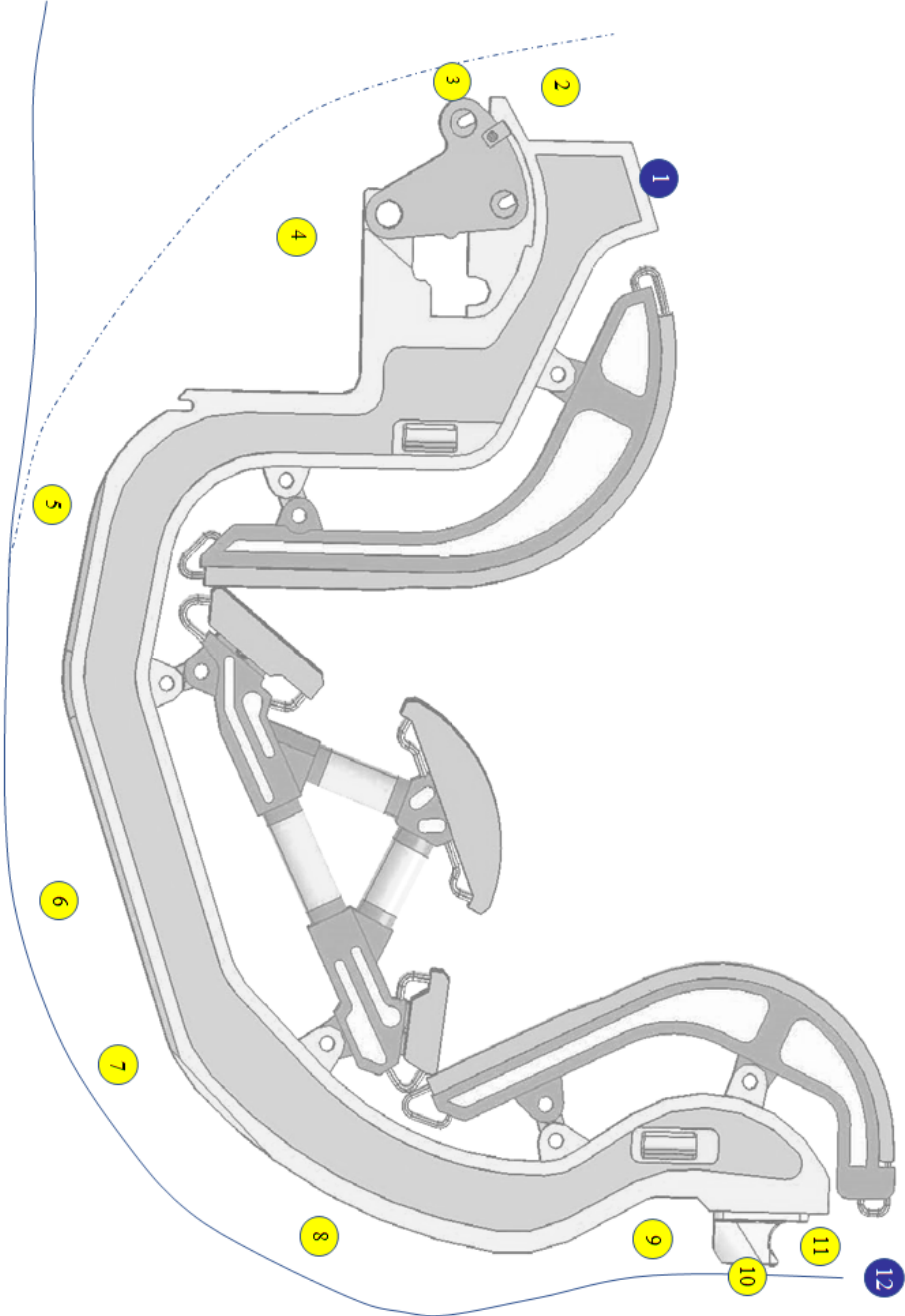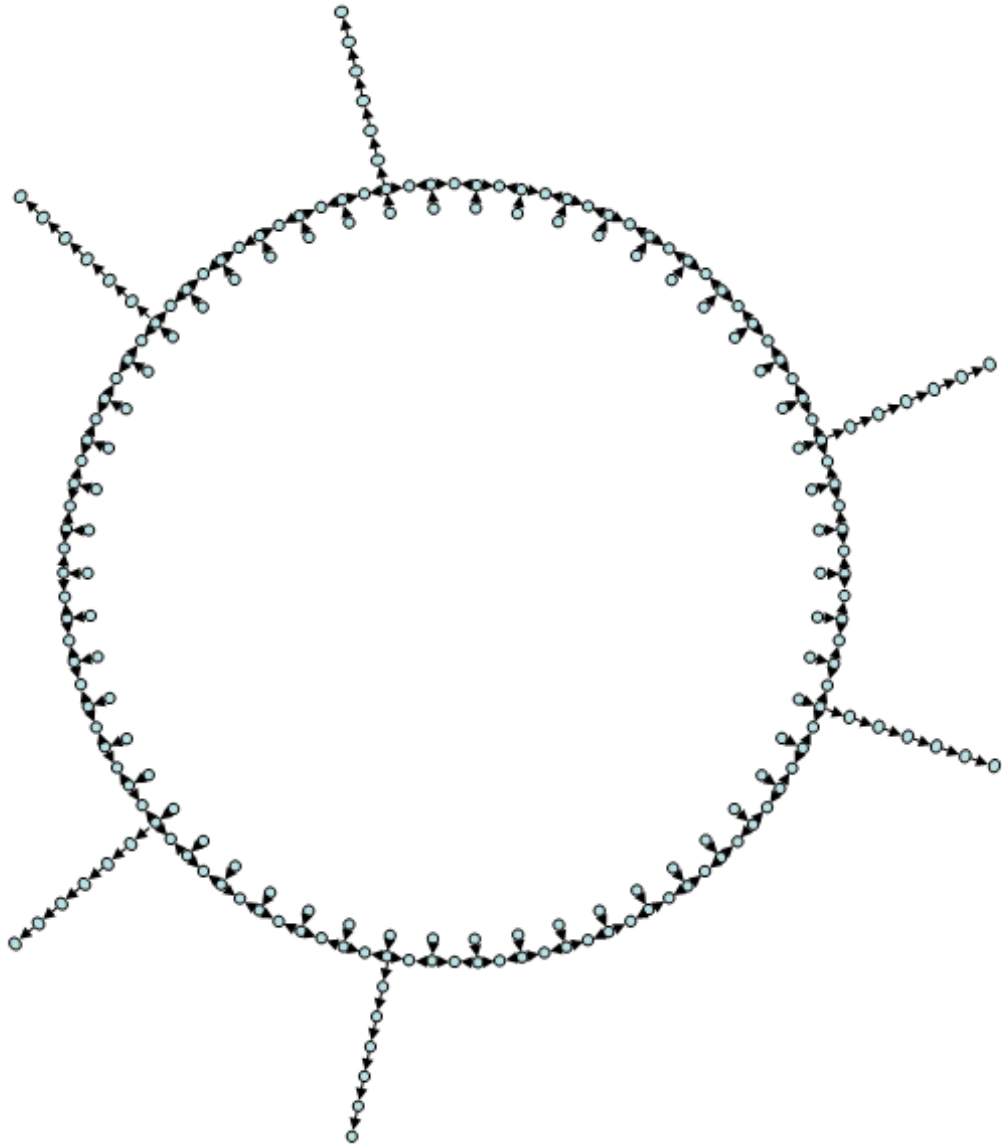
Figure 5.8: Schematic representation of the network channel configuration for the simulation of the radial gas flow between the divertor and the lower port regions.
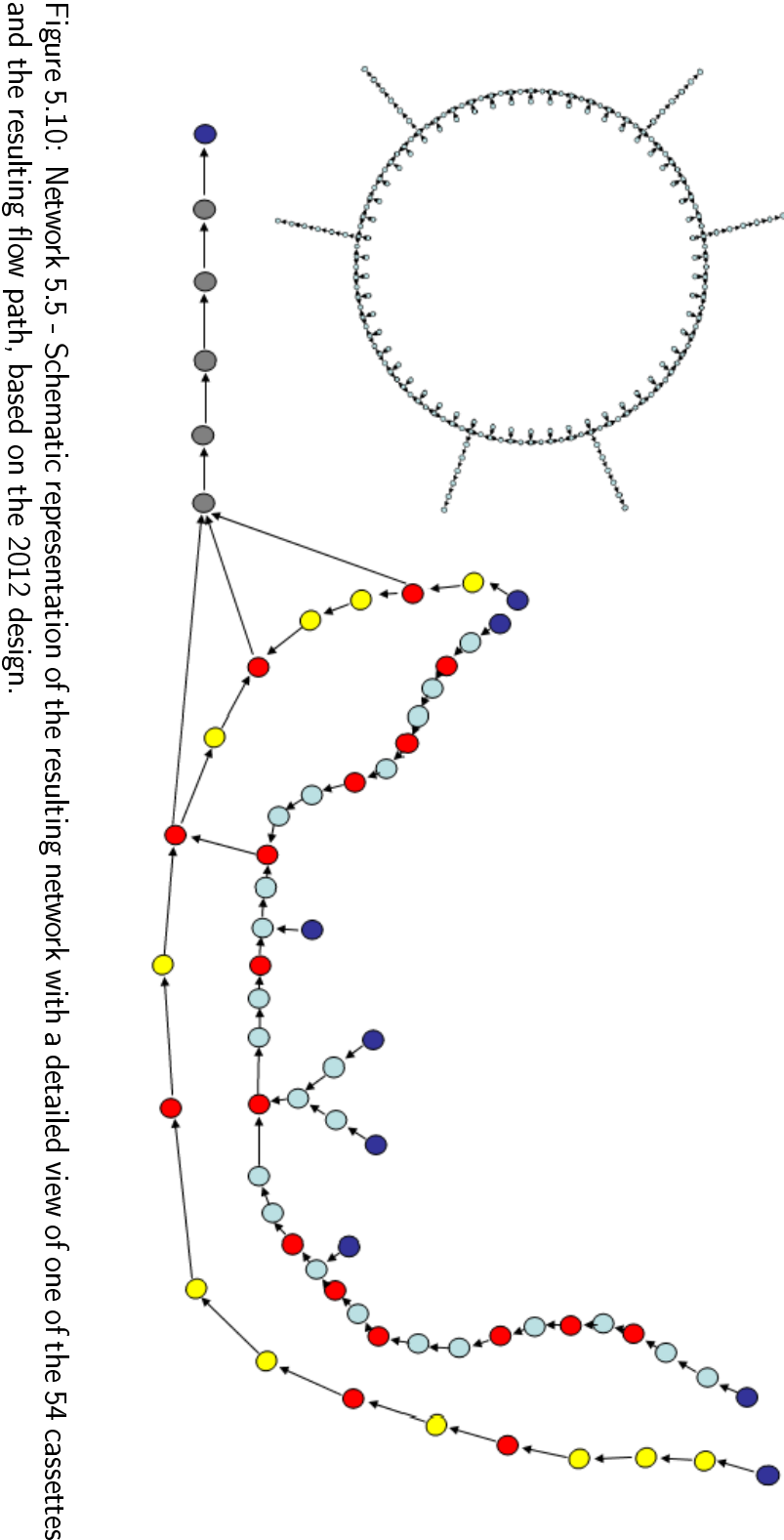
Figure 5.9: Network 5.5 - Schematic representation of the resulting network with a detailed view of one of the 54 cassettes and the resulting flow path, based on the 2012 design.

Figure 5.10: Network 5.5 - Schematic representation of the resulting network with a detailed view of one of the 54 cassettes and the resulting flow path, based on the 2012 design.
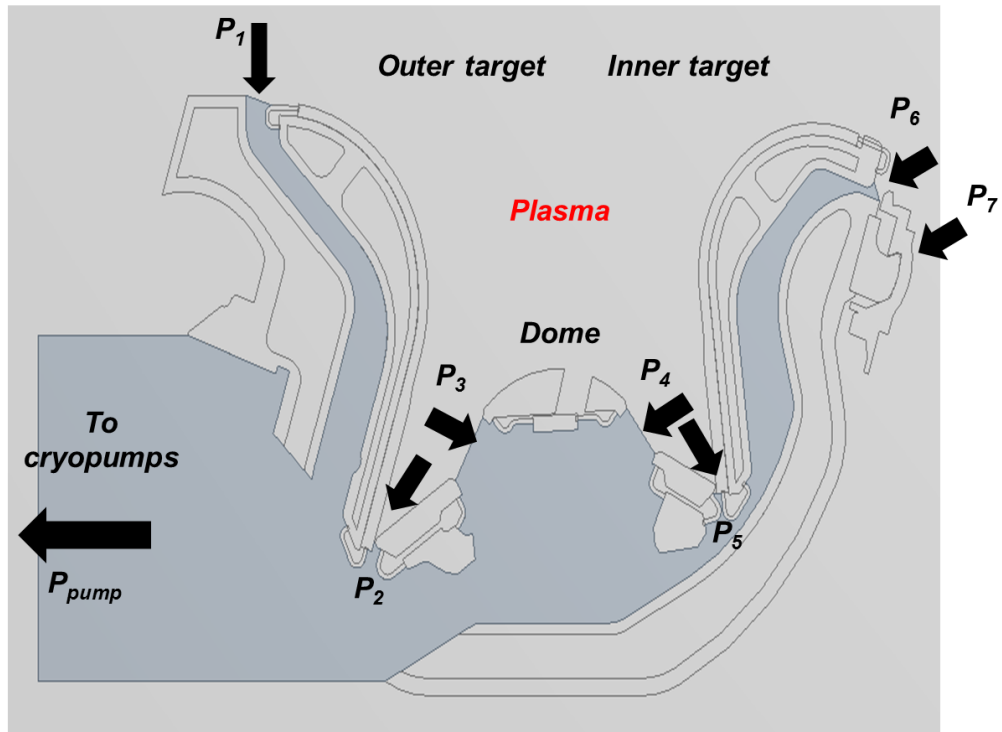
Figure 5.11: Network 5.5 - Locations of the predefined pressure values for each of the 54 cassettes and the four pumps for the 3 proposed operational scenarios.
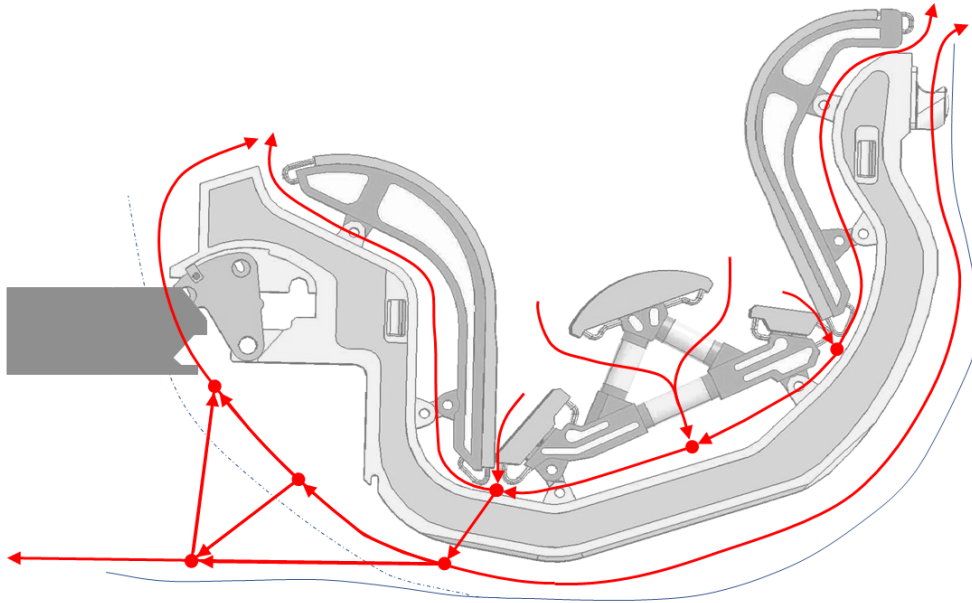
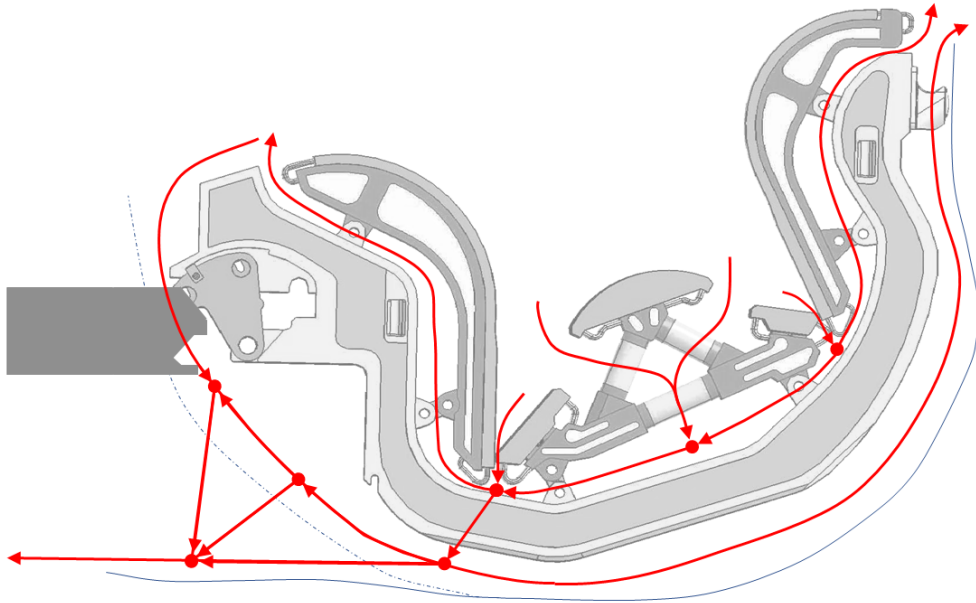Figure 5.12: Network 5.5 - Gas flow path in the cross-section along a cassette for operational scenario A.

Figure 5.13: Network 5.5 - Gas flow path in the cross-section along a cassette for operational scenario B.
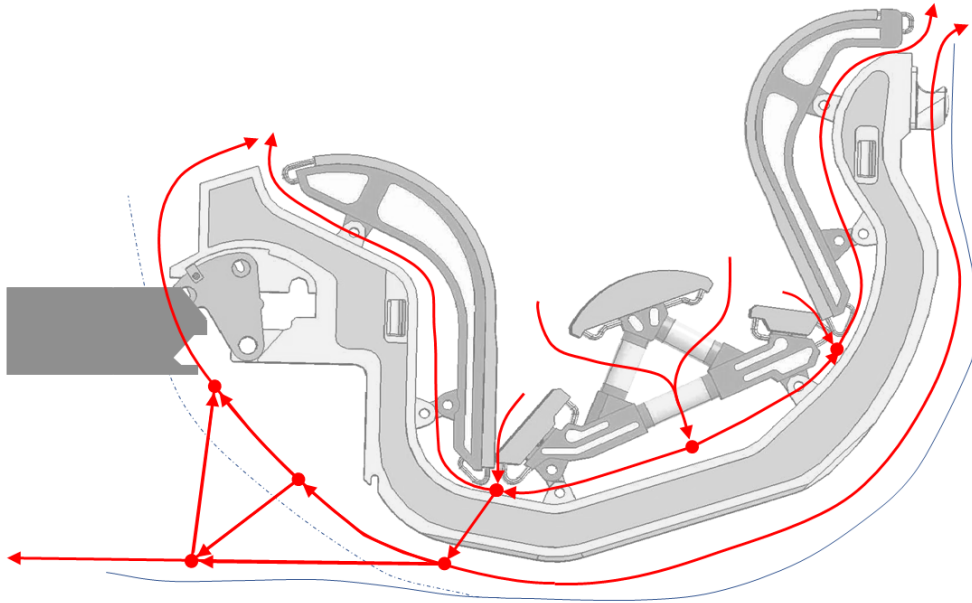
Figure 5.14: Network 5.5 - Gas flow path in the cross-section along a cassette for operational scenario C.

<div style="text-align: right;">**6**</div>

Summary, final remarks and future perspectives

6.1 Summary and contributions

In the recent years, extensive investigations have been conducted in an attempt to simulate gas pipe networks in the hydrodynamic regime based on the Navier-Stokes equations. As a result, several in-house and commercial codes have been developed in an attempt to understand the physics and the flow behavior in gas pipe networks appearing in various technological applications including, but not limited to, compressed air or natural gas networks. However, the corresponding work for case of gas pipe networks operating in applications related to vacuum pumping, metrology, industrial aerosol, porous media, and micro-fluidics is quite limited. This is mainly attributed to the increased complexity of the problem where kinetic modeling has to be combined with pipe networking.

The aim of the present thesis is to fill this gap and constitutes the first systematic and successful scientific effort in integrating the modeling gas flows through channels of various lengths and cross sections under any vacuum conditions in an integrated gas pipe network solver. Furthermore, ARIADNE, through the developed graphical interface, is a complete computational tool capable of simulating complex rarefied gas flow configurations operating at any pressure from the atmospheric down to ultra-high vacuum. The algorithm is validated through commercial and in-house developed algorithms and then is applied to solve various gas pipe networks including the neutral

<div style="text-align: right;">193</div>

6. CONCLUSIONS

gas pipe network of the ITER divertor pumping system which is considered as one of the most complex ones worldwide. A brief review of the subjects investigated in Chapters 2-5 is provided.

A detailed description of all pressure driven flow configurations involved in the present work has been presented in Chapter 2. Three main setups, with respect to channel's length, namely the flows through a) long, b) moderate and c) short channels have been employed. These flows are treated based on the linear theory for long and short channels, when the latter is applicable, as well as end effect theories for channels of moderate length and the more general nonlinear approach for short channels. Overall it has been demonstrated that for rarefied gas flows in long channels, linear kinetic modeling, as described by suitable kinetic model equations, may take advantage of all flow characteristics and properties and yield very accurate results in the whole range of the Knudsen number with minimal computational effort. For the case of the non-linear approach, similarly accurate results are acquired, however, the computational cost in quite increased. The corresponding kinetic equations along with the associated formulations have been provided and implemented to return adequate dense kinetic results to be integrated into the network code. Even more, the range of validity of each approach has also been examined.

Chapter 3 contains a detailed description of the developed Algorithm for Rarefied gas flow in Arbitrary Distribution Networks (ARIADNE). First of all, the kinetic results obtained for the rarefied flow through each tube of the network form a very dense grid of data in order to allow accurate representation of the operational conditions of an arbitrary gas pipe network. Interpolation between the available data points is performed by cubic splines for the flow rates in the case of long channels, by high order curve fitting for the increment lengths for the case of channels of moderate length and trilinear interpolation for the flow rate in terms of the pressure, length and rarefaction in the case of short channels.

The developed algorithm includes first the drawing of the network in a graphical environment and then the formulation and solution of the governing equations describing the flow conditions of the distribution system. In the drawing process of the network, the user, through the developed graphical interface, is capable of providing the input data including the coordinates of the nodes in a 3D space, the length and the diameter of the pipe elements, the pressure heads of the fixed-grade nodes and

194

information for the type of the gas and its properties. Even more, the demands (if any) at the nodes may also be provided. Once the geometry of the network is fixed, an iterative process is initiated between the pressure drop equations and the system of mass and energy conservation equations in order to successfully handle gas pipe networks operating from the free molecular, through the transition up to the slip and hydrodynamic regimes.

Additionally, the further upgrade of an in-house hydrodynamic solver, built in Matlab environment, used for the simulation of gas pipe networks in the hydrodynamic regime has also been presented. This latter upgrade refers to the extension of the range of the applicability of the hydrodynamic solver by introducing the formulas for the correct estimation of the friction factor by making use of slip boundary conditions.

The next two following chapters, namely Chapters 4 and 5, are devoted on the validation of the proposed algorithm and on its implementation in solving certain gas pipe networks of certain complexity. Chapter 4 is devoted to networks consisting of long channels or channels of moderate length with circular, orthogonal and trapezoidal cross channels. Results are based on the infinite capillary and the end effect theories. The code validation and benchmarking is achieved in the viscous regime by comparisons with the in-house hydrodynamic solver and in a wide range of the Knudsen number by comparisons with the ITERVAC code. Several simulations have been performed with the respect to *i)* the network's complexity, *ii)* the Knudsen number, *iii)* the piping elements' cross-section, *iv)* their individual geometrical characteristics (length and diameter) as well as *v)* the applicability and effectiveness in micro-geometries or in vacuum conditions. The corresponding results with the ones derived by the updated hydrodynamic solver reported excellent agreement in terms of the mass flow rate (and the conductance) through the pipes as well as the pressure heads at the nodes of the network. Similar results have been obtained for the cases where the ITERVAC software has been employed.

Last but not least, in Chapter 5 the more general and challenging case of networks consisting of channels of arbitrary length have been presented. Following similar procedure with the one in the previous chapter, several networks of arbitrary complexity have been simulated. Two networks of small and average complexity covering the whole range of rarefaction have been studied and a comparison has been performed by implementing the ITERVAC algorithm returning very good agreement. Furthermore,

the ARIADNE code has been used to demonstrate the effectiveness of the presented algorithm in simulating gas networks of arbitrary complexity and size. This has been achieved by presenting the results of a network consisting of all possible combinations with respect to the geometrical characteristics of the piping elements forming it. However, the true capabilities of ARIADNE have been demonstrated by modeling the 2012 ITER torus primary pumping system. The ITER divertor and lower port schematics have been translated into a network of piping elements of various lengths and cross sections. Results of the flow patterns and paths along the cassette for various operating scenarios and both qualitative and quantitative results, including the gas flow paths through the divertor, as well as the backflow and pumped throughputs, have been provided.

It is hoped that the present work will constitute a significant part of a more general algorithm which will be used as a significant engineering tool in the design and optimization of gaseous distribution networks operating under any rarefied conditions.

6.2 Future work

In its present state, ARIADNE constitutes fully integrated software tool, which in principle can be applied for the simulation, design and optimization of any piping network, irrespective of geometrical characteristics or pressure conditions. However, several upgrades may be introduced in the existing software in order to further improve either its range of applicability or feasibility.

- The developed codes may be further extended to tackle non-isothermal gas networks, by taking into consideration the gas transport that occurs in the network due to temperature gradients. In order to achieve this, an equally dense kinetic data base for all the flow conditions described in the present thesis for the case of the pressure driven flow has to be built. This is a quite straight-forward task, but with great requirements in time.

- A further addition of elements with specific geometrical characteristics that may appear in networks, may be a further upgrade of the software. Such elements as bellows or even corners and T-junctions, will require a further increase of the corresponding data base. However, especially for the case of

196

Ts', the formulation of the problem is multi parametric taking into account the radii of the inflow-outflow ducts forming the junction.

- The existing code may be further advanced with the implementation of optimization subroutines for optimal sensor placement and leak detection. One of the most popular optimization techniques for sensor selection is genetic algorithms. Genetic algorithms that have been developed by John Holland [51] are search algorithm based on the mechanics of natural selection and natural genetics. Several researchers have proposed methods to select locations of sensors for structural health monitoring [43], health assessment of aerospace systems [73] or leak detection and calibration [152].

- Several advancements may be implemented in the numerical methods ARIADNE is making use of. A more sophisticated/parallel solver for the system of equations formed or even a higher order of interpolating techniques for the estimation of more accurate values picked from the kinetic data base.

- Finally, apart of the vacuum flows or micro- geometries, a system of piping elements may be found in many areas. The further extension of the present software with respect to its area of applicability, may be the simulation of respiratory gas flows. The complex geometry of the bronchial tree, along with the several studies around the mechanics of respiratory gas flows [2, 42, 95], provide a promising basis for the applicability of the developed algorithm.

Appendices

A

Derivation of the Darcy-Weisbach equation

As it has already been mentioned, the flow of the gas inside the network configuration is assumed to be isothermal. However, since the Mach number computed in several cases may be around or even exceed the value of 0.3, the compressible Navier-Stokes equations are utilized for the formulation of the network solver in the hydrodynamic regime.

The differential equation for continuity is the mathematical formulation of the law of conservation of mass in a certain point in space and three-dimensional flow is:

$$\frac{\partial \rho}{\partial t} + \frac{\partial}{\partial \mathbf{x}}(\rho \mathbf{u}) = 0 \tag{A.1}$$

For the case of one-dimensional compressible flow through a channel of varying cross sections, from a cross section A_1 to a cross section A_2, the continuity equation takes the form

$$d(\rho u A) = 0 \Rightarrow \rho u A = ct \tag{A.2}$$

or

$$\rho_1 u_1 A_1 = \rho_2 u_2 A_2 \Rightarrow Q_1 = Q_2 \tag{A.3}$$

The generalized form of the momentum equations where the viscosity is constant is expressed by

$$\rho \frac{\partial u_j}{\partial t} + \rho u_k \frac{\partial u_j}{\partial x_k} = \frac{\partial \sigma_{ij}}{\partial x_i} + \rho f_i \tag{A.4}$$

By introducing the constitutive Navier-Stokes equations in the case of one-dimensional

fully developed flow, the momentum equation in the x-direction is described by

$$\rho u \frac{du}{dz} = -\frac{dP}{dz} + \rho g_x + \frac{d}{dx}\left(\mu \frac{du}{dx}\right) \tag{A.5}$$

and for a height difference equal to dz

$$\rho u du + dP + \rho g dz + dP_L = 0 \tag{A.6}$$

where dP_L are the losses due to friction replacing the third term of the equation. For the case of a cylindrical channel of diameter D and length L, the losses due to friction are computed by making use of the Darcy-Weisbach equation

$$dP_L = f_D \frac{L}{d} \rho \frac{u^2}{2} \tag{A.7}$$

where f_D is the friction factor estimated according to the Reynolds number in following paragraphs. Based on the momentum Eq. A.6 and for the case of horizontal flow or small height differences $(dz = 0)$, yields

$$\rho u du + dP + dP_L = 0 \tag{A.8}$$

The isothermal flow requires constant temperature distribution along the flow and an ideal gas is defined as a gas which is subject to the constitutive equation:

$$P = \rho R^* T \quad \text{or} \quad T = \frac{P}{\rho R_*} = ct \tag{A.9}$$

where P is the absolute pressure, ρ is the density, T is the absolute temperature and R^* is the specific gas constant. After some trivial mathematical manipulation to Eq. A.9, yields

$$\frac{dP}{P} = \frac{d\rho}{\rho} \Rightarrow dP = P\frac{d\rho}{\rho} \tag{A.10}$$

The Mach number (Ma) is given by:

$$\text{Ma} = \frac{u}{a} = \frac{u}{\sqrt{\gamma R^* T}} = \frac{u}{\sqrt{\gamma \frac{P}{\rho}}} \tag{A.11}$$

and by applying the same mathematical manipulation as in the previous equation

$$\ln \text{Ma} = \ln u - \ln(R^*T) \Rightarrow \frac{d\text{Ma}}{\text{Ma}} = \frac{du}{u} \tag{A.12}$$

The same formulation is applied to the continuity Eq. A.3, which in combination with Eq. A.12 and assuming a channel of constant cross sections returns

$$\rho u A = ct \rightarrow \frac{d\rho}{\rho} + \frac{du}{u} + \frac{dA}{A} = 0 \Rightarrow \frac{d\rho}{\rho} = -\frac{d\text{Ma}}{\text{Ma}} \tag{A.13}$$

The pressure drop due to friction is evaluated through the Darcy-Weisbach equation A.7, which for the case of a compressible flow, by introducing the Mach number and the speed of sound

$$a^2 = \gamma \frac{P}{\rho} \tag{A.14}$$

yields

$$dP_L = f\frac{dx}{d}\rho\frac{u^2}{2} = f\frac{dx}{d}\gamma\frac{P}{a^2}\frac{u^2}{2} = f\frac{dx}{d}\gamma P\frac{\text{Ma}^2}{2} \tag{A.15}$$

By introducing Eqs. A.10 and A.15 into the momentum Eq. A.8 and diving by P yields

$$-\frac{d\text{Ma}}{\text{Ma}} + \frac{\rho}{P}u^2\frac{du}{u} + f\frac{dx}{d}\gamma\frac{\text{Ma}^2}{2} = 0 \tag{A.16}$$

By further introducing $\frac{\rho}{P} = \frac{1}{R^*T} = \frac{\gamma}{\gamma R^*T} = \frac{\gamma}{a^2}$ and Eq. A.12 into Eq.A.16 we derive the x-momentum equation in terms of the Mach number given by

$$f\frac{dx}{d} = \frac{2d\text{Ma}}{\gamma\text{Ma}^3} - \frac{2d\text{Ma}}{\text{Ma}} \tag{A.17}$$

In the case where the flow is isothermal, the speed of sound a, as a function of temperature, remains constant and the following relation holds:

$$\frac{\text{Ma}_1}{\text{Ma}_2} = \frac{u_1}{u_2} = \frac{\rho_2}{\rho_1} = \frac{P_2}{P_1} \tag{A.18}$$

wherein the first ratio is derived from the equation of the speed of sound, the middle of the constant mass flow rate and the latter by applying the constitutive equation. Here, the subscripts 1 and 2 indicate the upstream and downstream fluid properties

in the direction of the flow and in this case the entrance and the exit of a pipe, respectively. The mass flow rate is given by $\dot{M} = \rho u A$ and by introducing Eqs. A.14 and A.9 yields

$$\dot{M} = \rho u A = A\gamma \frac{P}{a^2}\frac{u^2}{u} = A\frac{\gamma P \text{Ma}^2}{u} = A\frac{\gamma \text{Ma}^2 \rho \text{R}^*\text{T}}{u} \qquad (A.19)$$

and by rearranging for Ma^2

$$\text{Ma}^2 = \frac{\dot{M}u}{A\gamma\rho R^* T} \qquad (A.20)$$

By integrating Eq. A.17 between the entrance and the exit of a pipe, denoted by 1 and 2 respectively, we deduce

$$\int\limits_1^2 \frac{f}{d}dx = \int\limits_1^2 \frac{2}{\gamma\text{Ma}^3}d\text{Ma} - \int\limits_1^2 \frac{2}{\text{Ma}}d\text{Ma} \Rightarrow$$
$$\Rightarrow f\frac{L}{d} = \frac{1}{\gamma\text{Ma}_1^2} - \frac{1}{\gamma\text{Ma}_2^2} - 2\ln\text{Ma}_2 + 2\ln\text{Ma}_1 \Rightarrow$$

$$\Rightarrow f\frac{L}{d} = \frac{1}{\gamma\text{Ma}_1^2} - \frac{1}{\gamma\text{Ma}_2^2} - \ln\text{Ma}_2^2 + \ln\text{Ma}_1^2 \Rightarrow$$
$$\Rightarrow f\frac{L}{d} = \frac{1}{\gamma\text{Ma}_1^2}\left(1 - \frac{\text{Ma}_1^2}{\text{Ma}_2^2}\right) - 2\ln\frac{\text{Ma}_2}{\text{Ma}_1} \qquad (A.21)$$

By properly combining Eqs. A.21 with A.18 and A.20 yields

$$f\frac{L}{d} = \frac{1}{\gamma\text{Ma}_1^2}\left(1 - \left(\frac{P_2}{P_1}\right)^2\right) - 2\ln\frac{P_1}{P_2} \Rightarrow$$
$$\Rightarrow f\frac{L}{d} = \frac{AR^* T\rho_1}{Mu_1}\left(1 - \left(\frac{P_2}{P_1}\right)^2\right) - 2\ln\frac{P_1}{P_2} \Rightarrow$$
$$\Rightarrow f\frac{L}{d} = \frac{AR^* T\rho_1(P_1^2 - P_2^2)}{Mu_1 p_1^2} - 2\ln\frac{P_1}{P_2} \Rightarrow$$
$$\Rightarrow f\frac{L}{d} = \frac{A(P_1^2 - P_2^2)}{Mu_1\rho_1 R^* T} - 2\ln\frac{P_1}{P_2} \Rightarrow$$
$$\Rightarrow f\frac{L}{d} = \frac{A^2(P_1^2 - P_2^2)}{M^2 R^* T} - 2\ln\frac{P_1}{P_2} \qquad (A.22)$$

and by rearranging for the pressure drop equations we deduce

$$P_1^2 - P_2^2 = \frac{M^2 R^* T}{A^2} \left(2 \ln \frac{P_1}{P_2} + f \frac{L}{d} \right) \tag{A.23}$$

By assuming the density of the gas inside the pipe as the mean value of the density between the pipe's ends $\rho_m = (\rho_1 + \rho_2)/2$ and according to the constitutive equation, the final expression for the pressure drop may be derived

$$P_L = P_1 - P_2 = \frac{M^2}{2\rho_m A^2} \left(2 \ln \frac{P_1}{P_2} + f \frac{L}{d} \right) \tag{A.24}$$

which is the basic equation implemented in the hydrodynamic solver for the simulation of the flow through a gaseous distribution system. As it seen, Eq. A.24 derives from the Darcy-Weisbach relation by introducing the necessary formulation for the compressible flow. It is noted that in the present case, the pressure drop along two points depends on the pressure at the points into consideration. As a result, the pressure drop cannot be evaluated directly as a function of the length, the diameter, the mass flow rate and the friction factor, but in the case where the pressures upstream and downstream the pipe are unknown, an iterative procedure is necessary, increasing significantly the computational cost.

B

Tables of kinetic coefficients

In the present appendix a brief description of all the required kinetic coefficients introduced into the ARIADNE code are summed up.

In general, the pressure driven flow of a rarefied gas through a tube of length L and radius R with the tube inlet and outlet pressures maintained at P_1 and P_2 respectively $(P_1 > P_2)$ is prescribed by three dimensionless parameters namely, *i)* the geometrical ratio L/R, *ii)* the pressure ratio P_2/P_1 and *iii)* the reference Knudsen number (Kn) or alternatively the reference rarefaction parameter (δ). A review of the four main approaches modeling rarefied gas flows through channels, implemented in the present work, has been provided in Chapter 2. The approaches include the infinite capillary and end effect theories for long and medium capillaries, as well as the linear and the nonlinear approach for short capillaries. Furthermore, these methodologies are organized and presented in a manner which is useful for their implementation in the present work.

In particular, for channels with $L/D_h > 50$, where L is the length and D_h the hydraulic diameter, the channel is considered as long and the available kinetic conductance results based on the theory of the infinite long channels are applied. For channels of moderate length $5 < L/D_h < 50$, the end correction theory is introduced. This theory has been recently successfully implemented to define the fictitious increment length which must be added to the channel length in order to provide accurate results for the conductance by taking into account the channel end effects. Thus, the kinetic data base has been enriched with the values of the increment length in terms of the gas rarefaction. Finally, for short channels, i.e. $L/D_h < 5$, the above theory is

not valid and depending on the local pressure gradient, extensive simulations based on either linear or non-linear kinetic theory have been performed to provide a complete set of results for the channel conductance in terms of gas rarefaction, pressure difference and channel length. These simulations are computationally very expensive.

The case of a tube much longer than its radius ($R/L << 1$) with dimensionless pressure gradient much less than one, i.e. $X_P << 1$, even for large pressure differences ΔP, is tackled by the infinite capillary theory where the flow is considered as fully developed. In this scenario, the pressure varies only in the flow direction and end effects are neglected. Even more, the reduced flow rate at each cross section $G(\delta)$ is a function only of δ. Tabulated values of the reduced flow rate $G(\delta)$ for various values of the accommodation coefficient α are shown in Table B.1.

In order to extend the validity of the infinite capillary theory from long to medium tubes, the end effect theory is introduced. As described in Section 2.2, the end effect corrections depend only on the rarefaction parameter of the tube inlet and outlet region and are presented in Table B.2 for completeness purposes.

In the case of a pressure driven flow with a small pressure difference $P_2/P_1 > 0.9$, the flow can be considered linear even for short tubes and thus the linear BGK model can be implemented. The flow depends only on the rarefaction parameter and the geometrical ratio of the tube. The solution of the linear problem provides the dimensionless flow rates which are presented for various values of the rarefaction parameter and dimensionless length in Table B.3

As described in Chapter 2, in the case where $L/R \leq 10$ and $P_2/P_1 \leq 0.9$, the flow cannot be considered as linear and the problem must be tackled either with the DSMC method or with suitable nonlinear kinetic models solved by the parallelized discrete velocity method. The nonlinear flow depends on all three flow parameters and the dimensionless flow rate for indicative values of the flow parameters are presented in Tables B.4 and B.5.

Table B.1: Kinetic coefficient G for flow through circular channels in terms of δ_0 and specular-diffuse boundary conditions (α=1, 0.85, 0.7 and 0.5).

		G		
δ_0	α=1	α=0.85	α=0.7	α=0.5
0	0.752	1.02	1.40	2.26
0.001	0.751	1.01	1.39	2.24
0.01	0.744	0.999	1.36	2.17
0.1	0.715	0.941	1.25	1.94
0.2	0.702			
0.3	0.695	0.896	1.18	1.79
0.5	0.689	0.879	1.14	1.73
0.6	0.688			
1	0.693	0.870	1.12	1.67
1.5	0.709	0.879	1.12	1.66
2	0.729	0.896	1.13	1.66
3	0.777	0.941	1.17	1.70
4	0.829	0.992	1.22	1.74
5	0.884	1.05	1.28	1.79
6	0.940	1.10	1.33	1.85
7	0.997	1.16	1.39	1.91
8	1.06	1.22	1.45	1.97
9	1.11	1.28	1.51	2.02
10	1.17	1.34	1.57	2.08
11	1.23	1.40	1.63	2.14
13	1.35	1.52	1.75	2.27
15	1.48	1.64	1.87	2.39
20	1.78	1.95	2.18	2.70
30	2.40	2.56	2.80	3.32
40	3.02	3.19	3.42	3.94
50	3.64	3.81	4.04	4.56
100	6.76	6.93	7.16	7.68
200	13.0	13.2	13.4	13.9
500	31.7	31.9	32.1	32.6
1000	62.5	62.7	62.9	63.5
.	.	.	.	.
∞	63.0	63.2	63.4	63.9

Table B.2: Length increment ΔL_{tube} for various values of the rarefaction parameter δ.

δ	0.005	0.05	0.1	0.2	0.4	0.6	0.8	1	2
ΔL_{tube}	2.22	1.72	1.52	1.33	1.16	1.07	1.01	0.964	0.841

δ	4	6	8	10	...	∞
ΔL_{tube}	0.735	0.704	0.688	0.682	...	0.680

Table B.3: Flow rate W_{LIN} through a tube for various values of the rarefaction parameter δ and dimensionless length L/R, based on the linear BGK kinetic model with diffuse boundary conditions.

	W_{LIN}					
	δ					
L/R	0	0.1	1	2	5	10
0	0.999	1.04	1.37	1.72	2.77	4.35
1	0.672	0.696	0.892	1.10	1.70	2.63
5	0.311	0.316	0.373	0.440	0.642	0.988
10	0.191	0.192	0.217	0.251	0.362	0.554
20	0.110	0.108	0.118	0.136	0.195	0.296

Table B.4: Dimensionless flow rate W through short capillaries of cylindrical cross section vs. rarefaction parameter, pressure ratio and length (1/2).

		W						
		Rarefaction parameter of high pressure chamber (δ_1)						
L/R	P_2/P_1	0	0.1	0.5	1	2	5	10
	0.0	1.000	1.014	1.069	1.129	1.221	1.374	1.463
	0.1	0.900	0.910	1.000	1.032	1.180	1.350	1.435
0	0.3	0.700	0.719	0.788	0.862	0.987	1.221	1.366
	0.5	0.500	0.509	0.582	0.613	0.778	1.040	1.188
	0.7	0.3	0.305	0.354	0.38	0.493	0.717	0.914
	0.9	0.1	0.102	0.121	0.14	0.176	0.28	0.432
	0.0	0.953	0.965	1.018	1.074	1.165	1.312	1.404
	0.1	0.856	0.869	0.924	0.984	1.08	1.27	1.380
0.1	0.3	0.669	0.687	0.752	0.823	0.942	1.171	1.321
	0.5	0.475	0.486	0.528	0.583	0.688	0.948	1.150
	0.7	0.286	0.292	0.321	0.361	0.436	0.654	0.885
	0.9	0.095	0.099	0.114	0.131	0.164	0.246	0.333
	0.0	0.801	0.812	0.855	0.902	0.981	1.117	1.220
	0.1	0.721	0.731	0.775	0.826	0.911	1.080	1.200
0.5	0.3	0.562	0.577	0.630	0.688	0.786	0.994	1.223
	0.5	0.399	0.409	0.444	0.488	0.573	0.796	1.010
	0.7	0.241	0.246	0.270	0.300	0.363	0.541	0.762
	0.9	0.080	0.083	0.095	0.109	0.135	0.212	0.299
	0.0	0.672	0.680	0.715	0.754	0.819	0.948	1.062
	0.1	0.605	0.613	0.648	0.689	0.761	0.913	1.050
1	0.3	0.471	0.483	0.525	0.571	0.652	0.834	1.000
	0.5	0.336	0.343	0.370	0.405	0.474	0.658	0.866
	0.7	0.201	0.205	0.224	0.249	0.298	0.440	0.640
	0.9	0.067	0.070	0.080	0.091	0.112	0.170	0.264
	0.0	0.514	0.52	0.544	0.572	0.62	0.732	0.855
	0.1	0.463	0.468	0.493	0.521	0.573	0.699	0.842
2	0.3	0.36	0.368	0.396	0.428	0.486	0.63	0.795
	0.5	0.256	0.26	0.28	0.304	0.351	0.486	0.669
	0.7	0.153	0.156	0.17	0.19	0.22	0.319	0.471
	0.9	0.051	0.053	0.059	0.066	0.08	0.119	0.176
	0.0	0.311	0.312	0.322	0.334	0.361	0.436	0.543
	0.1	0.279	0.281	0.291	0.304	0.33	0.412	0.529
5	0.3	0.217	0.22	0.232	0.247	0.275	0.36	0.485
	0.5	0.155	0.156	0.163	0.175	0.197	0.271	0.388
	0.7	0.093	0.093	0.1	0.106	0.123	0.174	0.263
	0.9	0.031	0.031	0.035	0.038	0.044	0.064	0.098

Table B.5: Dimensionless flow rate W through short capillaries of cylindrical cross section vs. rarefaction parameter, pressure ratio and length (2/2).

		W						
		Rarefaction parameter of high pressure chamber (δ_1)						
L/R	P_2/P_1	20	50	100	200	500	1000	2000
0	0.0	1.512	1.534	1.533	1.529	1.526	1.523	1.522
	0.1	1.500	1.510	1.520	1.52	1.52	1.52	1.52
	0.3	1.437	1.440	1.450	1.45	1.46	1.46	1.46
	0.5	1.300	1.310	1.340	1.35	1.36	1.36	1.36
	0.7	1.05	1.09	1.13	1.13	1.15	1.14	1.14
	0.9	0.584	0.606	0.628	0.628	0.64	0.634	0.634
0.1	0.0	1.462	1.498	1.508	1.512	1.515	1.515	1.517
	0.1	1.45	1.49	1.51	1.51	1.51	1.51	1.51
	0.3	1.406	1.420	1.440	1.45	1.45	1.45	1.45
	0.5	1.270	1.350	1.370	1.39	1.39	1.39	1.39
	0.7	1.030	1.120	1.150	1.16	1.17	1.16	1.16
	0.9	0.387	0.421	0.433	0.436	0.44	0.436	0.436
0.5	0.0	1.302	1.383	1.435	1.462	1.484	1.494	1.493
	0.1	1.290	1.380	1.430	1.46	1.48	1.49	1.49
	0.3	1.267	1.330	1.390	1.43	1.45	1.46	1.46
	0.5	1.150	1.280	1.350	1.39	1.41	1.42	1.42
	0.7	0.937	1.080	1.150	1.19	1.20	1.20	1.20
	0.9	0.367	0.423	0.451	0.466	0.47	0.47	0.47
1	0.0	1.168	1.287	1.358	1.412	1.449	1.456	1.458
	0.1	1.160	1.280	1.350	1.41	1.45	1.46	1.46
	0.3	1.136	1.24	1.32	1.38	1.42	1.43	1.43
	0.5	1.04	1.20	1.29	1.35	1.39	1.40	1.40
	0.7	0.831	1.00	1.10	1.16	1.19	1.19	1.19
	0.9	0.415	0.499	0.549	0.579	0.594	0.594	0.594
2	0.0	0.974	1.156	1.259	1.339	1.397	1.406	1.404
	0.1	0.985	1.15	1.26	1.34	1.39	1.4	1.40
	0.3	0.96	1.11	1.23	1.31	1.36	1.37	1.37
	0.5	0.864	1.07	1.19	1.28	1.32	1.34	1.34
	0.7	0.672	0.884	1.00	1.09	1.13	1.13	1.13
	0.9	0.251	0.33	0.373	0.407	0.422	0.422	0.422
5	0.0	0.695	0.917	1.068	1.184	1.271	1.282	1.284
	0.1	0.695	0.917	1.068	1.184	1.271	1.282	1.284
	0.3	0.663	0.87	1.03	1.15	1.23	1.24	1.23
	0.5	0.571	0.828	0.993	1.11	1.18	1.2	1.19
	0.7	0.411	0.658	0.814	0.922	0.975	0.98	0.986
	0.9	0.164	0.263	0.325	0.368	0.389	0.391	0.393

References

[1] T. ABE. Derivation of the Lattice Boltzmann Method by Means of the Discrete Ordinate Method for the Boltzmann Equation. *Journal of Computational Physics*, **131**[1]:241–246, feb 1997. 12

[2] M. ABRAHAMYAN. Some Aspects of the Physics of Gas Flow in the Respiratory System. *International Journal of Clinical and Experimental Medical Sciences*, **4**[1]:1–4, 2018. 197

[3] V. D. AKINSHIN, A. I. MAKAROV, V. D. SELEZNEV, AND F. M. SHARIPOV. Flow of a rarefied gas in a plane channel of finite length for a wide range of knudsen numbers. *Journal of Applied Mechanics and Technical Physics*, **29**[1]:97–103, 1988. 32

[4] V. D. AKINSHIN, A. M. MAKAROV, V. D. SELEZNEV, AND F. M. SHARIPOV. Rarefied gas motion in a short planar channel over the entire knudsen number range. *Journal of Applied Mechanics and Technical Physics*, **30**[5]:713–717, 1990. 32

[5] A. ALEXEENKO, D. LEVIN, S. GIMELSHEIN, M. IVANOV, AND A. KETSDEVER. Numerical and experimental study of orifice flow in the transitional regime. In *35th AIAA Thermophysics Conference*. American Institute of Aeronautics and Astronautics, jun 2001. 14

[6] P. ANDRIES, P. LE TALLEC, J. P. PERLAT, AND B. PERTHAME. The Gaussian-BGK model of Boltzmann equation with small Prandtl number. *European Journal of Mechanics - B/Fluids*, **19**[6]:813–830, nov 2000. 9

[7] V. V. ARISTOV. *Direct Methods for Solving the Boltzmann Equation and Study of Nonequilibrium Flows*. Springer Netherlands, 2001. 46

[8] V. V. ARISTOV, E. M. SHAKHOV, V. A. TITAREV, AND S. A. ZABELOK. Comparative study for rarefied gas flow into vacuum through a short circular pipe. *Vacuum*, **103**:5–8, may 2014. 45

REFERENCES

[9] L. L. BAKER AND N. G. HADJICONSTANTINOU. Variance-reduced Monte Carlo solutions of the Boltzmann equation for low-speed gas flows: A discontinuous Galerkin formulation. *International Journal for Numerical Methods in Fluids*, **58**[4]:381–402, oct 2008. 12

[10] R. BALESCU. *Equilibrium and nonequilibrium statistical mechanics*. John Wiley and sons, New York, 1975. 3

[11] M. BAO AND H. YANG. Squeeze film air damping in MEMS. *Sensors and Actuators A: Physical*, **136**[1]:3–27, may 2007. 13

[12] P. L. BHATNAGAR, E. P. GROSS, AND M. KROOK. A Mode for Collision Processes in Gases. I. Small Amplitude Processes in Charged and Neutral One-Component Systems. *Physical Review*, **94**[3]:511–525, may 1954. 8

[13] G. A. BIRD. *Molecula Gas Dynamics and the Direct Simulation of Gas Flows*. Oxford University Press, Oxford, 1994. 12

[14] G. A. BIRD. Effect of inlet guide vanes and sharp blades on the performance of a turbomolecular pump. *Journal of Vacuum Science & Technology A: Vacuum, Surfaces, and Films*, **29**[1]:011016, jan 2011. 13

[15] L. BOLTZMANN. *Lectures on Gas Theory*. University of California Press, Berkeley, 1964. Translated by Stephen G. Brush. 2

[16] G. BREYANNIS, S. VAROUTIS, AND D. VALOUGEORGIS. Rarefied gas flow in concentric annular tube: Estimation of the Poiseuille number and the exact hydraulic diameter. *European Journal of Mechanics - B/Fluids*, **27**[5]:609–622, 2008. 30, 87

[17] C. CERCIGNANI. *The Boltzmann equation and its applications*. Springer, New York, 1988. 10

[18] C. CERCIGNANI AND C. D. PAGANI. Variational Approach to Boundary-Value Problems in Kinetic Theory. *Physics of Fluids*, **9**[6]:1167–1173, 1966. 12

216

[19] C. CERCIGNANI AND F. SHARIPOV. Gaseous mixture slit flow at intermediate Knudsen numbers. *Physics of Fluids A*, **4**[6]:1283–1289, 1992. 9

[20] CARLO CERCIGNANI. *Theory and application of the Boltzmann equation.* Scottish Academic Press Distributed by Chatto and Windus, Edinburgh London, 1975. 10

[21] S. CHAPMAN. On the law of distribution of molecular velocities and on the theory of viscosity and thermal conduction, in a non-uniform simple monoatomic gas. *Philosophical Transactions of the Royal Society of London*, **216**:279–341, 1916. 7

[22] S. CHAPMAN AND T. G. COWLING. *The mathematical theory of non-uniform gases.* Cambridge University Press, Cambridge, 1970. 9

[23] Z. CHAVIS AND R. WILMOTH. Plume Modeling and Application to Mars 2001 Odyssey Aerobraking. *Journal of Spacecraft and Rockets*, **42**:450–456, 2005. 14

[24] D. G. CORONELL AND K. F. JENSEN. Monte Carlo simulations of very low pressure chemical vapor deposition. *Journal of Computer-Aided Materials Design*, **1**:3–26, 1993. 14

[25] CHR. DAY, V. HAUER, G. CLASS, D. VALOUGEORGIS, AND M. WYKES. Development of a simulation code for ITER vacuum flows. In *Proceedings of the 21st IAEA conference*, IAEA Fusion Energy Conf., 2006. 15

[26] CHR. DAY AND D. MURDOCH. The ITER Vacuum Systems. *Journal of Physics: Conference Series*, **114**, 2008. 2, 13, 14

[27] R. G. DEISSLER. An analysis of second-order slip flow and temperature-jump boundary conditions for rarefied gases. *International Journal of Heat and Mass Transfer*, **7**[6]:681–694, 1964. 7

[28] N. DEO. *Graph Theory with Applications to Engineering and Computer Science.* Dover Publications Inc., 2016. 87

REFERENCES

[29] R. A. EAST. A reusable space-rescue vehicle: re-entry simulation. *Philosophical Transactions of the Royal Society A*, **357**:2177–2195, 1999. 14

[30] D. ENSKOG. Bermerkungen zu einer Fundamentalgleichung in der kinetischen gastheorie. *Phys. Z.*, **12**:533–539, 1911. 7

[31] J. H. FERZIGER AND H. G. KAPER. *Mathematical Theory of Transport Processes in Gases*. North-Holland, Amsterdam, 1972. 3, 7

[32] A. FREZZOTTI, G. P. GHIROLDI, AND L. GIBELLI. Solving the Boltzmann equation on GPUs. *Computer Physics Communications*, **182**[12]:2445–2453, dec 2011. 12

[33] M. GAD-EL-HAK. *The MEMS handbook*. The Mechanical engineering handbook series. CRC Press, 2002. 13

[34] M. A. GALLIS AND J. R. TORCZYNSKI. Direct simulation Monte Carlo-based expressions for the gas mass flow rate and pressure profile in a microscale tube. *Physics of Fluids*, **24**[1]:012005, jan 2012. 45

[35] M. A. GALLIS, J. R. TORCZYNSKI, D. J. RADER, AND G. A. BIRD. Convergence behavior of a new DSMC algorithm. *Journal of Computational Physics*, **228**[12]:4532–4548, jul 2009. 12

[36] Gas networks simulation. (Wikipedia source). 15

[37] S. GIORS, E. COLOMBO, F. INZOLI, F. SUBBA, AND R. ZANINO. Computational fluid dynamic model of a tapered Holweck vacuum pump operating in the viscous and transition regimes. i. vacuum performance. *Journal of Vacuum Science Technology A: Vacuum, Surfaces and Films*, **24**[4]:1584–1591, 2006. 13

[38] C. GLEASON-GONZÁLEZ, S. VAROUTIS, V. HAUER, AND CHR. DAY. Simulation of neutral gas flow in a tokamak divertor using the Direct Simulation MonteCarlo method. *Fusion Engineering and Design*, **89**[7-8]:1042–1047, oct 2014. 161

[39] P. A. GNOFFO. Planetary-entry gas dynamics. *Annual Review of Fluid Mechanics*, **31**:459–494, 1999. 2, 13, 14

[40] H. GRAD. On the kinetic theory of rarefied gases. *Communications on Pure and Applied Mathematics*, **2**[4]:331–407, 1949. 3

[41] G. P. GREYVENSTEIN AND D. P. LAURIE. A segregated CFD approach to pipe network analysis. *International Journal for Numerical Methods in Engineering*, **37**[21]:3685–3705, nov 1994. 15

[42] J. GROTBERG. Respiratory fluid mechanics. *Physics of Fluids*, **23**[2]:021301, feb 2011. 197

[43] H. Y. GUO, L. ZHANG, L. L. ZHANG, AND J. X. ZHOU. Optimal placement of sensors for structural health monitoring using improved genetic algorithms. *Smart Materials and Structures*, **13**[3]:528–534, apr 2004. 197

[44] G. HAGER AND G. WELLEIN. *Introduction to High Performance Computing for Scientists and Engineers*. Taylor & Francis GroupBookpoint Limited distributor, Abingdon Abingdon, 2010. 12

[45] B. B. HAMEL. Kinetic Model for Binary Gas Mixtures. *Physics of Fluids*, **8**[3]:418–425, 1965. 9

[46] V. HAUER AND CHR. DAY. Conductance modelling of ITER vacuum systems. *Fusion Engineering and Design*, **84**[2-6]:903–907, jun 2009. 161

[47] V. HAUER AND CHR. DAY. ITER divertor gas flow modelling. *Fusion Engineering and Design*, **98-99**:1775–1778, oct 2015. 161

[48] D. HILBERT. *Grundzüge einer allgemein Theorie der linearen Integralgleichungen*. Teubner, Leipzig, 1912. 3

[49] J. O. HIRSCHFELDER, C. F. CURTISS, AND R. B. BIRD. *The molecular theory of gases and liquids*. Wiley, New York, 1964. 9

[50] C. M. HO AND Y. C. TAI. Micro-electro-mechanical systems (MEMS) and fluid flows. *Annual Review of Fluid Mechanics*, **30**:579–612, 1998. 2, 13

REFERENCES

[51] J. H. HOLLAND. Genetic Algorithms. *Scientific American*, **267**[1]:66–73, 1992. 197

[52] L. H. HOLWAY. New statistical models for kinetic theory: methods of construction. *Physics of fluids*, **9**[9], 1966. 9

[53] M. HOURY, L. GARGIULO, C. BALORIN, V. BRUNO, D. KELLER, H. ROCHE, N. KAMMERER, Y. MEASSON, F. CARREL, AND V. SCHOEPFF. Diagnostics carried by a light multipurpose deployer for vacuum vessel interventions. *Fusion Engineering and Design*, **86**[9-11]:1868–1871, oct 2011. 14

[54] A. B. HUANG AND D. L. HARTLEY. Nonlinear Rarefied Couette Flow with Heat Transfer. *Physics of Fluids*, **11**[6]:1321–1326, 1968. 11

[55] M. IVANOV, A. KASHKOVSKY, S. GIMELSHEIN, G. MARKELOV, A. ALEXEENKO, Y. BONDAR, G. ZHUKOVA, S. NIKIFOROV, AND P. VASCHENKOV. SMILE system for 2D/3D DSMC computations. In *25th International Symposium on Rarefied Gas Dynamics*. AIP, 2006. 14

[56] M. S. IVANOV AND S. F. GIMELSHEIN. Computational hypersonic rarefied flows. *Annual Review of Fluid Mechanics*, **30**:469–505, 1998. 13

[57] I. N. IVCHENKO, S. K. LOYALKA, AND R. V. THOMPSON JR. *Analytical methods for problems of molecular transport*. Springer, Dordrecht, The Netherlands, 2007. 14

[58] A. R. JHA. *Cryogenic technology and applications*. Elsevier, Oxford, 2006. 14

[59] W. JITSCHIN AND S. LUDWIG. Dynamical behaviour of the Pirani sensor. *Vacuum*, **75**[2]:169–176, 2004. 2

[60] K. JOUSTEN. *Handbook of Vacuum Technology*. Wiley-VCH, Berlin, 2008. 29

[61] K. JOUSTEN, G. MESSER, AND D. WANDREY. A precision gas flowmeter for vacuum metrology. *Vacuum*, **44**[2]:135–141, 1993. 14

[62] G. E. KARNIADAKIS AND A. BESKOK. *Micro flows: Fundamentals and simulation*. Springer-Verlag, New York, 2002. 7, 13, 26

[63] H. KATSURAYAMA AND T. ABE. Particle Simulation of Electrodynamic Aerobraking in a Hypersonic Rarefied Regime. *AIP Conference Proceedings*, **1333**[1]:1301–1306, 2011. 14

[64] Y. Y. KLOSS, P. V. SHUVALOV, AND F. G. TCHEREMISSINE. Solving Boltzmann equation on GPU. *Procedia Computer Science*, **1**[1]:1083–1091, may 2010. 12

[65] M. KNUDSEN. Die Molekularstroemung der Gase durch Offnungen und die Effusion. *Annalen der Physik*, **333**[5]:999–1016, 1909. 5

[66] S. KOSUGE. Model Boltzmann equation for gas mixtures: Construction and numerical comparison. *European Journal of Mechanics - B/Fluids*, **28**[1]:170–184, jan 2009. 9

[67] P. KOWALCZYK, A. PALCZEWSKI, G. RUSSO, AND Z. WALENTA. Numerical solutions of the Boltzmann equation: comparison of different algorithms. *European Journal of Mechanics - B/Fluids*, **27**[1]:62–74, 2008. 11

[68] I. LAKATOS. *Proofs and refutations : the logic of mathematical discovery*. Cambridge University Press, Cambridge New York, 1976. 80

[69] G. J. LEBEAU AND F. E. LUMPKIN III. Application highlights of the DSMC Analysis Code (DAC) software for simulating rarefied flows. *Computer Methods in Applied Mechanics and Engineering*, **191**:595–609, 2001. 14

[70] R. LEGTENBERG, A. W. GROENEVELD, AND M. ELWENSPOEK. Comb-drive actuators for large displacements. *Journal of Micromechanics and Microengineering*, **6**[3]:320, 1996. 13

[71] G. LIU. A method for constructing a model form for the Boltzmann equation. *Physics of Fluids A: Fluid Dynamics*, **2**[2]:277–280, 1990. 9

[72] D. A. LOCKERBY AND J. M. REESE. Near Wall scaling of the Navier-Stokes constitutive relations for accurate micro gas flow simulations. In *5th*

International Conference on Nanochannels, Microchannels and Minichannels (ICNMM), June 2007. 7

[73] W. A. MAUL, G. KOPASAKIS, L. M. SANTI, T. S. SOWERS, AND A. CHICATELLI. Sensor selection and optimization for health assessment of aerospace systems. *Journal of Aerospace Computing, Information, and Communication*, **5**[1]:16–34, jan 2008. 197

[74] C. MAXWELL. On Stresses in Rarified Gases Arising from Inequalities of Temperature. *Philosophical Transactions of the Royal Society of London*, **170**:231–256, 1879. 10

[75] F. J. McCORMACK. Construction of linearized kinetic models for gaseous mixtures and molecular gases. *Physics of Fluids*, **16**[12]:2095–2105, 1973. 9

[76] J. A. McLENNAN. *Introduction to non-equilibrium statistical mechanics*. Prentice-Hall, 1996. 1

[77] L. MIEUSSENS. Discrete-Velocity Models and Numerical Schemes for the Boltzmann-BGK Equation in Plane and Axisymmetric Geometries. *Journal of Computational Physics*, **162**[2]:429–466, aug 2000. 46

[78] L. MIEUSSENS AND H. STRUCHTRUP. Numerical comparison of Bhatnagar-Gross-Krook models with proper Prandtl number. *Physics of Fluids*, **16**[8]:2797–2813, 2004. 9

[79] S. MISDANITIS, S. PANTAZIS, AND D. VALOUGEORGIS. Rarefied flow between plates of finite length via an efficient fully deterministic nonlinear algorithm. In *Proceedings*, 2nd European Conference on Microfluidics, 2010. 12

[80] S. MISDANITIS, S. PANTAZIS, AND D. VALOUGEORGIS. Pressure driven rarefied gas flow through a slit and an orifice. *Vacuum*, **86**[11]:1701–1708, may 2012. 43, 86

[81] S. MISDANITIS AND D. VALOUGEORGIS. Design of steady-state isothermal gas distribution systems consisting of long tubes in the whole range of the Knudsen number. *Journal of Vacuum Science & Technology A: Vacuum, Surfaces, and Films*, **29**[6]:061602, nov 2011. 82

222

[82] S. Misdanitis and D. Valougeorgis. Modeling of ITER related vacuum gas pumping distribution systems. *Fusion Engineering and Design*, **88**[9-10]:2352–2356, oct 2013. 82

[83] K. Moe, M. M. Moe, and S. D. Wallace. Improved Satellite Drag Coefficient Calculations from Orbital Measurements of Energy Accommodation. *Journal of Spacecraft and Rockets*, **35**[3]:266–272, may 1998. 2, 14

[84] T. F. Morse. Kinetic Model Equations for a Gas Mixture. *Physics of Fluids*, **7**[12]:2012–2013, 1964. 9

[85] E. P. Muntz. Rarefied Gas Dynamics. *Annual Review of Fluid Mechanics*, **21**:387–422, 1989. 13

[86] S. Naris and D. Valougeorgis. The driven cavity flow over the whole range of the Knudsen number. *Physics of Fluids*, **17**[9]:907106.1–907106.12, 2005. 11

[87] S. Naris and D. Valougeorgis. Rarefied gas flow in a triangular duct based on a boundary fitted lattice. *European Journal of Mechanics - B/Fluids*, **27**:810–822, 2008. 11, 25

[88] S. Naris, D. Valougeorgis, F. Sharipov, and D. Kalempa. Discrete velocity modelling of gaseous mixture flows in MEMS. *Superlattices and Microstructures*, **35**[3-6]:629–643, 2004. 9

[89] S. Naris, N. Vasileiadis, D. Valougeorgis, A. Hashad, and W. Sabuga. Computation of the effective area and associated uncertainties of non-rotating piston gauges FPG and FRS. *Metrologia*, **56**[1]:015004, nov 2018. 14

[90] W. D. Niven. *Scientific Papers of James Clerk Maxwell*. Dover Publications, Inc., New York, 1965. 2

[91] R. R. Nourgaliev, T. N. Dinh, T. G. Theofanous, and D.Joseph. The lattice Boltzmann equation method: theoretical interpretation, numerics and implications. *International Journal of Multiphase Flow*, **29**[1]:117–169, 2003. 12

REFERENCES

[92] S. H. Oh, K. C. Lee, J. Chun, M. Kim, and S. S. Lee. Micro heat flux sensor using copper electroplating in SU-8 microstructures. *Journal of Micromechanics and Microengineering*, **11**[3]:221, 2001. 13

[93] T. Ohwada, Y. Sone, and K. Aoki. Numerical analysis of the Poiseuille and thermal transpiration flows between two parallel plates on the basis of the Boltzmann equation for hard-sphere molecules. *Physics of Fluids A: Fluid Dynamics*, **1**[12]:2042–2049, 1989. 11

[94] A. J. Osiadacz. Method of steady-state simulation of a gas network. *International Journal of Systems Science*, **19**[11]:2395–2405, jan 1988. 15

[95] A. Otis and W. Bembower. Effect of Gas Density on Resistance to Respiratory Gas Flow in Man. *Journal of Applied Physiology*, **2**[6]:300–306, dec 1949. 197

[96] S. Pantazis. *Simulation of Transport Phenomena in Conditions far from Thermodynamic Equilibrium via Kinetic Theory with Applications in Vacuum Technology and MEMS*. Ph.D. thesis, University of Thessaly - Department of Mechanical Engineering, Volos, Greece, 2011. 42, 45, 47, 86

[97] S. Pantazis, S. Naris, C. Tantos, D. Valougeorgis, J. André, F. Millet, and J. P. Perin. Nonlinear vacuum gas flow through a short tube due to pressure and temperature gradients. *Fusion Engineering and Design*, **88**[9-10]:2384–2387, oct 2013. 86

[98] S. Pantazis and D. Valougeorgis. The Cercignani-Lampis boundary conditions in rectangular micro-channel flows. In *Proceedings*, 1st GASMEMS Workshop- Eindhoven, 2009. 11

[99] S. Pantazis and D. Valougeorgis. Heat transfer through rarefied gases between coaxial cylindrical surfaces with arbitrary temperature difference. *European Journal of Mechanics - B/Fluids*, **29**[6]:494–509, nov 2010. 46

[100] S. Pantazis and D. Valougeorgis. Efficient Simulation of Rarefied Gas Flows Through Tubes of Finite Length Based on Kinetic Model Equations. *AIP Conference Proceedings*, **1333**[1]:963–968, 2011. 12

224

[101] S. Pantazis and D. Valougeorgis. Rarefied gas flow through a cylindrical tube due to a small pressure difference. *European Journal of Mechanics - B/Fluids*, **38**:114–127, mar 2013. 36, 46, 86

[102] S. Pantazis, D. Valougeorgis, and F. Sharipov. End corrections for rarefied gas flows through capillaries of finite length. *Vacuum*, **97**:26–29, nov 2013. 85

[103] S. Pantazis, D. Valougeorgis, and F. Sharipov. End corrections for rarefied gas flows through circular tubes of finite length. *Vacuum*, **101**:306–312, mar 2014. 36, 37, 85

[104] S. Pantazis, S. Varoutis, V. Hauer, Chr. Day, and D. Valougeorgis. Gas-surface scattering effect on vacuum gas flows through rectangular channels. *Vacuum*, **85**[12]:1161–1164, jun 2011. 11

[105] Pipe2020: Gas. (Software's official web page). 15

[106] M. C. Potter and D. C. Wiggert. *Mechanics of Fluids*. Prentice Hall, 1997. 15

[107] Z. Poulakis. *Design optimization and damage detection in gas distribution networks with the use of classical and evolutionary algorithms*. Diploma thesis, Universiy of Thessaly, 2002. 15, 91, 94

[108] G. A. Radtke, N. G. Hadjiconstantinou, and W. Wagner. Low-noise Monte Carlo simulation of the variable hard sphere gas. *Physics of Fluids*, **23**[3]:030606, mar 2011. 12

[109] J. M. Reese, M. A. Gallis, and D. A. Lockerby. New directions in fluid dynamics: non-equilibrium aerodynamic and microsystem flows. *Philosophical Transactions of the Royal Society A*, **361**:2967–2988, 2003. 2, 7, 13

[110] D. Reiter, M. Baelmans, and P. Börner. The EIRENE and B2-EIRENE Codes. *Fusion Science and Technology*, **47**[2]:172–186, feb 2005. 160

REFERENCES

[111] O. I. ROVENSKAYA. Comparative analysis of the numerical solution of full Boltzmann and BGK model equations for the Poiseuille flow in a planar microchannel. *Computers & Fluids*, **81**:45–56, jul 2013. 45

[112] C. SCHERER, J. PROLO FILHO, AND L. BARICHELLO. An analytical approach to the unified solution of kinetic equations in rarefied gas dynamics. i. flow problems. *Zeitschrift für Angewandte Mathematik und Physik (ZAMP)*, **60**:70–115, 2009. 12

[113] E. M. SHAKHOV. Generalization of the Krook kinetic equation. *Fluid Dynamics*, **3**[95], 1968. 8

[114] E. M. SHAKHOV. Linearized two-dimensional problem of rarefied gas flow in a long channel. *Comput Math Math Phys*, **39**[7]:1192–1200, 1999. 32

[115] F. SHARIPOV. Rarefied gas flow through a long tube at arbitrary pressure and temperature drops. *Journal of Vacuum Science Technology A: Vacuum, Surfaces, and Films*, **15**[4]:2434–2436, 1997. 34

[116] F. SHARIPOV. Rarefied gas flow through a long rectangular channel. *Journal of Vacuum Science and Technology A*, **17**[5]:3062–3066, 1999. 24, 25

[117] F. SHARIPOV. Application of the Cercignani-Lampis scattering kernel to calculations of rarefied gas flows. I. Plane flow between two parallel plates. *European Journal of Mechanics - B/Fluids*, **21**:113–123, 2002. 11

[118] F. SHARIPOV. Application of the Cercignani-Lampis scattering kernel to calculations of rarefied gas flows. II. Slip and jump coefficients. *European Journal of Mechanics - B/Fluids*, **22**:133–143, 2003. 11

[119] F. SHARIPOV. Hypersonic flow of rarefied gas near the Brazilian satellite during its reentry into atmosphere. *Brazilian Journal of Physics*, **33**:398–405, 2003. 14

[120] F. SHARIPOV. *Rarefied Gas Dynamics : Fundamentals for Research and Practice*. Wiley-VCH, Weinheim, Germany, 2015. 93

226

[121] F. SHARIPOV AND G. BERTOLDO. Numerical solution of the linearized Boltz-mann equation for an arbitrary intermolecular potential. *Journal of Computa-tional Physics*, **228**:3345–3357, May 2009. 11

[122] F. SHARIPOV, P. FAHRENBACH, AND A. ZIPPA. Numerical modeling of the Holweck pump. *Journal of Vacuum Science and Technology A*, **23**[5]:1331–1339, 2005. 13

[123] F. SHARIPOV AND I. GRAUR. General approach to transient flows of rarefied gases through long capillaries. *Vacuum*, **100**:22–25, feb 2014. 85

[124] F. SHARIPOV AND V. SELEZNEV. Rarefied gas flow through a long tube at any pressure ratio. *Journal of Vacuum Science and Technology A*, **12**[5]:2933–2935, 1994. 25, 86

[125] F. SHARIPOV AND V. SELEZNEV. Data on internal rarefied gas flows. *Journal of Physical and Chemical Reference Data*, **27**[3]:657–706, 1998. 7, 8, 27, 32, 36, 85

[126] C. SHEN. *Rarefied Gas Dynamics: Fundamentals, Simulations and Micro Flows*. Springer, 2005. 7, 12

[127] Y. SONE. *Kinetic Theory and Fluid Dynamics*. Birkhaeuser, Boston, 2002. 7, 12

[128] H. STRUCHTRUP AND M. TORRILHON. Regularization of Grad's 13 moment equations: Derivation and linear analysis. *Physics of Fluids*, **15**[9]:2668–2680, 2003. 12

[129] P. J. SUN, J. Y. WU, P. ZHANG, L. XU, AND M. L. JIANG. Experimental study of the influences of degraded vacuum on multilayer insulation blankets. *Cryogenics*, **49**[12]:719–726, 2009. 13

[130] Q. SUN, I. D. BOYD, AND J. FAN. Development of an information preserva-tion method for subsonic, micro-scale gas flows. *AIP Conference Proceedings*, **585**[1]:547–553, 2001. 12

REFERENCES

[131] S. TAKATA, H. SUGIMOTO, AND S. KOSUGE. Gas separation by means of the Knudsen compressor. *European Journal of Mechanics - B/Fluids*, **26**[2]:155–181, 2007. 13

[132] V. A. TITAREV. Efficient Deterministic Modelling of Three-Dimensional Rarefied Gas Flows. *Communications in Computational Physics*, **12**[01]:162–192, jul 2012. 46

[133] V. A. TITAREV. Rarefied gas flow in a circular pipe of finite length. *Vacuum*, **94**:92–103, aug 2013. 36, 86

[134] V. A. TITAREV AND E. M. SHAKHOV. Computational study of a rarefied gas flow through a long circular pipe into vacuum. *Vacuum*, **86**[11]:1709–1716, may 2012. 45, 86

[135] V. A. TITAREV AND E. M. SHAKHOV. Efficient method for computing rarefied gas flow in a long finite plane channel. *Computational Mathematics and Mathematical Physics*, **52**[2]:269–284, feb 2012. 32

[136] K. TOMARIKAWA, S. YONEMURA, T. TOKUMASU, AND T. KOIDO. Numerical analysis of gas flow in porous media with surface reaction. *AIP Conference Proceedings*, **1333**[1]:796–801, 2011. 13

[137] R. J. TRUDEAU. *Introduction to Graph Theory*. Dover Publications Inc., 1994. 80

[138] W. UMRATH. *Fundamentals of Vacuum Technology*. Leybold, Cologne, 1998. 13

[139] D. VALOUGEORGIS. An analytical solution of the S-model kinetic equations. *Zeitschrift für Angewandte Mathematik und Physik (ZAMP)*, **54**:112–124, 2003. 12

[140] D. VALOUGEORGIS. The friction factor of a rarefied gas flow in a circular tube. *Physics of Fluids*, **19**[9]:091702, sep 2007. 30, 93

[141] D. VALOUGEORGIS AND S. NARIS. Acceleration schemes of the discrete velocity method: Gaseous flows in rectangular microchannels. *SIAM Journal of Scientific Computing*, **25**[2]:534–552, 2003. 11

[142] D. VALOUGEORGIS, N. VASILEIADIS, AND V. TITAREV. Validity range of linear kinetic modeling in rarefied pressure driven single gas flows through circular capillaries. *European Journal of Mechanics - B/Fluids*, **64**:2–7, jul 2017. 46, 47

[143] S. VAROUTIS. *Reverse design and optimization of incompressible and compressible networks*. Master's thesis, University of Thessaly, 2004. 15, 91, 94

[144] S. VAROUTIS. *Flows through channels of various cross sections in the whole range of the Knudsen number using deterministic and stochastic approaches (in Greek)*. Ph.D. thesis, University of Thessaly - Department of Mechanical Engineering, Volos, Greece, 2008. 87

[145] S. VAROUTIS, J. LIHNAROPOULOS, D. MATHIOULAKIS, A. TSEREPI, AND D. VALOUGEORGIS. Estimation of the Poiseuille number and of the exact hydraulic diameter in rarefied gas flows through channels of various cross sections. In *1st European Conference on Microfluidics*, 2008. 30, 31, 87

[146] S. VAROUTIS, S. NARIS, V. HAUER, CHR. DAY, AND D. VALOUGEORGIS. Computational and experimental study of gas flows through long channels of various cross sections in the whole range of the Knudsen number. *Journal of Vacuum Science and Technology A*, **27**[1]:89–100, 2009. 11

[147] S. VAROUTIS AND D. VALOUGEORGIS. Estimation of the Poiseuille Number in Gas Flows Through Rectangular Nano- and Micro-channels in the Whole Range of the Knudsen Number. In *IUTAM Symposium on Advances in Micro- and Nanofluidics*, pages 79–86. Springer Netherlands, 2009. 30

[148] S. VAROUTIS, D. VALOUGEORGIS, O. SAZHIN, AND F. SHARIPOV. Rarefied gas flow through short tubes into vacuum. *Journal of Vacuum Science & Technology A: Vacuum, Surfaces, and Films*, **26**[2]:228–238, mar 2008. 45, 46, 86

REFERENCES

[149] S. Varoutis, D. Valougeorgis, and F. Sharipov. Application of the integro-moment method to steady-state two-dimensional rarefied gas flows subject to boundary induced discontinuities. *Journal of Computational Physics*, **227**[12]:6272–6287, jun 2008. 12

[150] S. Varoutis, D. Valougeorgis, and F. Sharipov. Simulation of gas flow through tubes of finite length over the whole range of rarefaction for various pressure drop ratios. *Journal of Vacuum Science & Technology A: Vacuum, Surfaces, and Films*, **27**[6]:1377–1391, nov 2009. 45, 46, 86

[151] A. Venkattraman and A. A. Alexeenko. MolecularModels for DSMC Simulations of Metal Vapor Deposition. In *27th International Symposium on Rarefied Gas Dynamics*. AIP, 2011. 14

[152] J. P. Vítkovský, A. R. Simpson, and M. F. Lambert. Leak detection and calibration using transients and genetic algorithms. *Journal of Water Resources Planning and Management*, **126**[4]:262–265, jul 2000. 197

[153] W. Wagner. A convergence proof for Bird's direct simulation Monte Carlo method for the Boltzmann equation. *Journal of Statistical Physics*, **66**[3-4]:1011–1044, feb 1992. 12

[154] H. L. Weissberg. End Correction for Slow Viscous Flow through Long Tubes. *Physics of Fluids*, **5**[9]:1033, 1962. 32

[155] P. Welander. On the temperature jump in a rarefied gas. *Arkiv for fysik*, **7**:507–553, 1954. 8

[156] Y. Zheng and H. Struchtrup. Ellipsoidal statistical Bhatnagar-Gross-Krook model with velocity-dependent collision frequency. *Physics of Fluids*, **17**[12]:127103, 2005. 9

[157] X. Zhong, R. W. MacCormack, and D. R. Chapman. Stabilization of the Burnett Equations and Application to Hypersonic Flows. *AIAA Journal*, **31**[6]:1036–1043, 1993. 7